Development of Agro and Industrial Waste Based Nano-adsorbents for Decontamination of Water

Thesis submitted for the degree of

Doctor of Philosophy (Science)

Jadavpur University, India

By

Adwitiya Chakraborty

Registration Number: SCHEM110172

Date - 10.02.2022

Advanced Ceramics and Composites Division
CSIR-Central Glass and Ceramic Research Institute
Kolkata – 700 032, India

July 2024

सीएसआईआर–केन्द्रीय कॉच एवं सिरामिक अनुसंधान संस्थान
(वैज्ञानिक तथा औद्योगिक अनुसंधान परिषद)
विज्ञान एवं प्रौद्योगिकी मंत्रालय के अधीन, भारत सरकार
196, राजा एस. सी. मल्लिक रोड, कोलकाता - 700 032, भारत
CSIR - CENTRAL GLASS & CERAMIC RESEARCH INSTITUTE
(Council of Scientific & Industrial Research)
Under Ministry of Science & Technology, Government of India
196, Raja S. C. Mullick Road, Jadavpur, Kolkata - 700 032, India

CERTIFICATE FROM THE SUPERVISOR

This is to certify that the thesis entitled, **"Development of Agro and Industrial Waste Based Nano-adsorbents for Decontamination of Water"** submitted by **Smt. Adwitiya Chakraborty** who got her name registered on 10th February, 2022 for the award of Ph. D. (Science) Degree of Jadavpur University, is absolutely based upon her own work under the supervision of **Dr. Milan Kanti Naskar** and that neither this thesis nor any part of it has been submitted for either any degree / diploma or any other academic award anywhere before.

Milan Kanti Naskar 18/7/24

(Signature of the Supervisor, date with official seal)

Dr. Milan Kanti Naskar
Chief Scientist & Professor (AcSIR)
Head, Advanced Ceramics & Composites Division
CSIR-Central Glass & Ceramic Research Institute
196, Raja S.C. Mullick Road
Kolkata-700 032

दूरभाष / Phone : निदेशक / Director : +91 33 2473 5829, कार्यालय / Office : 2473 3469 / 76 / 77 / 96, 2483 7340-46, 2483 7349-50
DID Lines : 2483 8079 / 8082, फैक्स / Fax : (033) 2473 0957, 2473 6082, 2483 7399, 2483 8085, ई-मेल / Email : dir_office@cgcri.res.in
वेबसाइट / Website : www.cgcri.res.in

DECLARATION

I hereby declare that the work presented in this thesis entitled, "**Development of Agro and Industrial Waste Based Nano-adsorbents for Decontamination of Water**" has been carried out by me at the Advanced Ceramics and Composites Division (ACCD), CSIR-Central Glass and Ceramic Research Institute, Kolkata-700032, India under the supervision of **Dr. Milan Kanti Naskar**, Chief Scientist & Prof. (AcSIR), CSIR-Central Glass and Ceramic Research Institute, Kolkata-700032. Neither this thesis nor any part of it has been submitted for any degree / diploma or any other academic award anywhere before.

Adwitiya Chakraborty 18/07/2024

(Adwitiya Chakraborty, Senior Research Fellow)

Dedicated to my
Parents & Teachers

Acknowledgements

This thesis represents not only my laboratory work at CSIR-Central Glass and Ceramic Research Institute (CSIR-CGCRI), Kolkata, but also reflects a transformative journey that has reshaped my personality in many ways. This journey has been a collective effort, and I am indebted to all those whose wishes and blessings have made this possible. I would like to take this opportunity to extend my sincere gratitude to everyone who has been involved, directly or indirectly, in making the research work described in this thesis a reality.

First of all, I would like to express my deepest gratitude to my guide, Dr. Milan Kanti Naskar, Chief Scientist & Professor (AcSIR), Head, Advanced Ceramics and Composites Division (ACCD), CSIR-Central Glass & Ceramic Research Institute (CGCRI), Kolkata, for his unwavering support, guidance, and encouragement throughout my PhD journey. Without his patient guidance, kind assistance and steady suggestions I could not have completed this dissertation in the short period of time that it took.

I am grateful to the Director, CSIR-CGCRI, Dr. Suman Kumari Mishra for her kind permission and approval to carry out my thesis work in the Institute. I acknowledge DST, SERB for providing me fellowship for carrying out my research work.

I am greatly obliged to my Research Advisory Committee (RAC members, Prof. Kajal Krishna Rajak, Jadavpur University, Prof. Manirul Islam, Kalyani University) for their kind help, invaluable comments, suggestion and support during RAC meetings throughout my research tenure. Their critical evaluation and broad range of expertise is really appreciable and inspired me a lot during my journey.

I would like to express my sincere gratitude to Dr. Shirshendu Chakraborty, Dr. Soupitak Pal, Mr. Ajitesh Kar, Mrs. Soma Hansda of ACCD Division, CSIR-CGCRI for their constant support and encouragement throughout my Ph.D. work.

My deepest thanks and admiration go to Dr. Srabanti Ghosh, Senior Scientist, FMDD, CSIR-CGCRI whose help, support, valuable suggestion and encouragement have been priceless in my research work.

I am deeply obliged to Dr. Sandip Bysakh, Dr. Jiten Ghosh, Dr. Mousumi Majumder, Dr. Prashanta Kumar Sinha, Dr. Sunirmal Jana for their kind help during my research work.

I am also thankful to all other members of Materials Characterization Divisions for their support throughout my research work. Especially I do appreciate Ashok Da, Nitai Da, Titir Di, Kajari Di, Srikrishna da for their brilliant effort, kind help during my entire research work.

I shall fail in my appreciation, if I do not recognize the cooperation and support received generously from scientists and staff members of different R&D and support divisions/sections and adminstration of CSIR-CGCRI.

My days at CSIR-CGCRI would be incomplete without the presence of three very special individuals: Sanjiban Da, Mousumi di, and Swati di. Beyond their professional help, they brought a sense of camaraderie and joy to my daily life, making my days at CSIR-CGCRI not only productive but also truly memorable. I am immensely grateful to my seniors Ipsita Di, Sukanya Di for their constant guidance and loving support throughout my research work. I am very happy to be associated with adorable juniors Dipika, Teesta, Debjani and Sumona. I would like to give huge and warm thanks to my seniors and fellow research scholars Akila Di, Anirban Da, Sultan Da, Ripan Da, Sushmita Di, Hillol Da, Uttam, Biswajit, Himal, Shoroshi, Anirban, Ajay, Sushant, Anustup, Kaartika, Pritha, Saswata, Bibhas, Sundaram, Sankhadip, Dipanjan, Dipendu, Sourav, Soumita, Jishu, Labonyo and Raktima. I count it a true blessing to have Partha, Arpita, Tanushri, Monalisa, Preeti and Solange as my caring and inspiring companions here. The cherishing memories of their association in CSIR-CGCRI will always stay with me.

I would like to extend my heartful gratitude to my loving friends Dyuti, Shilpa, Riya, Somoshree, Srabana, Paromita, Arnab and Pratick, who not only supported me academically but also enriched my life personally. I am deeply thankful to my friend Deboo, inspired by whom I have learnt to appreciate the importance of cultivating a scientific mindset not only in research but also in broader aspects of life.

I would also like to take this opportunity to express my heartfelt gratitude to Madam (Mrs. Mausumi Naskar). Her motherly care, which I was blessed to receive in this journey away from home, is beyond words. Her kindness and compassionate demeanor have immensely influenced me which will remain inestimable as I continue on my future endeavours.

It is an ideal platform to express my deep-felt gratitude to my beloved parents (Baba-Maa), Didibhai and Dada who have continuously supported me to overcome all the complications during my entire Ph.D. tenure, keeping me aside from any difficulties in the family. Without their heartfelt blessings, I believe I would not have been able to accomplish my goal. A special thank goes to my Krishna Kakima, Mami, Monu Kaka, Laal Mama, Sona Maasi and Pisi, who gave their loving support in my academic journey. I would especially like to thank my very supportive brother Anupam for his invaluable assistance in research related work. I express my deepest thank to my other family members as well, whose prayers, motivation, and assistance greatly aided in my accomplishments.

Date: 18/07/2024

Adwitiya Chakraborty

(Adwitiya Chakraborty)

Table of Contents

Sr. No.	Contents	Page no.
I	List of Figures/Schemes	iv
II	List of Tables	ix
III	List of Abbreviations	xii
Chapter 1:	**A Brief Overview**	**1-34**
1.1	Introduction	1
1.1.1	Inorganic water contaminants	1
1.1.2	Organic water contaminants	2
1.2	Water decontamination process	3
1.2.1	Coagulation and flocculation	3
1.2.2	Ion exchange	3
1.2.3	Membrane filtration process	4
1.2.4	Adsorption process	5
1.2.5	Photocatalytic process	8
1.3	Types of adsorbents for removal of water contaminants	9
1.4	Types of photocatalysts for removal of water contaminants	11
1.5	Agro waste based materials	13
1.6	Industrial waste based materials	15
1.7	Rice husk ash based adsorbents for decontamination of water	17
1.8	Red mud (RM) based adsorbents and photocatalysts for decontamination of water	19
1.8.1	RM based adsorbents for the removal of different contaminants	19
1.8.2	RM based photocatalysts for the removal of different contaminants	24
1.9	Outline of dissertation work	25
	References	27
Chapter 2:	**Synthesis of rice husk ash derived zeolite based adsorbents for defluoridation of water**	

Chapter 2A	**MgO modified rice husk ash derived zeolite based adsorbents for defluoridation of water**	**35-53**
2A.1	Introduction	35
2A.2	Experimental	35
2A.2.1	Materials	35
2A.2.2	Characterization	36
2A.2.3	Adsorption experiment	36
2A.3	Results and discussion	37
2A.3.1	Characterization of zeoliteA-MgO adsorbent	37
2A.3.2	Adsorption study	40
2A.3.3	Kinetics study	46
2A.3.4	Adsorption Isotherms	47
2A.3.5	Adsorption Thermodynamics	48
2A.3.6	F^- ion removal mechanism	49
2A.4	Conclusion	50
	References	51
Chapter 2B	**Al_2O_3 modified rice husk ash derived zeolite based adsorbent for defluoridation of water; batch and column study**	**54-88**
2B.1	Introduction	54
2B.2	Experimental	55
2B.2.1	Materials	55
2B.2.2	Characterization	56
2B.2.3	Adsorption study	57
2B.3	Results and discussion	58
2B.3.1	Characterization of alumina gel@zeolite X nanocomposite	58
2B.3.2	Batch adsorption experiment	62
2B.3.2.1	Adsorption Kinetics	67
2B.3.2.2	Adsorption Isotherms	69
2B.3.2.3	Thermodynamic Parameters	71
2B.3.2.4	Adsorption mechanism	73
2B.3.3	Column adsorption study	74
2B.3.3.1	Kinetic models on breakthrough curves	76
2B.3.2.2	Desorption and regeneration study	84
2B.4	Conclusion	85
	References	86
Chapter 3:	**Red mud derived iron oxide nano-flakes for de-arsenification of water**	**89-116**
3.1	Introduction	89

3.2	Experimental	90
3.2.1	Materials	90
3.2.2	Characterization	91
3.2.3	Arsenic adsorption experiment	92
3.3	Results and Discussion	93
3.3.1	Characterization of α-Fe_2O_3	93
3.3.2	Arsenic adsorption study	99
3.3.3	Thermodynamic investigation	103
3.3.4	Adsorption Kinetics	106
3.3.5	Adsorption Isotherm	107
3.3.6	Adsorption mechanism	109
3.4	Conclusion	112
	References	113

Chapter 4: Red mud derived iron oxide based photocatalysts for the degradation of methylene blue dye **117-146**

4.1	Introduction	117
4.2	Experimental section	117
4.2.1	Materials and Methods	117
4.2.2	Characterization	119
4.2.3	Photocatalytic Study	120
4.2.4	Photochemical measurements	121
4.3	Results and discussion	121
4.3.1	Characterization of bare and doped iron oxide	121
4.3.2	Optical properties	129
4.3.3	Methylene blue degradation studies	130
4.3.4	Quenching Studies	135
4.3.5	Photoelectrochemical Performance and Mechanistic Study	136
4.4.	Conclusion	142
	References	143

Chapter 5: Summary and future directions **146-149**

5.1	Summary	146
5.2	Future directions	148

List of publications 150
Conference presentations 151
Reprints of the publications

List of Figures / Schemes

Figure No.	Description	Page no.
	Chapter 1: Brief overview	
1.1	Adsorption process for removal of contaminants from water	6
1.2	Photocatalytic process for degradation of pollutants	9
1.3	Crystal structure of hematite (α-Fe_2O_3)	12
1.4	Utilization of RHA obtained from rice mill	14
1.5	Alumina obtained from Bauxite *via* Bayer's process	16
	Chapter 2: Synthesis of rice husk ash derived zeolite based adsorbents for defluoridation of water	
	Chapter 2A: MgO modified rice husk ash derived zeolite based adsorbents for defluoridation of water	
2A.1	(a) XRD patterns (* indicates zeolite A peaks) (b)FTIR spectra of zeolite A-MgO powders.	37
2A.2	FESEM image of zeolite A-MgO composite powders.	38
2A.3	(a) N_2 adsorption-desorption isotherm and (b) pore size distribution of zeolite A-MgO composite.	39
2A.4	XPS spectra of zeolite A-MgO composite (a) Survey spectra (b) O (1s) (c) Si(2P) (d) Na(1s) (e) Al(2p) (f) Mg(2p).	40
2A.5	Effect of (a) contact time, (b) adsorbent dose, (c) initial fluoride ion concentration and (d) pH on the adsorption of F^- ions by zeolite A-MgO composite.	44
2A.6	Role of (a) reaction temperature, (b) competing ions and (c) regeneration study for F^- ions adsorption by zeolite A-MgO composite.	46

2A.7	Kinetics data with linear fitting of (a) pseudo-1st order and (b) pseudo-2nd order kinetic models.	47
2A.8	Isotherm plots: (a) Langmuir and (b) Freundlich for the adsorption of F^- ions.	48
2A.9	ln K_d vs. 1/T plot for F^- ions adsorption.	49
2A.10	A tentative mechanism for F^- ions adsorption by zeolite A-MgO composite.	50

Chapter 2B: Al_2O_3 modified rice husk ash derived zeolite based adsorbent for defluoridation of water; batch and column study

2B.1	Schematic diagram for the synthesis of alumina gel@zeolite X nanocomposite.	56
2B.2	(a) XRD pattern, (b) FTIR, (c) BET isotherm and (d) BJH pore size distribution (inset: pore size distribution by NLDFT) of alumina gel@ zeolite X nanocomposite.	59
2B.3	XPS of (a) full scan survey, (b) Al2p, (c) Si2p, (d) Na1s and (e) O1s spectra of alumina gel@zeolite X nanocomposite.	60
2B.4	(a) FESEM (low mag.), (b) FESEM (high mag.), (c) TEM images, (d) Particle size disribution and (e) EDS analysis of alumina gel@ zeolite X nanocomposite.	61
2B.5	Effect of contact time on (a) % fluoride adsorption (b) Adsorption capacity by alumina gel@ zeolite X nanocomposite.	62
2B.6	Effect of initial fluoride ion concentration on (a) % fluoride adsorption (b) Adsorption capacity by alumina gel@ zeolite X nanocomposite.	62
2B.7	Effect of adsorbent dose on (a) % fluoride adsorption (b) Adsorption capacity by alumina gel@ zeolite X nanocomposite.	63
2B.8	Effect of temperature on (a) % fluoride adsorption (b) Adsorption capacity by alumina gel@ zeolite X nanocomposite.	65
2B.9	Effect of pH on (a) % fluoride adsorption (b) Adsorption capacity for the adsorption of F^-ions by alumina gel@ zeolite X nanocomposite.	66
2B.10	Effect of (a) co-existing ion and (b) recyclability study for the adsorption of F^-ions by alumina gel@ zeolite X nanocomposite.	67

2B.11	Kinetics data with linear fitting of (a) pseudo-first-order and (b) pseudo-second-order for the adsorption of F^- ions by alumina gel@ zeolite X nanocomposite.	68
2B.12	Isotherm plots: (a) Langmuir and (b) Freundlich for the adsorption of F^- ions by alumina gel@ zeolite X nanocomposite.	70
2B.13	Plot of $ln\ K^o_{eq}$ versus 1/T for fluoride ions adsorption.	72
2B.14	A proposed mechanism for the adsorption of F^- ions by alumina gel@ zeolite X nanocomposite	74
2B.15	Breakthrough curves for adsorption of fluoride (a) at different initial concentrations, (b) at different flow rates and(c) at different bed heights.	76
2B.16	Linear regression analysis of Breakthrough curve using Adams Bohart Model at different (a) concentrations, (b) flow rates and (c) bed heights.	78
2B.17	Linear regression analysis of breakthrough curves using Thomas model at different (a) concentrations, (b) flow rates and (c) bed heights.	80
2B.18	Linear regression analysis of breakthrough curves using Yoon-Nelson model at different (a) concentrations, (b) flow rates and (c) bed heights.	82
2B.19	Linear Plot of BDST for fluoride adsorption.	84
2B.20	Desorption-regeneration cycle for fluoride removal.	85

Chapter 3: Red mud derived iron oxide nano-flakes for de-arsenification of water

3.1	Schematic diagram for the preparation of iron oxide extracted from red mud.	91
3.2	(a) XRD pattern, (b) FTIR and (c) Raman spectra of α-Fe_2O_3.	94
3.3	(a) BET isotherm, (b) BJH pore size distribution of α-Fe_2O_3.	95
3.4	XPS spectra of α-Fe_2O_3:(a)-(c) Fe2p and (d)-(f) O1s.	97
3.5	(a-c) FESEM images, (d-f) TEM images and (g-i) HRTEM images of α-Fe_2O_3 particles.	98

3.6	Effect of contact time on (a) % As(V) adsorption (b) Adsorption capacity on the adsorption of As(V) by α-Fe_2O_3 particles (c) % Adsorption of As(V) by α-Fe_2O_3 reaching below the WHO limit.	99
3.7	Effect of initial As(V) concentration on (a) % As(V) adsorption (b) Adsorption capacity on the adsorption of As(V) by α-Fe_2O_3 particles.	100
3.8	Effect of adsorbent dose on (a) % As(V) adsorption (b) Adsorption capacity on the adsorption of As(V) by α-Fe_2O_3 particles.	101
3.9	Effect of (a) pH on % As(V) adsorption (b) Adsorption capacity on the adsorption of As(V) by α-Fe_2O_3 particles.	102
3.10	Effect of temperature on % As(V) adsorption (b) Adsorption capacity on the adsorption of As(V) by α-Fe_2O_3 particles.	102
3.11	Plot of lnK_d versus 1/T for the adsorption for As(V) ions.	103
3.12	(a) Co-existing ions effect and (b) Recyclability study for the adsorption for As(V) ions.	105
3.13	Kinetics data with linear fitting of (a) pseudo-first-order and (b) pseudo-second-order.	106
3.14	(a) Langmuir and (b) Freundlich isotherms for the adsorption for As(V) ions.	108
3.15	Proposed mechanism for the adsorption of As(V) ions by α-Fe_2O_3 particles.	111
3.16	FTIR spectra of the FENH6 sample before and after As(V) adsorption.	111

Chapter 4: Red mud derived iron oxide based photocatalysts for the degradation of methylene blue dye

4.1	Schematic diagram for the preparation of bare and doped iron oxide extracted from red mud.	119
4.2	(a) XRD pattern, (b) Raman spectra and (c) FTIR spectra of bare and doped α-Fe_2O_3.	123
4.3	(a) BET isotherms, (b) BJH pore size distributions of bare and doped α-Fe_2O_3.	124

4.4	XPS spectra of (a) Survey, (b) Mn (2p), (c) Cu(2p), (d) Ce (3d), (e) Fe2p and (f) O1s for bare and doped α-Fe_2O_3.	126
4.5	FESEM images of bare and doped α-Fe_2O_3 particles :(a) FETP, (b)FMNTP, (c) FCUTP and (d)FCETP.	127
4.6	TEM images of bare and doped α-Fe_2O_3 particles: (a) FETP, (b) FMNTP, (c) FCUTP and (d) FCETP; HRTEM image of (e)FETP (f) FMNTP (g) FCUTP and (h) FCETP.	128
4.7	EDX spectra of doped α-Fe_2O_3 particles (a) FMNTP, (b) FCUTP and (c) FCETP.	129
4.8	K-M Plots of (a) FETP, (b) FMNTP, (c) FCUTP and (d) FCETP.	130
4.9	(a)-(d) UV-Visible absorption spectra and (e) degradation of MB for bare and doped α-Fe_2O_3 samples.	131
4.10	(a) Recyclability test (b) XRD pattern of FCUTP for photostability test.	132
4.11	The logarithm plots of the absorbance ($-\ln(C_t/C_0)$) with reaction time for bare and doped α-Fe_2O_3 sample: (a) FETP, (b) FMNTP, (c) FCUTP and (d) FCETP.	133
4.12	(a) Degradation of MB with time, (b) The logarithm plots of the absorbance ($-\ln(C_t/C_0$) with reaction time for Cu doped α-Fe_2O_3 sample (FCUTP).	134
4.13	TOC removal% at different reaction time.	135
4.14	Linear Sweep Voltammogram of (a) FETP, FMNTP, FCUTP, FCETP, (b) FCUTP-0.5%, FCUTP-2%, (c) Transient photocurrent spectra, (d) Nyquist plots of FETP, FMNTP, FCUTP, FCETP.	137
4.15	Mott-Schottky plots of (a) FETP (b) FMNTP (c) FCUTP (d) FCETP.	138
4.16	PL spectra of bare and doped α-Fe_2O_3.	140
4.17	Schematic representation of relative energy band diagram of doped α-Fe_2O_3.	141

List of Tables

Table No.	Description	Page no.
	Chapter 1: Brief overview	
1.1	Different red mud derived adsorbents and their adsorption capacities toward removal of different ions.	21
1.2	Different red mud derived adsorbents and their adsorption capacities towards removal of different inorganic anions, dyes and phenolic pollutants.	23
	Chapter 2: Synthesis of rice husk ash derived zeolite based adsorbents for defluoridation of water	
	Chapter 2A: MgO modified rice husk ash derived zeolite based adsorbents for defluoridation of water	
2A.1	XPS results of zeolite A-MgO composite	40
2A.2	% Adsorption with time for the removal of fluoride ions	41
2A.3	% Adsorption with adsorbent dose (gm/L) for the removal of fluoride ions	42
2A.4	% Adsorption with adsorbate dose (mg/L) for the removal of fluoride ions	43
2A.5	% Adsorption with change in pH	44
	Chapter 2B: Al_2O_3 modified rice husk ash derived zeolite based adsorbent for defluoridation of water; batch and column study	
2B.1	Adsorption capacity (mg/gm) of zeolite X and alumina gel@zeolite X nanocomposites	64
2B.2	Kinetic parameters for the adsorption of fluoride ions	68

2B.3	The parameters obtained from Langmuir and Freundlich models	70
2B.4	A comparative data on maximum adsorption capacity, kinetics and rate constant for fluoride ion adsorption by alumina gel@zeolite X nanocomposite and reported adsorbents	71
2B.5	Thermodynamic parameters of fluoride adsorption for different adsorbent doses	73
2B.6	Adams-Bohart Model Parameters	78
2B.7	Thomas Model Parameters	80
2B.8	Yoon-Nelson Model Parameters	82
2B.9	BDST Model Parameters	84

Chapter 3: Red mud derived iron oxide nano-flakes for de-arsenification of water

3.1	XRF Analysis of Sample FENH24	94
3.2	Thermodynamic parameters of Arsenic (V) adsorption for different sample with fixed adsorbent doses (0.25 gm/L)	104
3.3	Kinetic parameters for the adsorption of As(V) for adsorbent dose of 0.25 gm/L	107
3.4	The parameters obtained from Langmuir and Freundlich models.	108
3.5	A comparative data on maximum adsorption capacity for As (V) adsorption by synthesized α-Fe_2O_3 and reported adsorbents.	109

Chapter 4: Red mud derived iron oxide based photocatalysts for the degradation of methylene blue dye

4.1	The textural properties of bare and doped α-Fe_2O_3	124
4.2	The removal % of MB in the presence of different photocatalyst	132
4.3	The %adsorption and %degradation of MB, rate constant of the bare and doped α-Fe_2O_3 sample	134
4.4	Fitting parameters of Nyquist plots	137
4.5	Position of conduction band, valence band and donor density of as-synthesized materials	139

List of Abbreviations

AOP:	Advanced oxidation process
BDST:	Bed depth service time
BE:	Binding Energy
BET:	Brunauer-Emmett-Teller
BJH:	Barrett–Joyner–Halenda
CB:	Conduction band
CBM:	Conduction band minima
CNTs:	Carbon nanotubes
DFT:	Density functional theory
DI:	Deionised water
DLS:	Dynamic light scattering
ED:	Electrodialysis
EDX:	Energy Dispersive X-Ray Analysis
FESEM:	Field emission scanning electron microscope
FTIR:	Fourier transform infrared spectroscopy
GO:	Graphene oxide
HOMO:	Highest occupied molecular orbital
HRTEM:	High resolution transmission electron microscopy
IC:	Inorganic carbon
ICP- AES:	Inductively coupled plasma-atomic emission spectroscopy
ICP-MS:	Inductively coupled plasma mass spectroscopy
ID:	Inner diameter
IUPAC:	International Union of Pure and Applied Chemistry
IPA:	Isopropyl alcohol
ISE:	Ion selective electrode
JCPDS:	Joint Committee on Powder Diffraction Standards
KM:	Kulbelka-Munk
LUMO:	Lowest unoccupied molecular orbital
MB:	Methylene blue
MO:	Methyl orange

MF:	Microfiltration
NF:	Nanofiltration
NLDFT:	Nonlinear density functional theory
ppm:	parts-per million
PL:	Photoluminescence
PZC:	Point of zero charge
RHA:	Rice husk ash
RM:	Red mud
RO:	Reverse osmosis
TC:	Total carbon
TISAB:	Total ionic strength adjustment buffer
TOC:	Total organic carbon
UF:	Ultrafiltration
UV:	Ultraviolet
VB:	Valence band
WHO:	World Health Organization
XRF:	X-ray Fluorescence
XPS:	X-ray Photoelectron Spectroscopy
XRD:	X-ray Powder Diffraction

Chapter 1

Brief Overview

This chapter provides a general overview of common water pollutants with their removal methods along with some insights into different agro and industrial waste products. Based on the literature reports, several synthesis processes for the preparation of various adsorbents and photocatalysts derived from agro (rice husk ash) and industrial waste (red mud) are highlighted in this chapter.

1.1 Introduction

Environmental pollution is one of the critical and escalating challenges with far-reaching implications for the planet's health and sustainability. The ongoing scenario is led by a complex interplay of various human activities that continue to release pollutants into the air, water, and land, contributing to a myriad of environmental issues. Among those, water and land pollutions are of significant concerns.

In the contemporary world, water pollution is a pervasive problem that affects both developed and developing countries. Industrial discharges, agricultural runoff, and untreated sewage continue to contaminate water bodies, posing serious threats to aquatic ecosystems and human health. Depending on their natures, water contaminants can be categorised into two major groups: (a) inorganic contaminants and (b) organic contaminants.

1.1.1 Inorganic water contaminants

Inorganic water contaminants are generally originated from non-living sources like geological phenomena, industrial and agricultural activities etc. These type of contaminants hardly degrade over time persisting in the environment for extended periods resulting serious health issues to human beings.

There are several inorganic water contaminants i.e., toxic heavy metals like lead (Pb(II)), arsenic (in the form of arsenate (As(V) and arsenite As(III)), chromium (Cr(VI)), cadmium (Cd(II)), mercury (Hg(II)), nickel (Ni(II)), zinc (Zn(II)) etc. and non-metals like fluoride (F^-) nitrate (NO_3^-), sulphate (SO_4^{2-}) /sulphite (SO_3^{2-}), chloride (Cl^-), phosphate (PO_4^{3-}) etc.

Among these water contaminants, a brief overview of fluoride and arsenic, the most toxic components has been discussed below.

Fluoride

Source: Natural source of fluoride originates from rocks, soil, and water. Groundwater, in particular, may contain varying concentrations of fluoride depending on geological conditions.[1] In anthropogenic source, human activities, such as industrial discharges, mining, and the use of certain fertilizers and pesticides can contribute to elevated fluoride levels in water.[2]

Health impact: Excessive fluoride intake during tooth development can lead to dental fluorosis. In regions with high fluoride concentrations in drinking water, long-term exposure may lead to neurological damage, Alzheimer's syndrome skeletal fluorosis.[3] According to the World Health Organization (WHO), the optimal fluoride concentration in drinking water is around 0.5 to 1.5 mg/L.

Arsenic

Source: Arsenic is found in nature as Earth's crust in the form of rocks and minerals,[4] leaching into groundwater. Human activities such as mining, smelting, and the use of arsenic-containing pesticides, industrial discharges[5] etc. as anthropogenic sources may contribute to high arsenic levels in water.

Health impact: Chronic exposure to arsenic in drinking water is associated with an increased risk of cancer specially skin, lung, bladder etc. Long-term exposure has been linked to cardiovascular diseases, diabetes, and neurological problems.[6] The WHO guideline for arsenic in drinking water is 10 µg/L.[7]

1.1.2 Organic water contaminants

Organic contaminants are mainly carbon based compounds that can enter water sources through natural processes or human activities. These include pesticides, different type of industrial chemicals, pharmaceuticals etc. Among those, synthetic dyes are the most common organic pollutants which are widely used in textiles, cosmetics, printing industries. The synthetic dyes can be categorised mainly into three types as a) cationic, b) anionic and c) non-ionic dyes. The anionic dyes like brilliant red, methyl orange (MO), congo red etc are generally characterized by their negatively charged groups such as sulfonate, carboxylate etc. On the other hand, cationic dyes like methylene blue (MB), crystal violet, rhodamine B, thiazine dye etc. contain positively charged amino groups in their molecular structure. [8] Improper disposal of coloured dyes often cause water pollution affecting both surface and ground water. Among these dyes, MB is found to be one of the most toxic, carcinogenic, and non-biodegradable dyes that poses a serious threat to human health and the environment. Renal toxicity and subsequent kidney damage may result from high dose or prolonged exposure to MB as suggested from several studies.[9]

1.2 Water decontamination process:

Several techniques are adopted for decontamination of water. An overview of different commonly used processes for decontamination of water is illustrated in the following section.

1.2.1 Coagulation and flocculation: In the coagulation process, suspended particles get precipitated in the form of insoluble hydroxide in presence of coagulants. Flocculation process involves gradual mixing of water by promoting the coagulated particles to form larger aggregates. Through sedementation and filtration the contaminants finally get removed.[10] However, removal of trace amount of contaminants cannot be accomplished by this process. Also production of huge amount of sludge causing disposal issue makes it ineffective in some cases.[11]

1.2.2 Ion exchange: Ion exchange is a highly effective water treatment technique involving the use of ion exchange resin which are crosslinked organic polymer beads with charged functional groups. These resin facilitate the removal of dissolved ions from water by exchanging them with ions of similar charge. In the cation exchanger resin, the cationic species (Mg^{2+},Ca^{2+},other heavy metal ions etc.) are separated *via* electrostatic interactions with the negatively charged carboxylate ($-COO^-$) or sulfonate (SO_3^-) functional groups of resin by ion exchange process. On the other hand, the anions like $CrO_4^{2-}/Cr_2O_7^{2-}$, NO_3^-, $H_2AsO_4^-/HAsO_4^{2-}$ get adsorbed with the exchange of positively charged functional groups of quaternary ammonium ($-NR_3^+$) or primary, secondary, tertiary amines in anion exchanger resin. The ion exchange method offers numerous benefits in water purification by effectively removing heavy metal ions as well as softening water by removing calcium and magnesium ions.[12] Ion exchange method also has that advantage of having easy regeneration procedure maintaining a long term use of resin. However, it has certain limitations as follows:

- Only the ionisable components can be removed by this process. This process is not useful for the removal of organic or biological contaminants.
- Optimization of pH, ionic strength etc. are often necessary for each specific separation.
- Regular sanitization and regeneration are necessary. Failure to do so may lead to bacterial development on the resin surface which can further contaminate water.

1.2.3 Membrane filtration process: Membrane filtration is a separation process that utilizes membranes to selectively remove particles, contaminants from a fluid stream. These membranes act as barriers, permitting some components to flow through while keeping others depending on their differences in size, shape, charge, or other characteristics.[13] Typically, membranes used in membrane filtration processes are composed of variety of materials. Each material has unique qualities and performance characteristics ideal for particular usage. Membrane technologies can be categorised into two main types; a) pressure driven b) electrically driven process.[14]

Pressure driven membrane process is subcategorised into four types.

Microfiltration (MF): MF membranes have relatively larger pores (0.1 to 10 µm) compared to the other membrane types allowing them to remove suspended solids and some larger colloidal particles from feed water.[15]

Ultrafiltration (UF): Pore size of UF membranes ranges from 0.001 to 0.1 µm. Polyethersulfone membranes are used in ultrafiltration process. The driving force for separation in ultrafiltration can be pressure or concentration gradient depending on the specific application. This process is used to separate suspended solids, macromolecules, colloidal particles etc. from liquid stream.

*Nano filtration (NF)***:** NF utilizes polyamide membranes with pore sizes ranging from 0.001 to 0.01 µm. The surface charge of NF membranes, influenced by functional groups like carboxyl or sulfonic acid, crucially determines their selectivity and separation performance. In neutral and alkaline conditions, NF membranes carry a negative charge, facilitating the repulsion of negatively charged ions and molecules for selective removal during filtration. However, in acidic medium, the membrane surface may carry no charge or become less negatively charged, potentially affecting selectivity. NF proves highly effective in removing divalent ions, organic compounds, and some low molecular weight solutes. Nevertheless, monovalent ions and small molecules may pass through the membrane, making it suitable for specific water treatment applications.[16]

Reverse Osmosis (RO): RO process is an effective and proven technology which is widely used in water purification. In RO, a high pressure gradient is applied across the membrane to overcome osmotic pressure. Herein, water molecules are passed through a semi-permeable membrane having very small sized pores (<0.001µm) while rejecting dissolved particles or contaminants.[17] RO systems are extensively employed in various purification processes due to their ability to effectively remove organic contaminants and other inorganic based pollutants

like arsenate, chloride, fluoride, sulfate, lead etc. The membrane-based technology offers the advantage of separating components without altering their state as well as in the absence of using any chemicals *via* an energy-efficient and ideal process. However, this process has some limitations.[17]

- The membranes often get clogged or fouled by impurities reducing efficiencies; therefore, frequent cleaning or replacement of membrane components are required.
- The discarded water stream needs proper disposal to avoid secondary pollution.
- Reverse osmosis system can be expensive to set up which limits their applicability for some applications or regions with limited resources.

The electrically driven membrane process includes electrodialysis (ED). In ED process, an electric potential is applied across a series of ion-selective membranes. The generated ion concentration gradients drive the migration of ions through membranes.[18] Positively charged ions migrate towards the cathode through cation-selective membrane while negatively charged ions migrate toward the anode through anion-selective membrane. Therefore, this process is particularly useful for the removal of specific ions. Numerous factors, including feed water ionic content, pH, current density, flow rate, and ED cell structure determine the effectivity of the ED process.[19]

1.2.4 Adsorption process: It is a surface phenomenon in which molecules or atoms from a fluid (liquid or gas) adhere to the surface of a solid or liquid substrates, known as adsorbents. This process occurs due to the attractive forces between the adsorbate and adsorbent system, resulting in the accumulation of adsorbate molecules/ions (contaminants) on the surface of adsorbents. The adsorption process is influenced by several factors like pH, temperature, ionic strength as well as surface area of adsorbent. Changes in pH can alter the surface charge of the adsorbent material. It affects the degree of ionisation of the adsorbate leading to variation in adsorption behaviour. Materials with high surface area render more adsorption sites leading to increased adsorption capacities. Figure 1.1 shows a schematic pathway for adsorption process.

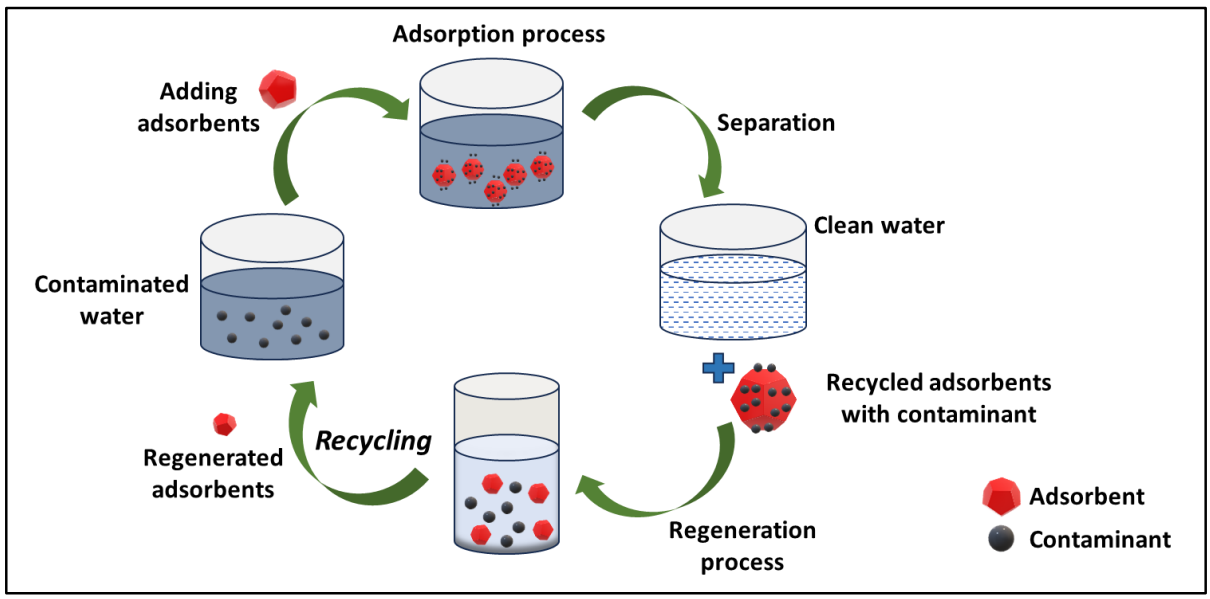

Figure 1.1: Adsorption process for removal of contaminants from water.

The adsorption process can be categorized into two types, (a) physical adsorption and (b) chemical adsorption.

Physical Adsorption: Physical adsorption or physisorption occurs due to weak intermolecular forces between the adsorbent and adsorbate molecules. This includes van der Waals force of attraction, hydrogen bonding and dipole-dipole interactions. It involves the formation of thin layer of adsorbate molecules while multilayer adsorption is also possible under certain circumstances. Physical adsorption exhibits no specificity toward adsorption sites. This process is reversible in nature and generally occurs at low temperature.

Chemical Adsorption: Chemical adsorption or chemisorption is governed by the formation of chemical bonds between adsorbent and adsorbate molecules. This process is generally irreversible in nature. Unlike physisorption, it exhibits specificity in adsorption sites with the formation of monolayer of adsorbate molecules on the adsorbent surface.

Application: Adsorption is a crucial phenomenon with diverse applications across various fields.

- It is widely used to remove impurities from gases. One common example is the removal of impurities like sulfur compounds, volatile organic compounds etc. from natural gas or biogas by using activated charcoal.[20]

- Adsorption of reactants onto the catalyst surface is a fundamental step in catalysis to facilitate chemical reactions.
- Adsorption chromatography is widely used in analytical chemistry and preparative chromatography for the separation and purification of complex mixtures.
- In water treatment process, adsorption serves as a vital mechanism for removing pollutants or contaminants. For example, arsenic contamination from water can be mitigated through specialized adsorbents such as iron oxide based materials, activated alumina etc. Zeolite based adsorbent materials are often used to remove different contaminants including fluoride and other heavy metals such as lead, cadmium etc. through ion exchange mechanism.[21] Additionally, adsorption techniques are often employed to remove different organic dyes from industrial effluents.[22]
- Adsorption onto porous materials serve as a promising approach in drug delivery systems.[23] It helps regulate and control the release rate of pharmaceutical compounds.

Adsorption process offers several advantages over other water treatment methods.

- *Versatility:* This process is very much effective in removing wide ranges of contaminants including organic compounds, heavy metals and other pollutants. Its versatility makes it suitable for treating diverse types of water sources such as, industrial water, drinking water and ground water.
- *Selectivity:* The selectivity toward particular contaminant is advantageous without affecting the overall water composition.
- *Minimal chemical utilization:* In contrast to other techniques like coagulation and flocculation, adsorption often uses little or no chemicals. This reduces the risk of introducing additional chemicals into water simplifying the treatment process.
- *Antifouling properties*: Adsorption systems are generally less susceptible toward fouling compared to membrane based process. The adsorbent surface can easily be regenerated to restore its adsorption capacity thereby reducing the system downtime and maintenance.
- *Environmentally benign*: Numerous adsorbents used in water treatment process are environmentally friendly and poses minimal risk to human health. Its ability to fully adsorb contaminants make it beneficial by not producing any other unwanted

by-products. Furthermore, adsorption can be integrated to sustainable water treatment approaches by using bio-based or renewable adsorbents.

While adsorption is versatile and effective water treatment process, it has some disadvantages. The scarcity of suitable adsorbents with high adsorption efficacy for specific pollutants is a significant hurdle. The non-selective nature of adsorption results in simultaneous adsorption of various ions or contaminants. This diminishes the capacity to target specific pollutants. Moreover, some adsorbents require surface modification or chemical activation to enhance their adsorption capacity leading to complexity in processing steps.

1.2.5 Photocatalytic process: Photocatalysis represents a promising area of research with diverse applications across environmental, energy and synthetic chemistry domains. It involves the process of photoexcitation in which a semiconductor material absorbs photons with energy equivalent to or greater than its bandgap. The photo generated electron-hole pairs are the key intermediates responsible for driving photocatalytic reactions (Fig.1.2). This process typically occurs primarily *via* two pathways: (a) direct pathway and (b) indirect pathway. The direct pathway involves photogenerated electrons and holes to participate directly in redox reaction with adsorbed reactant molecules on the catalyst surface. In the indirect pathway, the photogenerated electron-hole pairs react with adsorbed water molecule or molecular oxygen. This produce highly reactive hydroxyl (•OH) or superoxide ($O_2^{\bullet -}$) radicals capable of initiating redox reactions. The kinetics of photocatalytic reactions are influenced by various factors such as incident light intensity, wavelength, surface area of catalyst etc.

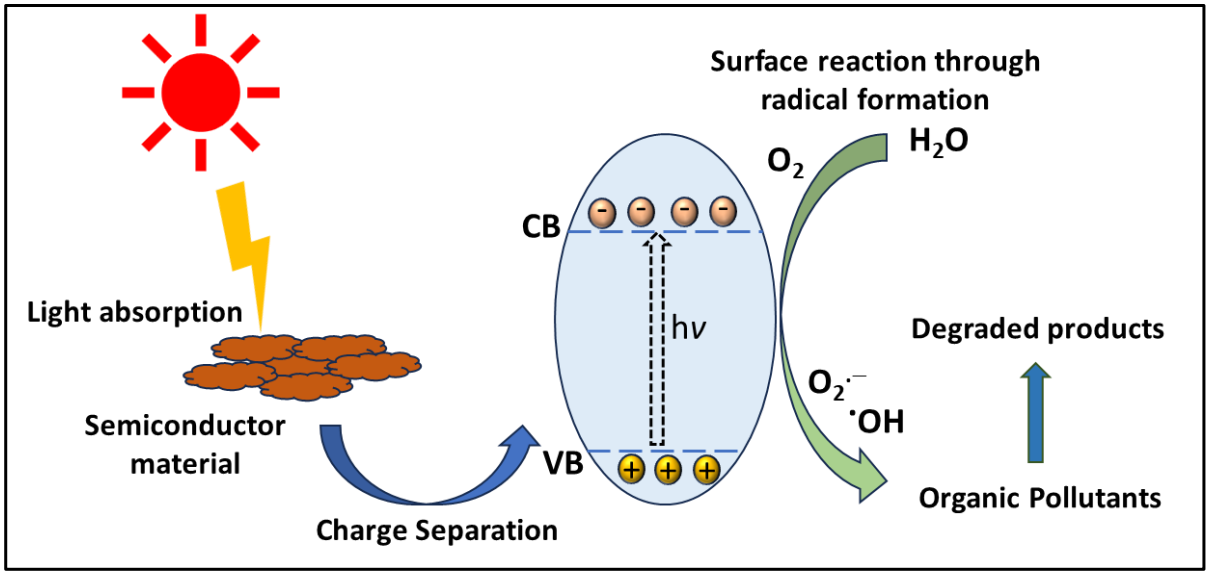

Figure 1.2: Photocatalytic process for degradation of pollutants.

There are two types of photocatalysts: (a) Homogeneous photocatalyst and (b) Heterogeneous photocatalyst. Homogeneous photocatalysts interact directly with reactants in solution and undergo chemical transformations. On the other hand, heterogeneous photocatalysts, usually semiconductor materials such as TiO_2, ZnO, Fe_2O_3 primarily react with the reactant molecules at the catalyst surface. Photocatalysis finds extensive applications in the degradation of organic pollutants, pesticides, pharmaceuticals etc. from waste water.[24] The photocatalytic system are also being explored for solar-driven water splitting to produce hydrogen fuel.[25] It offers greener and sustainable routes for various organic transformations by harnessing the light source. However, this process has challenges in terms of catalyst stability and light absorption efficiency. Additionally, charge carrier combination rate can also limit its overall efficiency. The recovery and reuse of catalyst materials from the reaction system can provide challenges impacting economical feasibility for large scale application.

Despite the above challenges, adsorption and photocatalysis are generally preferred choices over other water treatment processes toward eco-friendly alternatives for water treatment. In this dissertation work, the adsorption and photocatalysis processes have been followed to remove detrimental contaminants like fluoride, arsenic and organic dye (MB) from contaminated water.

1.3 Types of adsorbents for removal of water contaminants

Various adsorbent materials such as activated carbon, alumina, zeolite, clay, bone char, mixed metal oxides, layered double hydroxides etc. are utilized for the removal of different organic

and inorganic water pollutants. These materials function based on their unique properties and adsorption mechanism.

Activated Carbon: Activated carbon is a highly porous form of carbon with a large surface area, typically ranging from 500 to 1500 m^2/gm. The activation process is achieved by treating carbon material with oxidising agents at high temperature. Its complex pore structure, including micropores (<2 nm), mesopores (2-50 nm) and macropores (>50 nm) provide numerous adsorption sites for a wide range of molecules.[26,27]

Activated Alumina: Activated alumina is a highly porous form of aluminium oxide with high surface area ranging from 200-400 m^2/gm. It is usually synthesized by heating aluminium hydroxide or alumina hydrate at high temperature. This results removal of water molecules thereby forming porous structure. It exhibits high affinity, particularly for fluoride ions along with other contaminants.[28] Its adsorption capacity is primarily attributed to surface hydroxyl groups which can form hydrogen bonds with polar molecules and ions present in water.

Zeolites: Zeolites are crystalline aluminosilicates with porous structure and cation exchange properties. The porous materials are composed of silicon, aluminium and oxygen atoms arranged in framework that allows selective adsorption molecules based on their size and polarity.[29] Zeolites can be of two types: (a) natural zeolite and (b) synthetic zeolite. Natural zeolites are mineral formations that originate through geological processes. They generally exhibit lower surface area and non-uniform pore structures. In contrast, synthetic zeolites are crystalline aluminosilicate materials synthesized by precise chemical reactions and conditions.[30] It mimics the porous structure of natural zeolite. However, they offer tailored compositions, pore sizes and structures which enhances the overall performance. Therefore, synthetic zeolites like MCM-22, ZSM-5, ZSM-22, NaY, NaX etc. outperform natural zeolites in removing different contaminants.

Clay: Bentonite clay and other types of clay materials are natural adsorbents with layered structure and high surface area. Its high cation exchange capacity enables it to attract and adsorb ions like calcium, sodium, potassium and heavy metals from solution.[31,32]

Carbon nano tubes (CNT): CNT are cylindrical nanostructures (diameter ~1-100 nm) with a high aspect ratio and exceptional adsorption properties.[33] They can be single walled or multi-walled. They have shown potential toward removal of microorganisms, heavy metals and organic pollutants from water.[34]

Graphene-based materials: Graphene is a single layer of carbon atoms arranged in a two dimensional honeycomb lattice. Graphene based materials can take various forms which

includes pristine graphene sheets, graphene oxide, reduced graphene oxide etc. These materials can be used in different form including membrane filters, nanocomposites, adsorbent powders to remove water pollutants.[35]

Metal Oxide based materials: Metal oxides are a class of inorganic compounds composed of metal cations bonded to oxygen anions. Adsorption onto metal oxide surfaces can occur through various mechanism including chemisorption, physisorption, ion exchange, surface complexation and precipitation.[36] They exhibit selectivity towards specific contaminants based on their surface chemistry and interactions. For example, iron oxide nanoparticles are widely used as adsorbents for the removal of heavy metals like arsenic, lead, cadmium etc. and other inorganic pollutants from water.[37]

1.4 Types of photocatalysts for removal of water contaminants:

Photocatalysts can degrade or transform pollutants into harmless substances by harnessing the power of light. There are various types of photocatalysts with unique advantages for water treatment:

Hematite (α-Fe_2O_3): In crystal structure of Hematite (Fig. 1.3.), α-Fe_2O_3, shares a structural similarity with corundum, adopting a three-dimensional framework built from trigonally distorted octahedra FeO_6. These octahedra are interconnected with thirteen neighbours via one face, three edges, and six vertices.[38] The structure falls under the space group R3c exhibiting rhombohedral symmetry, with lattice parameters a = b = 5.431 Å, c = 13.021 Å in the hexagonal cell. Iron oxide based photocatalysts, particularly hematite (α-Fe_2O_3) has garnered attention for their photocatalytic properties. Hematite is a semiconductor material that has wide bandgap of approximately 2.1-2.2 eV. This primarily allows it to absorb light in UV and visible region generating reactive oxygen species responsible for degradation of organic pollutants. Surface engineering techniques, such as doping and heterojunction formation can enhance the surface reactivity and photocatalytic performance of hematite. Iron oxides are abundant and cost effective materials making them attractive for large scale applications in water treatment and environmental remedation.[39]

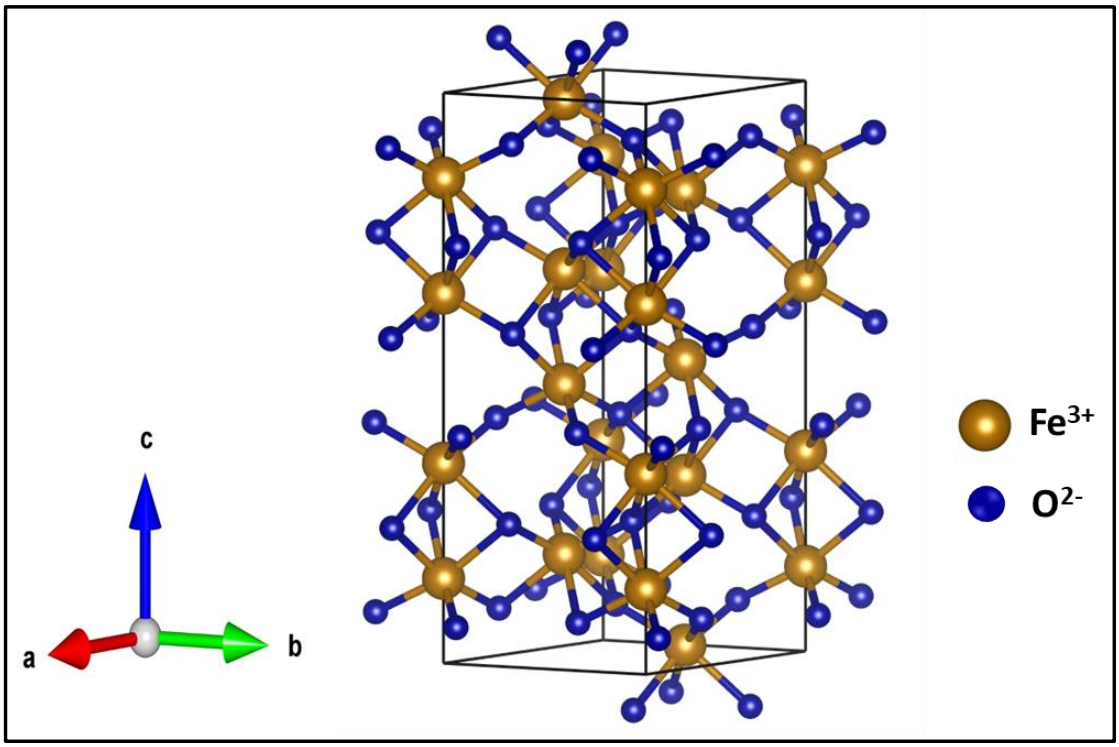

Figure 1.3: Crystal structure of hematite (α-Fe_2O_3).

Titanium dioxide (TiO_2): TiO_2 exists in several crystalline forms like anatase, rutile and brukite. Among these, anatase and rutile phases are the most extensively studied for their superior photocatalytic activity. The bandgap of TiO_2 depends on its crystalline phase. The anatase phase shows bandgap around 3.2 eV whereas rutile shows bandgap around 3 eV. This wide band gap enable TiO_2 to absorb UV light, with the little absorption in the visible region, limiting its activity to UV irradiation.[40]

Metal-Organic Frameworks (MOF): These are a class of porous materials consisting of metal ions or clusters coordinated with organic ligands to form extended three-dimensional structure. MOF based photocatalysts are synthesized by incorporating photo-active components such as semiconductor nanoparticles or organic chromophore into the MOF framework. The properties of MOF based photocatalysts, such as band gap, surface area and porosity can be tuned through rational design and synthetic strategies. This enables the optimization of photocatalytic performance and selectivity for specific applications such as pollutant degradation, hydrogen evolution etc.[41,42]

Carbon based photocatalysts: Carbon based photocatalysts encompass a wide range of materials with diverse properties and applications. Graphitic carbon nitride (g-C_3N_4) stands out for its polymeric structure, visible light capability and potential for applications in water splitting and pollutant degradation.[43] Carbon dots consisting of fluorescent carbon

nanoparticles exhibit strong light absorption in the UV and visible regions, making them suitable for various photocatalytic applications.[44] Graphene and graphene oxide with their exceptional electrical conductivity and high surface area show effectivity for photocatalytic reactions under visible light irradiation.[45] Functionalized CNT can enhance photocatalytic activity and selectivity by facilitating charge separation and improving surface reactivity.[46] Additionally, doped carbon materials exhibit improved visible light absorption and catalytic activity for various photocatalytic reactions including pollutant degradation, hydrogen productions and CO_2 reduction.[47]

Recently, there has been a notable shift in research focus towards synthesizing adsorbent or photocatalyst materials using agro or industrial wastes. Agro and industrial waste are often available in large quantities as by-products of agricultural and manufacturing process. Converting waste into functional materials for water treatment reduces the environmental impact of waste disposal. Additionally, waste based materials are typically available at low or no cost, making them economically attractive option for synthesis of adsorbents and photocatalysts materials.

A brief overview of different agro and industry based waste materials is provided in the following sections.

1.5 Agro waste based materials: Agro waste, also known as agricultural waste, refers to any residue or by-product generated from agricultural activities. The following are some examples of agro-waste materials.

Rice husk ash (RHA): Rice husk, the outer covering of rice grains, is a widely available agro waste material. It is composed primarily of cellulose, hemicellulose, lignin and silica. The silica content in a rice husk ranges from 15%-20%.This makes it one of the richest natural sources of silica.[48] RHA is the residue obtained after burning rice husk. It primarily comprises silica (SiO_2) constituting around 80-95% of its composition. It possesses high thermal stability making it suitable for applications in high temperature. The high surface area and adsorption capacity of RHA makes it suitable for water treatment applications.[49] Due to its pozzolanic properties, RHA serves as an additive in cement and concrete production.[50,51] Utilizing RHA in various applications (Fig. 1.4) help in reducing waste disposal issues associated with rice husk combustion.

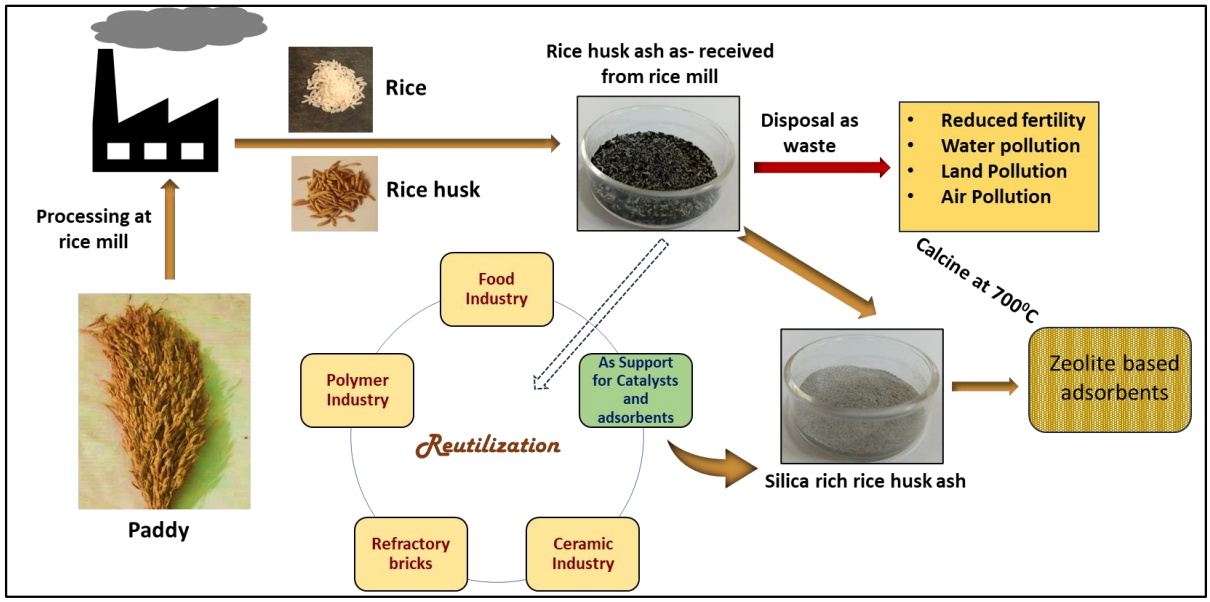

Figure 1.4: Utilization of RHA obtained from rice mill.

Baggase: Baggase is the fibrous residue left behind after sugarcane or agave stalks are crushed. It primarily consists of cellulose, hemicelluloses**,** lignin with small amount of sugar and protein. Baggase is fibrous in nature and typically has high moisture content. It is a valuable biomass resources with significant energy potential. It has different applications in water treatment, energy production, biofuel manufacturing, paper making and soil improvement.[52–54]

Wheat straw: Wheat straw is the stalk left after wheat grains are harvested. It is composed of high level of carbohydrates, proteins, minerals (calcium, phosphorous) etc. Its chemical composition makes it promising for biofuel production. Wheat straw can be utilized in various industrial applications including water treatment, paper making, cardboard production, and construction materials.[55,56]

Coconut/Almond/Walnut/Peanut shell: Coconut shells, almond shells, walnut shells, and peanut shells exhibit a diverse array of chemical properties that render them valuable resources for numerous applications. These agricultural wastes contain significant amounts of cellulose, lignin, and hemicellulose contributing to their structural integrity. They also offer valuable resources in the form of ash after combustion containing carbon, and residual nutrients such as potassium and phosphorus. Their surface area and porosity may impact their adsorption capacity and suitability for applications like water purification and gas adsorption. With their rich carbon content, these materials can be utilized in biochar production and carbon sequestration efforts. Moreover, their chemical composition makes them suitable for soil amendment, organic fertilizers, biofuel production, and composite materials.[57,58]

Corn stover: Corn stovers refer to the stalks, leaves and cobs left in the field after corn harvest. Like other agrowaste materials, lignocellulosic fibres are the integral constituents of it. It shows diverse applications in water treatment, bioenergy production, soil improvement and other industrial processes.[59,60]

Though the agrowaste materials offer potential benefits in renewable energy production, their improper disposal or management can leave negative impacts. Therefore, sustainable waste management strategies are essential to mitigate those adverse effects.

1.6 Industrial waste based materials: Industrial waste refers to any residual material generated during industrial processes.This waste can encompass a wide range of materials including solid, liquid or gaseous substances. Herein, some examples of industrial waste based materials and their detrimental effects are summarized below.

Red Mud: Red mud (RM), also known as bauxite residue, is generated during the processing of buxite into alumina in the Bayer's process (Fig. 1.5). It is highly alkaline with pH values typically ranging from 10-13. RM consists mainly of iron oxides (Fe_2O_3), aluminium oxides (Al_2O_3), silica (SiO_2) and various other compounds including titanium oxide (TiO_2), sodium oxide (Na_2O) and calcium oxide(CaO).[61] Large quantities of RM is generated annually worldwide with an estimated around 200 millions ton produced annually. Improper disposal of RM can lead to environmental pollution and ecological damage.The alkalinity of RM can affect soil and water quality.This can lead to soil degradation, reduced fertility and contamination of surface and ground water. Despite its environmental challenges, RM has been explored for various environmental applications. One significant application is its use as potential raw material for the synthesis of iron-rich ceramics, iron oxide pigments and adsorbents for water treatment. Additionally, RM also shows extensive use in construction materials, particularly in cement and concrete production.[62]

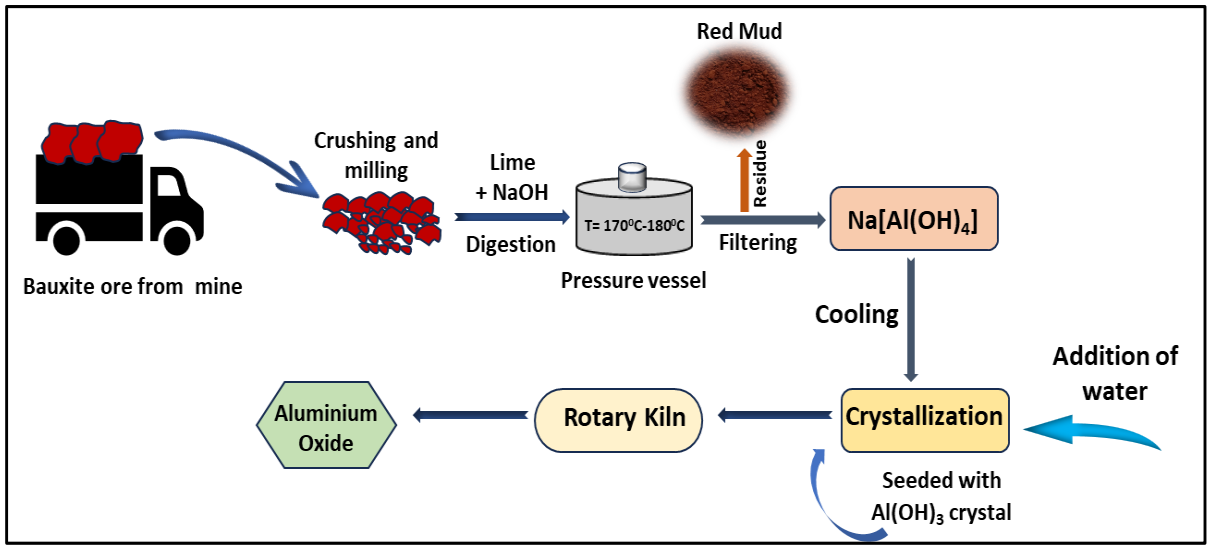

Figure 1.5: Alumina obtained from Bauxite *via* Bayer's process.

Fly ash: Fly ash is a by-product of coal combustion in thermal power plants. It is primarily composed of SiO_2, Al_2O_3 and Fe_2O_3. There are two main types of fly ash: Class F and Class C. Class F fly ash is produced from burning anthracite or bituminous coal and contains low levels of calcium oxide (CaO). Class C fly ash is produced from burning sub-bituminous or lignite coal and contains higher levels of CaO. However, its release into air can contribute to air pollution. Inhalation of fly ash particles can cause severe health issues. Regulations and proper handling procedures are essential to mitigate the risk. Fly ash, with its porous structure and high surface area, serves an efficient adsorbent for removing pollutants from aqueous solution and air stream.[63,64]

Steel slag: Steel slag is a by-product of steel manufacturing processes like blast furnaces or basic oxygen furnaces. It contains mainly SiO_2, Fe_2O_3, Al_2O_3 along with other alkali metal oxides.[65] Inappropriate disposal of steel slag often causes adverse effects to environment. Therefore, recycling and utlizing steel slag is a crucial step to minimise the environmental impacts. However, it can be effectively used as construction material including concrete production,bricks, lighweight aggregates, ceramics and adsorbents for decontamination of water.[66,67]

Waste tire and rubbers: These are often found as discarded from automotive industries, construction sites and manufacturing processes. Their slow decomposition rate often poses significant challenges to environment. However, these can be recycled into valuable materials such as adsorbent materials for water purification, biofuels, green chemicals, rubberized asphalt for road construction etc.[68–70]

Special wastes: Special wastes are materials that come from different chemical plants like pharmaceutical manufacturing, electronics production, metal fabrication and so on.[71] These contain a varety of hazardous substances including solvents, heavy metals and radioactive materials etc. which poses risk to human health and ecosystem. Solvent recycling techniques include distillation and filtering which minimises the requirement of new raw material.[72] Similar to this, heavy metal recycling involves methods like electroplating, ion exchange, or precipitation to recover valuable metals from industrial effluent or scrap materials.[73] Nevertheless, because of their inherent risks, recycling radioactive materials necessitates strict regulations and specialized facilities. Reprocessing or transmutation processes are frequently used to reduce radiological concerns.[74]

Herein, for improved adsorption efficiency, two types of waste material have been chosen for the synthesis of adsorbents and photocatalysts for the removal of inorganic and organic water contaminants. Agro waste rice husk ash has been chosen to synthesize zeolite based adsorbents for the removal of fluoride ion. On the other hand, industrial waste red mud has been utilized to synthesize iron oxide based adsorbents and photocatalysts for the removal of As(V) and MB, respectively.

Accordingly, a literature survey on different adsorbents and photocatalysts derived from RHA and red mud based waste materials have been summarized in the following section.

1.7 Rice husk ash based adsorbents for decontamination of water:

Rice husk ash (RHA) emerges as a highly appealing bio-based adsorbent material for pollutant removal owing to its abundance, renewability, and cost-effectiveness. The straightforward process of obtaining RHA through rice husk combustion at elevated temperatures (~ 700-900 ^{0}C) ensures low production costs. Moreover, the high silica content of RHA results in a porous structure, offering a large surface area and abundant active sites for pollutant adsorption. By repurposing agricultural waste into a valuable adsorbent, RHA not only mitigates environmental pollution but also contributes to the maintenance of ecosystem and water quality.

Numerous literatures have been reported till date based on preparation of RHA based adsorbents and their potential application toward removal of different contaminants from water. Inorganic and organic contaminants are removed using RHA based adsorbents.

Utilizing RHA, Zn(II) removal efficiency of 95.8% was achieved at an adsorbent dosage level of 10 g/L following pseudo-second order kinetic model with adsorption capacity of ~690 mg/gm.[75] Srivastava *et al*. synthesized mesoporous RHA with surface area of 36.44 m^2/gm for the removal of heavy metals.[76] The sorption of Pb(II) ions using RHA with adsorption capacity of 91.74 mg/gm was studied by Tarun *et al*.[77] Feng *et al*. studied adsorption of Pb(II) and Hg(II) by utilising RHA with adsorption capacity values of 9.86 and 3.05 mg/gm, respectively at 30 ^{0}C.[78] RHA based zeolite was reported to remove Fe (II), Cu (II), and As (V) with maximum removal percentages of 91.46%, 90%, and 87.81%, respectively.[79] Recently, iron-modified mesoporous NaY zeolite obtained from RHA was found to show effective removal of As(V) (99.90%) compared to the pristine unmodified zeolite (40.31%).[80] HCl treated RHA was found to effectively remove heavy metal ions of Cr(VI), Pb(II) and Zn(II) with maximum adsorption efficiencies of 87.12, 88.63 and 99.28%, respectively.[81] Allophane, an aluminosilicate substance, derived from RHA showed phosphate removal of 35.1 and 4.3 mg/gm with type I and type II allophanes, respectively.[82] Surface modification of RHA using acetic acid showed a significant removal of Cu^{2+} with 99% efficiency.[83] Fe-Mn oxides@SiO_2 nanoparticles derived from RHA showed 70.5% removal of Co(II) from waste water.[84] MgO nanoparticles obtained from magnesium salt in the presence of moringa oleifera leaf extract was impregnated into RHA which resulted Cr(VI) and Pb(II) removal of 79.20 and 96.02%, respectively from mining waste water.[85]

Different organic contaminants are also removed using RHA or RHA based adsorbent materials. Chandrasekhar and Pramada studied the effect of pH and pore volume on the adsorption of MB dye using RHA.[86] Lakshmi *et al*., investigated the effect of temperature on Indigo Carmine (IC) dye removal using RHA with optimum adsorbent dosage of 10 gm/L.[87] In another study, RHA showed promising adsorption capacities of 1.53×10^{-4}, 8.07×10^{-5}, and 1.63×10^{-6} mol/gm of phenolic compounds like phenol, resorcinol and 2-chlorophenol, respectively.[88] Mahi and co-workers found that RHA with higher surface area showed more adsorption efficiency of phenol (0.886 mg/gm) as compared to rice husk (0.0022mg/gm).[89] 3-aminopropyltriethoxysilane functionalized RHA revealed maximum adsorption capacity of 8.2 mg/gm at pH 6 for the removal of humic acid from water.[90] A hydrogel composite of biopolymer starch (ST) and RHA showed an impressive adsorption capacity of 1906.3 mg/gm in just 60 min for the removal of MB.[91] A mesoporous geopolymer composed of RHA and metakaolin exhibited 70.8% removal of methyl violet 10B dye with adsorbent dosage of 1.5 gm/L.[92] Sulphuric acid pre-treated RHA with surface area 138 m^2/gm was utilized by Jahid *et*

al. for the removal of MB which showed maximum adsorption capacity of 107 mg/gm at pH 8 within 60 min.[93] Recently, RHA was found to be an effective adsorbent for the removal of antibiotic ofloxacin showing maximum adsorption percentage of 79.71% with adsorption capacity of 6.28 mg/gm, at pH 6.[94] Novel nZSM-5 zeolite from RHA was reported to show high adsorption capacity of 125.43 mg/gm for the removal of CV.[95] Thiol modified (using 3-Mercaptopropyltrimethoxysilane) magnetic mesoporous silica (magMCM-41) nanoparticles obtained from RHA resulted 83.44 and 79.38% removal of 2,4-Dichlorophenoxyacetic acid and glyphosate, respectively with their adsorption capacity values of 120.36 and 108.53 mg/gm.[96] Congo Red (CR) and Naphthol Green B (NGB) could be removed from aqueous solution using cetyltrimethyl ammonium bromide (CTAB) functionalized sodium silicate derived from RHA with maximum capacities of 73.04 and 86.59 mg/gm, respectively at 303 K.[97] Mesoporous silica (SBA-16) with surface area 461 m^2/gm obtained from RHA showed removal of Rhodamine B dye with maximum adsorption capacity of 166.7 mg/gm as calculated from Langmuir model.[98]

1.8 Red mud (RM) based adsorbents and photocatalysts for decontamination of water

RM has acquired considerable interest due to its remarkable efficacy as an adsorbent material in mitigating water pollution. However, the caustic nature of RM poses several environmental and human health risks. Therefore, it needs to be neutralized before using as decontaminating agents. The physico-chemical characteristics of RM can be tuned using a variety of treatment techniques, such as heat treatment, neutralization, acidification etc.[99] For water decontamination, RM is utilized both as adsorbent material as well as photocatalyst due to abundant presence of Fe_2O_3 content.

1.8.1 Red mud based adsorbents for the removal of different contaminants

Application of red mud based adsorbents for the removal of different inorganic contaminants:

Metal ions represent a significant category of pollutants in aquatic environment. Among them arsenic is especially notable because of its pervasiveness in natural water and its severe threat to human health. Adsorption process has been extensively used to remove arsenic from waste water.[100] Altundo *et al.* utilized red mud to remove both As(III) and As(V) from water with

adsorption capacities of 8.86 and 6.86 μmol/gm, respectively.[101] With As concentration of 133.5 μmol/L using RM dosage of 20 gm/L, adsorption equilibrium was reached within 45 and 90 mins for As(III) and As(V), respectively. Interestingly, the adsorption of As(III) and As(V) are exothermic and endothermic in nature, respectively. In a study, activated seawater-neutralized red mud i.e., activated Bauxsol (AB) showed equilibrium within 3 and 6 h for As(V) and As(III), respectively which followed pseudo-first-order kinetics.[102] The optimal pH for As(V) adsorption was found to be 4.5, and almost complete removal was achieved regardless to the initial As(V) concentration. The adsorption capacity of activated red mud (ARM) for removing Cr(VI) from both synthetic aqueous solutions and industrial effluents was investigated.[103]The Langmuir monolayer capacity of ARM for Cr(VI) was determined to be 30.74 mmol/gm. Dursun *et al*. investigated the use of red mud activated with HCl for Cr(VI) removal.[104] It was found that the optimal red mud dose and pH value resulted in approximately 70% removal efficiency for chromate. It is reported that the primary components, Fe_2O_3 and Al_2O_3 in red mud caused the removal of Cr(VI) from water.[105,106] Table 1.1 summarizes adsorption capacities of red mud derived adsorbents toward removal of different ions.

Table 1.1: Different red mud derived adsorbents and their adsorption capacities toward removal of different ions.

Type of adsorbents	Contaminant metal ions	Adsorption capacity (mg/gm)	References
Red mud	Ni(II)	13.69	[107]
BRA	Cr(III)	17	[108]
BRB	Cr(III)	33	[108]
ZVI@GRM	Pb(II)	188.67	[109]
ZVI@GRM	Cr(VI)	51.55	[109]
Modified Red mud	Pb(II)	551.11	[110]
Immobilized Red mud	Mn(II)	57.25	[111]
ICRM@600	U(VI)	59.45	[112]
Fe-biochar RM composite	As(V)	13.40	[113]
Fe-biochar RM composite	Ni(II)	17.60	[113]
AMD catalysed RM	Sb(V)	1638	[114]
AMD catalysed RM	As(V)	109	[114]
AMD catalysed RM	Pb(II)	509	[114]
MZ-20	Sr(II)	172	[115]

Tor *et al*. found that granular RM (GRM) was effective in removing fluoride from water with adsorption capacity of 0.644 mg/gm at pH 4.7 wherein equilibrium was reached after 6 hours, irrespective of the initial fluoride concentration.[116] Cengeloglu *et al*. investigated that the pristine RM and the HCl activated RM showed nitrate adsorption capacities of 1.859 and 5.858 mmol/gm, respectively, and the equilibrium was reached within 60 min.[117] In another batch process, HCl treated RM with enhanced surface area and total pore volume rendered phosphate adsorption capacity of 0.58 mg/gm at 40°C (pH 5.5).[118] The efficacy of RM–Chitosan beads (Rm-Ch) was investigated for removal of fluoride, chromate, and phosphate ions from water with adsorption capacities of 6.15, 30.88 and 23.54 mg/gm, respectively.[119] The adsorption

process was exothermic following pseudo-second-order kinetics. Recently, RM-based geopolymer microspheres (RM@GMs: 75–150 μm) with adsorbent dosage of 1 gm/L showed fluoride adsorption capacity of 76.57 mg/gm within 45 min at pH 2 following pseudo-second order kinetic model.[120]

Application of red mud based adsorbents for the removal of different dyes and phenolic compounds:

Effluents particularly coloured dyes and phenolic pollutants are considered as highly toxic to aquatic life affecting the overall quality of natural water sources. Researchers have investigated the utilization of RM as a promising adsorbent material for removing dyes and toxic phenolic compounds from wastewater. HCl-activated RM was found to effectively remove Congo Red (CR) dye from water at pH of 7.0 with maximum adsorption capacity of 7.08 mg/gm within 90 mins.[121] Zhang *et al*. utilized acid-treated RM to remove Malachite Green (MG) and CV dyes with maximum adsorption capacities of 336.4 and 60.5 mg/gm, respectively at pH >3.2.[122] Hydrazine sulphate activated RM was utilized to remove up to 94% Indigo Carmine (IC) dye with adsorption capacity of 62.6 mg/gm.[123] In another study, mesostructured RM based material with high surface area was employed for the removal of MB where maximum adsorption capacities of 232 mg/gm and 274 mg/gm were achieved at pH 7 for different variant of RM.[124] RM derived adsorbent materials were also utilized in removing phenol and phenol derivatives like 2-chlorophenol, 4-chlorophenol, and 2,4-dichlorophenol etc. from wastewater.[125] High adsorption capacities for 2,4-dichlorophenol and 4-chlorophenol with removal efficiency of 94–97% were observed at pH 6 while removal% for 2-chlorophenol and phenol was in the range of 50–81% at pH 4-5. Tor *et al*. investigated the removal of phenol from water using HCl-activated RM which exhibited a higher adsorption capacity (8.156 mg/gm) compared to neutralized RM (4.127 mg/gm) at 25 ± 1°C (pH 6).[126]

A summary of adsorption capacity of red mud derived adsorbents for different inorganic anions, dyes and phenolic pollutants is presented in Table 1.2.

Table 1.2: Different RM derived adsorbents and their adsorption capacities towards removal of different inorganic anions, dyes and phenolic pollutants.

Type of Adsorbent	Contaminant dyes and phenolic compounds	Adsorption capacity (mg/gm)	References
Acid activated RM	Phosphate	202.90	[127]
$AlCl_3$ modified RM	Fluoride	91.28	[128]
Activated RM	Nitrate	5.85	[129]
Ce modified RM	Fluoride	14.74	[130]
α-Fe_2O_3 microsphere	Congo Red	342.57	[131]
SFO@NaP1	MB	47.90	[132]
RSM-optimised RM	Reactive Blue 2	118.24	[133]
RSM-optimised RM	Reactive Black 5	121.02	[133]
RSM-optimised RM	Reactive Red 24	129.19	[133]
RSM-optimised RM	Reactive Yellow 15	142.64	[133]
RM-MK geopolymer	MB	19.96	[134]
ARM/NiOOH	Congo Red	348.00	[135]
g-C_3N_4/RM-MK-GP	MB	170.90	[136]
Activated RM	Phenol	1.79	[137]
Treated RM	Phenol	49.30	[138]

1.8.2 Red mud based photocatalysts for the removal of different contaminants

Red mud characterized by its complex matrix of metal oxides, predominantly iron and aluminium, possesses inherent photocatalytic activity under appropriate light irradiation. By harnessing the photoactive components within RM, researchers have started exploring its suitability towards the development of efficient and eco-friendly photocatalytic applications.

In a study, HCl modified RM with surface area of 317.14 m^2/gm showed 94.2% removal of MO with adsorbent dose of 0.7 gm/L.[139] RM-based ZnO-Fe_2O_3 composite catalyst exhibited promising results in detoxifying Orange II, achieving a removal efficiency of 57.7% at 973 K.[140] Cobalt-doped neutralized RM of dosage 0.08 gm revealed 97.21% MB degradation within 150 min at pH 9 starting with 20 mg/L of dye concentration.[141] Recently, Xiaoqiang *et al* reported that reduced Graphene Oxide (rGO) modified RM composite (RM-H/rGO) showed 99.8% degradation of Rhodamine blue (RhB) within 20 mins.[142] They have also studied the removal of various organic contaminants at a wide range of pH. The incorporation of rGO was reported to serve a dual purpose i.e., it impeded the recombination of charge carriers and expedited the Fe^{3+}/Fe^{2+} cycle during the heterogenous Fenton process. In another study, zero-valent iron heterogeneous Fenton catalyst (RMB-900) exhibited 98% removal of Acid Red G within 10 min, which was 6.7 times higher reaction rate constant than that of commercial zero-valent iron.[143] Geopolymer microspheres derived from a combination of RM and granulated blast furnace slag were functionalized by loading BiOX (where X = Cl, Br, I) photocatalysts onto their surfaces leading to a significant improvement in formaldehyde gas adsorption of around 85.71% within 60 min.[144] Ferrous oxalate dihydrate photocatalyst of different variants derived from ferric oxalate and RM were utilized for photo-Fenton degradation of MB with 95.5-97.6% efficiency within 10-30 min.[145] A novel composite, Fe_3O_4@C/RM synthesized from RM in combination of carbon black (derived from scrap tires) showed 95.9% removal of orange II dye within 90 min in the presence of peroxymonosulfate.[146] RM was utilized as a primary material to produce TiO_2/RM composite which exhibited remarkable efficacy in removing tetracycline hydrochloride from water under visible light.[147] Among the various component ratios, TiO_2/RM-0.5 with dosage of 0.5 gm/L showed approximately 80.9% removal of TC solution (10 mg/L) within 2 h. A cutting-edge Z-scheme-heterojunction g-C_3N_4/RM composite was synthesized using RM and melamine as precursor materials.[148] The composite was found to show a notable enhancement in the spatial separation of photogenerated carriers which facilitated the efficient degradation of formaldehyde of 63.04%

within 2 h. RM based biochar obtained from grapefruit peel showed enhanced performance in activating peroxydisulfate (PDS) for degrading 89.98% RhB at pH 4.6 starting with 20 mg/L concentration of adsorbate.[149]

1.9 Outline of dissertation work

Water pollution is a pressing global concern posing significant threats to human health and ecosystems. With growing industrialization, agricultural activities and urbanization, the release of pollutants into water bodies is becoming widespread, necessitating the development of effective and sustainable water treatment technologies. It is worth mentioning that various research groups have devoted their expertise in synthesis of different porous adsorbents and photocatalysts for decontamination of water. However, challenges still exist in terms of synthetic procedure, availability of precursor resources and environmental issues. In this context, utilization of agricultural and industrial waste materials for water remediation has emerged as promising approach to address environmental challenges valorising waste resources.

This dissertation work focuses on the utilization of agro waste rice husk ash (RHA) as adsorbents and industrial waste red mud (RM) as adsorbents as well as photocatalysts for the decontamination of water.

The primary objective of the present study comprises

- To investigate the efficacy of RHA and RM based adsorbents for the removal of various water contaminants like As(V) and fluoride.
- To evaluate the photocatalytic activity of RM based photocatalysts for the degradation of methylene blue (MB) under visible light irradiation.
- To assess the synergistic effects of combining adsorption and photocatalysis for enhanced water decontamination.
- To elucidate the mechanisms underlying the pollutant removal processes and explore the factors influencing adsorption and photocatalytic performance.

Chapter 1 describes a general overview of different type of water decontamination processes, utilization of different adsorbent and photocatalyst materials. A comprehensive overview of the existing literature is illustrated on utilization of RHA and RM based adsorbent materials as well as photocatalytic activity of latter for the removal of different inorganic and organic based water contaminants.

Chapter 2 explores the application of rice husk ash derived zeolite-based adsorbents for the removal of fluoride from water. This chapter is divided into two subsections, 2A and 2B. 2A part delves into the investigation of MgO-modified zeolite as an effective adsorbent for fluoride removal from water. This study explores the synthesis process of MgO-modified zeolite and evaluates its performance in removing fluoride ions under various experimental conditions with mechanistic insights of fluoride adsorption process. 2B part focuses on the utilization of Al_2O_3-modified zeolite as an alternative adsorbent for fluoride removal from water. This study investigates the synthesis methodology of Al_2O_3 modified zeolite and examines its adsorption capacity for fluoride ions in aqueous solutions through batch and column adsorption experiments.

Chapter 3 demonstrates hydrothermal synthesis of hematite (α-Fe_2O_3) from red mud precursor with tuned morphology and textural property. The synthesized materials have been applied as adsorbent for the removal of As(V) from contaminated water under different experimental conditions.

Chapter 4 illustrates synthesis of metal (Cu, Mn, Ce) doped hematite (α-Fe_2O_3) obtained from RM toward their photocatalytic efficiency for degradation of MB. A structure property correlation is established for photocatalytic degradation of MB. By examining the electrochemical properties, a probable mechanism was proposed based on enhanced e^-/h^+ pair separation and migration of RM based photocatalyst.

Chapter 5 demonstrates summary of the work described in the thesis and the possible future perspective of the entire thesis work.

References:

1 A. Chowdhury, M. K. Adak, A. Mukherjee, P. Dhak, J. Khatun and D. Dhak, *J. Hydrol. (Amst)*, 2019, **574**, 333–359.

2 H. G. Mikkonen, R. van de Graaff, A. T. Mikkonen, B. O. Clarke, R. Dasika, C. J. Wallis and S. M. Reichman, *Environ. L. Pollut.*, 2018, **242**, 1838–1849.

3 H. Kabir, A. K. Gupta and S. Tripathy, *Crit. Rev. Environ. Sc.i Technol.*, 2020, **50**, 1116–1193.

4 J. C. Ng, J. Wang and A. Shraim, *Chemosphere*, 2003, **52**, 1353–1359.

5 D. A. Polya and M. Lawson, *Arsenic*, 2015, pp. 23–60.

6 S. Prakash and A. K. Verma, *Int. J. Biol. Innov.*, 2021, **03**, 38–47.

7 S. J. S. Flora, in *Handbook of Arsenic Toxicology*, ed. S. J. S. Flora, Academic Press, Oxford, 2015,1–49.

8 A. R. P. Hidayat, L. L. Zulfa, A. R. Widyanto, R. Abdullah, Y. Kusumawati and R. Ediati, *RSC. Adv.*, 2023, **13**, 12320–12343.

9 A. Mukhopadhyay, S. Duttagupta and A. Mukherjee, *J. Environ. Chem. Eng.*, 2022, **10**, 107560.

10 J. Bratby, *Coagulation and flocculation in water and wastewater treatment*, IWA publishing, 2016.

11 K. O. Iwuozor, *Adv. J. Chem.A*, 2019, **2**, 105–127.

12 W. He, K. Ai, X. Ren, S. Wang and L. Lu, *J. Mater. Chem. A Mater.*, 2017, **5**, 19593–19606.

13 A. P. Reverberi, L. Maga, C. Cerrato and B. Fabiano, *Curr. Opin. Chem. Eng.*, 2014, **6**, 75–82.

14 R. Singh, *Membrane technology and engineering for water purification: application, systems design and operation*, Butterworth-Heinemann, 2014.

15 J.-D. Lee, S.-H. Lee, M.-H. Jo, P.-K. Park, C.-H. Lee and J.-W. Kwak, *Environ. Sci. Technol.*, 2000, **34**, 3780–3788.

16 S. Palit, in *Water Purification*, ed. A. M. Grumezescu, Academic Press, 2017, 587–620.

17 I. G. Wenten and Khoiruddin, *Desalination*, 2016, **391**, 112–125.

18 S. Al-Amshawee, M. Y. B. M. Yunus, A. A. M. Azoddein, D. G. Hassell, I. H. Dakhil and H. A. Hasan, *J. Chem. Eng.,* 2020, **380**, 122231.

19 M. Akhter, G. Habib and S. U. Qamar, *J. Membr. Sci. Technol.*, 2018, 8, 1000182.

20 M. M. Jamolovich and N. K. Ibodullaevich, *Austrian J. Technol. Nature. Sci*, 2023, 21–23.

21 A. Kumar, H. Joshi and A. Kumar, *Sep. Purif. Rev.*, 2021, **50**, 283–314.

22 A. K. Badawi, M. Abd Elkodous and G. A. M. Ali, *RSC. Adv.*, 2021, **11**, 36528–36553.

23 M. Beiranvand, S. Farhadi and A. Mohammadi-Gholami, *RSC. Adv.*, 2022, **12**, 34438–34453.

24 S. Mishra and B. Sundaram, *Mater.Today Proc*.,2023, **20**, 3442-3454.

25 X. Tao, Y. Zhao, S. Wang, C. Li and R. Li, *Chem. Soc. Rev.*, 2022, **51**, 3561–3608.

26 Y. A. B. Neolaka, A. A. P. Riwu, U. O. Aigbe, K. E. Ukhurebor, R. B. Onyancha, H. Darmokoesoemo and H. S. Kusuma, *Results. Chem.*, 2023, **5**, 100711.

27 S. Husien, R. M. El-taweel, A. I. Salim, I. S. Fahim, L. A. Said and A. G. Radwan, *Curr. Res. in Green Sustain. Chem.*, 2022, **5**, 100325.

28 S. I. Alhassan, L. Huang, Y. He, L. Yan, B. Wu and H. Wang, *Crit. Rev. Environ. Sci. Technol.*, 2021, **51**, 2051–2085.

29 E. Kianfar and A. Mahler, *Zeolites: advances in research and applications*, 2020, 1-243.

30 M. Król, *Crystals (Basel)*, 2020, **10**, 622.

31 B. O. Otunola and O. O. Ololade, *Environ Technol Innov*, 2020, **18**, 100692.

32 A. Gil, L. Santamaría, S. A. Korili, M. A. Vicente, L. V Barbosa, S. D. De Souza, L. Marçal, E. H. De Faria and K. J. Ciuffi, *J. Environ. Chem. Eng.*, 2021, **9**, 105808.

33 W. Zhao, Y. Tian, X. Chu, L. Cui, H. Zhang, M. Li and P. Zhao, *Sep. Purif. Technol.*, 2021, **257**, 117917.

34 B. Arora and P. Attri, *J. Comp. Sci.*, 2020, **4**, 135.

35 F. Khan, M. S. Khan, S. Kamal, M. Arshad, S. I. Ahmad and S. A. A. Nami, *J. Mater. Chem. C Mater.*, 2020, **8**, 15940–15955.

36 L. Wang, C. Shi, L. Pan, X. Zhang and J.-J. Zou, *Nanoscale*, 2020, **12**, 4790–4815.

37 R. K. Sharma, K. Solanki, R. Dixit, S. Sharma and S. Dutta, *Environ. Sci. (Camb)*, 2021, **7**, 818–860.

38 M. Mohapatra and A. S, *Int. J. Eng., Sci. Technol.*, 2010, **2**, 127-146.

39 Y. Kumar, R. Kumar, P. Raizada, A. A. P. Khan, A. Singh, Q. Van Le, V.-H. Nguyen, R. Selvasembian, S. Thakur and P. Singh, *J. Environ. Chem. Eng*, 2022, **10**, 107427.

40 S. R. Damkale, S. S. Arbuj, G. G. Umarji, S. B. Rane and B. B. Kale, *RSC Adv*, 2021, **11**, 7587–7599.

41 N. Kitchamsetti, C. S. Chakra, A. L. F. De Barros and D. Kim, *Nanomaterials*, 2023, **13**, 336.

42 S. P. Tripathy, S. Subudhi, A. Ray, P. Behera, A. Bhaumik and K. Parida, *Langmuir*, 2022, **38**, 1766–1780.

43 L. Wang, K. Wang, T. He, Y. Zhao, H. Song and H. Wang, *ACS Sustain. Chem. Eng.*, 2020, **8**, 16048–16085.

44 K. Akbar, E. Moretti and A. Vomiero, *Adv. Opt. Mater.*, 2021, **9**, 2100532.

45 F. Khan, M. S. Khan, S. Kamal, M. Arshad, S. I. Ahmad and S. A. A. Nami, *J. Mater. Chem. C. Mater.*, 2020, **8**, 15940–15955.

46 Z. Lian, C. Wei, B. Gao, X. Yang, Y. Chan, J. Wang, G. Z. Chen, K. S. Koh, Y. Shi and Y. Yan, *RSC Adv.*, 2020, **10**, 9210–9225.

47 A. Khan, M. Goepel, J. C. Colmenares and R. Gläser, *ACS Sustain. Chem. Eng.*, 2020, **8**, 4708–4727.

48 B. A. Tayeh, R. Alyousef, H. Alabduljabbar and A. Alaskar, *J. Clean. Prod.*, 2021, **312**, 127734.

49 T. Hongo, M. Moriura, Y. Hatada and H. Abiko, *ACS Omega*, 2021, **6**, 21604–21612.

50 L. Hu, Z. He, Y. Shao, X. Cai and S. Zhang, *Constr. Build Mater.*, 2021, **294**, 123482.

51 S. A. Endale, W. Z. Taffese, D.-H. Vo and M. D. Yehualaw, *Sustainability*, 2022, **15**, 137.

52 N. Ungureanu, V. Vlăduț and S.-Ștefan Biriș, *Sustainability*, 2022, **14**, 11089.

53 S. J. Guevara-Martínez, M. C. Chávez-Parga, J. Espino-Valencia and M. Arroyo-Albiter, *Rev. Mex. Ing. Quim.*, 2021, **20**, 333–344.

54 V. N. Gardare, S. Yadav, D. N. Avhad and V. K. Rathod, *Desalination Water. Treat.*, 2015, **56**, 2872–2878.

55 T. Mkilima, Y. Zharkenov, A. Abduova, N. Sarypbekova, K. Kirgizbayeva, I. Zhumadilov, F. Kenzhekulova, M. Abilkhas and S. Zharassov, *Case Stud. Chem. Environ. Eng.*,2024,**9** 100662.

56 M. J. Ahmed, I. Anastopoulos, D. Kalderis, M. Haris and M. Usman, *Environ. Res.*, 2024, **250**, 118507.

57 J. O. P. Nayagam and K. Prasanna, *Chemosphere*, 2022, **291**, 132737.

58 A. Kali, A. Amar, I. Loulidi, M. Jabri, C. Hadey, H. Lgaz, A. A. Alrashdi and F. Boukhlifi, *Biomass Convers. Biorefin.*, 2024, **14**, 3655–3666.

59 T. Y. Chong, M. C. Law and Y. S. Chan, *J. Polym. Environ.*, 2021, **29**, 363–381.

60 J. C. de Andrade Neto, G. J. Pereira and A. de A. Morandim-Giannetti, *Cellulose*, 2020, **27**, 6317–6331.

61 X. Wang, Q. Zhan, X. Zhang, Y. Su and J. Zhou, *J. Build. Eng.*, 2024, **84**, 108518.

62 A. Niu and C. Lin, *J. Environ. Manage.*, 2024, **351**, 119660.

63 C. Orozco, S. Tangtermsirikul, T. Sugiyama and S. Babel, *Sci. Rep.*, 2023, **13**, 18254.

64 H.-H. T. Nguyen, H. T. Nguyen, S. F. Ahmed, N. Rajamohan, M. Yusuf, A. Sharma, P. Arunkumar, B. Deepanraj, H.-T. Tran and A. Al-Gheethi, *Environ. Res.*, 2023, 115800.

65 Y. Li, F. Liu, F. Yu and T. Du, *Structures*, 2024, **63**, 106352.

66 P. Kumar and S. Shukla, *Mater. Today Proc.*, 2023, **78**, 145–152.

67 C. Shi, X. Wang, S. Zhou, X. Zuo and C. Wang, *J. Water Proc. Eng.*, 2022, **47**, 102666.

68 Z. Zhao, S. Wu, J. Xie, C. Yang, X. Yang, S. Chen and Q. Liu, *Constr Build Mater*, 2023, **399**, 132572.

69 B. E. Rogachuk and J. A. Okolie, *Chem. Eng. J. Adv.*, 2023, **14**, 100476.

70 M. T. Islam, R. Saenz-Arana, C. Hernandez, T. Guinto, M. A. Ahsan, D. T. Bragg, H. Wang, B. Alvarado-Tenorio and J. C. Noveron, *J. Environ. Chem. Eng.*, 2018, **6**, 3070–3082.

71 X. Peng, Y. Jiang, Z. Chen, A. I. Osman, M. Farghali, D. W. Rooney and P.-S. Yap, *Environ. Chem. Lett.*, 2023, **21**, 765–801.

72 C. J. Clarke, W.-C. Tu, O. Levers, A. Brohl and J. P. Hallett, *Chem. Rev.*, 2018, **118**, 747–800.

73 M. Yadav, G. Singh and R. N. Jadeja, *Pollutants and Water Management: Resources, Strategies and Scarcity*, 2021, 377–397.

74 S. A. Darda, H. A. Gabbar, V. Damideh, M. Aboughaly and I. Hassen, *J. Radioanal. Nucl. Chem.*, 2021, **329**, 15–31.

75 A. K. Bhattacharya, S. N. Mandal and S. K. Das, *J. Chem. Eng.,*2006, **123**, 43–51.

76 V. C. Srivastava, I. D. Mall and I. M. Mishra, *J. Hazard. Mater.*, 2006, **134**, 257–267.

77 T. K. Naiya, A. K. Bhattacharya, S. Mandal and S. K. Das, *J. Hazard. Mater.*, 2009, **163**, 1254–1264.

78 Q. Feng, Q. Lin, F. Gong, S. Sugita and M. Shoya, *J. Colloid Interface. Sci.*, 2004, **278**, 1–8.

79 S. Banerjee, S. Barman and G. Halder, *Groundw. Sustain Dev.*, 2017, **5**, 137–151.

80 S. Sivalingam and S. Sen, *Ind. Eng. Chem. Res.*, 2019, **58**, 14073–14087.

81 A. K. Priya, V. Yogeshwaran, S. Rajendran, T. K. A. Hoang, M. Soto-Moscoso, A. A. Ghfar and C. Bathula, *Chemosphere*, 2022, **286**, 131796.

82 S. Ohta, K. Yoshida and T. Hongo, *J. Environ. Chem. Eng.*, 2022, **10**, 108634.

83 G. C. Pathiraja, D. K. De Silva, L. Dhanapala and N. Nanayakkara, *Desalination Water Treat.*, 2015, **54**, 547–556.

84 H. Sharififard and R. Hayati, *Int. J. Environ. Anal. Chem.*, 1–24.

85 L. S. Mustapha, S. O. Jacob-Oricha, M. D. Yahya, S. Y. Lau, A. S. Yusuff and K. S. Obayomi, *Environ. Adv.*, 2024, **15**, 100507.

86 S. Chandrasekhar and P. N. Pramada, *Adsorption*, 2006, **12**, 27–43.

87 U. R. Lakshmi, V. C. Srivastava, I. D. Mall and D. H. Lataye, *J. Environ. Manage.*, 2009, **90**, 710–720.

88 D. N. Mbui, P. M. Shiundu, R. M. Ndonye and G. N. Kamau, *J. Environ. Monit.*, 2002, **4**, 978–984.

89 A. H. Mahvi, A. Maleki and A. Eslami, *Am. J. Appl. Sci.*,2004,**4**,321-326.

90 A. Imyim and E. Prapalimrungsi, *J. Hazard. Mater.*, 2010, **184**, 775–781.

91 A. C. N. de Azevedo, M. G. Vaz, R. F. Gomes, A. G. B. Pereira, A. R. Fajardo and F. H. A. Rodrigues, *Iran. Polym. J.*, 2017, **26**, 93–105.

92 T. R. Barbosa, E. L. Foletto, G. L. Dotto and S. L. Jahn, *Ceram Int.*, 2018, **44**, 416–423.

93 J. Bin Haider, Md. I. Haque, M. Hoque, Md. M. Hossen, M. Mottakin, Md. A. Khaleque, M. A. H. Johir, J. L. Zhou, M. B. Ahmed and M. Zargar, *J. Clean Prod.*, 2022, **380**, 135121.

94 G. Kaur, N. Singh and A. Rajor, *J. Contam. Hydrol.*, 2021, **236**, 103737.

95 S. Sivalingam and S. Sen, *J. Mater. Res. Technol.*, 2020, **9**, 14853–14864.

96 R. J. Zadeh, M. H. Sayadi and M. R. Rezaei, *J. Environ. Chem. Eng.*, 2021, **9**, 104804.

97 N. M. Fadimatou, P. N. Fotsing, A. Mandjewil, J. M. Siewe, J. Vieillard, G. L. Dotto, E. D. Woumfo and P. T. Ngueagni, *Emergent Mater.*,2024,**34**,456-469.

98 S. S. El-Shafey, S. A. Sayed Ahmed, R. M. Aboelenin and N. A. Fathy, *Desalination Water Treat.*, 2024, **317**, 100179.

99 Y.-F. ZHOU and R. J. HAYNES, *Crit. Rev. Environ. Sci. Technol.*, 2010, **40**, 909–977.

100 D. Mohan and C. U. Pittman, *J. Hazard. Mater.*, 2007, **142**, 1–53.

101 H. Soner Altundoğan, S. Altundoğan, F. Tümen and M. Bildik, *Waste Manage.*, 2000, **20**, 761–767.

102 H. Genç-Fuhrman, J. C. Tjell and D. McConchie, *Environ. Sci. Technol.*, 2004, **38**, 2428–2434.

103 J. Pradhan, S. N. Das and R. S. Thakur, *J. Colloid Interface. Sci.*, 1999, **217**, 137–141.

104 S. Dursun, D. Guclu, A. Berktay and T. Guner, *Asian J. Chem.*, 2008, **20**, 6473–6478.

105 X. Qi, H. Wang, L. Zhang, B. Xu, Q. Shi and L. Fengting, *Chemosphere*, 2019, **245**, 125560.

106 Y. Zhao, J. Zhang and C. Zheng, *Fuel*, 2013, **109**, 86–93.

107 Y. Hannachi, N. A. Shapovalov and A. Hannachi, *Korean J. Chem. Eng.*, 2010, **27**, 152–158.

108 X. Qi, H. Wang, L. Zhang, B. Xu, Q. Shi and F. Li, *Chemosphere*, 2020, **245**, 125560.

109 Y. Du, M. Dai, J. Cao and C. Peng, *RSC Adv.*, 2019, **9**, 33486–33496.

110 F. Lyu, S. Niu, L. Wang, R. Liu, W. Sun and D. He, *J. Hazard Mater.*, 2021, **406**, 124678.

111 Y. Li, H. Huang, Z. Xu, H. Ma and Y. Guo, *J. Clean Prod.*, 2020, **253**, 119955.

112 W. Wu, Z. Chen, Y. Huang, J. Li, D. Chen, N. Chen and M. Su, *J. Hazard Mater.*, 2021, **409**, 124925.

113 K. Yoon, D.-W. Cho, A. Bhatnagar and H. Song, *Environ Res.*, 2020, **188**, 109809.

114 D.-R. Zhang, H.-R. Chen, J.-L. Xia, Z.-Y. Nie, X.-J. Zhao and E. Pakostova, *J. Chem. Eng.*, 2023, **465**, 142867.

115 Z. Chen, X. Li, H. Liu, W. Xu, J. Yu, Y. Zang, G. Hu, T. Hu, J. Jiang, P. Mao, Y. Pan and Y. Wei, *Micropor. Mesopor. Mat.*, 2024, **370**, 113069.

116 A. Tor, N. Danaoglu, G. Arslan and Y. Cengeloglu, *J. Hazard. Mater.*, 2009, **164**, 271–278.

117 Y. Cengeloglu, A. Tor, M. Ersoz and G. Arslan, *Sep. Purif. Technol.*, 2006, **51**, 374–378.

118 W. Huang, S. Wang, Z. Zhu, L. Li, X. Yao, V. Rudolph and F. Haghseresht, *J. Hazard. Mater.*, 2008, **158**, 35–42.

119 S. Tandekar, S. Korde and R. M. Jugade, *Carbohydr. Polym. Technol. Appl.*, 2021, **2**, 100128.

120 M. Yi, K. Wang, H. Wei, D. Wei, X. Wei, B. Wei, L. Shao, T. Fujita and X. Cui, *J. Hazard. Mater.*, 2023, **442**, 130027.

121 A. Tor and Y. Cengeloglu, *J. Hazard. Mater.*, 2006, **138**, 409–415.

122 L. Zhang, H. Zhang, W. Guo and Y. Tian, *Appl. Clay Sci.*, 2014, **93–94**, 85–93.

123 A. N. Babu, D. S. Reddy, P. Sharma, G. S. Kumar, K. Ravindhranath and G. V. K. Mohan, *Mater. Today Proc.*, 2019, **17**, 198–208.

124 Z.-P. Hu, Z.-M. Gao, X. Liu and Z.-Y. Yuan, *Adsorpt. Sci. Technol.*, 2017, **36**, 62–79.

125 V. K. Gupta, I. Ali and V. K. Saini, *Environ. Sci Technol.*, 2004, **38**, 4012–4018.

126 A. Tor, Y. Cengeloglu and M. Ersoz, *Desalination*, 2009, **242**, 19–28.

127 C. Liu, Y. Li Z. Luan, Z. Chen, Z. Zhang and Z. Jia, *J. Environ. Sci.*, 2007, **19**, 1166–1170.

128 N. Wei, Z.-K. Luan, J. Wang, L. Shi, Y. Zhao and J. Wu, *Chinese J. Inorg. Chem*, 2009, **25**, 849–854.

129 Y. Cengeloglu, A. Tor, M. Ersoz and G. Arslan, *Sep. Purif Technol.*, 2006, **51**, 374–378.

130 D. Wang, L. Luo, Y. Chen, S. Chen, X. Qiu and M. Liu, *Mater. Today Sustain.*, 2023, **24**, 100502.

131 J. Wang, P. Sun, H. Xue, J. Chen, H. Zhang and W. Zhu, *J. Phys. Chem. Sol.*, 2020, **140**, 109379.

132 Y. Cheng, L. Xu, Z. Jiang, C. Liu, Q. Zhang, Y. Zou, Y. Chen, J. Li and X. Liu, *J. Chem. Eng.*, 2021, **417**, 128090.

133 V. K. Singh, A. Sett and S. Karmakar, *J. Chem. Eng.*, 2024, **481**, 148373.

134 N. P. F. Gonçalves, S. M. Olhero, J. A. Labrincha and R. M. Novais, *J. Clean Prod.*, 2023, **383**, 135315.

135 D.-A. Xie, Y. Sun, Y.-L. Yang, X.-L. Shi, G. Suo, X. Hou, X. Ye, L. Zhang and Z.-G. Chen, *J. Colloid Interface. Sci.*, 2024, **664**, 136–145.

136 K. Kaya-Özkiper, A. Uzun and S. Soyer-Uzun, *Chem. Eng. Sci.*, 2024, **284**, 119398.

137 M. Shirzad-Siboni, S.-J. Jafari, M. Farrokhi and J. K. Yang, *Environ. Eng. Res.*, 2013, **18**, 247–252.

138 A. Mandal, B. B. Dey and S. K. Das, *Water Pract. Technol.*, 2020, **15**, 705–722.

139 M. Ma, G. Wang, Z. Yang, S. Huang, W. Guo and Y. Shen, *Adv. Mater. Sci. Eng*, **2015**, 907539.

140 Y. Li, G. Wei, L. Shao, Z. Li, F. Yu, J. Liu, X. Yang, Q. Lu, A. Li, Y. Huang and L. Zhang, *J Clean Prod.*, 2019, **207**, 717–727.

141 M. Sahu and R. Patel, *J. Ind. Eng. Chem*, 2016, **40**, 72–82.

142 X. An, Z. Hou, Y. Yu, J. Wang, H. Lan, H. Liu and J. Qu, *Colloids Surf A Physico. Chem Eng Asp.*, 2022, **640**, 128461.

143 H. Li, B. Shi, X. Fu, H. Zhang and H. Yang, *J. Environ. Chem. Eng.*, 2023, **11**, 109998.

144 P. Lu, N. Zhang, Y. Wang, Y. Wang, J. Zhang, Q. Cai and Y. Zhang, *Materials*, 2024, **17**, 1585.

145 Y. Yang, N. Wang and H. Gu, *Environ. Sci. Pollut. Res.*, 2023, **30**, 85210–85222.

146 X. Wang, X. Sun, P. Dai and D. Xu, *Water Air Soil Pollut.*, 2023, **234**, 676.

147 F. Meng, Y. Ling, Y. Li, D. Liu, K. Wei, L. Sun and Z. Sang, *Surf. Interfaces*, 2022, **35**, 102482.

148 Y. Wang, N. Zhang, C. Zhang, Y. Wang, P. Lu and Y. Zhang, *J. Clean Prod.*, 2024, **444**, 141280.

149 S. Deng, M. Yang, Q. An, Z. Li, B. Zhao and B. Ran, *Environ. Sci. Pollut. Res.*, 2023, **30**, 119034–119049.

Chapter 2

Synthesis of rice husk ash derived zeolite based adsorbents for defluoridation of water

This chapter contains two parts : 2A and 2B

Part 2A: This part illustrates the study of MgO-modified zeolite toward effective adsorption of fluoride ions from contaminated water.

Part 2B: This part describes the defluoridation of water by Al_2O_3 modified zeolite through batch and column studies.

Chapter 2A

MgO modified rice husk ash derived zeolite based adsorbent for defluoridation of water

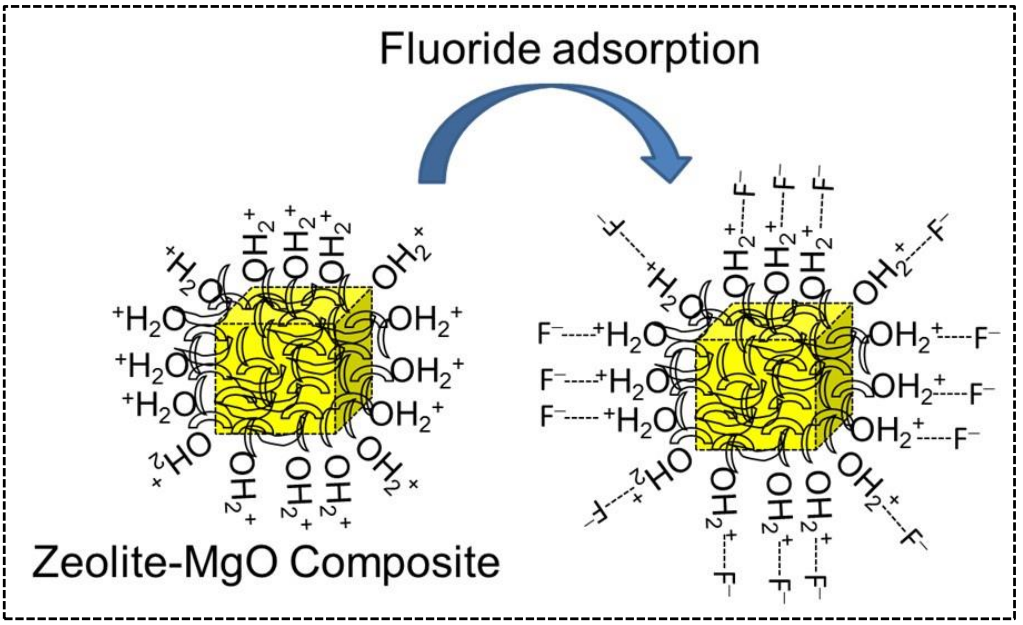

Publication from this Chapter:

Adwitiya Chakraborty and Milan Kanti Naskar, "Study on the synthesis and structural properties of zeoliteA-MgO composite for defluoridation of water", ***Transactions of the Indian Ceramic Society,*** **2021, 80(3), 199-207.**

2A.1 Introduction

In ground water fluoride toxicity is a major concern to human health and other living organisms. Fluoride in drinking water has beneficial as well as detrimental effects depending upon its concentration, exceeding the permissible limit can cause many health issues. Among many common techniques, adsorption process is suitably applied for fluoride removal particularly, for low concentration of fluoride level in water because of low processing cost, ease of operation and high efficiency.[1] Different adsorbent materials like porous alumina,[2,3] layered double hydroxide,[4]rare earth oxide,[5] Fe-Ce-Ni nano adsorbent,[6] porous MgO,[7] bone char[8] etc. are used for fluoride removal from water. It is reported that activated alumina and magnesium oxide are commonly used adsorbents for defluoridation due to their high specific binding sites to adsorb fluoride through inner-sphere complexation.[9,10] However, leaching tendency of alumina as a soluble species into the treated effluent is the major constraint for defluoridation.[11] Due to high isoelectric point (in alkaline pH) of MgO, it possesses strong electrostatic interaction with anionic pollutants like fluoride, arsenate/arsenite etc. favouring anionic decontamination of water. Mg-modified zeolite was used for the removal of heavy metal contaminants from water.[12] Rice husk ash is an agro-waste material which can be used for the synthesis of zeolite.[13]Modification of MgO with rice husk ash derived zeolite can lower the cost of MgO precursor.

In the present work, zeolite A obtained from agro-waste rice husk ash is used for the preparation of zeolite A-MgO composite by a simple processing condition. The objective of this study is to synthesize an efficient adsorbent material by a simple process, and its utilization for defluoridation of water with the effects of contact time, temperature, pH, competing ions, sample dose, initial fluoride concentration and recyclability test. The adsorption behaviour was understood by kinetic models (pseudo-first order and pseudo-second order) and adsorption isotherms (Langmuir and Freundlich). To understand the nature of adsorption process, thermodynamic study was performed. A tentative formation mechanism in removing F^- ions by zeolite A-MgO composite was proposed.

2A.2 Experimental

2A.2.1 Materials

Magnesium chloride hexahydrate ($MgCl_2.6H_2O$) (>98%), urea [$CO(NH_2)_2$], and sodium fluoride (NaF) (>97%) were purchased from Merck, India while sodium aluminate (45% Na_2O + 55% Al_2O_3) was procured from Sigma-Aldrich. Rice husk ash (95% SiO_2) was

collected from J.M. Biotech Pvt. Ltd., India. Millipore water was used throughout the experiment.

Preparation of zeolite A-MgO composite

In a typical experiment, 2 gm of zeolite A synthesized from rice husk ash[14] was added into 80mL of 0.5 M $MgCl_2$ solution in the presence of 10 gm of urea under stirring for 20 min. The whole dispersion was poured into 100 mL Teflon-lined autoclave followed by hydrothermal reaction at 150 ^oC for 5 h. The prepared product was centrifuged and washed with water for several times until the supernatant liquid is almost neutral (pH 7-8). The sample was dried at 70 ^oC for 4 h followed by calcination at 600 ^oC for 2 h to obtain zeolite A-MgO composite.

2A.2.2 Characterization

The synthesized zeolite A-MgO composite was characterized by X-ray diffraction (X'Pert Pro XRD (Philips), PW 3050/60), Fourier transform infrared spectroscopy (Spectrum two, PerkinElmer), X-ray photoelectron spectroscopy (ULVAC-PHI), BET surface area, pore size analysis (Quantachrome (ASIQ, MP) and field emission scanning electron microscopy (Zeiss, Supra^{TM} 35VP).

2A.2.3 Adsorption experiment

For adsorption experiment, 1L stock solution of NaF (7.24 mg/L) was prepared. Batch adsorption experiment was carried out with 20 mL (7.24 mg/L) stock NaF solution and 0.02 gm (1 gm/L) sample dose under stirring for a specific time at room temperature maintaining pH of solution ~ 6.7. After adsorption of F^- ions, the sample (adsorbent) was separated by filtration and F^-ions concentrations in solution were measured by Ion Selective Electrode (ISE) (Versa Star 90, Orion) using TISAB buffer solution. The adsorption capacity at equilibrium q_e(mg/gm) was calculated as follows:

$$q_e = (C_0 - C_e)\ (V/m) \qquad (2A.1)$$

where, C_0 and C_e are the initial and equilibrium F^- concentrations in mg/L, respectively, while V is the volume of F^- concentration in L and m is the sample dose in gm.

2A.3 Results and discussion

2A.3.1 *Characterization of zeoliteA-MgO adsorbent*

Fig. 2A.1(a) shows the XRD patterns of zeolite A-MgO powders. The characteristic peaks of MgO (JCPDF File # 75-0447) were noticed corresponding to (hkl) values of (111), (200), (220), (311) and (222) at 2θ around 36.5, 42.8, 62.2, 74.6 and 78.5, respectively. However, in the presence of MgO particles surrounding onto zeolite A crystal, the intensity of zeolite A peaks (JCPDF File # 39-222) became lower or hidden at 2θ around 7.2, 10.2, 12.5, 21.7, 24.1, 26.1, 27.2, 29.9 and 30.8 with (hkl) values of (200), (220), (222), (600), (622), (640), (642), (644) and (660), respectively. Here, preferential orientation of MgO crystals in their respective crystallographic planes is observed compared to that of zeolite A crystals.

Fig. 2A.1(b) shows the FTIR spectra of zeolite A-MgO composite powders. The broad absorption bands at around 590 and 857 cm^{-1} are due to stretching vibration mode of Mg-O-Mg.[15–17] However, the absorption band centred at 1429 cm^{-1} could be assigned due to CO_3^{2-} ions. The aerial chemisorption of H_2O and CO_2 molecules onto the porous MgO surface caused the formation of CO_3^{2-} ions.[18] The presence of zeolite A was confirmed from its characteristic vibration bands at 464, 685, 792, 1022, 1644 and 3438 cm^{-1}.[19] Si-O-Al bending vibration was appeared at 464 cm^{-1}, while Si-O-Si and Si-O-Al symmetric stretching vibrations were observed at 685 and 792 cm^{-1}, respectively. The absorption band at 1022 cm^{-1} was attributed to Si-O-Si and Si-O-Al asymmetric stretching vibration. The H-O-H bending and stretching vibrations appeared at 1644 and 3438 cm^{-1}, respectively.

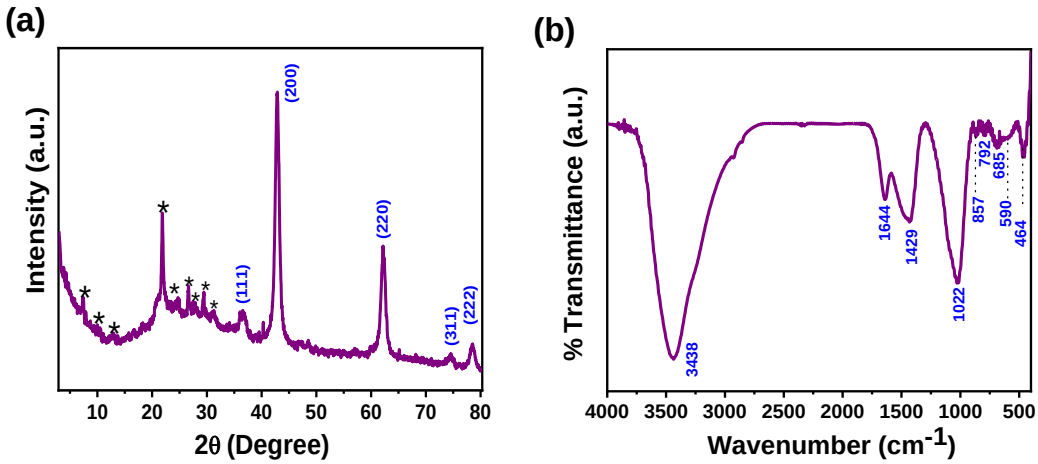

Figure 2A.1: (a) XRD patterns (* indicates zeolite A peaks) (b)FTIR spectra of zeolite A-MgO powders.

Fig. 2A.2 shows the FESEM image of zeolite A-MgO composite powders. It demonstrates that cube-shaped zeolite A particles of dimension around 1 μm are surrounded by nano-sheet like MgO particles with thickness in the range of 50-70 nm. It is understood that during hydrothermal reaction of $MgCl_2$ and urea in the presence of zeolite A, nucleation of as-prepared $Mg_5(CO_3)_4(OH)_2.4H_2O$ occurred[17] onto the surface of zeolite A particles followed by the growth of the former as nanosheet like structure. However, after calcination at 600 ^oC/2 h, $Mg_5(CO_3)_4(OH)_2.4H_2O$ are converted into MgO particles without any structural changes.

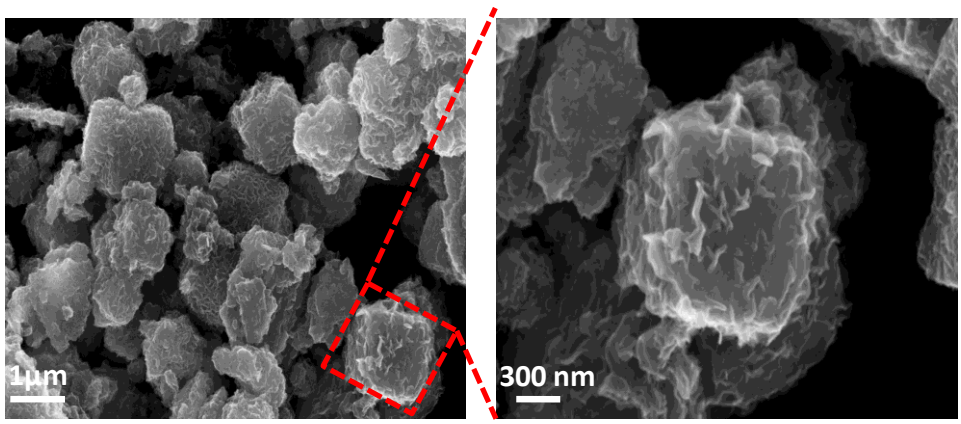

Figure 2A.2: FESEM image of zeolite A-MgO composite powders.

Fig. 2A.3(a) shows BET isotherm of zeolite A-MgO composite. A horizontal plateau of the isotherm at lower p/p_o<4.5 indicates the microporous characteristics of zeolite A. However, the appearance of hysteresis loop within the range of 0.45-0.99 of p/p_o illustrates the formation of interparticle mesopores of zeolite as well as those of MgO particles. The isotherm resembles group IV, H3 type as per IUPAC classification signifying slit-like mesopores of the sample. The BET surface area of the sample was measured as 69 m^2/gm having of external (mesopore) surface area of 35 m^2/gm and micropore surface area of 34 m^2/gm. The pore volume and pore size of the sample were 0.36 cm^3/gm and 3.9 nm, respectively. Fig. 2A.3(b) shows the pore size distribution curve (BJH desorption) of the sample indicating a sharp peak at around 3.9 nm. It is reported[14] that the BET surface area of starting zeolite particles in the absence of MgO was found to be 54 m^2/gm with mesopore and micropore surface area values of 31 and 23 m^2/gm, respectively. The pore volume and pore size of the pure zeolite were calculated as 0.0092 cm^3/gm and 3.9 nm, respectively. It indicates that presence of MgO in zeolite A-MgO composite enhances both the BET surface area and pore volume which could help facilitate its adsorption performance for

defluoridation of water. However, the pore size remained same for both in the presence and absence of MgO in zeolite A. The surface textural properties i.e., surface area, pore volume and pore size played a significant role for the adsorption of fluoride ions from aqueous solution.

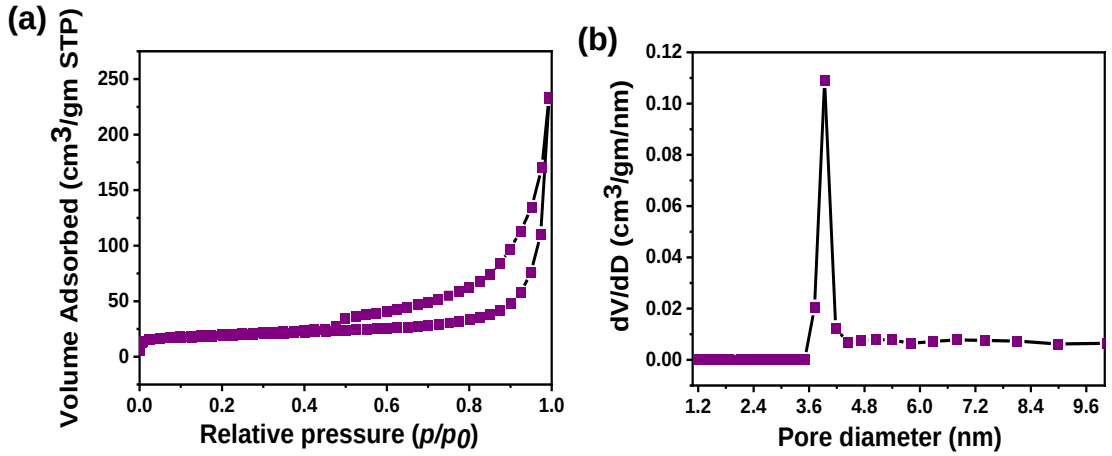

Figure 2A.3: (a) N_2 adsorption-desorption isotherm and (b) pore size distribution of zeolite A-MgO composite.

XPS study was performed to analyse the chemical state, electronic structure and electronic states of materials by determining their binding energy. It reveals the binding energies of O1s, Si2p, Na1s, Al2p and Mg2p appearing at 531.6, 102.4, 1072.2,74.2 and 49.9 eV, respectively (Fig. 2A.4). XPS results are shown in Table 2A.1 which also shows the atomic % of the elements, Al, Si, Na, Mg and O as 5.87, 6.58, 0.73, 19.72 and 67.10%, respectively. The presence of significant amount of Mg as Mg(II) ions contributed for adsorption of fluoride ions from aqueous solution.

Table 2A.1: XPS results of zeolite A-MgO composite.

Electronic state of the elements	Binding Energy (eV)	Atomic %
O1s	531.6	67.10
Si2p	102.4	6.58
Na1s	1072.2	0.73
Al2p	74.2	5.87
Mg2p	49.9	19.72

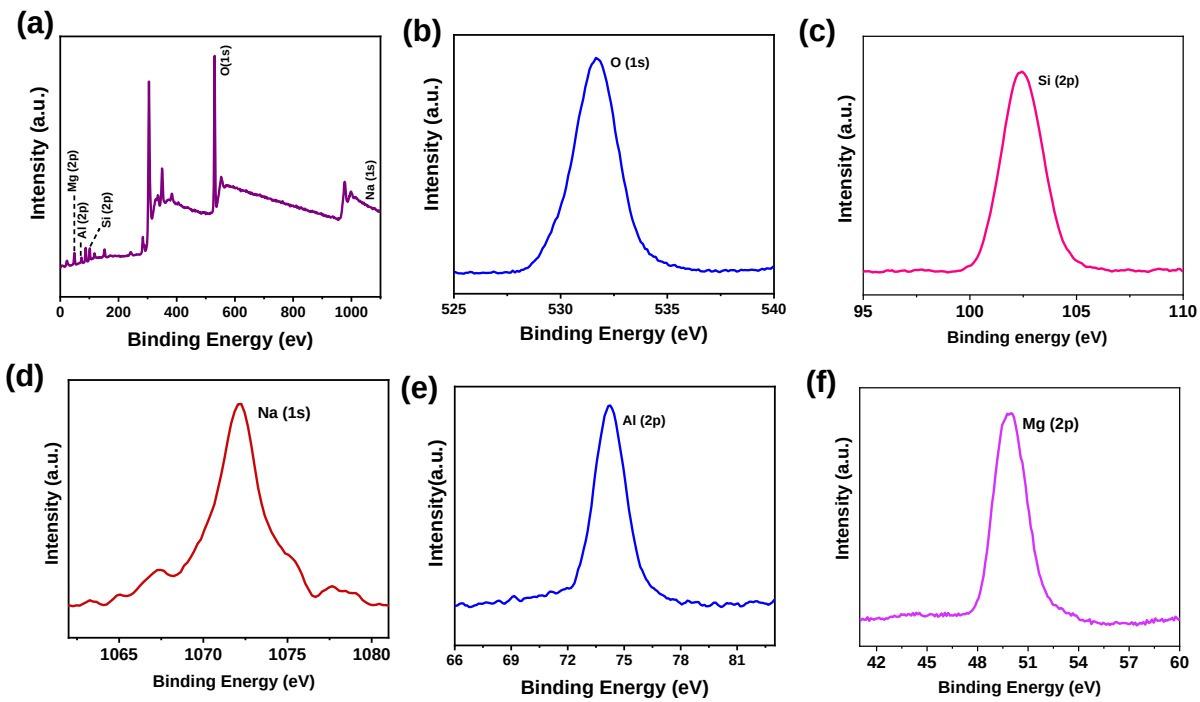

Figure 2A.4: XPS spectra of zeolite A-MgO composite (a) Survey spectra (b) O (1s) (c) Si (2P) (d) Na (1s) (e) Al (2p) (f) Mg (2p).

2A.3.2 Adsorption study

Role of contact time

Table 2A.2 shows variation of fluoride ion adsorption (%) with time using zeolite A- MgO composite having initial fluoride concentration of 7.24 mg/L, adsorbent dose of 1 gm/L at pH 6.8 and temperature 30 ^{o}C. It indicates that about 72% adsorption occurred within 5 mins of

contact time between adsorbent (zeolite A supported MgO) and adsorbate (aqueous solution containing F^- ions). After that adsorption (%) of F^- ions increased slowly and reached a maximum value of about 94% within 90 mins (Fig. 2A.5(a)). It demonstrates that after a certain time, the adsorption sites of the adsorbent got saturated preventing further adsorption.

Table 2A.2: % Adsorption with time for the removal of fluoride ions.

Time (min)	% Adsorption
0	0.00
5	72.23
10	77.35
20	84.94
40	92.91
60	93.88
90	94.14
120	94.19
150	94.22
180	94.24

Role of adsorbent dose

To study the role of adsorbent dose on the adsorption of F^- ions, the amount of adsorbent was taken in the range of 0.5-10 gm/L using adsorbate (F^- ions) concentration of 7.24 mg/L at pH 6.8, temperature 30 ^oC and duration of contact time as 120 min. Table 2A.3 shows that % adsorption increased sharply from 88.7 to 96.7% with increase in adsorbent doses from 0.5 to 2 gm/L. However, no significant increase in % adsorption was noticed with adsorbent doses above 2 gm/L. A maximum % adsorption of 98% was obtained using loading capacity of the adsorbent as 10 gm/L (Fig. 2A.5(b)). Initially up to a certain loading of adsorbent, the abundance of more adsorbent surface sites facilitates the uptake capacity of F^- ions.[20] However, it becomes saturated after an optimum concentration of adsorbent loading.

Table 2A.3: % Adsorption with adsorbent dose (gm/L) for the removal of fluoride ions.

Adsorbent dose (gm/L)	% Adsorption
0.5	88.68
1.0	94.19
2.0	96.74
4.0	97.22
6.0	97.54
8.0	97.87
10.0	98.04

Role of initial F^- ions concentration (Adsorbate dose)

To study the role of adsorbate dose on the adsorption of F^- ions, different concentrations of adsorbate doses ranging from 7.24 to 232 mg/L were chosen using adsorbent dose of 1 gm/L at pH 6.8 and contact time of 120 min at 30 ^oC. Table 2A.4 shows that with increase in F^- ions concentrations up to 49.6 mg/L, the % adsorption of F^- ions decreased slowly from 94 to 91% followed by sharp fall of adsorption efficiency down to 45% with increase in adsorbate doses from 49.6 to 232 mg/L (Fig.2A.5(c)). With increase in F^- ions concentration in solution, the adsorbent sites are saturated with the abundance of F^- ions.[21] It inhibits further adsorption of F^- ions due to repulsion of negatively charged F^- ions.

Table 2A.4: % Adsorption with adsorbate dose (mg/L) for the removal of fluoride ions.

Adsorbate dose (mg/L)	% Adsorption
7.24	94.19
16.1	93.52
23.1	93.16
49.6	91.05
96	63.33
115	59.39
182	50.16
232	45.25

Role of pH

The pH of solution plays a vital role for the removal of F^- ions from contaminated water. It monitors the surface charge of the adsorbent. In general, the adsorption of negatively charged contaminants is favoured in acidic pH while alkaline pH facilitates the adsorption of positively charged contaminants. Table 2A.5 shows the effect of pH (in the range 2.4 to 10) on the adsorption of F^- ions with F^- concentration (initial) of 7.27 mg/L, adsorbent dose of 1 g/L and contact time of 120 min at 30 ^oC. It exhibits that up to pH 5.1, the % adsorption remained almost constant around 95.5% followed by slight decrease to 94.2% at pH 6.8. However, after pH 6.8, a significant decrease of 85.9% and 81.9% adsorption were noticed at pH 8.5 and 10, respectively (Fig. 2A.5(d)). In alkaline pH, a sudden decrease in F^- ion adsorption % could be attributed to repulsion between negatively charged OH^- and F^- ions rendering hindrance of F^- ion adsorption onto the adsorption sites.[22]

Table 2A.5: % Adsorption with change in pH.

pH	% Adsorption
2.4	95.63
3.8	95.69
5.1	95.51
6.8	94.19
8.5	85.91
10	81.90

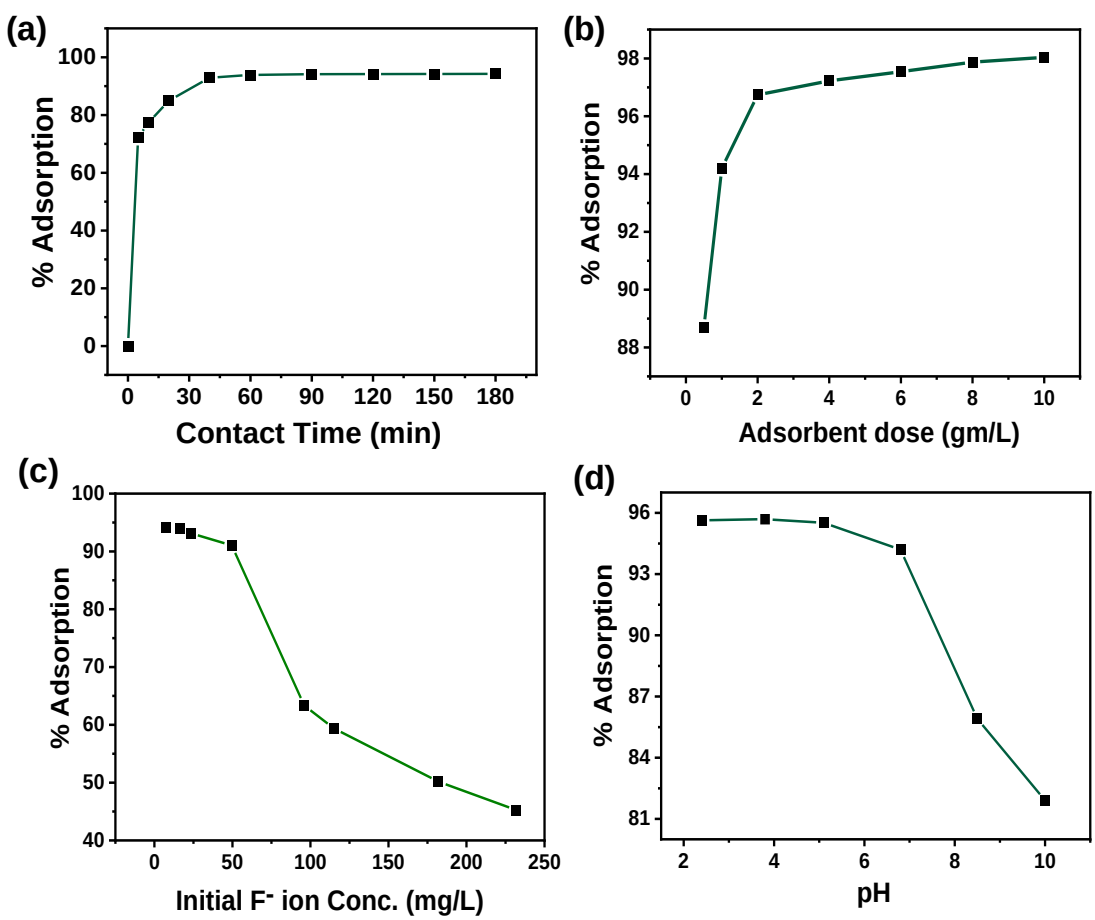

Figure 2A.5: Effect of (a) contact time, (b) adsorbent dose, (c) initial fluoride ion concentration and (d) pH on the adsorption of F^- ions by zeolite A-MgO composite.

Role of temperature

The role of temperature on the adsorption of F^- ions was investigated by changing the temperatures in the range of 30-70 ^oC with F^- concentration (initial) of 7.27 mg/L, adsorbent dose of 1 gm/L and contact time of 120 min at pH 6.8. Fig. 2A.6(a) shows that F^- ions adsorption (%) was enhanced with increasing temperatures from 30 to 70 ^oC. With rise in temperature, F^- ions diffusion rate is increased through the pore surface of the adsorbent materials rendering higher adsorption rate.[23]

Role of co-existing anions

The presence of co-existing anions like chloride (Cl^-), nitrate (NO_3^-), phosphate (PO_4^{3-}) and sulphate (SO_4^{2-}) in ground water could influence the adsorption efficiency of the adsorbent materials for the removal of F^- ions. Fig. 2A.6(b) shows the role of various competing ions on the removal % of F^- ions with adsorbate dose of 7.27 mg/L, adsorbent dose of 1 gm/L and contact time of 120 min at pH 6.8. It reveals that the % adsorption of F^-, Cl^-, NO_3^-, PO_4^{3-} and SO_4^{2-} ions contributed as 94.2, 4.6, 14.2, 28.8 and 34%, respectively. It is clear that the competing ions, PO_4^{3-} and SO_4^{2-} have significant affect for the removal of fluoride ions with the competition for their adsorption onto the adsorbent surface.[24] The hydrated ionic radii of the competing ions follow in the order of Cl^- (3.32 Å) < NO_3^- (3.35 Å) < PO_4^{3-} (3.39 Å) < SO_4^{2-} (3.79 Å).[25] It is clear that PO_4^{3-} and SO_4^{2-} ions have larger hydrated ionic radii compared to Cl^- and NO_3^- ions; therefore, outer sphere complex formation *via* long range electrostatic force was enhanced by PO_4^{3-} and SO_4^{2-} ions than that of Cl^- and NO_3^- ions having smaller hydrated radius.[25]

Recyclability test

Recyclability test was performed using adsorbent concentration of 1 gm/L after adsorption of adsorbate (F^- ions) of concentration 7.27 mg/L under stirring for 2 h in batch mode at 30 ^oC of pH 6.8. After adsorption, the adsorbent sample was regenerated by treating with Na_2CO_3 solution (0.1 M) with stirring condition for about 18 h followed by washing with DI water and drying. Fig. 2A.6(c) shows that up to 3rd cycle, there is no significant change in decreasing the adsorption %; however, it starts decreasing slightly as 90% and 87% for 4th and 5th cycles, respectively. Interestingly, mesoporous alumina[2] and alumina modified NaA

zeolite[14] also revealed that adsorption efficiency of the adsorbents decreased after 3rd cycles for the removal of fluoride ions. During several times regeneration using Na_2CO_3, the surface structural changes of the adsorbent could occur with excess OH^- ions leading to surface passivation toward the adsorption of negatively charged F^- ions.

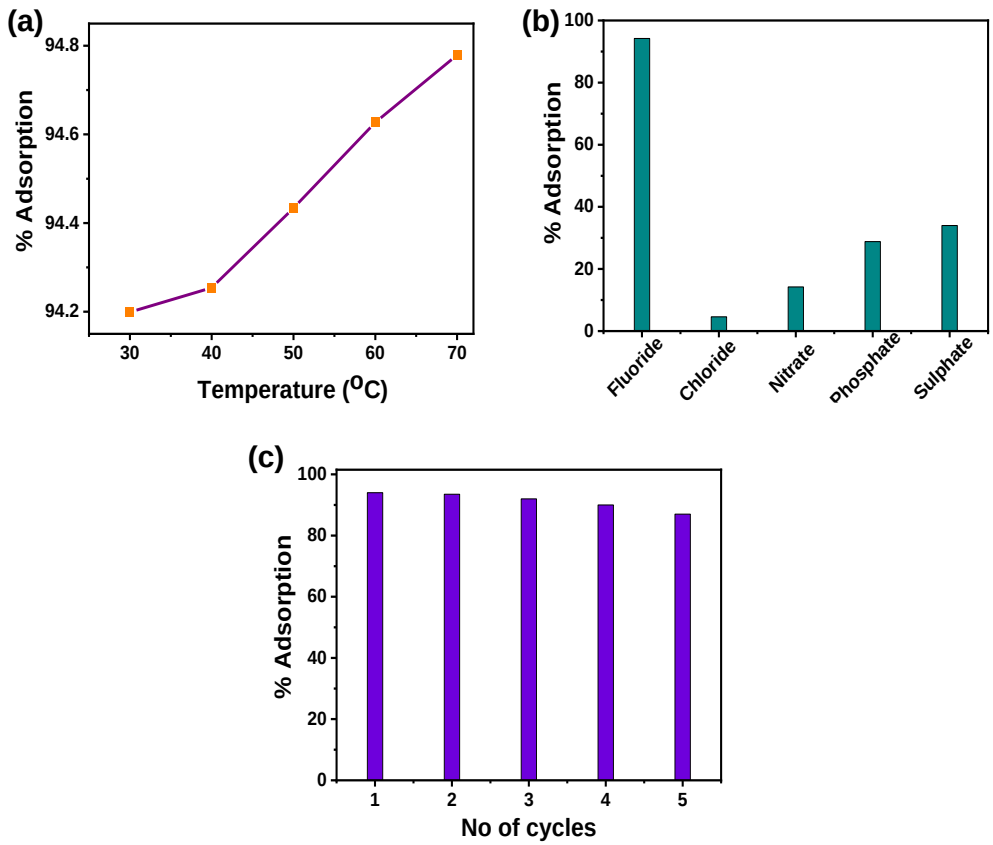

Figure 2A.6: Role of (a) reaction temperature, (b) competing ions and (c) regeneration study for F^- ions adsorption by zeolite A-MgO composite.

2A.3.3 Kinetics study

For kinetics study of adsorption, pseudo-1st order and pseudo-2nd order kinetics models were applied. The mathematical expression for pseudo-first-order kinetics model is:

$$\ln (q_e - q_t) = -k_1 t + \ln q_e \qquad (2A.2)$$

where, q_e (mg/gm) and q_t (mg/gm) are the amounts of F^- ions adsorbed at equilibrium and at time t (min), respectively. The pseudo-1st order kinetics was interpreted by plotting $\ln (q_e - q_t)$ *vs*.t which was almost linear (Fig. 2A.7(a)). The first order rate constant (k_1) and q_e are obtained from the slope and intercept of the curves, respectively. The linear form of the pseudo-2nd order kinetics is expressed as:

$$t/q_t = 1/k_2 q_e^2 + (1/q_e)t \qquad (2A.3)$$

By plotting t/q_t *vs.*t, a straight line is obtained and the values of q_e (mg/gm) and k_2 (2^{nd} order rate constant) are determined from the intercept and slope of the fitting curve, respectively (Fig. 2A.7(b)).From pseudo-1^{st} order kinetics plot, the values of k_1, q_e and R^2 values are calculated as 0.0559 min^{-1}, 1.994 mg/gm and 0.9385, respectively, while pseudo-2^{nd} order kinetics plot renders the values of k_2, q_e and R^2 as 0.1116 gm/mg/min, 6.8870 mg/gm and 0.9994, respectively. It is obvious that pseudo-2^{nd} order model is better fitted than pseudo-1^{st} order model because of higher correlation co-efficient (R^2) value of the former model indicating higher F^- ions adsorption at equilibrium (q_e). It signifies that adsorption process is followed by chemisorption with the formation of monolayer.

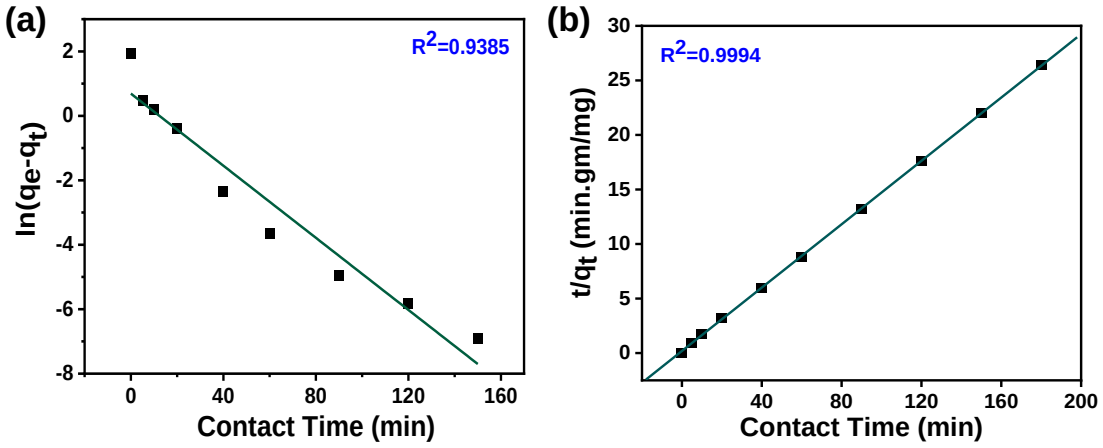

Figure 2A.7: Kinetics data with linear fitting of (a) pseudo-1^{st} order and (b) pseudo-2^{nd} order kinetic models.

2A.3.4 Adsorption Isotherms

For adsorption study, the adsorption isotherm is an important parameter in terms of quantitative relationship between the adsorbed amount and concentration of adsorbate at equilibrium, reflecting how the adsorbate molecules are adsorbed on the surface of the adsorbent. The equilibrium data for the adsorption process was fitted to Langmuir and Freundlich isotherm models.[26] The linearized form of Langmuir isotherm is expressed as:

$$C_e/q_e = C_e/q_m + 1/K_L.q_m \qquad (2A.4)$$

where, q_m (mg/gm) and K_L are the maximum adsorption capacity and Langmuir adsorption constant, respectively. By plotting Ce/qe vs. Ce, the q_m can be obtained from the slope

wherein K_L is obtained intercept of the linear plot. On the other hand, the linearized form of Freundlich isotherm is represented as:

$$\log q_e = \log K_F + 1/n_F \log C_e \qquad (2A.5)$$

By plotting log q_e vs. log C_e, n_F (adsorption intensity) and K_F, the Freundlich constant can be obtained from the slope and intercept of the linear curve, respectively. Fig.2A.8 shows (a) Langmuir and (b) Freundlich isotherms for the adsorption of F^- ions. From the Langmuir isotherm, q_m and K_L are calculated as 107.64 mg/gm and 0.074 L/mg, respectively with R^2 value of 0.9804. The n_F and K_F values of Freundlich isotherm are determined as 2.2753 and 13.30, respectively with R^2 value of 0.9535. From the curves it is obvious that Langmuir isotherm having higher R^2 value is better fitted for the adsorption of F^- ions by zeolite A-MgO composite. It signifies that adsorption process is governed by the formation of monolayer of the adsorbate onto the uniform adsorbent surface.

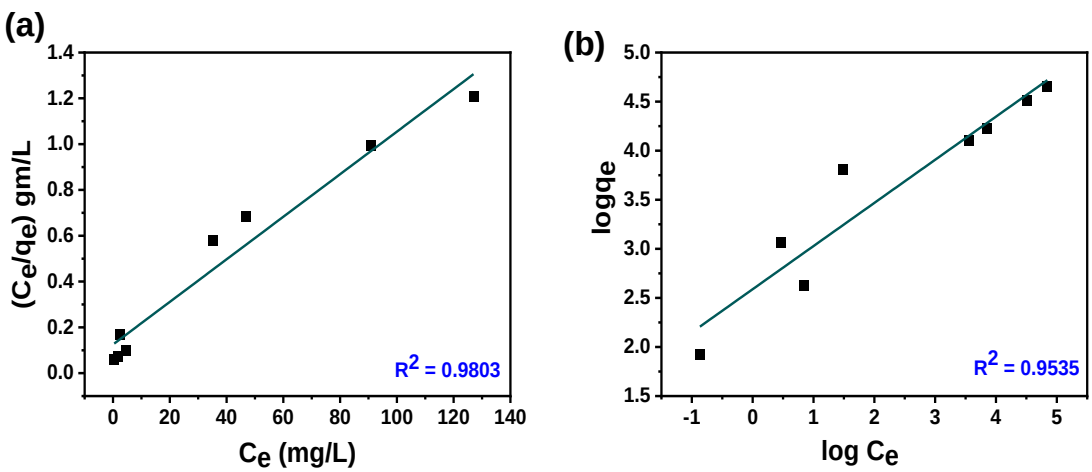

Figure 2A.8: Isotherm plots: (a) Langmuir and (b) Freundlich for the adsorption of F^- ions.

2A.3.5 Adsorption Thermodynamics

The nature of adsorption process was explained by measuring three thermodynamic parameters like changes of standard Gibbs free energy (ΔG^o), entropy (ΔS^o) and enthalpy (ΔH^o). These parameters can be determined as follows:

$$\Delta G° = - RT1nK_d \qquad (2A.6)$$

$$1nK_d = \Delta S^o/R - \Delta H^o/RT \qquad (2A.7)$$

where, $K_d = q_e/C_e$, is the equilibrium constant, R and T are the universal gas constant (8.314 J/mol/K) and absolute temperature in Kelvin, respectively. From the plot lnK_d vs. 1/T (eqn, 2A.7), ΔS^o and ΔH^o are obtained from the intercept and slope of the linear plot, respectively

(Fig. 2A.9). The values of ΔG° at different temperature are obtained from the following equation:

$$\Delta G^\circ = \Delta H^o - T\Delta S^o \qquad (2A.8)$$

From the plot (Fig. 2A.9), the values of ΔS^o and ΔH^o are found as 0.03148 kJ/mol/K and +2.526 kJ/mol, respectively. The values of standard Gibbs free energy change (ΔG^o) are calculated as –7.0124, –7.3272, –7.6420, –7.9302 and –8.2736 kJ/mol at 303 K, 313 K, 323 K, 333 K and 343 K, respectively. The negative values of ΔG^o signify the spontaneity of the adsorption process while the +ΔH° indicates endothermic reaction of F^- ion adsorption. It is demonstrated that adsorbate ions got increased at the solid liquid interface during adsorption process.[27]

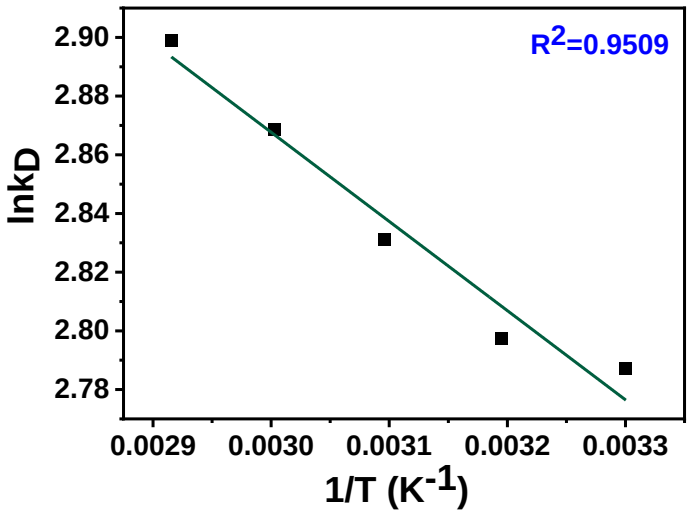

Figure 2A.9: ln K_d vs. 1/T plot for F^- ions adsorption.

2A.3.6 F^- ion removal mechanism

A tentative mechanism for the removal of fluoride ion from aqueous solution is shown in Fig. 2A.10. MgO powders adhered onto zeolite particles (Zeo-MgO) interacts with water molecules forming Zeo-$Mg(OH)_2$ having abundance of surface hydroxyl groups in MgO. In the presence of F^- ions in aqueous solution, Zeo-$Mg(OH)_2$ is transformed into Zeo-$Mg(OH)_{2-x}F_x$ leaving hydroxyl ions (OH^-) in solution.[7] Thus, the pH of the solution is increased hindering the adsorption of F^- ions competing with OH^- ions. However, under acidic medium at low pH, Zeo-$Mg(OH)_2$ is converted into positive species of Zeo-$Mg(OH)_2^{2+}$ which behave

as a facile adsorption sites for the removal of F^- ions in aqueous solution *via* electrostatic attraction.

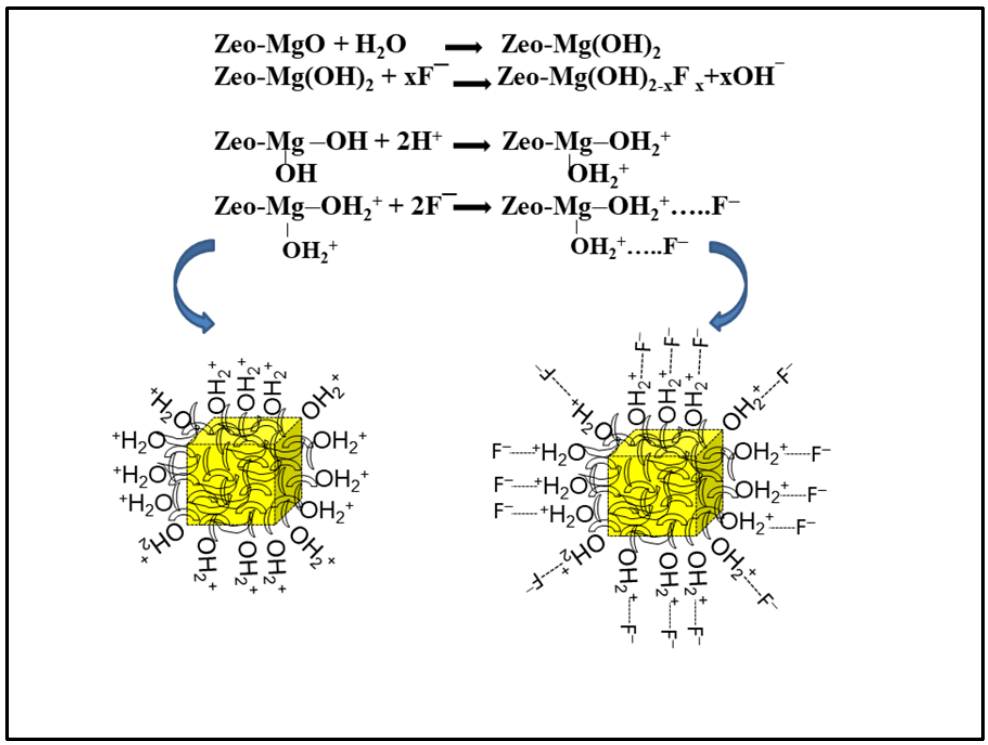

Figure 2A.10: A tentative mechanism for F^- ions adsorption by zeolite A-MgO composite.

2A.4 Conclusion

For the removal of F^- ions from aqueous solution, a suitable adsorbent i.e., Zeolite A-MgO composite powders was prepared by hydrothermal technique at 150 ^oC/5 h in the presence of aqueous solution of $MgCl_2$ and urea followed by heating at 600 ^oC/2 h. XRD analysis of the product showed preferential crystallization of MgO along with cubic NaA zeolite phase which were further confirmed by FTIR. FESEM image revealed cube-shaped zeolite A particles of dimension around 1 μm surrounded by nano-sheet like MgO particles with thickness in the range of 50-70 nm. The BET surface area, pore volume and pore size of the adsorbent were found to be 69 m^2/gm, 0.36 cm^3/gm and 3.9 nm, respectively. XPS study showed the characteristic binding energies of O1s, Si2p, Na1s, Al2p and Mg2p at 531.6, 102.4, 1072.2,74.2 and 49.9 eV, respectively. The product exhibited that 72% fluoride adsorption occurred within 5 mins followed by 94% removal within 90 mins. Initially up to a certain loading of adsorbent, the abundance of more adsorbent surface sites facilitates the uptake capacity of F^- ions followed by saturation after an optimum concentration of adsorbent loading. With increase in adsorbate concentration, the adsorbent sites are saturated

with the abundance of F^- ions inhibiting further adsorption of F^- ions due to repulsion of negatively charged F^- ions. In acidic pH, F^- ions removal was facilitated due to electrostatic attraction followed by sudden fall of F^- ions adsorption in alkaline pH because of electrostatic repulsion. F^- ions adsorption % increased with rise in temperatures from 30 to 70 ^oC. For competing ions, PO_4^{3-} and SO_4^{2-} ions had significant affect for the removal of fluoride with the competition for their adsorption onto the adsorbent surface. For recyclability test, there is no significant decrease for F^- ions removal up to 3rd cycle followed by slight decrease in 4th and 5th cycle. For kinetics study, pseudo-second-order model is better fitted indicating higher F^- ions adsorption at equilibrium. Adsorption isotherm was better fitted with Langmuir model signifying monolayer formation of the adsorbate onto the uniform adsorbent surface. In thermodynamic study, the negative values of ΔG^o signified the spontaneity of the adsorption process.

References

1 A. Bhatnagar, E. Kumar and M. Sillanpää, J. *Chem. Eng.*, 2011, **171**, 811–840.

2 S. Kundu, I. H. Chowdhury, P. K. Sinha and M. K. Naskar, *J. Chem. Eng. Data.*, 2017, **62**, 2067–2074.

3 D. Dayananda, V. R. Sarva, S. V. Prasad, J. Arunachalam and N. N. Ghosh, *Particul. Sci. Technol.*, 2015, **33**, 8–16.

4 A. Elhalil, S. Qourzal, F. Z. Mahjoubi, R. Elmoubarki, M. Farnane, H. Tounsadi, M. Sadiq, M. Abdennouri and N. Barka, *Emerg. Contam.*, 2016, **2**, 42–48.

5 A. M. Raichur and M. J. Basu, *Sep. Purif. Technol.*, 2001, **24**, 121–127.

6 A. Dhillon and D. Kumar, *J. Mater Chem A. Mater.*, 2015, **3**, 4215–4228.

7 L.-X. Li, D. Xu, X.-Q. Li, W.-C. Liu and Y. Jia, *New J. Chem.*, 2014, **38**, 5445–5452.

8 S. S. A. Alkurdi, R. A. Al-Juboori, J. Bundschuh and I. Hamawand, *Environ Int.*, 2019, **127**, 704–719.

9 S. G. Lee, J.-W. Ha, E.-H. Sohn, I. J. Park and S.-B. Lee, *Korean J. Chem. Eng.*, 2017, **34**, 2738–2747.

10 D. Kang, X. Yu, M. Ge, M. Lin, X. Yang and Y. Jing, *J. Chem. Eng.*, 2018, **345**, 252–259.

11 M. Mahinroosta and A. Allahverdi, *J. Environ. Manage.*, 2018, **223**, 452–468.

12 H.-J. Choi, S.-W. Yu and K. H. Kim, *J Taiwan Inst. Chem Eng.*, 2016, **63**, 482–489.

13 V. P. Mallapur and J. U. K. Oubagaranadin, *T. Indian Ceram. Soc.*, 2017, **76**, 1–13.

14 M. K. Naskar, *J. Asian Ceram. Soc.*, 2020, **8**, 437–447.

15 M. Balamurugan, S. Saravanan and T. Soga, *E-J. Surf. Sci. Nanotech.*, 2014, **12**, 363–367.

16 L.-Z. Pei, W.-Y. Yin, J.-F. Wang, J. Chen, C.-G. Fan and Q.-F. Zhang, *Mater. Res.*, 2010, **13**, 339–343.

17 D. K. Chanda, D. Mukherjee, P. S. Das, C. K. Ghosh and A. K. Mukhopadhyay, *T. Indian Ceram. Soc.*, 2018, **77**, 235–243.

18 I. H. Chowdhury, A. H. Chowdhury, P. Bose, S. Mandal and M. K. Naskar, *RSC Adv.*, 2016, **6**, 6038–6047.

19 A. Kumar and M. K. Naskar, *Int. J. Appl. Ceram. Technol.*, 2019, **16**, 1525–1532.

20 N. Thakur, S. A. Kumar, H. Parab, A. K. Pandey, P. Bhatt, S. D. Kumar and A. V. R. Reddy, *RSC Adv.*, 2014, **4**, 10350–10357.

21 A. Teimouri, S. G. Nasab, S. Habibollahi, M. Fazel-Najafabadi and A. N. Chermahini, *RSC Adv.*, 2015, **5**, 6771–6781.

22 D. Dayananda, V. R. Sarva, S. V Prasad, J. Arunachalam, P. Parameswaran and N. N. Ghosh, *Appl. Surf. Sci.*, 2015, **329**, 1–10.

23 S. VenkataMohan, S. V Ramanaiah, B. Rajkumar and P. N. Sarma, *J. Hazard. Mater.*, 2007, **141**, 465–474.

24 X. Dou, Y. Zhang, H. Wang, T. Wang and Y. Wang, *Water Res.*, 2011, **45**, 3571–3578.

25 Y. Li, C. Zhang, Y. Jiang, T.-J. Wang and H. Wang, *Desalination*, 2016, **399**, 171–177.

26 M. S. Onyango, Y. Kojima, O. Aoyi, E. C. Bernardo and H. Matsuda, *J. Colloid Interface Sci.*, 2004, **279**, 341–350.

27 N. Viswanathan, S. M. Prabhu and S. Meenakshi, *J. Fluor. Chem.*, 2013, **153**, 143–150.

Chapter 2B

Al_2O_3 modified rice husk ash derived zeolite based adsorbent for defluoridation of water : Batch and column studies

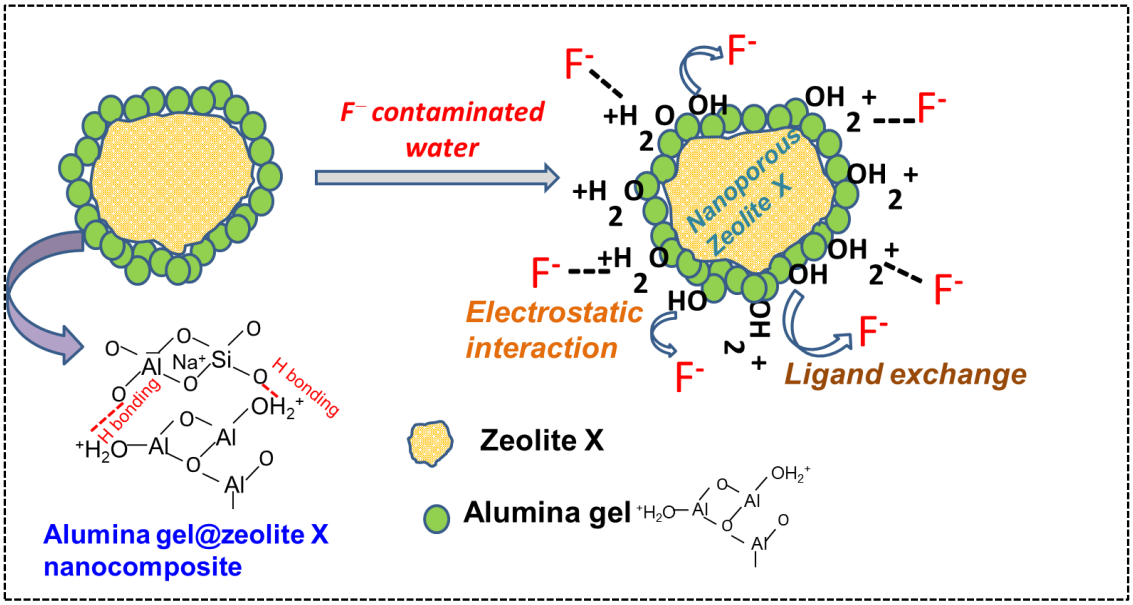

Publication from this Chapter:

Adwitiya Chakraborty and Milan Kanti Naskar, "Sol-gel synthesis of alumina gel@zeolite X nanocomposite for high performance water defluoridation: Batch and column adsorption study", ***Materials Advances,* 2022, 3, 8544-8556.**

2B.1 Introduction

Fluoride toxicity has harmful effect on human beings causing different health issues therefore, defluoridation of groundwater is becoming essential worldwide. Selection of effective adsorbent material is crucial for defluoridation *via* adsorption technique. The adsorbents are chosen based on their physico-chemical properties like porosity, surface area, favourable kinetic and transport properties, thermo-chemical stability, regenerative capacity and low cost. Water defluoridation commonly employs a variety of adsorbent materials like ceramic based metal oxides (alumina, magnesia, calcia, iron oxide etc),[1] alumina dispersed charcoal,[2] etc. Due to their unique crystalline structure, zeolites are often used as a potential adsorbent for the removal of different water contaminants. It is worth mentioning that zeolite without any modification show nominal adsorption efficiency within the range of 25-50 mg/gm towards the removal of heavy metals.[3] Therefore, prior modification of different adsorbent materials is needed towards water decontamination applications. In a recent time, Angaru *et al.* have reported the removal of industrial effluents using sodium alginate (SA) and carboxymethylcellulose (CMC) entrapped with bimetallic magnetic (nano zero valent iron and nickel) fly ash zeolite (ZFN) with composition of SA : CMC : ZFN as 1 : 1 : 1 (weight ratio).[4,5] The adsorption capacities for Cu(II) and Cr (VI) were found to be 63.29 and 10.15 mg/gm, respectively. For defluoridation of water, different modified zeolites as adsorbents are also reported.[6,7] Recently Rita *et al.* reported alum modified zeolite and its efficiency toward fluoride removal with maximum adsorption capacity of 2.43 mg/gm.[8] Yang *et al.* prepared Mn-Ti modified zeolite for water defluoridation resulting maximum adsorption capacity of 2.17 mg/gm.[9] Aluminium coated natural zeolite was also found to be effective toward fluoride removal.[10] However, preparation of zeolite based composite adsorbent *via* simple route with high adsorption capacity still remains a great challenge.

With the above motivation, in the present study alumina gel@zeolite X nanocomposite is synthesized by sol-gel process followed by its structural and surface textural properties analysis. The synthesized material was utilized to investigate its fluoride ions uptake capacity from water with batch and fixed bed column study. In a batch process, the performance of the adsorbent was studied by varying adsorbate and adsorbent concentration, pH, temperature and competing ions effect, whereas in column adsorption process breakthrough study was performed in terms of initial fluoride concentration, flow rate and bed height of the column. The adsorption behavioural pattern of the adsorbent for removal of fluoride was accomplished by applying different kinetic models.

2B.2 Experimental

2B.2.1 Materials

Aluminium nitrate nonahydrate [$Al(NO_3)_3.9H_2O$] (>98%), ammonia (NH_3) solution (25 wt%), sodium hydroxide (NaOH) pellet (>97%), and sodium fluoride (NaF) (>97%) were purchased from Merck, India while sodium aluminate (45% Na_2O + 55% Al_2O_3) was procured from Sigma-Aldrich. Rice husk ash (95% SiO_2) was collected from J.M. Biotech Pvt. Ltd., India.

Synthesis of alumina gel @zeoliteX nanocomposite

Zeolite X was prepared from rice husk ash (RHA) as silica source.[11] In a typical process, 7 gm of RHA was digested in the presence of 5.25 M NaOH solution (50 mL) under stirring at 85 ^oC for 2 h. Sodium aluminate powder (4.4 gm) in 20 mL water was introduced in the above digested dispersion followed by stirring for 20 min. The whole dispersion was hydrothermally treated at 90 ^oC for 6 h to obtain zeolite X powder. Alumina sol was prepared by slow addition of ammonia solution into 1 M aluminium nitrate solution under stirring at 60 ^oC for 8-10 h until a translucent sol was obtained at pH around 4-5. For the synthesis of alumina gel@zeolite X composite, 5 gm of as-prepared zeolite X was added into 100 mL of alumina sol under stirring at 70 ^oC for 2 h, the pH was maintained at around 7 by addition of ammonia solution yielding a viscous slurry mass. It was then dried at around 100 ^oC for 4-6 h to obtain alumina gel@zeoliteX nanocomposite.

The synthesis procedure for alumina gel@zeolite X nanocomposite is shown schematically in Fig. 2B.1. In the first step, zeolite X was synthesized by digestion of rice husk ash (RHA) in the presence of sodium hydroxide and sodium aluminate. Under hydrothermal reaction at 90 ^oC for 6 h, silicate of RHA extract interacts with sodium aluminate yielding zeolite X with the formation of Al-O-Si network in which negatively charged AlO_4 and SiO_4 species are counterbalanced by non-bridging Na^+ ion in the network structure. In the second step for the preparation of alumina sol, aluminium nitrate solution undergoes hydrolysis and polymerization reaction in the presence of NH_3 solution at 60 ^oC/8-10 h rendering alumina sol with Al-O-Al network structure. At pH 4-5, the sol particles are protonated which interacts with Al-O-Si network of zeolite X particles through hydrogen bonding resulting alumina sol-zeolite X suspension. By adding further NH_3 solution at 70 ^oC/2 h up to pH ~7, a slurry viscous mass composing of alumina sol and zeolite X particles is

formed. After heat treatment at 100 °C, the slurry is transformed into alumina gel@ zeolite X nanocomposite composed of adhered alumina nanoparticles surrounding micron sized zeolite X particles.

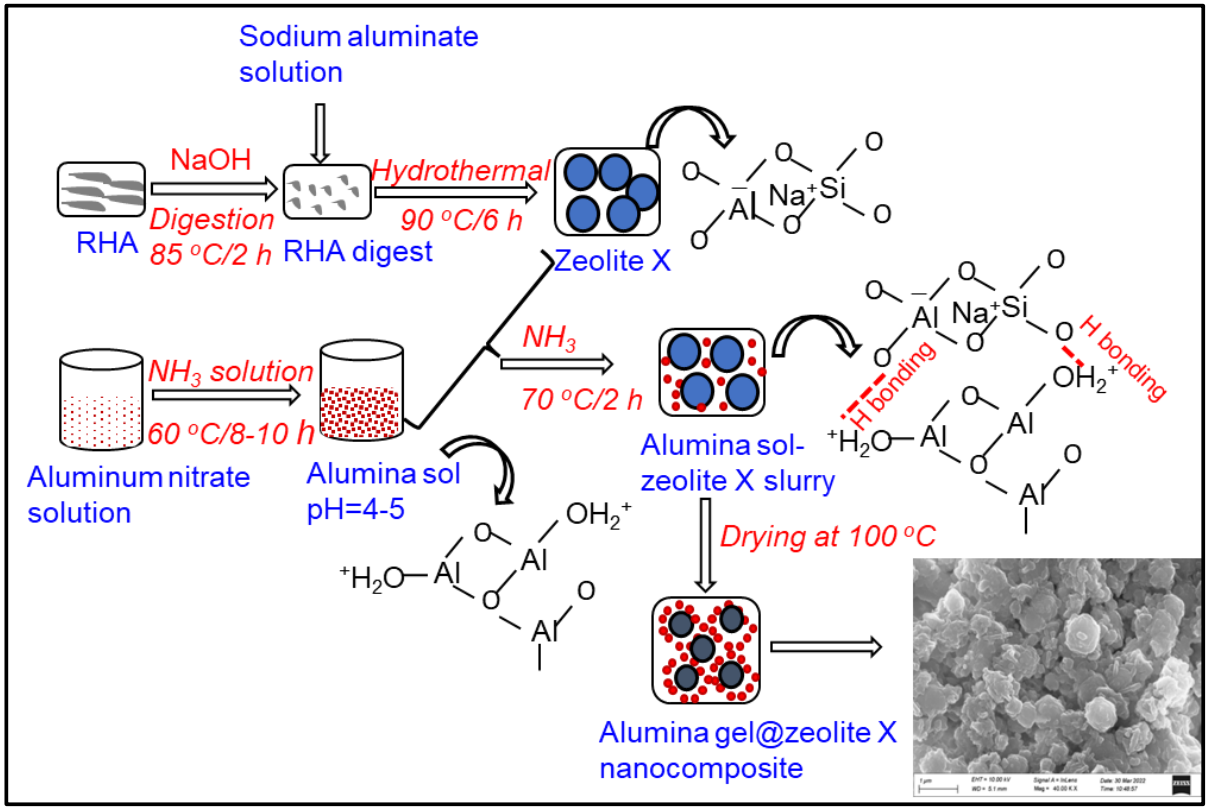

Figure 2B.1: Schematic diagram for the synthesis of alumina gel@zeolite X nanocomposite.

2B.2.2 Characterization

The synthesized alumina gel@zeolite X nanocomposite was characterized by X-ray diffraction (XRD) operating with Philips X'Pert Pro XRD, PW 3050/60) using CuK_{α} radiation, X-ray photoelectron spectroscopy(XPS,ULVAC-PHI), Fourier Transform Infrared, FTIR (Spectrum two, PerkinElmer), N_2 adsorption-desorption isotherms (Quantachrome (ASIQ MP), field emission scanning electron microscopy (FESEM, Zeiss, SupraTM 35VP, Oberkochen, Germany) and transmission electron microscopy (TEM, Tecnai G2 30ST (FEI)). The particle size of nanocomposite was also evaluated by dynamic light scattering (DLS) method (Zetasizer, ZEN 3600, Malvern, UK).

2B.2.3 Adsorption Study

Batch adsorption study

For fluoride ion adsorption in a batch study, different experimental parameters like adsorbate and adsorbent concentrations, contact time, pH, temperature and competing ions were varied. For recyclability and competing ion effect, adsorbent dose of 2 gm/L was used. Adsorption kinetic studies were performed by varying the initial fluoride concentration for each of the adsorbent dose i.e., 0.5, 1 and 2 gm/L. Fluoride measurement was done using Ion Selective Electrode, ISE (Orion Versa Star 90). The amount of q_e (mg/gm) was calculated using the following equation.

$$q_{e=}(C_0 - C_e)\left({}^{V}/_{m}\right) \qquad (2B.1)$$

Where, C_0 and $C_e$represent the initial and final concentration of adsorbate (mg/L), respectively, whereas V and m are solution volume (L) and mass (gm) of the adsorbent, respectively.

For regeneration study, 2 gm/L of adsorbent after adsorption treatment with 5 mg/L fluoride (F^-) solution for 120 min at pH 6.5, was treated with 0.1 M Na_2CO_3 solution under stirring condition for 20 h. It was then filtered and washed with DI water followed by drying to obtain regenerated sample.

Column adsorption study

Continuous column adsorption study was performed in a glass column of 3 cm ID and 60 cm height. A glass wool of 0.5 mm was placed above the adsorbent. For column study, different concentrations of influent fluoride solution (2, 5 and 8 mg/L) was used for downward flow. The flow rates were adjusted at 5, 10 and 15 mL/min and the bed heights were maintained as 5, 10 and 15 cm. At regular time intervals, the samples were collected from the exit of the column and fluoride ion concentrations were measured by ISE. It is worth noting that for column study, downward flow was chosen because it helps prevent bed lifting of the column. For operational and dynamic behaviour of adsorption column, breakthrough time and shape of the breakthrough curve was studied. For breakthrough curve, C_t/C_0 was plotted as a function of time, where C_0 and C_t are the influent and effluent fluoride concentration at time t, respectively. The amount of fluoride concentration adsorbed (q_{total}) by alumina@zeolite X gel nanocomposite in the column was determined from the area under breakthrough curve of C_{ads} (mg/L) *vs* time (t) multiplied by the flow rate using the following equation:

$$q_{total} = A\frac{Q}{1000} = \frac{Q}{1000}\int_{t=0}^{t_e} C_{ads}\, dt \quad \text{(2B.2)}$$

Where, Q (mL/min) is the flow rate, A is the area under the breakthrough curve, t is the total flow time and C_{ads} (mg/L) is the adsorbed concentration (C_0-C_t).

The amount of total fluoride ions introduced as influent in the column (m_{total}) was determined by the following equation:

$$m_{total} = \frac{C_0 \times Q \times t_{total}}{1000} \quad \text{(2B.3)}$$

The removal percentage (X%) of fluoride ions is calculated as follows:

$$X\% = \frac{q_{total}}{m_{total}} \times 100 \quad \text{(2B.4)}$$

The desorption experiment was done by passing 0.1 M NaOH solution at a flow rate of 2 mL/min followed by washing with DI water until pH of the effluent reached at ~6.5.

2B.3 Results and discussion

2B.3.1 Characterization of alumina gel@zeolite X nanocomposite

Fig. 2B.2(a) shows the XRD pattern of alumina gel@zeolite X nanocomposite with the appearance of characteristic peaks of zeolite X at 2θ values of 6.1, 11.7, 15.4, 20.1, 23.3, 26.6, 30.9 and 33.6 corroborating to the hkl values of (111), (311), (331), (440), (533), (642), (157) and (664), respectively (JCPDF File # 39-218). However, no characteristic peaks of crystalline alumina polymorphs were noticed indicating its amorphous gel stage in the synthesized material which was confirmed by comparing with pure zeolite X crystalline peak obtained from our previous study.[11]

FTIR spectrum of the material is shown in Fig. 2B.2(b). The appearance of absorption bands at 3440 and 1640 cm^{-1} is due to OH stretching and bending vibrations, respectively. The Si-O-Si stretching and bending vibrations are located at 990 and 460 cm^{-1}, respectively; whereas Si-O-Al bending vibration is confirmed at 579 cm^{-1}.[12] The shifting of stretching vibration of Si-O-Si to lower wavenumber is attributed to decrease in bond strength with internal hydrogen bonding as Si-O….HO-Si and Si-O…HO-Al.[7]The absorption bands at 662 and 735 cm^{-1} are the signature of Si-O/Al-O S4R symmetric bending and stretching vibrations of zeolite X, respectively.[13] It is to be noted that a sharp absorption peak appeared at 1385

cm^{-1} is due to the presence of NO_3^- ions accumulated during the synthesis of alumina sol from aluminium nitrate precursor.

BET surface area of alumina gel@ zeolite X composite was calculated from N_2 adsorption-desorption isotherm (Fig.2B.2(c)). The total surface area was found to be 257 m^2/gm comprising of micropore surface area of 198 m^2/gm and mesopore surface area of 59 m^2/gm. The BET isotherm shows typical IV type with H3 hysteresis loop signifying mesopore characteristics above the relative pressure (p/p_o) of 0.4. However, the horizontal plateau at lower p/p_o range indicates the zeolitic micropores. The total pore volume of the sample was estimated as 0.166 cm^3/gm. Fig. 2B.2(d) shows the BJH pore size distribution curve with pore size of 3.9 nm from desorption data, and the inset corresponds to pore size distribution obtained from NLDFT method revealing cylindrical pores with pore sizes of 0.98, 2.6 and 4.8 nm. It is to be pointed out that unmodified zeolite X shows surface area of 703 m^2/gm with micropore and mesopore surface area values of 623 and 80 m^2/gm, respectively.[11] Interestingly, surface area decreased after modification of zeolite X with alumina gel. However, adsorption efficiency of alumina gel modified zeolite X is higher than that of unmodified zeolite X (discussed in the next section). It is inferred that for adsorption of fluoride ions, surface area of the adsorbent is not the sole factor but the presence of alumina gel with abundance of surface hydroxyl ions plays a significant role.

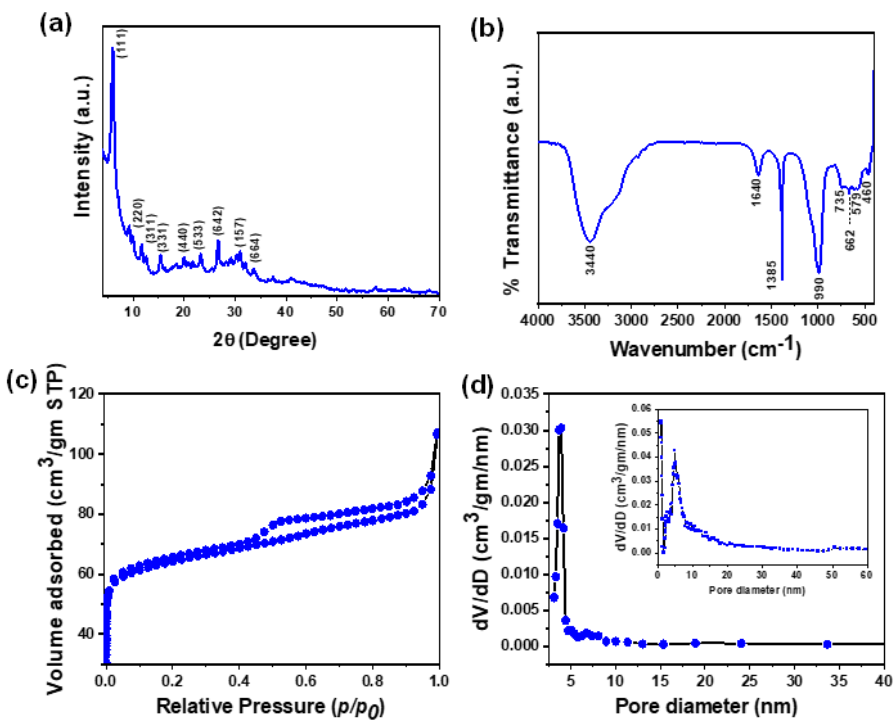

Figure 2B.2: (a) XRD pattern, (b) FTIR, (c) BET isotherm and (d) BJH pore size distribution (inset: pore size distribution by NLDFT) of alumina gel@ zeolite X nanocomposite.

XPS of the sample was performed to study the surface chemical analysis i.e., chemical and electronic states of the elements, binding energy of the specific element and the composition of the elements present in the sample. Fig. 2B.3 shows XPS of alumina gel@ zeolite X nanocomposite: (a) full scan survey and (b) Al2p, (c) Si2p, (d) Na1s and (e) O1s deconvoluted spectra. The Al2p spectrum is centred at 74.18 eV associated with BE of Al-O bond while BE for Na1s is found at 1072eV. The deconvoluted $Si2p_{3/2}$ spectra with BE at 101.8 and 102.8 eV correspond to $Si\text{-}O^{-}$(non-bridging) and Si-O-Si (bridging) bonds, respectively.[14] Interestingly, the O1s deconvoluted spectra show the BE at 530.2, 531.6 and 533.2eV which signify the presence of lattice oxygen (42.4%), surface oxygen defects (49.2%) and adsorbed hydroxyl (OH^{-}) groups (8.4%), respectively.[15] The elemental composition (atomic%) of Al, Si, Na and O was found to be 19.15, 5.84, 0.33 and 74.67%, respectively. The Al and O contents are contributed from both the zeolite X and alumina gel components in the nanocomposite while Si and Na are originated from zeolite X.

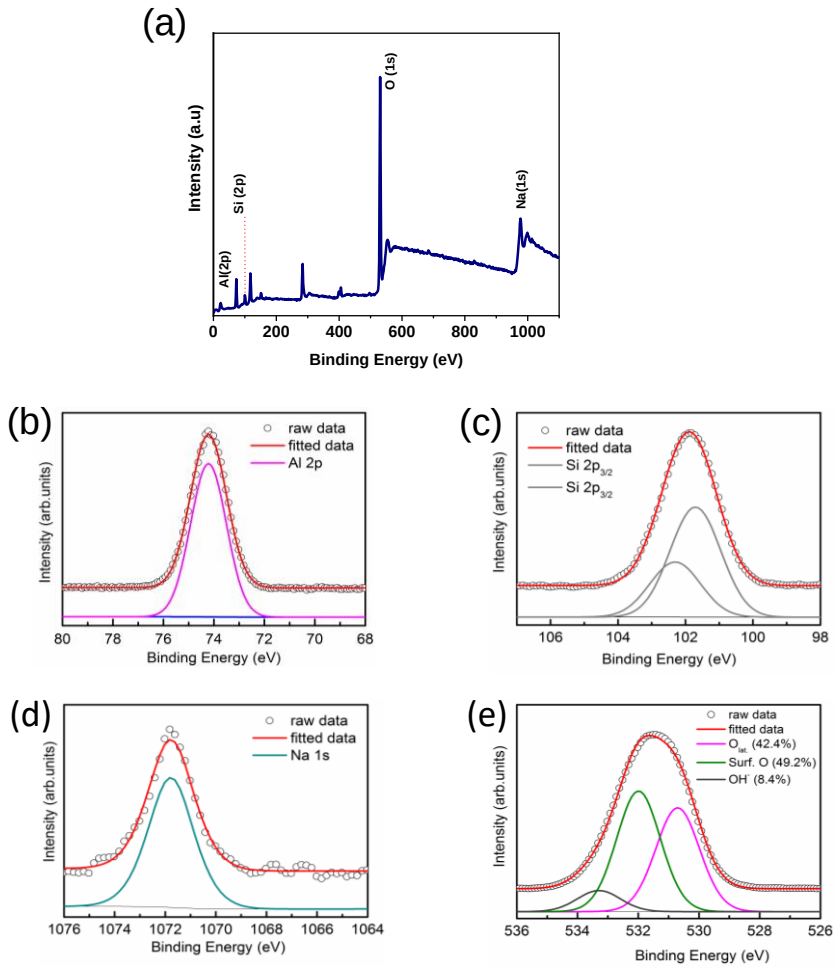

Figure 2B.3: XPS of (a) full scan survey, (b) Al 2p, (c) Si 2p, (d) Na 1s and (e) O 1s spectra of alumina gel@zeolite X nanocomposite.

Microstructural study of the synthesized material is carried out by FESEM and TEM. Figs. 2B.4(a),(b) shows FESEM micrographs with low and high magnification image. It is noticed that nano meter sized alumina gel particles (50-100 nm) with high surface charge are aggregated surrounding the zeolite X particles. The gel particles with Al-O-Al linkage interacts with zeolite X *via* hydrogen bonding and/or electrostatic interaction. The TEM image of alumina gel@zeolite X nanocomposite also confirms the adherence of nano meter sized aggregated alumina gel particles around the spheroid shaped zeolite X particles of size around 0.5-1 μm (Fig. 2B.4(c)). The adhered alumina gel particles are indicated with dotted red line. The particle size of nanocomposite was also determined by dynamic light scattering (DLS) method indicating average particle size of 1.2 μm (Fig. 2B.4(d)). The atomic% composition of the element present in the material is determined from EDS analysis (Fig. 2B.4(e)). It reveals Al, Si, Na and O atomic% as 20.82, 11.30, 1.15 and 66.73%, respectively.

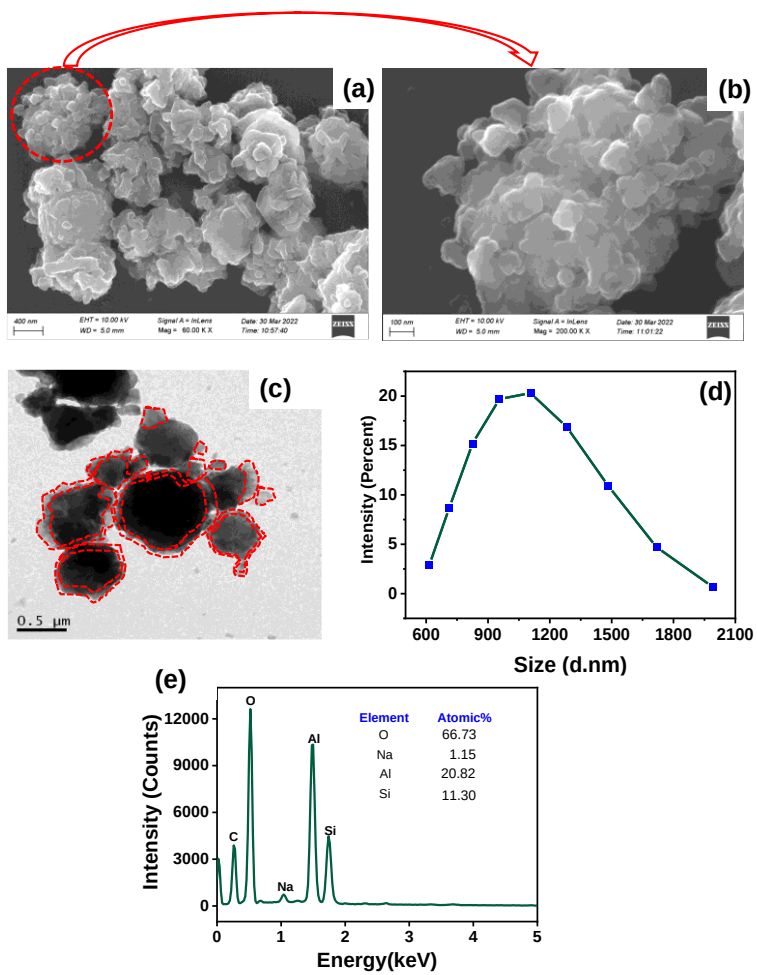

Figure 2B.4: (a) FESEM (low mag.), (b) FESEM (high mag.), (c) TEM images, (d) Particle size disribution and (e) EDS analysis of alumina gel@ zeolite X nanocomposite.

2B.3.2 Batch adsorption experiment

Effect of contact time

Fig. 2B.5(a) shows % removal of F^- ions with contact time keeping the initial concentration of 5 mg/L (pH~6.5) at 30 ^oC for different adsorbent doses of 0.5,1 and 2 gm/L. It is clear that at 120 min of adsorption, equilibrium is reached with % adsorption of 96.2,99 and 99.7% for adsorbent dosages of 0.5, 1 and 2 gm/L, respectively. Fig. 2B.5(b) shows the change in adsorption capacity (q_t) with time. It reveals that adsorption capacity is maximum for 0.5 gm/L of adsorbent dose which is in decreasing order with increasing the dose concentration.

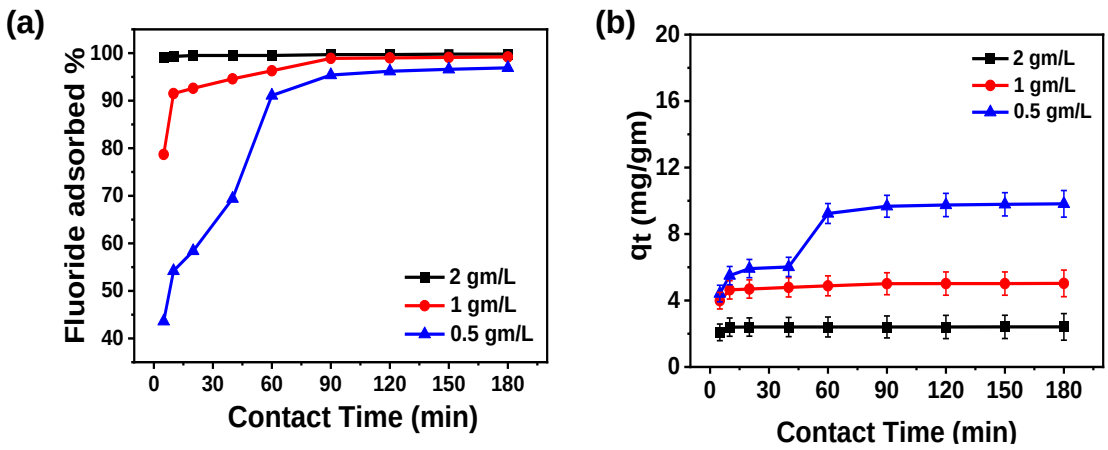

Figure 2B.5: Effect of contact time on (a) % fluoride adsorption (b) Adsorption capacity by alumina gel@ zeolite X nanocomposite.

Effect of initial F^- ion concentration

Fig. 2B.6(a) shows that with increase in initial F^- concentration (pH~6.5), % adsorption decreases for different adsorbent dosages of 0.5, 1 and 2 gm/L for 120 min contact time at 30 ^oC. The decreasing trend can be explained by the fact that with increasing F^- ions, the adsorption sites get more screened by the accumulated adsorbate species with the saturation of co-ordination sites rendering less adsorption.[16] Fig. 2B.6(b) shows that adsorption capacity (q_e) increased sharply with adsorbate dose. The adsorption capacity is becoming higher with decreasing adsorbent dose.

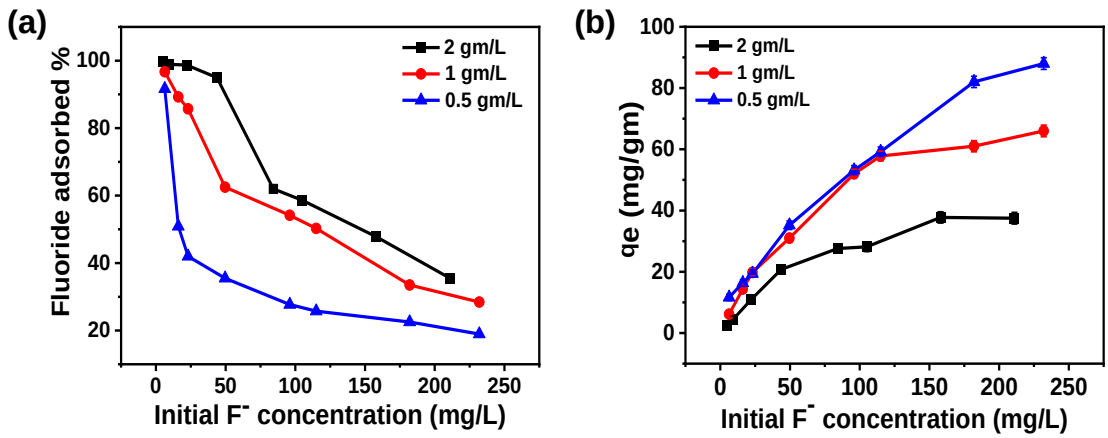

Figure 2B.6: Effect of initial fluoride ion concentration on (a) % fluoride adsorption (b) Adsorption capacity by alumina gel@ zeolite X nanocomposite.

Effect of adsorbent dose

Fig. 2B.7(a) reveals that with increase in adsorbent dose, the % removal increased sharply up to 4gm/L followed by reaching saturation limit after 8 gm/L. It is worth noting that with increase in adsorbent dose, the accessible adsorption sites get increased rendering larger amount of fluoride uptake.[17] However, fluoride uptake capacity is becoming saturated after a certain adsorbent dosage. The % adsorption is >99% for adsorbent dose in the range of 4-10 gm/L. Fig. 2B.7(b) shows that adsorption capacity (q_e) decreased with increasing adsorbent dose.

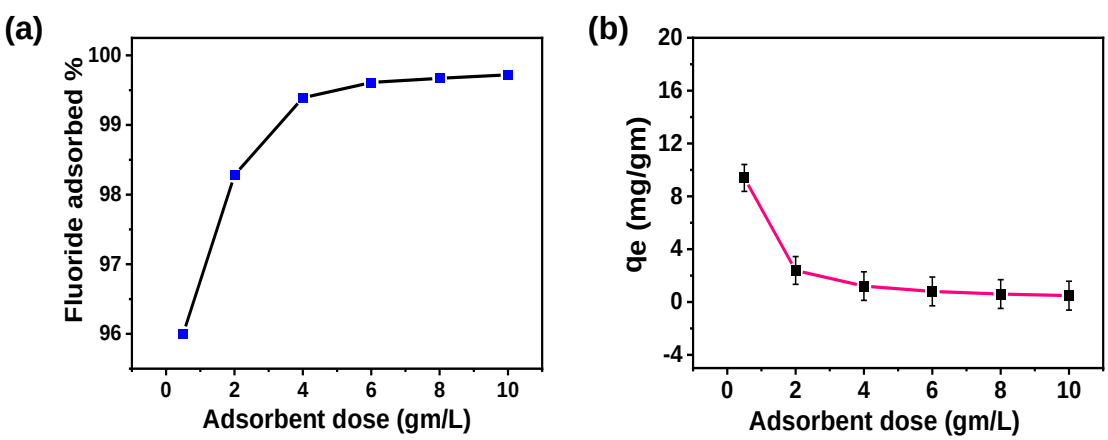

Figure 2B.7: Effect of adsorbent dose on (a) % fluoride adsorption (b) Adsorption capacity by alumina gel@ zeolite X nanocomposite.

To compare the adsorption capacity (mg/gm) of alumina gel@ zeolite X nanocomposite with respect to zeolite X for the removal of fluoride, the same experiment was

carried out for 120 min with different adsorbent dosages (0.5, 1, 2 gm/L). The adsorption capacities for both the zeolite X and alumina gel@zeoliteX were measured (Table 2B.1). It was found that adsorption capacity values for zeolite X were 2.6, 0.70 and 0.55 mg/gm for adsorbate dosages of 0.5, 1, 2 gm/L, respectively, whereas those were 9.75, 5.02 and 2.40 mg/gm for alumina gel@ zeolite X nanocomposites, respectively. It is worth noting that modified zeolite (alumina gel@ zeolite X) enhances the adsorption capacity for fluoride ions removal.

Table 2B.1: Adsorption capacity (mg/gm) of zeolite X and alumina gel@zeolite X nanocomposites.

Time (min)	Initial adsorbate conc. (mg/L)	Adsorbent dose(gm/L)	Adsorption capacity (mg/gm) of zeolite X	Adsorption capacity (mg/gm) of alumina gel@ zeolite X
120	5	0.50	2.6	9.75
		1.00	0.70	5.02
		2.00	0.55	2.40

Effect of Temperature

To study the temperature effect on adsorption, the initial F^- concentration was maintained at 5 mg/L for 120 min contact time at pH 6.5. Fig. 2B.8(a) shows that % adsorption increases significantly with increase in temperature for 0.5 gm/L to 2gm/L adsorbent dose; The increasing trend with temperature is attributed to the endothermic nature of the process, therefore showing better fluoride removal efficiency. Fig. 2B.8(b) shows that adsorption capacity (q_e) increased slightly with increasing temperature.

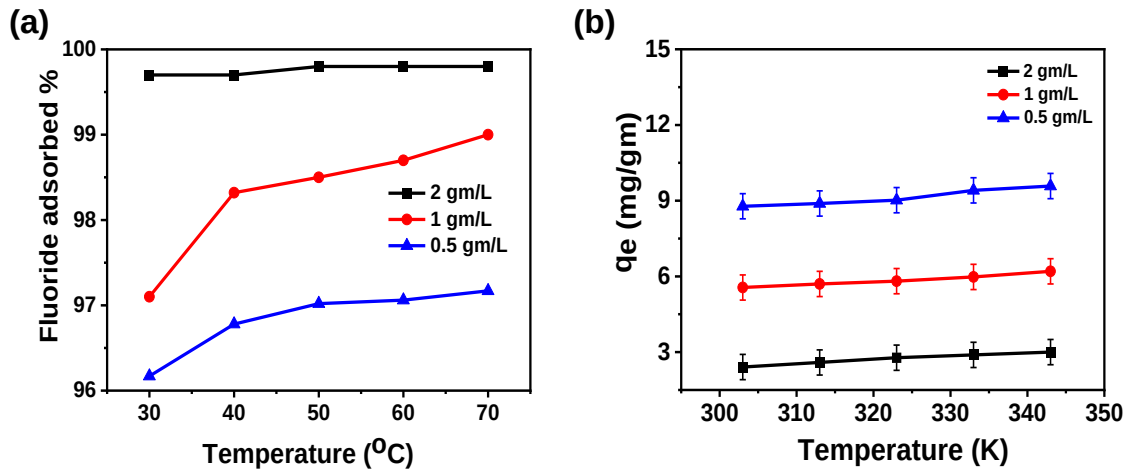

Figure 2B.8: Effect of temperature on (a) % fluoride adsorption (b) Adsorption capacity by alumina gel@ zeolite X nanocomposite.

Effect of pH

The pH of aqueous solution plays a pivotal role on adsorption because positively charged hydrogen ions and negatively charged hydroxyl ions on the adsorbent surface interact with F^- ions during adsorption. Fig. 2B.9(a) shows that for 0.5 gm/L adsorbent dose, the % adsorption drastically falls after neutral pH. On the other hand, for 1-2 gm/L adsorbent doses no significant change of % adsorption is occurred through a wide range of pH. It is obvious that at higher pH, particularly for lower adsorbent doses (0.5 gm/L), the affluence of hydroxyl ion diminishes the adsorption of negatively charged fluoride ion rendering a decreasing trend in adsorption. However, pH has a minimal effect for higher concentration of adsorbent which is important for practical application. Fig. 2B.9(b) shows the change in adsorption capacity (q_e) with pH. The adsorption capacity is maximum for adsorbent dose of 0.5 gm/L; however, it decreased significantly after pH ~6.5. For adsorbent dose of 1-2 gm/L, the adsorption capacity remains almost same throughout a wide range of pH (3-10).

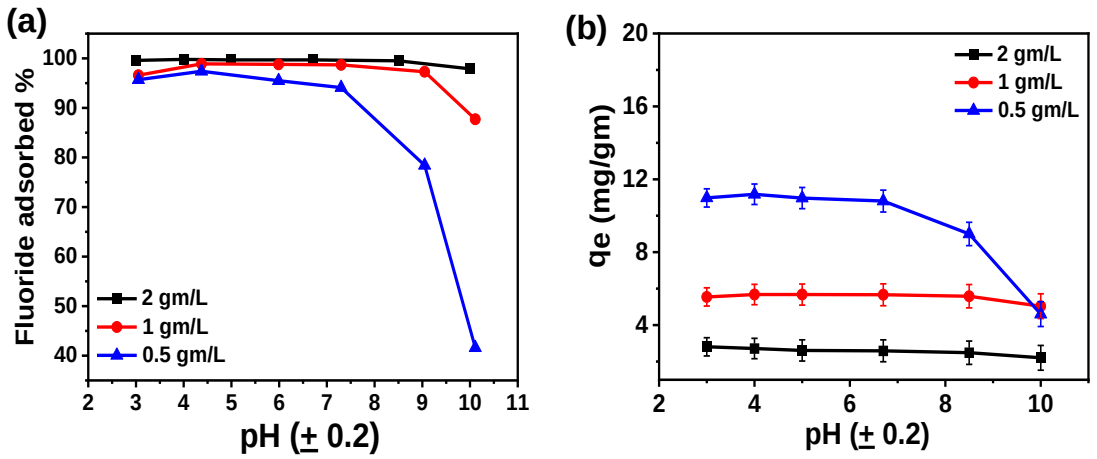

Figure 2B.9: Effect of pH on (a) % fluoride adsorption (b) Adsorption capacity for the adsorption of F^-ions by alumina gel@ zeolite X nanocomposite.

Effect of co-existing anions

The presence of various co-existing anions in natural groundwater may challenge the removal efficiency of the adsorbent material during adsorption of fluoride ions. The effect of co-existing anions like sulphate (SO_4^{2-}), chloride (Cl^-), nitrate (NO_3^-), phosphate (PO_4^{3-}) was studied. Fig. 2B.10(a) reveals that % adsorption of F^- is becoming 97.7% in the presence of Cl^-, NO_3^-, PO_4^{3-} and SO_4^{2-} ions which contributed 6.9, 2.6, 19.7 and 9.88% adsorption, respectively. It is to be noted that lyotropic series of different anions for Al^{3+} is in the order of $F^- > SO_4^{2-} > Cl^- > NO_3^-$ which reflected the adsorption affinities of these anions with the adsorbent containing Al^{3+}.[18] Due to larger hydrated ionic radius of phosphate ion compared to other competing ions, the phosphate ion has tendency to form outer sphere complexes held by long range electrostatic force rendering higher adsorption.[19] Moreover, PO_4^{3-} ions are readily hydrolyzed in solution rendering more hydroxyl ions, and the adsorption sites become negative. It causes electrostatic repulsion with F^- ions. Thus, a negative effect is resulted for adsorption of F^- ions in the presence of PO_4^{3-}ions.[20]

Regeneration study

To study the effectivity of the adsorbent, the regeneration study is one of the most important processes to be performed and generally an alkaline solution is chosen to fulfil this purpose as the hydroxyl ions show the ion exchange ability with fluoride ion. Regeneration process was continued up to five cycles and F^- adsorption run was continued for each cycle. It is

found that>90% adsorption is noticed up to 3rd cycle followed by gradual decrease in fluoride removal efficiency for 4th and 5th cycles (Fig. 2B.10(b)). During regeneration, the fluoride ions get desorbed by the adsorption of the hydroxyl ion. It is attributed to the fact that after regeneration with some cycles, some hydroxyl groups are entrapped at the adsorbent surface which could not be removed completely by washing with water. It inhibits to some extent further adsorption of fluoride ions due to anion-anion repulsion between entrapped OH^- ions of the adsorbent and F^- ions of adsorbate. Thus, removal efficiency starts decreasing gradually after 4th cycle.

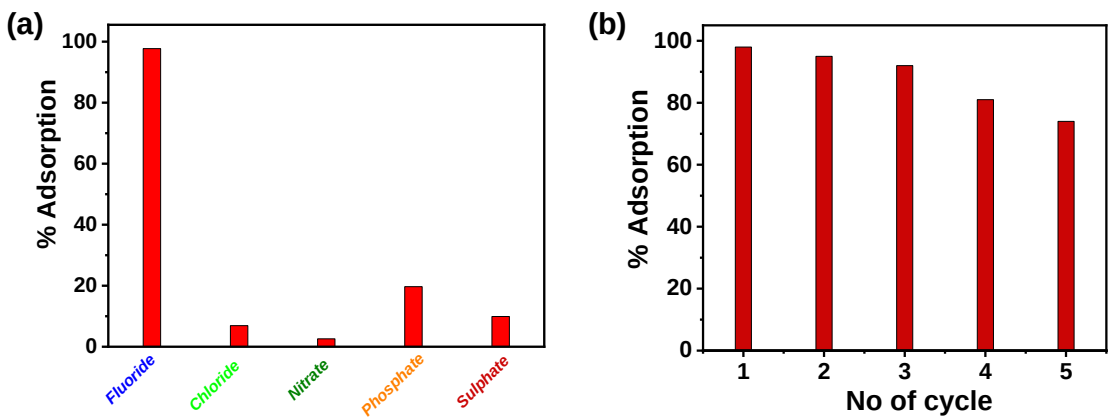

Figure 2B.10: Effect of (a) co-existing ion and (b) recyclability study for the adsorption of F^-ions by alumina gel@ zeolite X nanocomposite.

2B.3.2.1 Adsorption Kinetics

The pseudo first-order and pseudo-second order kinetics models were applied for adsorption study. Table 2B.2 presents the mathematical expressions and kinetic parameters obtained from the above models. For first order kinetics, q_e and k_1 (first order rate constant) can be determined from the intercept and slope, respectively obtained from the linear plot of ln (q_e-q_t) *vs* t, while for second order kinetics, by plotting t/q_t vs t, the values of q_e and k_2 (second order rate constant) can be obtained from the intercept and slope, respectively. The linear fitting curves with the kinetic data are shown in Figs. 2B.11(a) and 2B.11(b) for pseudo-first-order and pseudo-second-order models, respectively. From the curves it is clear that pseudo-second-order model is best fitted with correlation co-efficient (R^2) values close to unity, signifying chemisorption process of the adsorption. It is obvious that for different adsorbent doses, F^- adsorption decreased with increasing adsorbent doses.

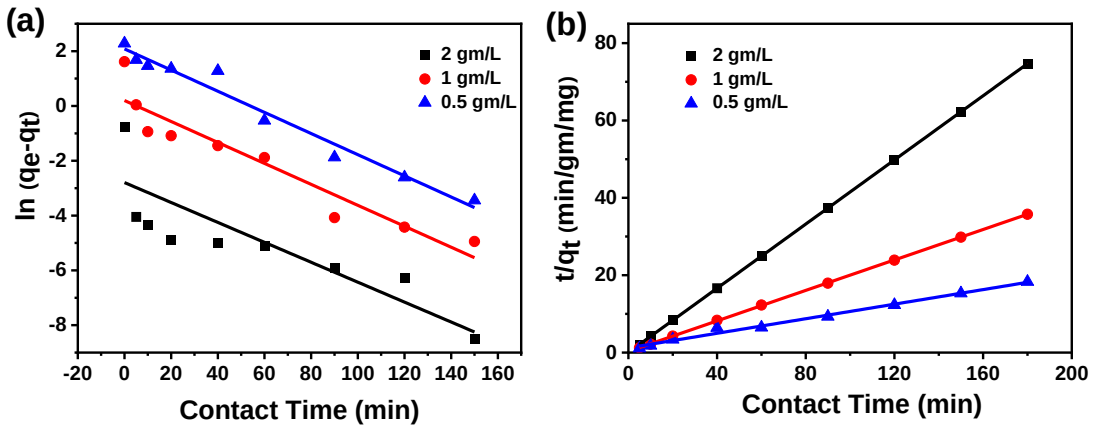

Figure 2B.11: Kinetics data with linear fitting of (a) pseudo-first-order and (b) pseudo-second-order for the adsorption of F^- ions by alumina gel@ zeolite X nanocomposite.

Table 2B.2: Kinetic parameters for the adsorption of fluoride ions.

Model	**Mathematical expression**		**Adsorbent dose (gm/L)**		
			0.5	1.0	2.0
Pseudo-first order kinetics	$\ln (q_e-q_t) = -k_1 t + \ln q_e$	k_1 (min^{-1})	0.03861	0.03824	0.03636
		q_e(mg/gm)	8.026	1.2200	0.06110
		R^2	0.9657	0.8823	0.5616
		S.E (Intercept)	0.346	0.375	0.729
		S.E(Slope)	0.003	0.004	0.008
Pseudo-second order kinetics	$t/q_t = 1/k_2 q_e^2 + (1/q_e)t$	k_2 (gm/mg·min)	0.0729	0.1239	4.52
		q_e(mg/gm)	10.62	5.07	2.411
		R^2	0.9999	0.9999	0.9999
		S.E (Intercept)	0.198	0.056	0.011
		S.E(Slope)	0.002	0.0005	0.0001

Note: q_e and q_t (mg/ gm) are the amounts of fluoride adsorbed at equilibrium and time t (min), and k_1 (min^{-1}) and k_2 (gm/mg/min) are the first and second-order rate constants, respectively, SE = Standard Error.

2B.3.2.2 Adsorption Isotherms

The equilibrium adsorption data for different adsorbent doses of 0.5,1 and 2 gm/L was fitted with Langmuir and Freundlich isotherm models. Table 2B.3 represents the linear form of the two models along with the parameters calculated from the two isotherm curves. For Langmuir Isotherm, the linear plot of C_e/q_e vs. C_e, the maximum adsorption capacity (q_m(mg/gm)) and Langmuir adsorption constant (K_L) can be determined from the slope and intercept, respectively (Fig. 2B.12(a)); whereas, for Freundlich isotherm, by plotting log q_e vs. log C_e, the adsorption intensity (n_F) and K_F (Freundlich constant) can be determined from the slope and intercept of the linear plot, respectively (Fig. 2B.12(b)). The higher correlation coefficient R^2 obtained from the Langmuir isotherm curve indicates the best fitting for the adsorption of F^- removal. It is clear that there is an increasing trend of adsorption capacity with decrease in adsorbent dose rendering a maximum adsorption of 104.16 mg/gm for the adsorbent dose of 0.5 gm/L. A comparative data on maximum adsorption capacity, kinetics and rate constant for fluoride ion adsorption by alumina gel@ zeolite X nanocomposite and reported adsorbents is presented in Table 2B.4, which shows better adsorption capacity of the present synthesized nanocomposite.

Table 2B.3: The parameters obtained from Langmuir and Freundlich models.

Adsorbent dose (gm/L)			**0.5**	**1.0**	**2.0**
Langmuir isotherm	$C_e/q_e=C_e/q_m+1/K_L.q_m$	K_L (L/mg)	0.0217	0.0972	0.26431
		q_m (mg/gm)	103.62	68.119	37.608
		R^2	0.8973	0.9877	0.9822
		S.E (Intercept)	0.113	0.0476	0.080
		S.E (Slope)	0.001	0.0006	0.001
Freundlich isotherm	$\log q_e = \log K_F + 1/n_F \log C_e$	K_L (L/mg)	10.452	11.668	10.739
		q_m (mg/gm)	2.653	2.764	3.495
		R^2	0.8781	0.9826	0.9245
		S.E (Intercept)	0.197	0.061	0.106
		S.E(Slope)	0.052	0.018	0.030

Note: q_e is the amounts of fluoride adsorbed at equilibrium and q_m is q_e for a complete monolayer, i.e., maximum adsorption capacity (mg/gm), K_L is adsorption equilibrium constant (L/mg); K_F and n_F are empirical constants, indicating the adsorption capacity and adsorption intensity, respectively, SE = Standard Error.

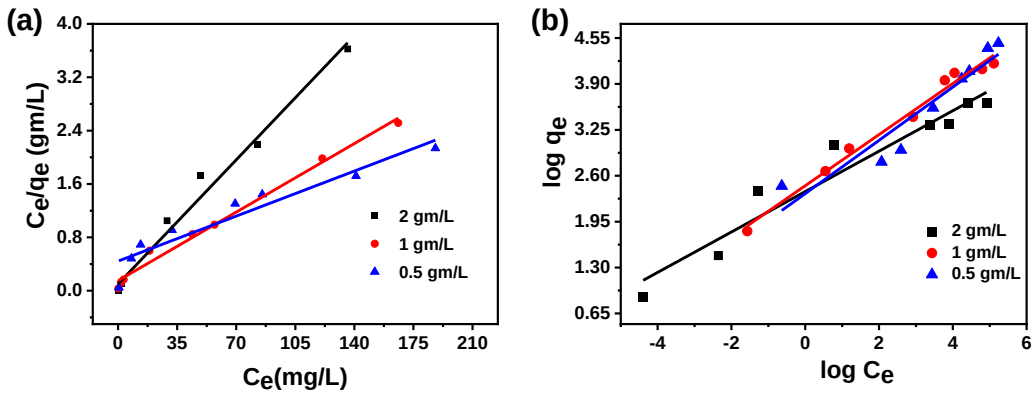

Figure 2B.12: Isotherm plots: (a) Langmuir and (b) Freundlich for the adsorption of F^- ions by alumina gel@ zeolite X nanocomposite.

Table 2B.4: A comparative data on maximum adsorption capacity, kinetics and rate constant for fluoride ion adsorption by alumina gel@zeolite X nanocomposite and reported adsorbents.

Adsorbents	Maximum adsorption capacity (mg/gm) at 25 °C	Kinetics	Value of rate constant *k*	Ref
Bentonite/chitosan beads	1.16	Pseudo second order	149.67 (gm/mg.min)	21
Crystalline gamma alumina	32.00	Pseudo second order	0.03 (gm/mg.min)	22
Ceramic adsorbent	2.16	Pseudo second order	0.64 (gm/mg.min)	23
AlFe650/C	13.64	Pseudo second order	0.07 (gm/mg.min)	24
Aluminium impregnated chitosan	1.73	First order	0.101 min^{-1}	25
Aluminium coated modified zeolite	11.52	Pseudo second order	0.6804 (gm/mg.min)	26
Alumina gel@zeolite X	103.62	Pseudo second order	0.0729 (gm/mg.min)	Present work

2B.3.2.3 Thermodynamic parameters

The thermodynamic parameters such as Gibbs free energy (ΔG^o), enthalpy (ΔH^o) and entropy (ΔS^o) were calculated using the following equations.[27]

$$\Delta G^o = -RTlnK^o{}_{eq} \quad \text{where } K^o{}_{eq} = \frac{(C_0 - C_e)}{C_e}$$

$$ln\, K^o{}_{eq} = \Delta S^o/R - \Delta H^o/RT \qquad (2B.5)$$

where $K^o{}_{eq}$ is the equilibrium constant,[28–30] R represents the universal gas constant (8.314 J /mol/K) and T is the temperature in Kelvin scale. The Gibb's free energy (ΔG^o) values obtained for the adsorption process at all temperatures are listed in Table 2B.5. ΔH^o and ΔS^o

were determined from the slope and intercept of the plot of $ln\ K^{o}_{eq}$ vs. 1/T (Fig. 2B.13). The positive values of ΔH^{o} indicate the adsorption process to be endothermic which was observed for all the three adsorbent doses 0.5, 0.1and 2gm/L, as well as the value of ΔS^{o} was also found to be positive for all three cases indicating the increasing trend of randomness of the adsorption process. The negative value of ΔG^{o} indicates the process is spontaneous which in turn was found to be more negative with increasing temperature.[31]

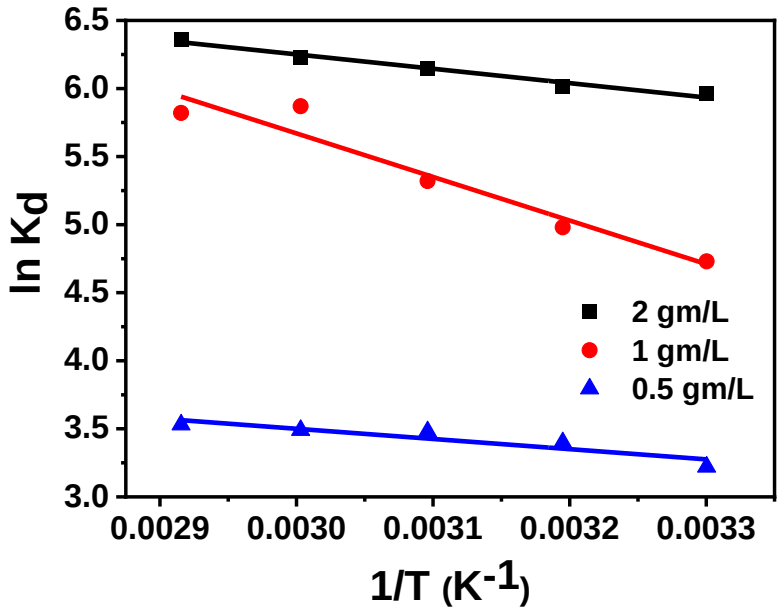

Figure 2B.13: Plot of $ln\ K^{o}_{eq}$ versus 1/T for fluoride ions adsorption.

Table 2B.5: Thermodynamic parameters of fluoride adsorption for different adsorbent doses.

Adsorbent dose (gm/L)	ΔH° (kJ/mol)	ΔS° (J/mol.K)	ΔG° (kJ/mol)
0.5	+6.225	+47.772	−8.249 at 303K −8.726 at 313K −9.204 at 323K −9.682 at 333K −10.160 at 343K
1.0	+26.603	+126.87	−11.575 at 303K −12.835 at 313K −14.095 at 323K −15.355at 333K −16.615 at 343 K
2.0	+8.878	+78.31	−14.84 at 303 K −15.629 at 313 K −16.4129 at 323K −17.1959at 333K −17.9789 at 343 K

2B.3.2.4 Adsorption mechanism

Fig. 2B.14 shows schematically a proposed mechanism for adsorption of F^- ions by alumina gel@zeolite X nanocomposite. Two possible ways could take place for fluoride adsorption onto the adsorbent surface: (i) electrostatic attraction between protonated hydroxyl groups and fluoride ions and (ii) ion exchange of fluoride ions with surface hydroxyl groups. To understand the adsorption mechanism, point of zero charge (pH_{pzc}) of the nanocomposite was studied varying pH condition. The pH_{pzc} was calculated by the familiar mass titration

method[32] varying different adsorbent concentrations (0.005 to 4 gm) which were added to 10 mL of 0.01 N NaCl solution. An asymptomatic value of pH was found to reach with increasing the mass of the adsorbent and the equilibrium pH was considered to be the pH_{pzc} which was found to be around 5.7. Nanoporous zeolite X with high surface area enhances adherence of nanometer size alumina gel particles in the adsorbent. Alumina gel contains a plethora of hydroxyl groups on its surface. In acidic medium, below the pH_{pzc}, these hydroxyl groups get protonated which help facilitate adsorption of fluoride ions. However, in alkaline medium where solution pH is greater than pH_{pzc} some of the hydroxyl groups could be exchanged with fluoride ions, the rest hydroxyl groups take part in electrostatic repulsion with negatively changed fluoride ions. Thus, at higher pH the electrostatic repulsion prevails over exchange capability between negatively charged hydroxyl and fluoride ions. It is worth mentioning that nanoporous zeolite having high surface area and surface hydroxyl groups (protonated and non-protonated) of alumina gel play a significant role for adsorption of fluoride ions from aqueous solution.

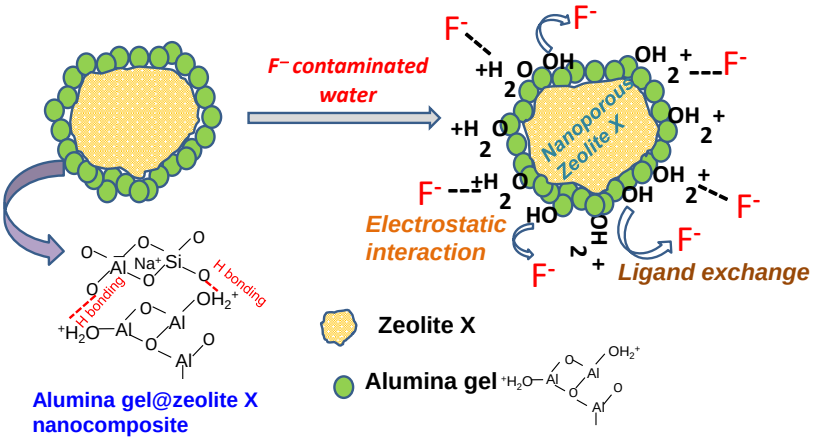

Figure 2B.14: A proposed mechanism for the adsorption of F^- ions by alumina gel@ zeolite X nanocomposite.

2B.3.3 Column adsorption study

Effect of initial fluoride concentration

To study the effect of influent concentration on the breakthrough curve, the initial fluoride concentration was varied from 2 to 8 mg/L keeping the bed height at 10 cm and flow rate at 10 ml/min. Fig. 2B.15(a) shows the breakthrough curve obtained at different fluoride concentrations. It illustrates that the time taken for bed saturation was longer for low initial fluoride concentration. At lower concentration gradient, the required amount of fluorinated

water was higher due to slower transportation with increase in mass transfer interface causing decrease in mass transfer coefficient. As the initial fluoride concentration increases, the slope of the breakthrough curve becomes steeper, giving rise to smaller breakthrough and exhaustion time. It was found that breakthrough time (C_t/C_o=0.05) occurred after 94, 59 and 36 h for fluoride concentrations of 2, 5 and 8 mg/L, respectively. The phenomenon could be explained by the fact that with increasing the fluoride concentration, the number of available fluoride ion increases rendering rapid saturation of the bed column within a particular time span. At the saturation stage, the excess fluoride ions remain unadsorbed, and the uptake capacity of the column gets reduced. It is worth mentioning that mass diffusion process is affected by the concentration gradient of fluoride ions. The higher concentration gradient with higher driving force renders maximum mass transfer.

Effect of flow rate

The effect of flow rate was studied at 5, 10 and 20 mL/min keeping the bed height at 10 cm and initial feed concentration at 5 mg/L. The breakthrough curves at different flow rates are shown in Fig. 2B.15(b). At lower flow rate, adsorption process was found to be very effective initially due to the availability of more adsorption sites which gradually decreases with time leading to less effective adsorption. It was observed that with increasing flow rate, the breakthrough curve becomes steeper giving rise to decreasing breakthrough time as well as adsorbed ion concentration. At faster flow rate the solute could not reside in the column for longer time and the fluoride ions leave the column before the adsorption equilibrium can reach.[33,34] Thus, at lower flow rate, the contact time of the fluoride ions with the adsorbent materials becomes more with high interparticle diffusion which causes the removal efficiency higher leading to higher breakthrough and exhaustion time. The interparticle diffusion is the rate of diffusion after the early stages of adsorption determined by various parameters like mass of adsorbent, initial concentration of adsorbate and particle size.

Effect of bed height

Fig. 2B.15(c) shows the breakthrough curves obtained for the adsorption of fluoride ions with bed heights of 5, 10 and 15 cm in which 30, 60 and 90 gm of adsorbent were loaded, respectively in the column, keeping the flow rate as 10 mL/min and initial feed concentration as 5 mg/L. From the breakthrough profile it is observed that curve for 5 cm bed height is steeper compared to 10 and 15 cm i.e., breakthrough time and exhausation time increase with

increasing bed height. With increasing bed volume the adsorption sites also increase which leads to greater mass-transfer interface with larger amount of fluoride ions adsorption. It is reported that with increase in adsorbent volume in column the diffusive mass-transfer overrides the axial dispersion of adsorbate. Therefore, efficient removal of contaminants can be achieved by increasing bed height which in turn will furnish more active sites for considerable adsorption.

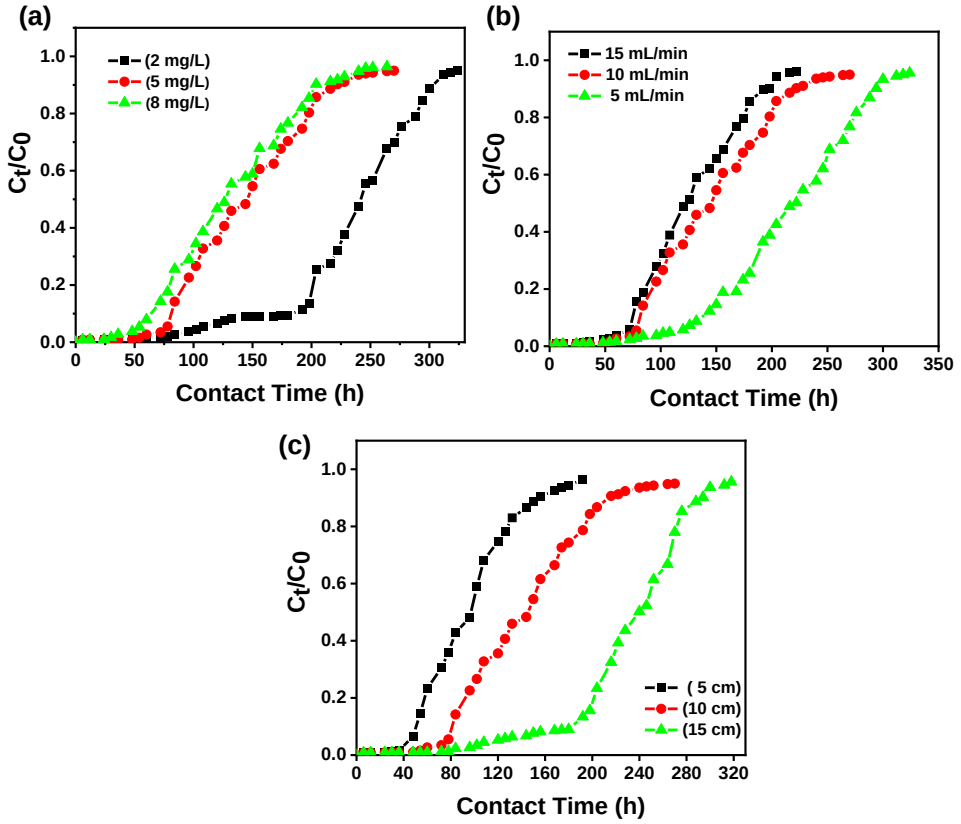

Figure 2B.15: Breakthrough curves for adsorption of fluoride (a) at different initial concentrations, (b) at different flow rates and(c) at different bed heights.

2B.3.3.1 Kinetic models on breakthrough curves

For evaluating adsorption efficiency, adsorption study on fixed bed column is advantageous over batch mode. Effective study of breakthrough curves could be explained by different mathematical models. In this study, the adsorption behavioural pattern of alumina gel@ zeolite X nanocomposite for the removal of fluoride was accomplished by applying different models like Adams-Bohart,[35] Thomas,[36] Yoon-Nelson[37] and bed depth service time (BDST)[38] for ascertaining the individual factors of the column along with the extrapolation of breakthrough curves.

Adams-Bohart model

The adsorption capacity of the adsorbent as well as the initial part of breakthrough curves can be predicted by Adams-Bohart model. It also helps to predict the saturation concentration of adsorbate. This model considers surface reaction theory by defining a relationship between C_t/C_0 and t in a continuous arrangement in which instantaneous equilibrium is not attained. The mathematical expression of this model can be written as-

$$ln\left(\frac{C_t}{C_0}\right) = K_{AB}C_0t - K_{AB}N_0\left(\frac{Z}{F}\right) \qquad (2B.6)$$

Where,C_t and C_0 indicates effluent and influent adsorbate concentration at time t,K_{AB}(L/mg.h) represents Adams-Bohart rate constant, N_0 (mg/L), Z (cm) and F (cm/min) refer to sorption capacity of bed, bed height and linear velocity, respectively. By plotting $ln\left(\frac{C_t}{C_0}\right)$ against time (t), line fitting curves are obtained. The values of N_0 and K_{AB} are obtained from the slope and intercept of the linear plots, respectively. Fig. 2B.16 shows linear regression analysis of breakthrough curves using Adams-Bohart model at different (a) concentrations, (b) flow rates and (c) bed heights. Table 2B.6 summarizes the calculated parameters obtained from linear regression analysis. It is noticed that kinetic constant K_{AB} increases with increasing flow rate and decreases with increasing initial fluoride concentration and bed height. It is to be noted that at the initial stages of the column adsorption study the entire system was occupied by the external mass transfer.[39] Interestingly, the adsorption capacity N_0 increases with increasing influent concentration and flow rate, but a reverse trend is observed for bed height which has been found to be similar with Mukherjee *et al.* in their study of biosorption of fluoride by immobilized bead of NaA zeolite.[40]

Table 2B.6: Adams-Bohart Model Parameters.

C_0 (mg/L)	Q(ml/min)	Z(cm)	$K_{AB}\times10^{-3}$ (L/mg h)	N_0(mg/L)	R^2
2	10	10	8.60	5072.13	0.9729
5	10	10	4.09	9214.74	0.8258
8	10	10	2.35	13782.75	0.8120
5	5	10	3.18	6481.32	0.9584
5	10	10	3.78	9970.38	0.8258
5	15	10	4.50	12564.18	0.8727
5	10	5	5.00	13886	0.7802
5	10	10	3.80	9917.06	0.8250
5	10	15	3.29	8983.81	0.9776

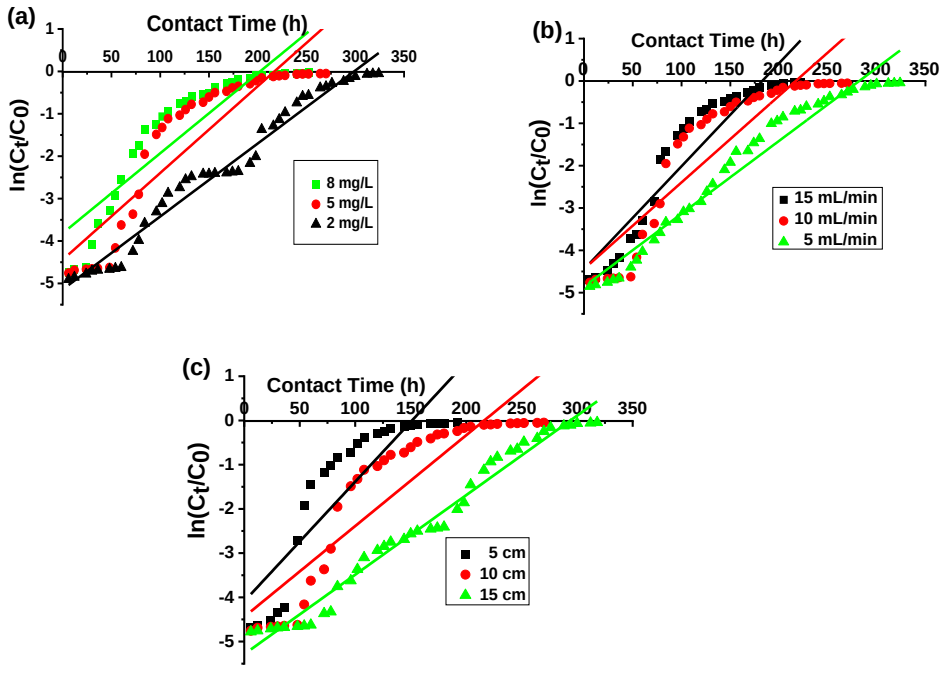

Figure 2B.16: Linear regression analysis of Breakthrough curve using Adams Bohart Model at different (a) concentrations, (b) flow rates and (c) bed heights.

Thomas model

Thomas model is one of the most acceptable and widely used model for the interpretation of performance theory of the adsorption process in fixed bed columns. The assumptions of this model mainly hold as: 1) adsorption-desorption process follow Langmuir kinetics, 2) pseudo-second order reversible reaction kinetics and 3) negligible axial dispersion. Thomas model is applicable where external resistance and intraparticle diffusion become insignificant throughout the mass transfer process.[41] The linearized form of Thomas model is shown in the following equation.

$$ln\left(\frac{C_0}{C_t}-1\right)=\frac{k_{Th}\times q_0\times W}{Q}-k_{Th}\times C_0\times t \qquad (2B.7)$$

Where, C_0(mg/L) and C_t (mg/L) correspond to inlet and outlet fluoride concentrations, respectively, k_{Th} (L/mg.h) is the Thomas rate constant, q_0 (mg/g) refers to equilibrium fluoride uptake per gm of adsorbent, W(g) indicates the mass of the adsorbent, Q (mL/min) is the flow rate and t as flow time. By plotting $ln\left(\frac{C_0}{C_t}-1\right)$ vs time t, line fitting curves are obtained. The values of of k_{Th} and q_0 can be obtained from the slope and intercept of the linearized plot, respectively. Fig. 2B.17 shows linear regression analysis of breakthrough curves using Thomas model at different (a) concentrations, (b) flow rates and (c) bed heights. Table 2B.7 summarizes the calculated parameters obtained from linear regression analysis of Thomas model. Thomas rate constant k_{Th} increases with increasing flow rate and decreases with influent fluoride concentration and bed height. It is attributed to mass transport resistance which decreases with increase in flow rate and decrease in initial fluoride concentration and bed height of the packed column. The adsorption capacity, q_0 (mg/g) increases with increasing initial fluoride concentration and flow rate; however, it decreases with bed height. The higher regression coefficient (R^2) values obtained from Thomas model compared to other models fit well with the experimental data. It demonstrates that internal and external diffusions are not the rate limiting step.[42]

Table 2B.7: Thomas Model Parameters.

C_0 (mg/L)	Q(ml/min)	Z(cm)	$K_{Th} \times 10^{-3}$ (L/mg h)	q_0(mg/g)	R^2
2	10	10	12.22	4.729	0.9621
5	10	10	6.602	7.799	0.9638
8	10	10	3.96	11.232	0.9728
5	5	10	4.73	5.86	0.9918
5	10	10	6.11	8.425	0.9638
5	15	10	7.21	10.77	0.9827
5	10	5	8.45	11.302	0.9516
5	10	10	6.20	8.326	0.9631
5	10	15	4.77	8.335	0.95233

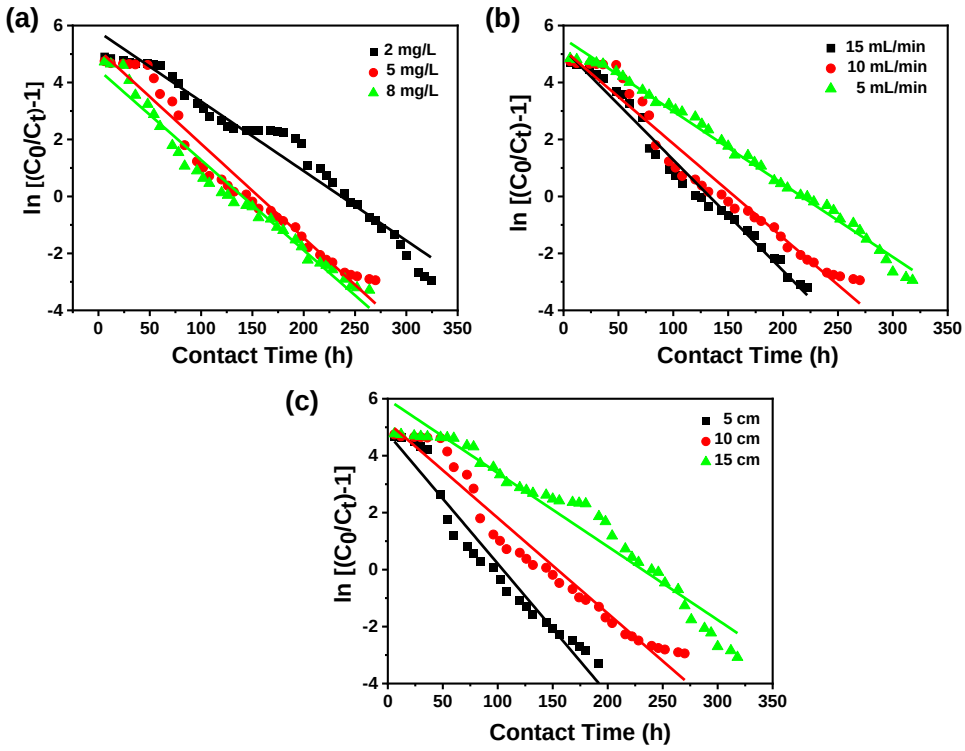

Figure 2B.17: Linear regression analysis of breakthrough curves using Thomas model at different (a) concentrations, (b) flow rates and (c) bed heights.

Yoon-Nelson model

A simple model was established by Yoon and Nelson for analysing breakthrough performance of the column. Yoon and Nelson model refers that decrease rate of adsorption probability for each adsorbate molecule is proportional to the adsorbate adsorption probability and adsorbate breakthrough probability. It is a simple model because it does not require any detail data regarding characteristics of adsorbate, type of adsorbent or physical properties of adsorption bed. The mathematical expression of this model is given as follows:

$$ln\left(\frac{C_t}{C_0-C_t}\right) = K_{YN}t - K_{YN}\tau \qquad (2B.8)$$

where, K_{YN} represents Yoon-Nelson rate constant, τ corresponds to time required for 50% breakthrough, C_t(mg/L) and C_0 (mg/L) are effluent and initial fluoride concentrations, respectively and t (h) is the flow time. By plotting $ln\left(\frac{C_0}{C_t}-1\right)$ vs time t, line fitting curves are obtained. The values of of K_{YN} and τ can be obtained from the slope and intercept of the linearized plot, respectively. Fig. 2B.18 shows linear regression analysis of breakthrough curves using Yoon-Nelson model at different (a) concentrations, (b) flow rates and (c) bed heights. Table 2B.8 summarizes the calculated parameters obtained from linear regression analysis of Yoon-Nelson model. Yoon-Nelson rate constant K_{YN} increases with increasing flow rate and initial fluoride concentration while it decreases with increasing bed height. It is to be noted that the values of K_{YN} were found to decrease with increasing τ values upon increasing bed height which indicates that the adsorbate breakthrough was taking longer duration with increasing bed height. Meanwhile K_{YN} was found to increase with increasing flow rate and initial fluoride concentration while their corresponding τ value shows a decreasing trend.

Table 2B.8: Yoon-Nelson Model Parameters.

C_0 (mg/L)	Q(ml/min)	Z(cm)	$K_{YN} \times 10^{-3}$ (hr^{-1})	τ(hr)	R^2
2	10	10	24.43	236.54	0.9622
5	10	10	33.01	156	0.9638
8	10	10	31.77	140	0.9732
5	5	10	25.71	216.24	0.9961
5	10	10	33.01	155.99	0.9638
5	15	10	38.95	132.95	0.9827
5	10	5	45.66	104	0.9513
5	10	10	33.48	154.21	0.9631
5	10	15	25.79	231.51	0.9523

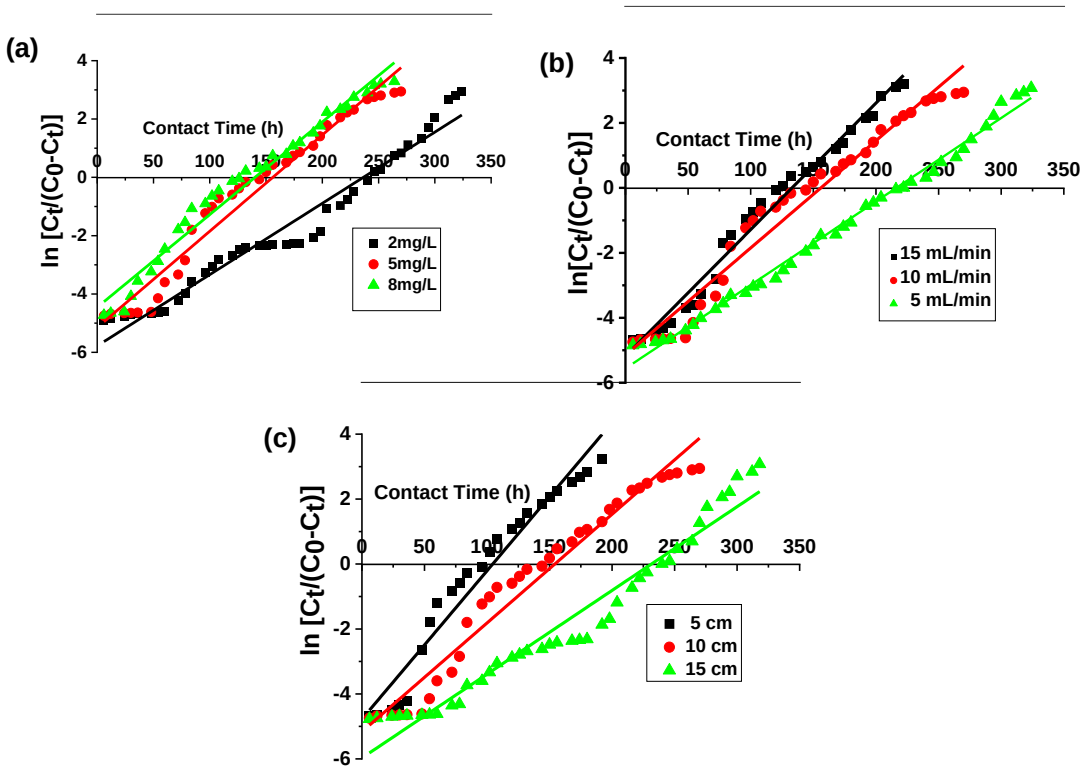

Figure 2B.18: Linear regression analysis of breakthrough curves using Yoon-Nelson model at different (a) concentrations, (b) flow rates and (c) bed heights.

Bed depth service time (BDST) Model

The BDST model holds a simple relation between bed depth and service time. This model helps anticipate the sustainability of the removal capacity of certain amount of adsorbent material before the revival is required. The assumptions of this model are that the adsorption rate is proportional to the residual capacity of adsorbent as well as the concentration of the adsorbing solute. BDST model neglects both the external and internal mass transfer resistance. A linear relationship between bed height (Z) and service time (t)was proposed by Hutchins[38] which is as follows:

$$t = \frac{N_0 Z}{C_0 V} - \frac{1}{K_a C_0} ln\left[\frac{C_0}{C_t} - 1\right] \qquad (2B.9)$$

Where K_a (L/mg hr) is the rate constant, N_0 (mg/L) is the sorption capacity, C_0 is the initial fluoride concentration (mg/L), C_b is the effluent concentration (mg/L) and V (cm/h) corresponds to the linear velocity. The service time was selected as the time when $\frac{C_t}{C_0}$ attains the value 0.05. By plotting service time (t) *vs* bed depth (Z) at flow rate 19 mL/min, the values of N_0 and K_a can be calculated from the slope and the intercept of the plot, respectively (Fig. 2B.19). The linear plot with regression co-efficient (R^2) 0.9974 indicates the validity of the BDST model with this column experiment. The BDST model parameters are shown in Table 2B.9. The adsorption capacity (N_0) and rate constant (K_a) were calculated as 2933.55 mg/L and 0.0430 L/mg.h, respectively. The rate constant signifies the transfer rate from fluid to solid phases. For avoidance of breakthrough short bed height is required for high K_a, and for low K_a value bed depth should be high.

Among various kinetic models for column study, the better correlation with experimental data (R^2) ranging from 0.95 to 0.99 is fitted for Thomas, Yoon-Nelson and BDST models. Thomas model with no external and internal dispersion limits is dependent on Langmuir adsorption-desorption energy following second-order reversible reaction kinetics. Yoon-Nelson model is based on the assumption that adsorption rate is proportional to the rate of decrease in adsorption. BDST model signifies that rate of adsorption is maintained by surface reaction between adsorbate and unused capacity of adsorbent.

Table 2B.9: BDST Model Parameters.

C_0 (mg/L)	Q (ml/min)	Z (cm)	N_0 (mg/L)	K_a(L/mg hr)	R^2
5	10	5	2933.55	0.0430	0.9974
5	10	10			
5	10	15			

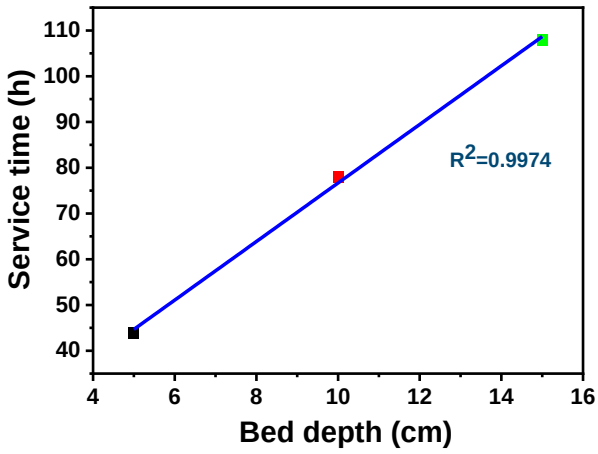

Figure 2B.19: Linear Plot of BDST for fluoride adsorption.

2B.3.2.2 Desorption and regeneration study

After exhaustion point is reached in fixed bed column experiment, the adsorbent alumina gel @ zeolite X nanocomposite is regenerated by desorption of the adsorbed fluoride ions. Fig. 2b.20 shows the desorption-regeneration cycle for fluoride removal. It was observed that % removal of fluoride ions decrease as 99, 90, 78 and 69% for 1st, 2nd, 3rd and 4th cycle, respectively. The adsorption capacity of regenerated adsorbent was decreasing in each cycle which is attributed to the fact that some quantity of fluoride ions got trapped into the pores of the adsorbent which was difficult to remove during desorption process, deactivating for adsorption of fluoride ions to some extent.

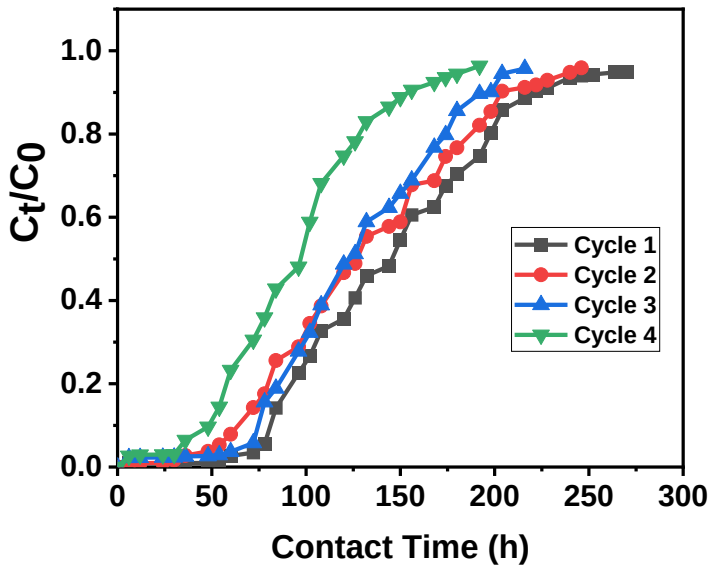

Figure 2B.20: Desorption-regeneration cycle for fluoride removal.

2B.4 Conclusion

Alumina gel@ zeolite X nanocomposite was prepared by sol-gel process using alumina sol and hydrothermally synthesized zeolite X particles. Microstructural study confirms that alumina gel particles (50-100 nm) are aggregated surrounding the micron sized (0.5-1 μm) zeolite X particles. The synthesized material was utilized for the adsorption of F^- ions *via* batch and column studies. In a batch study, % adsorption increases with contact time, adsorbent doses and temperature while it decreases with initial F^- ion concentrations. pH has a minimal effect for adsorbent dose of 1-2 gm/L. Langmuir isotherm shows the best fitting for the adsorption of F^-rendering a maximum adsorption of 104.16 mg/gm. The adsorption process is endothermic with negative value of ΔG^0 indicating spontaneity of the process. In column study, Thomas model fitted well with the experimental data and breakthrough curve prediction, demonstrating that internal and external diffusions are not the rate limiting step. The adsorption capacity, q_0 (mg/gm) increased with increasing initial fluoride concentration and flow rate; however, it decreased with bed height. The present work is significant for the development of nanocomposite based materials toward the removal of different contaminants from water.

References

1 P. Loganathan, S. Vigneswaran, J. Kandasamy and R. Naidu, *J Hazard Mater.*, 2013, **248**, 1–19.

2 E. Tchomgui-Kamga, V. Alonzo, C. P. Nanseu-Njiki, N. Audebrand, E. Ngameni and A. Darchen, *Carbon N. Y.*, 2010, **48**, 333–343.

3 L. F. de Magalhães, G. R. da Silva, A. E. C. Peres and M. R. R. Kooh, *Adsorpt. Sci. Technol.*, 2022, **20**, 4544104.

4 G. K. R. Angaru, L. P. Lingamdinne, Y.-L. Choi, J. R. Koduru, J.-K. Yang and Y.-Y. Chang, *Mater. Today Chem.*, 2021, **22**, 100577.

5 G. K. R. Angaru, Y.-L. Choi, L. P. Lingamdinne, J. R. Koduru, J.-K. Yang, Y.-Y. Chang and R. R. Karri, *Sci Rep.*, 2022, **12**, 3430.

6 P. Ghomashi, A. Charkhi, M. Kazemeini and T. Yousefi, *J. Water Environ. Nanotechnol.*, 2020, **5**, 270–282.

7 M. K. Naskar, *J. Asian Ceram. Soc.*, 2020, **8**, 437–447.

8 R. N. Tabi, F. O. Agyemang, K. Mensah-Darkwa, E. K. Arthur, E. Gikunoo and F. Momade, *Mater. Chem. Phys.*, 2021, **261**, 124229.

9 B. Yang, G. Sun, B. Quan, J. Tang, C. Zhang, C. Jia, Y. Tang, X. Wang, M. Zhao and W. Wang, *Water (Basel)*, 2021, **13**, 3343.

10 Y. D. Wirtu, F. Melak, M. Yitbarek and H. Astatkie, *Groundw Sustain Dev.*, 2021, **12**, 100525.

11 A. Kumar and M. K. Naskar, *J. Asian Ceram. Soc.*, 2019, **7**, 355–360.

12 B. Yan, S. Liu, M. L. Chastain, S. Yang and J. Chen, *Sci Rep.*, 2021, **11**, 3316.

13 K. Byrappa and B. V. S. Kumar, *Asian J. Chem.*, 2007, **19**, 4933.

14 J. Abenojar, I. Colera, M. A. Martínez and F. Velasco, *J. Adhes Sci. Technol.*, 2010, **24**, 1841–1854.

15 M. Roy, S. Basak and M. K. Naskar, *Phys. Chem. Chem. Phys.*, 2016, **18**, 5253–5263.

16 A. Teimouri, S. G. Nasab, S. Habibollahi, M. Fazel-Najafabadi and A. N. Chermahini, *RSC Adv.*, 2015, **5**, 6771–6781.

17 N. Thakur, S. A. Kumar, D. N. Wagh, S. Das, A. K. Pandey, S. D. Kumar and A. V. R. Reddy, *J. Hazard Mater.*, 2012, **201**, 193–201.

18 C. Y. Hu, S. L. Lo and W. H. Kuan, *Water Res.*, 2003, **37**, 4513–4523.

19 M. S. Onyango, Y. Kojima, O. Aoyi, E. C. Bernardo and H. Matsuda, *J. Colloid Interface Sci.*, 2004, **279**, 341–350.

20 P. Pillai, S. Dharaskar and M. Khalid, *Chemosphere*, 2021, **284**, 131317.

21 Y. Zhang, D. Wang, B. Liu, X. Gao, W. Xu, P. Liang and Y. Xu, .

22 P. Chinnakoti, A. L. A. Chunduri, R. K. Vankayala, S. Patnaik and V. Kamisetti, *Appl Water Sci.*, 2017, **7**, 2413–2423.

23 N. Chen, Z. Zhang, C. Feng, M. Li, D. Zhu, R. Chen and N. Sugiura, *J. Hazard Mater.*, 2010, **183**, 460–465.

24 E. Tchomgui-Kamga, V. Alonzo, C. P. Nanseu-Njiki, N. Audebrand, E. Ngameni and A. Darchen, *Carbon N. Y.*, 2010, **48**, 333–343.

25 S. K. Swain, R. K. Dey, M. Islam, R. K. Patel, U. Jha, T. Patnaik and C. Airoldi, *Sep Sci Technol.*, 2009, **44**, 2096–2116.

26 Y. D. Wirtu, F. Melak, M. Yitbarek and H. Astatkie, *Groundw Sustain Dev.*, 2021, **12**, 100525.

27 K. Narasimharao, L. P. Lingamdinne, S. Al-Thabaiti, M. Mokhtar, A. Alsheshri, S. Y. Alfaifi, Y.-Y. Chang and J. R. Koduru, *J. Water Process. Eng.*, 2022, **47**, 102746.

28 P. Senthil Kumar, P. S. A. Fernando, R. T. Ahmed, R. Srinath, M. Priyadharshini, A. M. Vignesh and A. Thanjiappan, *Chem. Eng. Commun.*, 2014, **201**, 1526–1547.

29 A. Rahmani-Sani, A. Hosseini-Bandegharaei, S.-H. Hosseini, K. Kharghani, H. Zarei and A. Rastegar, *J. Hazard Mater.*, 2015, **286**, 152–163.

30 A. Saravanan, S. Jeevanantham, P. S. Kumar, S. Varjani, P. R. Yaashikaa and S. Karishma, *Ind. Crops Prod.*, 2020, **153**, 112613.

31 J. He, X. Cai, K. Chen, Y. Li, K. Zhang, Z. Jin, F. Meng, N. Liu, X. Wang and L. Kong, *J. Colloid Interface. Sci.*, 2016, **484**, 162–172.

32 J. S. Noh and J. A. Schwarz, *J. Colloid Interface. Sci.*, 1989, **130**, 157–164.

33 P. G. Hiremath and T. Theodore, *Period. Polytech. Chem. Eng.*, 2017, **61**, 188–199.

34 S. Kudari, *Int J.. Adv Res Publicat.*, 2017, **1**, 174–178.

35 G. S. Bohart and E. Q. Adams, *J. Am. Chem. Soc.*, 1920, **42**, 523–544.

36 H. C. Thomas, *J. Am. Chem. Soc.*, 1944, **66**, 1664–1666.

37 Y. H. Yoon and J. H. Nelson, *Am. Ind Hyg. Assoc J.*, 1984, **45**, 509–516.

38 R. A. Hutchins, *J. Chem. Eng.*, 1973, **80**, 133–138.

39 M. Jaroniec, *Surf. Sci.*, 1975, **50**, 553–564.

40 S. Mukherjee, A. A. Khan, S. Barman and G. Halder, *Environ. Prog. Sustain. Energy.*, 2020, **39**, e13465.

41 A. A. Ahmad and B. H. Hameed, *J. Hazard Mater.*, 2010, **175**, 298–303.

42 C. Murutu, M. S. Onyango, A. Ochieng and F. A. O. Otieno, *Water SA.*, 2012, **38**, 279–286.

Chapter 3

Red mud derived iron oxide nano-flakes for de-arsenification of water

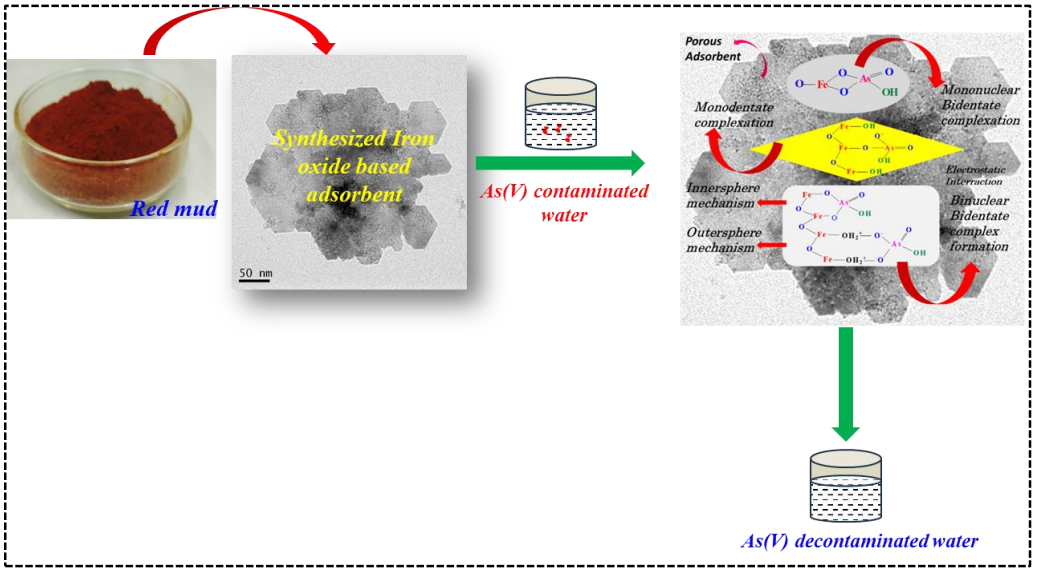

Publication from this Chapter:

Adwitiya Chakraborty, Prashanta Kumar Sinha and Milan Kanti Naskar, "Low temperature synthesis of iron oxide nanoflakes for favorable dearsenification of water", ***ACS Omega,* 2023, 8,32,29281-29291.**

3.1 Introduction

Arsenic contamination in groundwater is a serious concern for the living beings. As a silent killer, arsenic (As) causes various complications in human organ system like skin cancer, pigmentation, Blackfoot disease. cardiovascular disease, lungs, urinary bladder, kidney related ailments etc.[1–3] The most commonly arsenic in natural water is in the form of oxyanions as arsenite (AsO_3^{3-}) and arsenate (AsO_4^{3-}) depending on redox conditions with pH, the former is more toxic than the latter.[4] However, the arsenate species (As(V)) mostly exists in surface water because of its thermodynamic stable form.[5] Arsenic removal from ground water has been accomplished using a variety of techniques, including oxidation and sedimentation,[6] co-precipitation,[7] membrane separation,[8] coagulation and filtering,[9] ion exchange, reverse osmosis, electrolysis, adsorption, and many others.[10–14] Adsorption technology has shown promise for the removal of arsenic from water because to its simple design, ease of operation, high efficiency, greater regeneration ability, and wide applicability in small scale treatment plants.[15] Chutia *et al.* showed the adsorption capacity of zeolites of type H-MFI-24 (H24) and H-MFI-90 (H90) as 35.8 and 34.8 mg/gm for the removal of arsenic starting with arsenic concentration of 10 mg/L at pH 6.5 using sample dose of 2 gm/L .[16] The maximum adsorption capacity of the MOF-based adsorbent material used in numerous studies on the adsorption of arsenic was found to be 90.92 mg/gm which could be attributed to mesoporous structure facilitating mass transfer within the pores during adsorption process.[17] Yao *et al.* showed the adsorption capacity of iron oxide/activated carbon magnetic composite as 17.86 mg/gm with initial As concentration of 10 mg/L at pH 6 for 60 min contact time using sample dose of 5 gm/L.[18] Arsenic and other hazardous ions were also shown to be very effectively removed by polymer-based composite.[19] Layered double hydroxides,[20–22] hierarchical porous ZIF-8[23] and iron based materials[24–26] are found to be commonly used for As(V). Pintor *et al.* showed adsorption capacity of iron coated cork granulates as 4.3 and 4.9 mg/gm for the removal of As(V) and As(III), respectively with their initial concentration of 25 mg/L at 20 ^{o}C for 24 h contact time using 2.5 gm/L of sample dose.[24] Iron based layered double hydroxides exhibited efficient arsenic adsorption due to their synergistic effect of interlayered structure and the presence of iron containing metal-oxygen bonds facilitating electrostatic interactions with arsenite/arsenate oxyanions[27–30]

Arsenic removal from contaminated water using low cost adsorbents is highly demanding particularly in rural area community having low income. Babazad *et al* used carbonized rice husk for the removal of lead and arsenic from aqueous solution.[31] Nguyen *et*

al reported arsenic removal from ground water using laterite.[32] Red mud (RM) is a waste product in aluminium industry. RM contains mainly iron and aluminium oxide/hydroxides with a small amount of silica, TiO_2, Na_2O and CaO.[33,34] The oxides/hydroxides of iron, aluminium and titanium are effective for the adsorption of As(V). It is worth noting that raw red mud has lower arsenic adsorption capacity compared to modified RM or synthesized iron oxides/hydroxides as adsorbents. Numerous researchers have reported using modified red mud to successfully remove arsenic from an aqueous solution.[35–40] Recently, Yu *et al.* reported arsenic removal from aqueous solution using porous red mud beads.[41]

In the present work, iron constituent from RM was extracted by acid leaching followed by hydrothermal reaction in the presence of aqueous ammonia. Synthesis of iron oxide with high surface area from RM by a simple hydrothermal process without further heat treatment is rarely reported to the best of our knowledge. In this study, it is demonstrated that how the reaction time affects the crystallinity and surface properties of the material toward adsorption efficiency of arsenic. The synthesized product was used for the removal of As(V) from aqueous solution. Kinetic studies were performed for the adsorption of arsenic by changing different parameters like concentration of adsorbates and adsorbents, time, pH and temperature.

3.2 Experimental

3.2.1 Materials

The industrial waste red mud was collected from Utkal Aluminium International Ltd., Odisha, India. Hydrochloric acid (HCl) (37 wt.%), ammonia (NH_3) (25%) and standard arsenic acid (H_3AsO_4, 1000 mg/L) were purchased from Merck, India whereas sodium arsenate heptahydrate ($Na_2HAsO_4.7H_2O$, 98-102.0 %) was collected from Loba Chemie Pvt. Ltd.

Preparation of iron oxide from red mud

Fig. 3.1 shows schematically for the preparation of iron oxide extracted from RM. For the extraction of Fe(III) from RM, 40 gm of crushed RM powder was leached with 400 mL 6M HCl under reflux condition at 90 ^oC for 3 h. The leachate was separated out by centrifugation and the concentration of Fe(III) was found to be 1M. For the preparation of iron oxide based adsorbent, 10 mL of RM extract was taken in a beaker followed by dropwise addition of NH_4OH under stirring to raise the pH 8-9. A brown solid mass was obtained which was diluted to 70 mL by adding Millipore water under stirring condition. After 30 min of stirring, the whole dispersion was transferred into a Teflon-lined hydrothermal autoclave and was kept at 150 ^oC

for 6-24 h. The brown coloured products were collected by centrifugation and repeated washing with Millipore water followed by drying at 60 ^{o}C for 6 h. The samples are designated as FENH-6, FENH-12 and FENH-24 for hydrothermal treatment of 6 h, 12 h and 24 h, respectively at 150 ^{o}C.

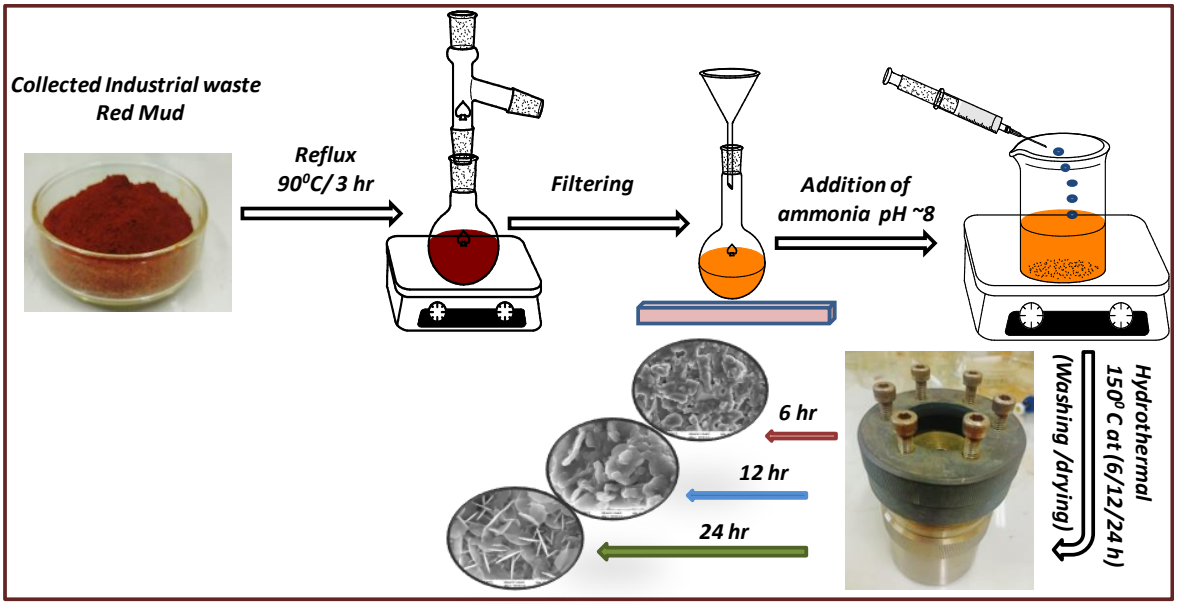

Figure 3.1: Schematic diagram for the preparation of iron oxide extracted from red mud.

3.2.2 Characterization

The synthesized materials were characterized by Fourier transform infrared (FTIR) spectroscopy(Spectrum two, PerkinElmer), Raman spectroscopy(Horiba T6400 spectrometer with 532 nm laser),X-ray diffraction (XRD) (PhilipsX'Pert Pro PW 3050/60, using Ni-filtered Cu-K_{α} radiation, λ= 0.15418 nm), X-ray photoelectron spectroscopy (XPS)(PHI 5000 Versa Probe II, ULVAC-PHI with AlK_{α} radiation), X-ray fluorescence (XRF) (PANalytical, Axios, Almelo, Netherland), FESEM (Model: Zeiss, Supra 35VP, Oberkochen, Germany),N_2 adsorption-desorption study (Quantachrome (ASIQ MP) where the specific surface area was measured by BET (Brumauer-Emmett-Teller) method and pore size distributions were calculated from BJH (Barrett-Joyner-Halenda) method. The microstructural analysis of the samples was performed by Field emission scanning electron microscopy (FE-SEM) (Model: Zeiss, Supra 35VP, Oberkochen, Germany) and transmission electron microscopy (TEM) (Tecnai G2 30ST (FEI).

3.2.3 Arsenic adsorption experiment

Adsorption kinetics study of arsenic from aqueous solution was performed by varying different parameters like contact time, initial arsenic concentration, sample dose, temperature, pH and competing ions effect. Sample dose (adsorbent) was varied from 0.1 to 1 gm/L with initial arsenic concentration of 5 mg/L. For variation of time (5-180 min), pH (1.5-11.5), temperature (303-343 K) effect, sample dose was fixed at 0.25 gm/L with initial arsenic concentration of 2 mg/L and for competing ions (chloride, nitrate, sulphate and phosphate) the initial concentration of each component was fixed around 5mg/L with sample dose 1gm/L. For adsorption isotherm study, initial As(V) concentration was varied from 2 to 20 mg/L with sample dose of 0.50 gm/L at equilibrium time of 180 min, temperature (303 K) and pH (6.5). The As(V) concentration after adsorption was determined by Inductively Coupled Plasma Atomic Emission Spectrometer (ICP-AES), ARCOS 130 MV, Spectro Analytical Instruments GmbH, Kleve, Germany and Inductively Coupled Plasma Mass Spectrometer (ICP-MS), NexION 300X, PerkinElmer, USA.

The equilibrium adsorption capacity, q_e (mg/gm) was determined from the following equation:

$$q_{e=}(C_0 - C_e)\left({}^{V}/_{m}\right) \qquad (3.1)$$

Where,C_0 and C_e are the initial and final concentration of arsenic (mg/L), respectively, while V and m represent the solution volume in litre and mass in gram of the sample, respectively.

Noh and Schwarz method[42] was adopted for determination of point of zero charge (pH_{pzc}). In this method, different sample quantities (5 mg to 2 gm) were taken in 10 mL 1 mM NaCl each under stirring for 24 h followed by their pH measurement. A plot of pH vs. sample mass was drawn in which pH approached to an asymptotic value by which the pH_{pzc} of the sample was determined.

For the regeneration of the adsorbent the exhausted adsorbent material was digested with 0.1 M NaOH for 24 hours followed by repeated washing with Millipore water and drying. Thereafter for the recyclability test, 1 gm/L of regenerated sample dose was stirred with 2 mg/L arsenic containing aqueous solution (20 mL) for 120 min at pH 6.5, which were performed with total of five adsorption-desorption cycles.

3.3 Results and Discussion

3.3.1 Characterization of α-Fe_2O_3

Fig. 3.2(a) shows the XRD patterns of the sample obtained from hydrothermal treatment of red mud extract at 150 ^oC for 6-24 h. It confirms the crystalline phase of α-Fe_2O_3 with 2Θ values of 24.27, 33.22, 35.77, 41.09, 49.74, 54.36, 57.91, 62.82 and 64.49 corresponding to hkl values of (012), (104), (110), (113), (024), (116), (018), (214) and (300), respectively (JCPDS File No. 86-0550). It is noticed that with increasing the reaction time, crystallinity of α-Fe_2O_3 phase becomes higher. To ascertain the presence of other impurities in the prepared sample, XRF analysis was conducted. Table 3.1 showed that iron oxide and alumina contents were 81.40% and 14.30%, respectively in the presence of trace amount of other impurities.

FTIR study of the prepared samples obtained at 150 ^oC for 6-24 h is shown in Fig. 3.2(b). The appearance of vibration bands at 472 and 576 cm^{-1} are the signature of stretching vibration of Fe-O bond.[43,44] A broad band at 1099 cm^{-1} indicates the stretching vibration of Fe-OH-Fe.[45] The absorption peaks at 1405 and 1635 cm^{-1} are ascribed to O-H bending vibration while the absorption band at 3445 cm^{-1} is due to O-H stretching vibration of absorbed water molecules in the sample. However, in the instance of the sample FENH24, a shoulder peak is noticed at 3144 cm^{-1}.[46] This peak indicates that the hydrogen-bonded OH is in its stretching vibrational state. It is interesting to note that as reaction time increases, polymeric association takes place, and hydrogen bonding plays a significant part in this process which facilitates in the formation of nanoflake structure.[47]

Fig. 3.2(c) shows Raman spectra of the products obtained at 150 ^oC for 6-24h. The appearance of vibration band at 222 cm^{-1} corresponds to symmetric stretching vibration of Fe-O in A_{1g} phonon mode. The bands at 288, 405 and 609 $cm^{-1}$are assigned to E_g phonon mode of vibration which are the signature of α-Fe_2O_3. It is reported that hematite (α-Fe_2O_3) belonging to R3c space group generally exhibits seven phonon lines comprising two A_{1g} and five E_g phonon modes.[48,49] However, in the present study, four phonon mode of vibrations i.e. one A_{1g} and three E_g was obtained.

Table 3.1: XRF Analysis of Sample FENH2.

Composition	Wt (%)
Na_2O	0.070
Al_2O_3	14.299
MgO	0.106
SiO_2	0.419
P_2O_5	0.103
SO_3	0.117
CaO	0.866
TiO_2	1.301
Fe_2O_3	81.396
Cl	1.323

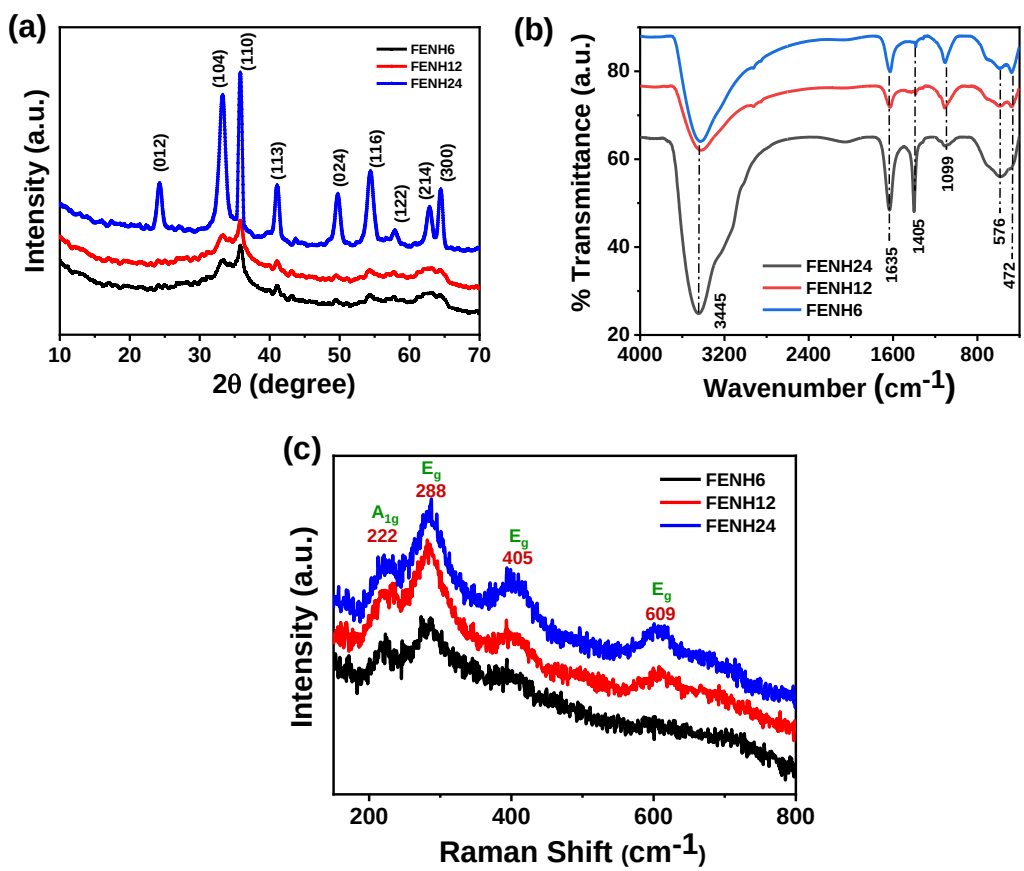

Figure 3.2: (a) XRD pattern, (b) FTIR and (c) Raman spectra of α-Fe_2O_3.

Fig. 3.3(a) shows the BET isotherm of hydrothermally treated sample at 150 ºC for 6, 12 and 24 h reaction time. It is noticed that surface area values are maximum of 347 and 331 m^2/gm, for 6 and 12 h treated samples, respectively followed by sudden decrease to 136 m^2/gm for 24 h treated sample. The BET curve shows a drastic decrease in surface area for the sample FENH24 which could be understood by high crystallite growth and crystallinity at 24 h reaction time. For 6-12 h reaction time, crystallization occurs slowly reflecting lower intensity of α-Fe_2O_3 peaks in XRD pattern. In kinetically controlled systems, amorphous to crystalline phase transitions are frequent.[50] These transitions involve an initial fast-growing amorphous phase and a slow crystallisation, resulting in a gradual trend in increasing crystallite size, which was found to be 2.1, 4.2 and 16.4 nm for FeNH6, FENH12, and FENH24, respectively. Therefore, a rapid increase in crystallite size from 4.2 to 16.4 nm for FENH12 and FENH24, respectively lead to reduced surface area of the latter. The BET isotherms show type IV as per IUPAC classification which is the signature of mesoporous characteristics. However, the nature of hysteresis loops of the isotherm in 6-12 h samples is H2 type signifying ink-bottle like mesopores while that of 24 h treated sample is H3 type indicating slit-like pores.[51] Interestingly, the total pore volume of the three samples heat treated at 6, 12 and 24 h are comparable at around 0.33-0.36 cm^3/gm, whereas the average pore diameter calculated from BJH desorption plot (Fig. 3.3(b)) is found in the range of 3.5-3.7 nm. It is worth noting that surface properties particularly, the surface area has a significant role toward the adsorption of water contaminants from aqueous solution.

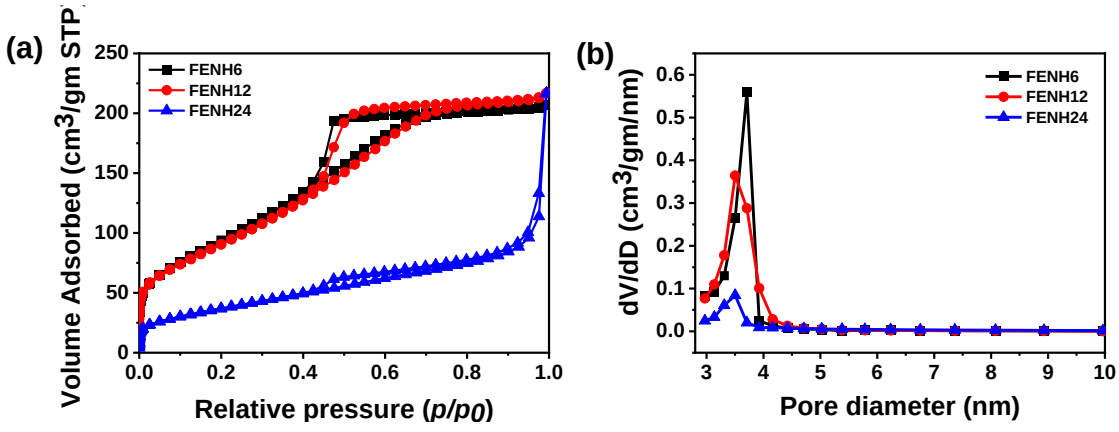

Figure 3.3: (a) BET isotherm, (b) BJH pore size distribution of α-Fe_2O_3.

To investigate the surface chemical analysis, XPS study was performed. Figs. 3.4 show XPS spectra of Fe2p and O1s, respectively for as synthesized (a)FENH6 (b) FENH12 and (c)

FENH24. The appearance of peaks at around 710.6 eV and 724 eV could be attributed to the spin orbit doublets of $Fe2p_{3/2}$ and $Fe2p_{1/2}$, respectively[52] confirming the existence of the Fe(III) state. The corresponding shake-up satellite peaks for $Fe2p_{3/2}$ and $Fe2p_{1/2}$ were found to be 719 and 729 eV, respectively. The peak at 709.2 eV with satellite peak at around 715 eV confirms the existence of Fe(II) in case of FENH6 and FENH12 samples attributing to the coexistence of Fe(II)-Fe(III) prior to the formation of stable α-Fe_2O_3. However, no primary peak for Fe(II) $2p_{3/2}$ was noticed in case of FENH24. It is demonstrated that the crystal structure of α-Fe_2O_3 contains Fe(II) sites, which could be originated *via* electron hopping.[53,54] The deconvoluted peaks of O1s spectra are shown at 530.6, 531.2 and 532 eV(Fig. 3.4(d)-(f)) signifying the lattice oxygen in Fe-O, surface oxygen defects and oxygen in adsorbed hydroxyl groups, respectively[55,56] with their percentage abundance of 25.7%, 36%and 38.3% for FENH24 sample. The lattice oxygen, surface oxygen defects and oxygen in adsorbed hydroxyl groups for FENH6 are 46.77%, 25.05% and 28.17%, respectively whereas those for FENH12 samples are found to be 48.08%, 32.45% and 34.9%, respectively. It is worth mentioning that surface oxygen defects and oxygen in adsorbed hydroxyl groups are in increasing trend as FENH6<FENH12<FENH24. It could affect their adsorption efficiency for As(V). However, the surface area values of the samples follow as: FENH6>FENH12>FENH24 which demonstrate a pronounced effect on adsorption efficiency superseding the effects of surface oxygen defects and oxygen in adsorbed hydroxyl groups.

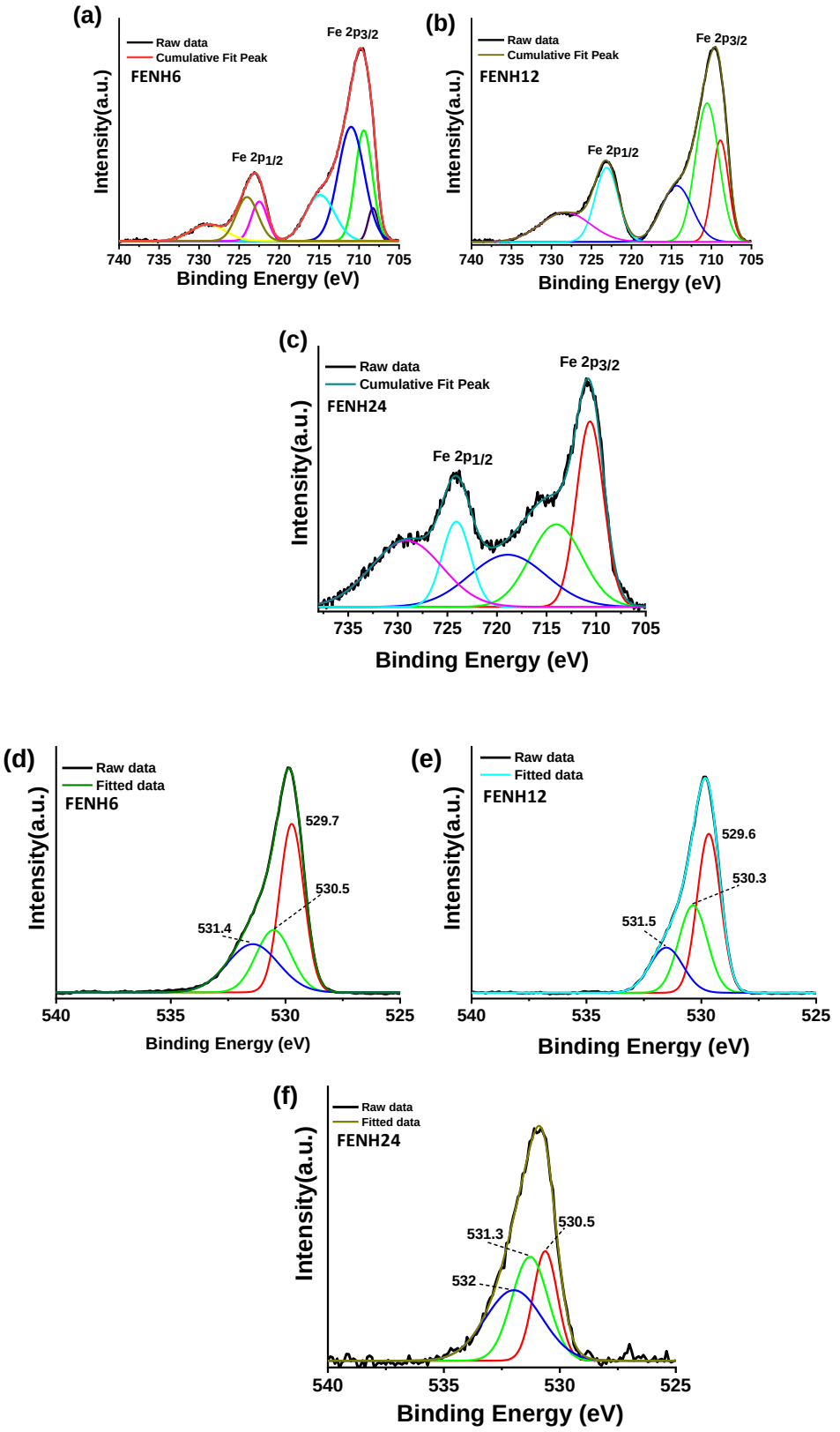

Figure 3.4: XPS spectra of α-Fe_2O_3:(a)-(c) Fe2p and (d)-(f) O1s.

Morphology of the synthesized products was examined by FESEM and TEM. Fig. 3.5(a)-(c) shows the FESEM microstructures obtained at 150 ^{o}C for different reaction times of 6, 12 and 24 h, respectively. It is noticed that for lower reaction time (6 h), highly agglomerated particles are obtained. However, with increase in reaction time of 12 h, nanoflake-like particles start growing. A complete nanoflake-like assembly with petal-like structure of α-Fe_2O_3 was obtained for 24 h reaction time. During hydrothermal reaction at 150 ^{o}C, dissolution of the agglomerated particles takes place rendering high entropy of the system. With increasing reaction time, the nascent nuclei start growing in a certain crystallographic orientation generating flake-like structure minimizing entropy of the system. TEM image of the sample is shown in Fig. 4(d)-(f) for 6, 12 and 24 h reaction time, respectively. It reveals nanopores in the samples. Interestingly, with a close observation of TEM microstructures it is revealed that very tiny α-Fe_2O_3 particles of size in the range of 2-5 nm assembled in a petal-shaped particles, particularly for 24 h reaction time. The HRTEM images of α-Fe_2O_3particles are shown in Fig. 3.5 (g)-(i) for three different reaction times of 6, 12 and 24 h, respectively. It indicates the lattice fringes of (110) plane corresponding to the lattice spacing of 0.25 nm which corroborated to the high intensity peak of α-Fe_2O_3obtained from XRD pattern (Fig. 3.2(a)).

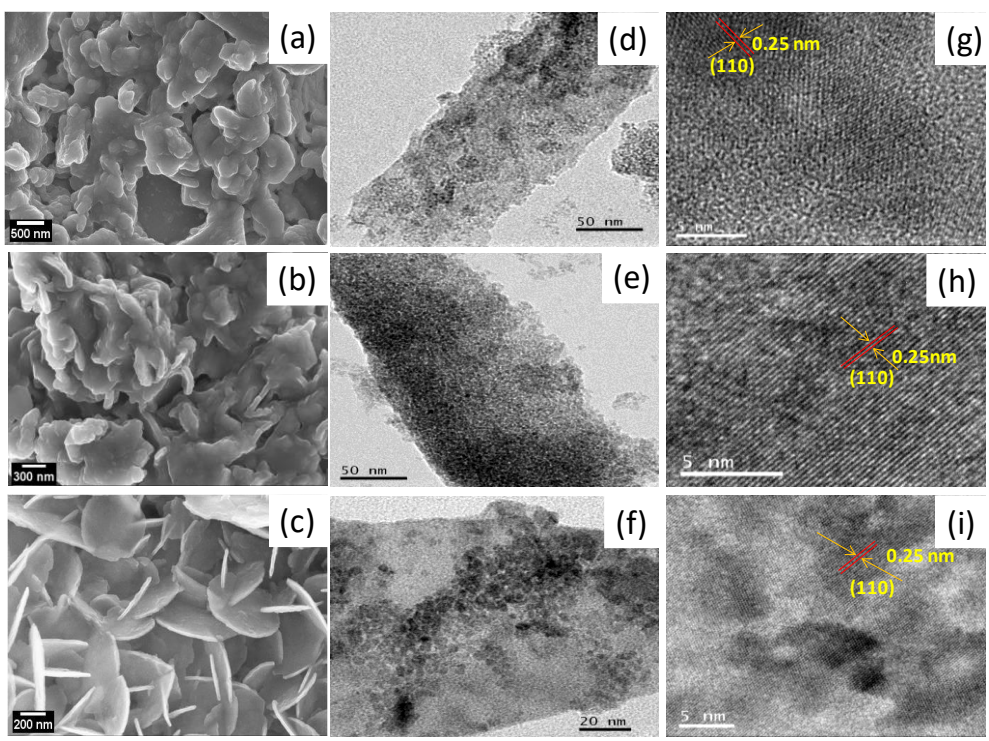

Figure 3.5: (a-c) FESEM images, (d-f) TEM images and (g-i) HRTEM images of α-Fe_2O_3 particles.

3.3.2 Arsenic adsorption study

Effect of contact time

The percentage adsorption of As(V) from aqueous solution with contact time is shown in Fig. 3.6(a) keeping the initial As(V) concentration of 2 mg/L (pH~6.8) with sample dose of 0.25 gm/L at 30 ^{o}C. It is noticed that the % adsorption of As(V) increased sharply up to 60 min of contact time reaching equilibrium at 120 min of adsorption with % adsorption of 99, 96.6 and 92%, for the samples FENH6, FENH12 and FENH 24 prepared at reaction time of 6 h, 12 h and 24 h, respectively. Adsorption capacity (q_t) with time of the samples is shown in Fig. 3.6(b), which reaches maximum values of 7.9, 7.7 and 7.4 (mg/gm) for FENH6, FENH12 and FENH24, respectively. It is demonstrated that arsenic level could be lowered down to 2-3 µg/L (<10 µg/L as per WHO's limit) with contaminated real water (64 µg/L) using 0.25 gm/L of sample dose within 5 min. of adsorption. Fig. 3.6(c) shows that the samples FENH6, FENH12 and FENH24 resulted 96, 95 and 94.4 % adsorption within a short time of adsorption (5 min), respectively.

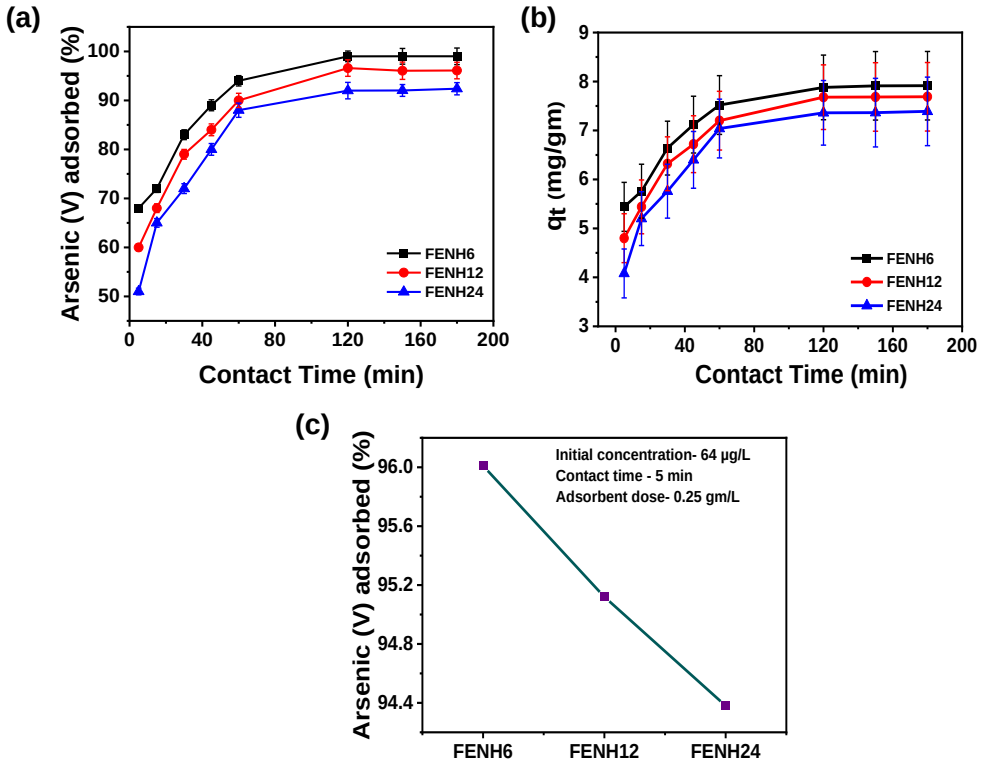

Figure 3.6: Effect of contact time on (a) % As(V) adsorption (b) Adsorption capacity on the adsorption of As(V) by α-Fe_2O_3 particles (c) % Adsorption of As(V) by α-Fe_2O_3 reaching below the WHO limit.

Effect of initial As(V) concentration

Fig. 3.7(a) shows that the % adsorption is in decreasing trend with increasing the As(V) concentration from 2 to 20 mg/L (pH~6.8 at 30 ^{o}C for 120 min contact time) using 0.50 gm/L of sample dosage. It is noteworthy that with increasing As(V) concentration, the adsorption sites are getting shielded with the accumulation of contaminated ions, and co-ordination sites are becoming saturated resulting lower adsorption.[57,58] The adsorption capacity (q_e) is in increasing trend with increasing initial arsenic concentrations (Fig 3.7(b)).

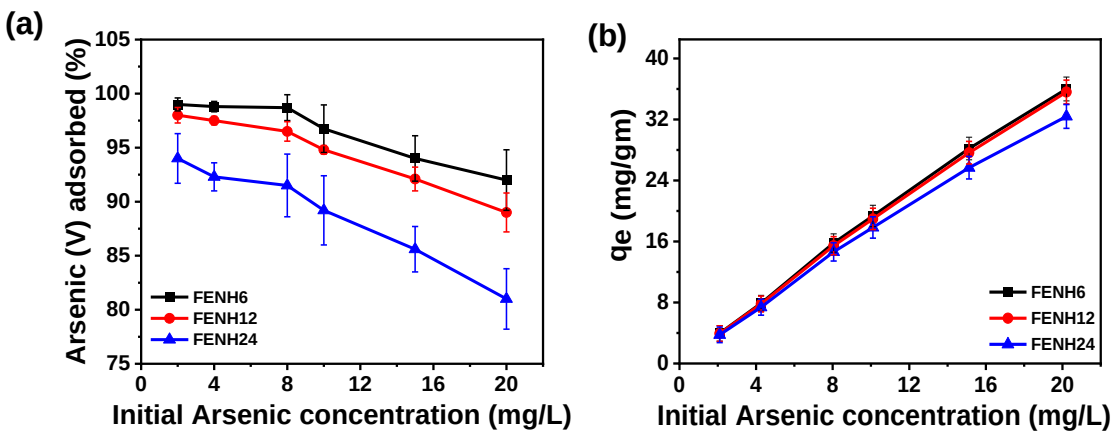

Figure 3.7: Effect of initial As(V) concentration on (a) % As(V) adsorption (b) Adsorption capacity on the adsorption of As(V) by α-Fe_2O_3 particles.

Effect of sample dose

Fig. 3.8(a) shows that with increase in sample dose, the % adsorption is sharply increased up to 0.4 gm/L of sample dosage followed by slow increase up to 1.0 gm/L of adsorbent using 5 mg/L of As(V) contaminated water. With increase in sample dose, there is abundance of adsorption sites which facilitates more amount of As(V) adsorption uptake. However, the adsorption capacity (q_e) decreased with increasing sample doses (Fig. 3.8(b)).

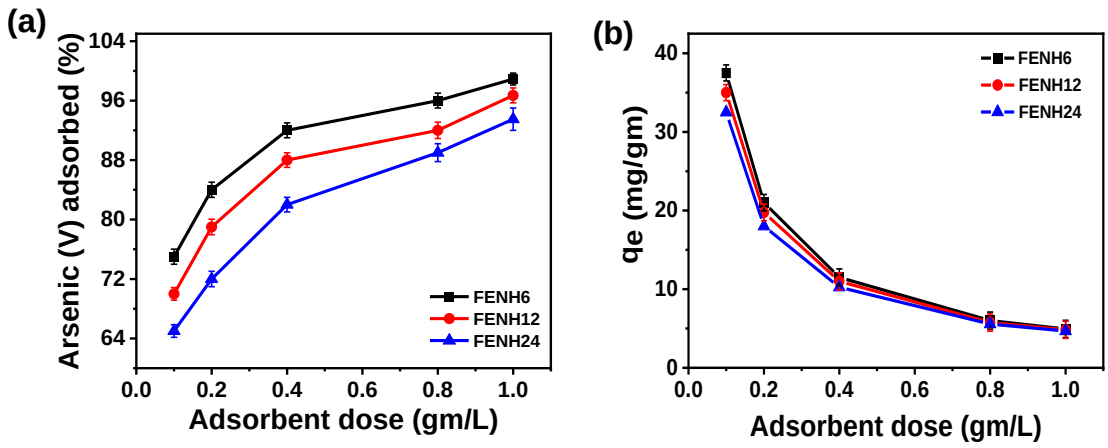

Figure 3.8: Effect of adsorbent dose on (a) % As(V) adsorption (b) Adsorption capacity on the adsorption of As(V) by α-Fe_2O_3 particles.

Effect of pH

The role of pH in aqueous solution is important for the adsorption of As(V) by the surface charged (positively charged H^+ ions and negatively charged OH^- ions) of adsorbent sample.[59] Fig. 3.9(a) shows that using 2 mg/L arsenic contaminated water with sample dose of 0.25 gm/L, the adsorption (%) of As(V) remains almost constant (>96%) up to pH 8.8 for all the samples FENH6, FENH12 and FENH24, respectively. However, it falls sharply in alkaline pH (9.9-11.7) and reaches to minimum values of 76, 72 and 67%, at pH 11.7 for the samples FENH6, FENH12 and FENH24, respectively. Interestingly, the adsorption capacity (q_e) of all the samples remains practically same of about 7.8 mg/gm within a wide range of pH (1.5-8.8) followed by its sharp decrease within the pH range of 9.9-11.7 (Fig. 3.9(b)). To understand the effect of pH on As(V) adsorption, the measurement of point of zero charge (pH_{PZC}) of the sample was done which was found to be around 9.9. It is clear that below pH_{PZC}, there is abundance of positively charged surface of the adsorbent which helps facilitate to interact with the negatively charged species of As(V) through electrostatic attraction rendering higher % adsorption and adsorption capacity. However, with increase in pH above pH_{PZC}($pH>pH_{PZC}$), the negatively charged surface repels the negatively charged adsorbate decreasing the adsorption efficiency of the samples.

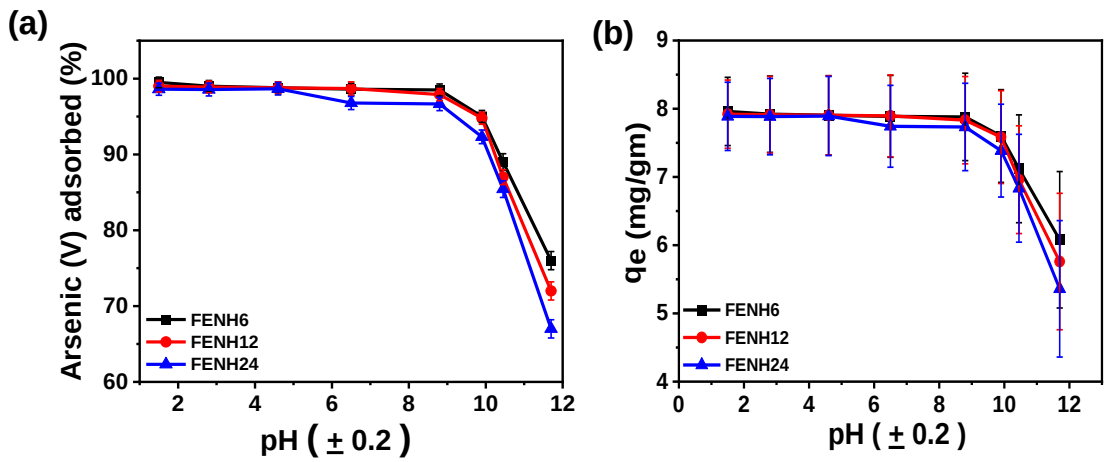

Figure 3.9: Effect of (a) pH on % As(V) adsorption (b) Adsorption capacity on the adsorption of As(V) by α-Fe_2O_3 particles.

Effect of Temperature

For temperature effect on As(V) adsorption, the initial As(V) concentration was kept at 2 mg/L with sample dose of 0.25 gm/L for 60min of contact time at pH 6.8. Fig. 3.10(a) shows that As(V) adsorption in aqueous solution increases with rise in temperature. Interestingly, the increasing trend was more significant for the sample FENH24 (synthesized for 24 h reaction time at 150 ^oC). Fig. 3.10(b) also reveals that adsorption capacity increased with rise in temperature. It is worth noting that the increase of As(V) adsorption efficiency with temperature signifies the endothermic process of adsorption resulting higher efficiency of As(V) adsorption.

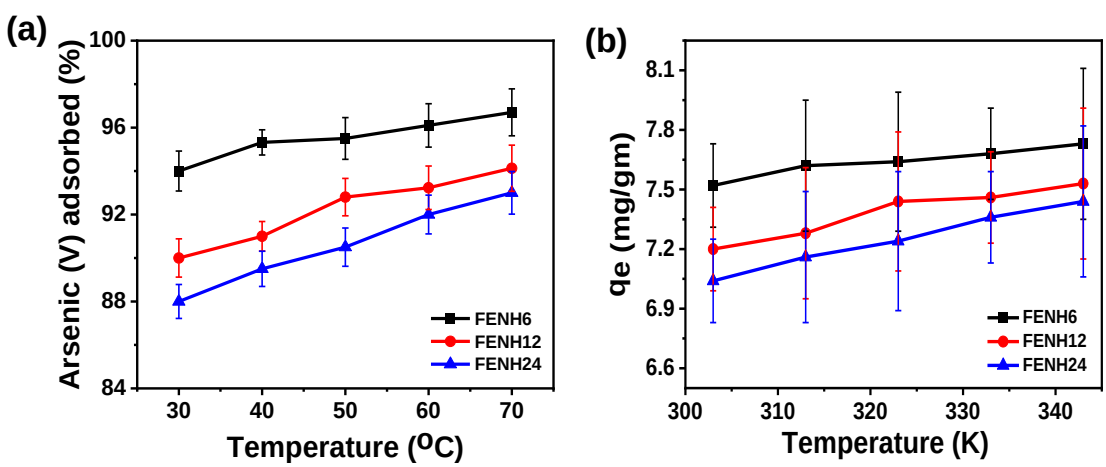

Figure 3.10: Effect of temperature on % As(V) adsorption (b) Adsorption capacity on the adsorption of As(V) by α-Fe_2O_3 particles.

3.3.3 Thermodynamic investigation

The thermodynamic study on As(V) adsorption process was carried out at different temperature at 303, 313, 323, 333 and 343 K. The thermodynamic parameters like enthalpy (ΔH^o), entropy (ΔS^o) and Gibbs free energy (ΔG^o) were derived as follows:

$$K^o{}_{eq} = (C_0\text{-}C_e)/C_e \qquad (3.2)$$

$$ln\ K^o{}_{eq} = \Delta S^o/R - \Delta H^o/RT \qquad (3.3)$$

$$\Delta G^o = -RTlnK^o{}_{eq} \qquad (3.4)$$

Where, $K^o{}_{eq}$ is the equilibrium constant, T (K) is the temperature and R is the universal gas constant (8.314 J /mol/K)

By plotting $\ln K^0{}_{eq}$ vs. 1/T from equation (3.3), the values of ΔH^o and ΔS^o can be obtained from the slope and intercept of the plot, respectively (Fig. 3.11). Table 3.2 shows the thermodynamic parameters values of ΔH^o, ΔS^o and ΔG^o for all the samples. The endothermic nature of As(V) adsorption process was confirmed by positive values of ΔH^o. Further, the positive values of ΔS^o demonstrate that there prevails randomness at the solid-liquid interface during adsorption process. The spontaneity of the adsorption process was confirmed by the negative values of ΔG^o. It is to be noted that with increase in temperature, ΔG^o values are becoming more and more negative indicating favourable adsorption of As(V) with temperature,[60] and it is chemisorption rather than physisorption. It is to be noted that for the samples prepared at different temperatures, the values of ΔS^o are comparable for the samples FENH12 and FENH24 while it is increased for the sample FENH6. However, $-\Delta G^o$ values are in decreasing trend as FENH6>FENH12>FENH24. It indicates that with increasing reaction time, the adsorption process by the sample is becoming less favourable due to lower ΔS^o and $-\Delta G^o$ values, particularly for FENH24.

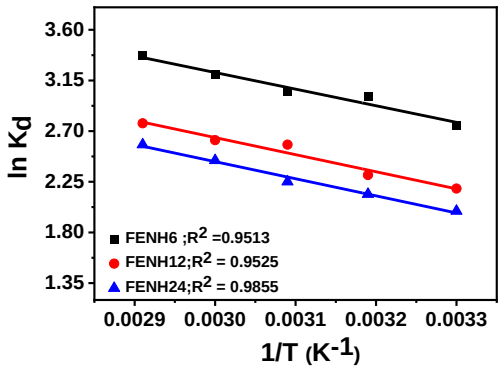

Figure 3.11: Plot of $\ln K_d$ versus 1/T for the adsorption for As(V).

Table 3.2: Thermodynamic parameters of As(V) adsorption for different sample with fixed adsorbent doses (0.25 gm/L).

Sample ID	ΔH^o (kJ/mol)	ΔS^o (J/mol.K)	ΔG^o (kJ/mol)
FENH6	+12.2698	+63.5189	−6.9947 at 303K −7.6337 at 313K −8.2727 at 323K −8.9117 at 333K −9.5577 at 343K
FENH12	+12.6331	+59.8693	−5.265 at 303K −5.855 at 313K −6.445 at 323K −7.035at 333K −7.625 at 343 K
FENH24	+12.6364	+58.0982	−4.9376 at 303 K −5.5176 at 313 K −6.0976 at 323K −6.6776 at 333K −7.2576 at 343 K

Effect of co-existing anions

In natural underground water, various co-existing ions may be present which have susceptibility to compete with the arsenic at the active surface of the adsorbent. In this study the effect of common co-existing ions such as chloride (Cl^-), nitrate (NO_3^-), phosphate (PO_4^{3-}) and sulphate (SO_4^{2-}) has been evaluated on the adsorption of As(V) using each contaminant concentration and sample dose of 5 mg/L and 1 gm/L, respectively. Fig. 3.12(a) shows that in

the presence of above co-existing anions, the % adsorptions for As(V) were 97.5, 92.3 and 89.9%, for the samples FENH6, FENH12 and FENH24, respectively along with % removal of Cl^-, NO_3^-, PO_4^{3-} and SO_4^{2-} as 30-34, 47-50, 93-96 and 87-90%, respectively. It is noticed that the adsorption affinity for different anions with the adsorbent follows in the order of As(V)>PO_4^{3-}>SO_4^{2-}> NO_3^->Cl^-. Here, PO_4^{3-} ion due to its same chemical nature with arsenate has strong competitive effect with As(V) for adsorption sites of the adsorbent inhibiting As(V) adsorption. The order of hydrated ionic radius of anions are SO_4^{2-}> NO_3^->Cl^-. Therefore, SO_4^{2-} ions due to its larger ionic radius, form outer-sphere complexes with Fe(III) of adsorbent through long range electrostatic force compared to $NO_3^-$and Cl^- ions.

Recyclability study

For minimizing cost of water treatment reusing the adsorbent materials after adsorption of As(V) contaminant water, regeneration study is of utmost important. In this regard, used adsorbent is treated with alkaline solution to exchange negatively charged arsenate (As(V)) with hydroxyl ions. Fig. 3.12(b) shows the recyclability study of three different samples FENH6, FENH12 and FENH24. It illustrates that up to 3rd cycle, the adsorption is >90% followed by gradual fall of As(V) adsorption up to 5th cycle indicating the % adsorption of >60%.It is to be noted that after some cycles, the adsorption efficiency becomes lower because the adsorbed exchangeable hydroxide ions start trapping within the pore structure of adsorbent which are difficult to wash out with water. Therefore, adsorption is becoming hindered due to electrostatic repulsion between negatively charges hydroxide and arsenate ions.

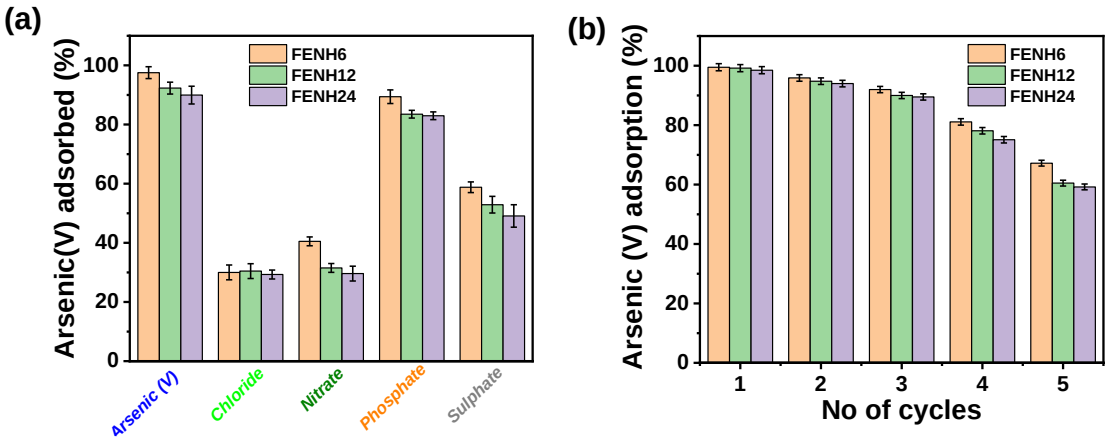

Figure 3.12: (a) Co-existing ions effect and (b) Recyclability study for the adsorption for As(V) ions.

3.3.4 Adsorption Kinetics

For kinetics study of adsorption, the experimental data was fitted with pseudo-first order and pseudo-second order models. The mathematical expression of the two models are shown in Table 3.3. From pseudo-first order kinetics model, by plotting $\ln(q_e-q_t)$ *vs* t, the adsorption capacity at equilibrium (q_e) and rate constant (k_1) are evaluated from the intercept and slope, respectively. On the other hand, for pseudo-second order kinetics, the equilibrium adsorption capacity (q_e) and second order rate constant (k_2) are determined from the intercept and slope, respectively by plotting t/q_t vs t. Figs. 3.13 (a) and (b) show the linear fitting curves for pseudo-first-order and pseudo-second-order models, respectively. The relevant parameters obtained from pseudo-first order and pseudo-second order kinetics model are presented in Table 3.3. The correlation co-efficient (R^2) for pseudo-second-order model approaches to 1 with high degree of linearity (best fitting curve) which signifies chemisorption process for As(V) adsorption. The equilibrium adsorption capacity (q_e) was around 8 mg/gm for three samples FENH6, FENH12 and FENH24 with a nominal decrease in values with increase in reaction time for the preparation of adsorbent materials.

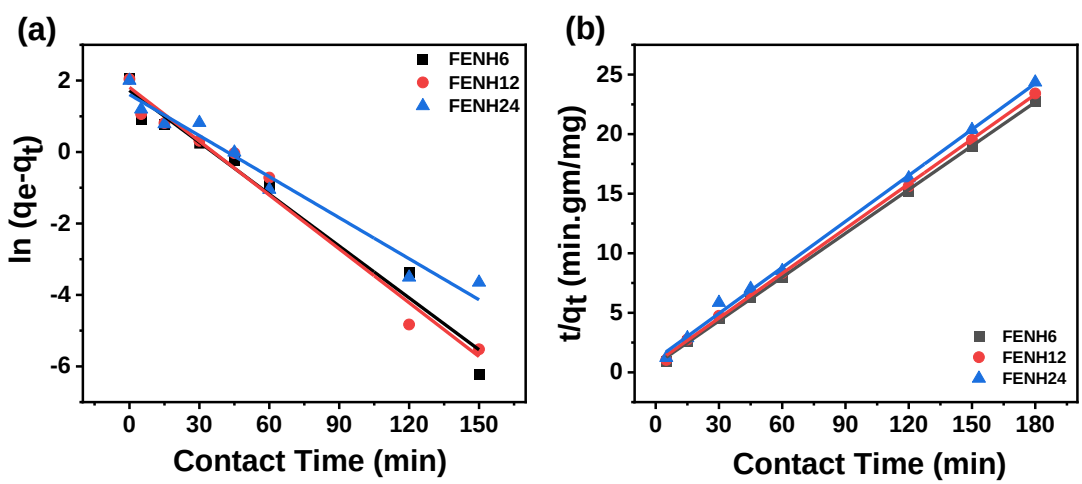

Figure 3.13: Kinetics data with linear fitting of (a) pseudo-first-order and (b) pseudo-second-order.

Table 3.3: Kinetic parameters for the adsorption of As(V) for adsorbent dose of 0.25 gm/L.

Model	Mathematical expression		Sample ID		
			FENH6	FENH12	FENH24
Pseudo-first order kinetics	$\ln (q_e-q_t) = -k_1 t + \ln q_e$	k_1 (min^{-1})	0.0484	0.0502	0.0383
		q_e(mg/gm)	5.6046	6.1080	4.9888
		R^2	0.9640	0.9745	0.9620
		S.E (Intercept)	0.2603	0.2262	0.2119
		S.E(Slope)	0.0035	0.0030	0.0028
Pseudo-second order kinetics	$t/q_t = 1/k_2 q_e^2 + (1/q_e)t$	k_2 (gm/mg/min)	0.0230	0.0196	0.0152
		q_e(mg/gm)	8.1699	7.9872	7.7700
		R^2	0.9994	0.9992	0.9970
		S.E (Intercept)	0.1060	0.1270	0.1577
		S.E(Slope)	0.0010	0.0013	0.0026

3.3.5 Adsorption Isotherms

To assess the adsorption performance of arsenic at the solid-liquid interface, Langmuir and Freundlich isotherm models were used. The linear expression of the two models are shown in Table 3.4. From Langmuir isotherm, by plotting C_e/q_e vs. C_e, the maximum adsorption capacity (q_m(mg/gm)) and Langmuir adsorption constant (K_L)are obtained from the slope and intercept, respectively (Fig. 3.14(a)). By plotting log q_e vs. log C_e, in Freundlich isotherm, the adsorption intensity (n_F) and K_F (Freundlich constant) can be obtained from the slope and intercept, respectively (Fig. 3.14(b)). The Langmuir isotherm illustrates that adsorption process is uniform with monolayer formation whereas Freundlich isotherm is considered for multilayer non-uniform and reversible adsorption. The relevant parameters determined from Langmuir and Freundlich isotherm are revealed in Table 3.4. The correlation coefficient R^2 ($\geq$0.98) obtained from Langmuir isotherm indicates best fittings for As(V) adsorption as compared to Freundlich isotherm. It is noticed that the maximum adsorption capacity values calculated from Langmuir isotherm were found to be 41.1, 36.8 and 32 mg/gm for the samples FENH6, FENH12 and FENH24, respectively which were higher than those obtained from humic acid

grafted magnetic nanoparticles.[61] However, a study regarding the adsorption capacity compared to other adsorbent materials has also been done which is represented in a tabular form in Table 3.5 exhibiting better adsorptivity of synthesized α-Fe_2O_3.

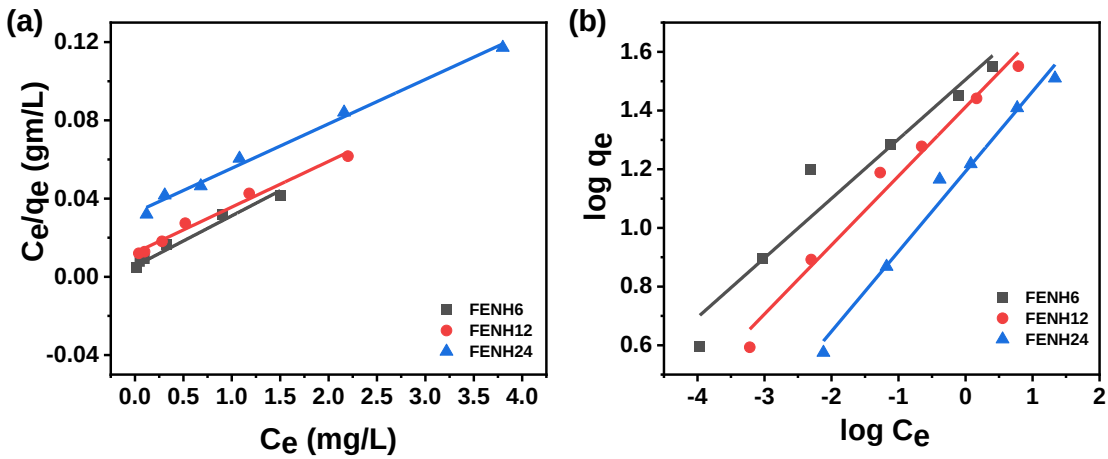

Figure 3.14: (a) Langmuir and (b) Freundlich isotherms for the adsorption for As(V) ions.

Table 3.4: The parameters obtained from Langmuir and Freundlich models.

Adsorbent dose (0.50 gm/L)			**FENH6**	**FENH12**	**FENH24**
Langmuir isotherm	$C_e/q_e=C_e/q_m+1/K_L.q_m$	K_L (L/mg)	3.3956	2.3129	0.9759
		q_m (mg/gm)	41.1353	36.8595	31.0655
		R^2	0.9790	0.9977	0.9822
		S.E (Intercept)	0.0011	0.0006	0.0032
		S.E (Slope)	0.0015	0.0005	0.017
Freundlich isotherm	$\log q_e = \log K_F + 1/n_F \log C_e$	K_F (mg/gm)	31.6956	24.2940	16.6264
		n_F	1.8402	1.7008	2.031
		R^2	0.9772	0.9552	0.9123
		S.E (Intercept)	0.0851	0.0951	0.0800
		S.E(Slope)	0.0370	0.0544	0.0675

Table 3.5: A comparative data on maximum adsorption capacity of synthesized α-Fe_2O_3 and reported adsorbents for As(V).

Adsorbents	pH Maintained	Adsorbate concentration	Adsorption capacity	Ref
Iron oxide coated Natural rock	7.5	40 μg/L	0.36 mg/gm	62
Green synthesized α-Al_2O_3	6.5	2-30 mg/L	38.47 mg/gm	63
Chitosan-MNP	3.0	5-500 mg/L	10.40 mg/gm	64
Magnetic nano particle impregnated Chitosan Beads	6.8	50 mg/L	35.70 mg/gm	65
Iron Chitosan Composite	7.0	10 mg/L	22.50 mg/gm	66
Iron oxide coated sponge (IOCSP)	6.5-7.3	5 mg/L	4.50 mg/gm	67
RM derived α-Fe_2O_3	6.8	2-20 mg/L	41 mg/gm	Present work

3.3.6 Adsorption mechanism

Surface property as well as ligand binding ability of the adsorbent materials plays a pivotal role in the adsorption process. Iron oxide based adsorbents are found to be prone to arsenic adsorption mainly due to their physico-chemical properties which assists the adsorption of arsenic over a wide pH range. Fig. 3.15 shows a proposed mechanism for the adsorption of As(V) ions by by α-Fe_2O_3 particles. It is demonstrated that arsenic adsorption on iron oxide based materials occurs through inner-sphere surface complex *via* monodentate, bidentate or tridentate ligand, and outer sphere surface complex. Inner sphere surface complexation takes

place over a wide range of pH i.e., below or above pH_{PZC}[68] The outer sphere complexation is governed by electrostatic force of attraction between the negatively charged arsenate ions and positive surface of iron oxide based adsorbent. It is dominated at lower $pH<pH_{PZC}$. The Fe(III) in α-Fe_2O_3 molecule can act as a Lewis acid because of vacant d orbital, while in arsenate ions with filled p electron of oxygen behaves as Lewis base. As a result a dπ-pπ bonding occurs between the adsorbent molecules of iron oxide and binding ligands of arsenate during the formation of inner sphere complexes. However, the arsenate ions could bind to the adsorbent surface by the hydration layer with water molecule forming outer sphere complexes where electrostatic interaction, vander Waals forces of attraction, hydrogen bonding etc., could led to a significant role for effective adsorption.[69] It is mentioned worthy that as per XRF results, alumina content in the synthesized product is less quantity (14.30%) as compared to α-Fe_2O_3 (81.40%). It is reported that in the presence of both iron oxide and aluminium oxide as adsorbents, iron oxide preferably adsorbed As(V).[70,71] During As(V) adsorption, iron oxide forms both the inner sphere and outer sphere complexation with arsenate species ($HAsO_4^{2-}$), while alumina as positively charged aluminium hydroxide species $[Al(OH)_3\text{-}2H]^{2+}$ interacts with arsenate species *via* electrostatic interaction (outer sphere complexation) only.[72] In the present work, iron oxide with its high concentration plays more significant role for adsorption of As(V) which could supersede the adsorption ability of alumina. In order to comprehend the adsorption mechanism, Fig. 3.16 depicts the FTIR study of the sample (FENH6) dose before and after As(V) adsorption. The emergence of a new peak at 858 cm^{-1} indicates the formation of As-O bonds during adsorption onto Fe surface.[73]

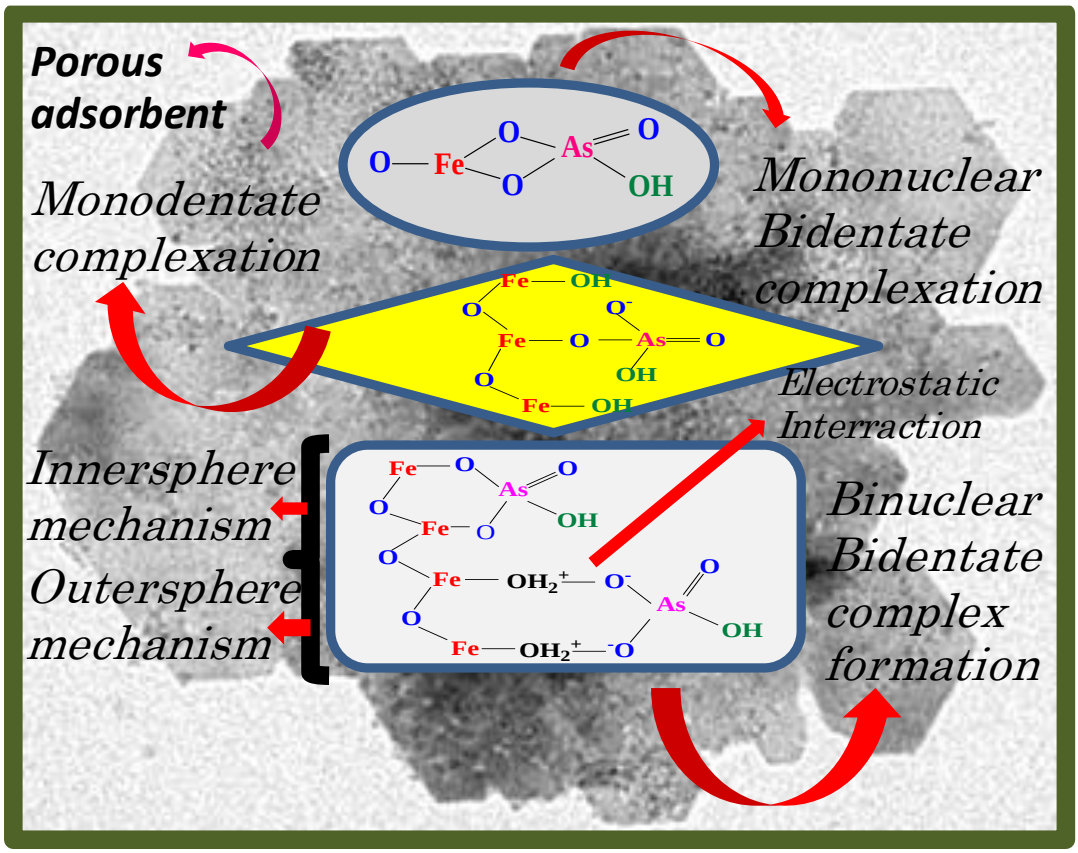

Figure 3.15: Proposed mechanism for the adsorption of As(V) ions by α-Fe_2O_3 particles.

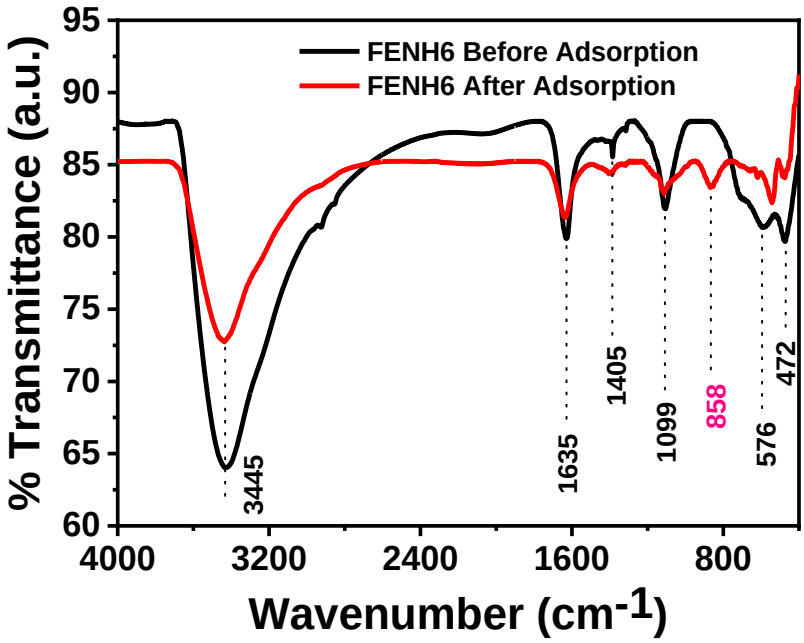

Figure 3.16: FTIR spectra of the FENH6 sample before and after As(V) adsorption.

3.4 Conclusion

We have prepared iron oxide nanoflakes from RM extract by hydrothermal reaction at low temperature (150 ^{o}C/6-24 h). The synthesized product was utilized for the adsorption of As(V)from aqueous solution. For competitive ions effect, the adsorption affinity for different anions with the adsorbent follows in the order of As(V)>PO_4^{3-}>SO_4^{2-}> NO_3^->Cl^-.The spontaneity of the adsorption process was confirmed by the negative values of ΔG^o favouring adsorption of As(V) *via* a chemisorption process. The pseudo-second order kinetics and Langmuir isotherm models exhibit the best fitting for the adsorption of As(V). Arsenic adsorption on iron oxide based materials occurs through inner-sphere surface complex *via* monodentate, bidentate or tridentate ligand, and outer sphere surface complex by electrostatic interaction, van der Waals force of attraction, hydrogen bonding etc. The present study shows a direction in designing for fabrication of iron oxide based nano-adsorbents using industrial wastes for effective performance of de-arsenification of water.

References

1 K. S. M. Abdul, S. S. Jayasinghe, E. P. S. Chandana, C. Jayasumana and P. M. C. S. De Silva, *Environ. Toxicol. Pharmacol.*, 2015, **40**, 828–846.

2 A. Sarkar and B. Paul, *Chemosphere*, 2016, **158**, 37–49.

3 M. A. Sandoval, R. Fuentes, J. L. Nava, O. Coreño, Y. Li and J. H. Hernández, *Sep Purif. Technol.*, 2019, **208**, 208–216.

4 J. Liu, P. Wu, S. Li, M. Chen, W. Cai, D. Zou, N. Zhu and Z. Dang, *Chemosphere*, 2019, **225**, 115–125.

5 I. Akin, G. Arslan, A. Tor, M. Ersoz and Y. Cengeloglu, *J. Hazard. Mater.*, 2012, **235**, 62–68.

6 K. J. Bisceglia, K. J. Rader, R. F. Carbonaro, K. J. Farley, J. D. Mahony and D. M. Di Toro, *Environ. Sci. Technol.*, 2005, **39**, 9217–9222.

7 R. J. De Klerk, Y. Jia, R. Daenzer, M. A. Gomez and G. P. Demopoulos, *Hydrometallurgy*, 2012, **111**, 65–72.

8 M. T. Uddin, M. S. I. Mozumder, A. Figoli, M. A. Islam and E. Drioli, *Indian J. Chem. Technol.,* 2007,**14**, 441-450.

9 I. Kumar and A. R. Quaff, *Int. J. of Environ. Sci.Technol.*, 2019, **16**, 5989–5994.

10 Z. Cheng, F. Fu, D. D. Dionysiou and B. Tang, *Water Res.*, 2016, **96**, 22–31.

11 R. K. Misra, S. K. Jain and P. K. Khatri, *J. Hazard Mater.*, 2011, **185**, 1508–1512.

12 A. Abejón, A. Garea and A. Irabien, *Sep. Purif. Technol.*, 2015, **144**, 46–53.

13 S. Yuan, S. Xie, K. Zhao, Y. Gan and Y. Wang, *Sci. Total. Environ.*, 2018, **644**, 1630–1640.

14 S. He, C. Han, H. Wang, W. Zhu, S. He, D. He and Y. Luo, *J. Chem. Eng. Data.*, 2015, **60**, 1300–1310.

15 N. K. Niazi, I. Bibi, M. Shahid, Y. S. Ok, S. M. Shaheen, J. Rinklebe, H. Wang, B. Murtaza, E. Islam and M. F. Nawaz, *Sci.Total Environ.*, 2018, **621**, 1642–1651.

16 P. Chutia, S. Kato, T. Kojima and S. Satokawa, *J. Hazard Mater.*, 2009, **162**, 440–447.

17 J. Li, X. Wang, G. Zhao, C. Chen, Z. Chai, A. Alsaedi, T. Hayat and X. Wang, *Chem. Soc. Rev.*, 2018, **47**, 2322–2356.

18 S. Yao, Z. Liu and Z. Shi, *J. Environ. Health Sci. Eng.*, 2014, **12**, 1–8.

19 G. Zhao, X. Huang, Z. Tang, Q. Huang, F. Niu and X. Wang, *Polym. Chem.*, 2018, **9**, 3562–3582.

20 S. Kundu, I. H. Chowdhury and M. K. Naskar, *J. Chem. Eng. Data.*, 2018, **63**, 559–573.

21 Y. Huang, Z. Liu, A. Bo, X. Tang, W. Martens, L. Kou, Y. Gu, G. Carja, H. Zhu and S. Sarina, *J. Colloid Interface. Sci.*, 2022, **608**, 2358–2366.

22 L. Hongtao, L. Shuxia, Z. Hua, Q. Yanling, Y. Daqiang, Z. Jianfu and Z. Zhiliang, *RSC Adv.*, 2018, **8**, 33301–33313.

23 L. Shi, Z. Shu, K. Wang, J. Zhou and T. Li, *ACS Appl. Nano Mater.*, 2023, **6**, 1744–1754.

24 A. M. A. Pintor, B. R. C. Vieira, S. C. R. Santos, R. A. R. Boaventura and C. M. S. Botelho, *Sci. Total Environ.*, 2018, **642**, 1075–1089.

25 F. Li, H. Guo, X. Zhou, K. Zhao, J. Shen, F. Liu and C. Wei, *Chemosphere*, 2017, **168**, 777–785.

26 Y. Wang, P. Zhang, T. C. Zhang, G. Xiang, X. Wang, S. Pehkonen and S. Yuan, *Nanoscale Adv*, 2020, **2**, 2018–2024.

27 L. Yu, H. Liu, C. Liu, H. Lan and J. Qu, *Part. Part. Syst. Charact.*, 2016, **33**, 323–331.

28 G. Zhang, X. Xu, Q. Ji, R. Liu, H. Liu, J. Qu and J. Li, *ACS Appl Mater. Interfaces.*, 2017, **9**, 14868–14877.

29 H. Lu, Z. Zhu, H. Zhang, J. Zhu and Y. Qiu, *J.Chem. Eng.*, 2015, **276**, 365–375.

30 A. R. Sari, A. Yulianingtias, R. A. Melinda, A. Mirwan and C. Irawan, J. Rekayasa Kim. Lingkung. 2021, **16**(1), 45-51.

31 Z. Babazad, F. Kaveh, M. Ebadi, R. Z. Mehrabian and M. H. Juibari, *Heliyon*, 2021, **7**(3), e06631.

32 T. H. Nguyen, H. N. Tran, H. A. Vu, M. V. Trinh, T. V. Nguyen, P. Loganathan, S. Vigneswaran, T. M. Nguyen, D. L. Vu and T. H. H. Nguyen, *Sci.Total Environ.*, 2020, **699**, 134267.

33 S. Sanchez-Segado, T. Makanyire, L. Escudero-Castejon, Y. Hara and A. Jha, *Green chem.*, 2015, **17**, 2059–2080.

34 M. A. Khairul, J. Zanganeh and B. Moghtaderi, *Resour. Conserv Recycl.*, 2019, **141**, 483–498.

35 J. S. Roy, G. Bhattacharya, D. Chauhan, S. Deshmukh, R. Upadhyay, R. Priyadarshini and S. Sinha Roy, *SN Appl Sci.*, 2020, **2**, 1–11.

36 C. G. Joseph, Y. H. T. Yap, V. Krishnan and G. L. Puma, *Environ. Eng. Res.*, 2020, **25**(6), 795-806.

37 C. Wu, L. Huang, S.-G. Xue, Y.-Y. Huang, W. Hartley, M. Cui and M.-H. Wong, *Environ Sci. Pollut. Res. Int*., 2017, **24**, 18168–18178.

38 R. Biswas and A. Sarkar, *Environ Sci Pollut Res. Int*, 2021, **28**, 40665–40677.

39 D. Yang, A. Sasaki and M. Endo, *J Water Environ. Technol*, 2018, **16**, 115–126.

40 A. A. Shoppert, I. V Loginova, D. A. Rogozhnikov, K. A. Karimov and L. I. Chaikin, *Minerals*, 2019, **9**, 60.

41 Y. Xu, Y. Yin, M. Guo, G. Xu, L. Li and C. Liu, *Water Supply*, 2022, **22**, 3980–3992.

42 J. S. Noh and J. A. Schwarz, *J. Colloid Interface. Sci.*, 1989, **130**, 157–164.

43 R. K., M. Jaculine, M. Jose, S. Verma, A. A. M. Prince, K. Ilangovan, K. Sethusankar and J. Das, *Superlattices Microstruct.*, 2015, **86**,306-312.

44 M. Roy and M. K. Naskar, *Phys. Chem. Chem. Phys.*, 2016, **18**, 20528–20541.

45 J. Gao, B. Wang, W. Li, L. Cui, Y. Guo and F. Cheng, *Sep Purif. Technol.*, 2023, **306**, 122545.

46 A. Loaiza-Gil, J. Arenas, M. Villarroel, F. Imbert, H. del Castillo and B. Fontal, *J. Mol Catal A. Chem.*, 2005, **228**, 339–344.

47 L.-S. Zhong, J.-S. Hu, A.-M. Cao, Q. Liu, W.-G. Song and L.-J. Wan, *Chem. Mater*, 2007, **19**, 1648–1655.

48 R. Reveendran and M. A. Khadar, *Mater. Chem. Phys.*, 2018, **219**, 142–154.

49 M. Testa-Anta, M. A. Ramos-Docampo, M. Comesaña-Hermo, B. Rivas-Murias and V. Salgueiriño, *Nanoscale Adv.*, 2019, **1**, 2086–2103.

50 J. L. Carter, J. A. Cusumano and J. H. Sinfelt, *J. Phys. Chem.*, 1966, **70**, 2257–2263.

51 S. Ghosh, R. Das and M. K. Naskar, *J. Am. Ceram.Soc.*, 2016, **99**, 2273–2282.

52 D. Zhang, X. Fan, A. Yang and X. Zong, *J. Colloid Interface. Sci.*, 2018, **523**, 217–225.

53 X. J. Wu, Z. Z. Zhang, Q. S. Liang and J. Meng, *J. Cryst. Growth*, 2012, **340**, 74–77.

54 K. Wu, Y. Lu, Y. Liu, Y. Liu, M. Shen, M. Debliquy and C. Zhang, *Ceram. Int.*, 2020, **46**, 28835–28843.

55 R. Munoz, C. Sanchez-Sanchez, P. Merino, E. Lopez-Elvira, C. Munuera, P. Gant, M. F. Lopez, A. Castellanos-Gomez, J. A. Martín-Gago and M. Garcia-Hernandez, *Appl Surf. Sci.*, 2020, **504**, 144439.

56 M. Roy, S. Basak and M. K. Naskar, *Phys. Chem. Chem. Phys*, 2016, **18**, 5253–5263.

57 A. Chakraborty and M. K. Naskar, *Mater Adv*, 2022, **3**, 8544–8556.

58 A. Teimouri, S. Ghanavati Nasab, S. Habibollahi, M. Fazel-Najafabadi and A. N. Chermahini, *RSC Adv*, 2015, **5**, 6771–6781.

59 J. Alchouron, C. Navarathna, H. D. Chludil, N. B. Dewage, F. Perez, C. U. Pittman Jr, A. S. Vega and T. E. Mlsna, *Sci. Total Environ.*, 2020, **706**, 135943.

60 J. He, X. Cai, K. Chen, Y. Li, K. Zhang, Z. Jin, F. Meng, N. Liu, X. Wang, L. Kong, X. Huang and J. Liu, *J Colloid Interface Sci.*, 2016, **484**, 162–172.

61 M. Rashid, G. E. Sterbinsky, M. A. G. Pinilla, Y. Cai and K. E. O'Shea, *J. Phys. Chem.*, 2018, **122**, 13540–13547.

62 S. K. Maji, A. Pal and T. Pal, *J. Hazard. Mater.*, 2008, **151**, 811–820.

63 D. Mukherjee, S. Ghosh, S. Majumdar and K. Annapurna, *J. Environ. Chem Eng.*, 2016, **4**, 639–650.

64 G. A. Kloster, M. Valiente, N. E. Marcovich and M. A. Mosiewicki, *Int J Biol. Macromol.*, 2020, **165**, 1286–1295.

65 J. Wang, W. Xu, L. Chen, X. Huang and J. Liu, *J. Chem. Eng.*, 2014, **251**, 25–34.

66 A. G. Anjali Gupta, V. S. Chauhan and N. S. Nalini Sankararamakrishnan, Water Res., 2009,**43**,3862-3870.

67 T. V. Nguyen, S. Vigneswaran, H. H. Ngo and J. Kandasamy, *J Hazard Mater.*, 2010, **182**, 723–729.

68 S. Aredes, B. Klein and M. Pawlik, *J. Clean Prod.*, 2013, **60**, 71–76.

69 L. Hao, M. Liu, N. Wang and G. Li, *RSC Adv.*, 2018, **8**, 39545–39560.

70 J. Youngran, F. A. N. Maohong, J. Van Leeuwen and J. F. Belczyk, *J. Environ. Sci.*, 2007, **19**, 910–919.

71 Y. Jeong, M. Fan, S. Singh, C.-L. Chuang, B. Saha and J. H. Van Leeuwen, *Chem. Eng. Process*, 2007, **46**, 1030–1039.

72 C. Han, H. Li, H. Pu, H. Yu, L. Deng, S. Huang and Y. Luo, *J. Chem. Eng.*, 2013, **217**, 1–9.

73 Z. Zhou, Y. Liu, S. Liu, H. Liu, G. Zeng, X. Tan, C. Yang, Y. Ding, Z. Yan and X. Cai, *J. Chem. Eng*, 2017, **314**, 223–231.

Chapter 4

Red mud derived iron oxide based photocatalysts for the degradation of methylene blue dye

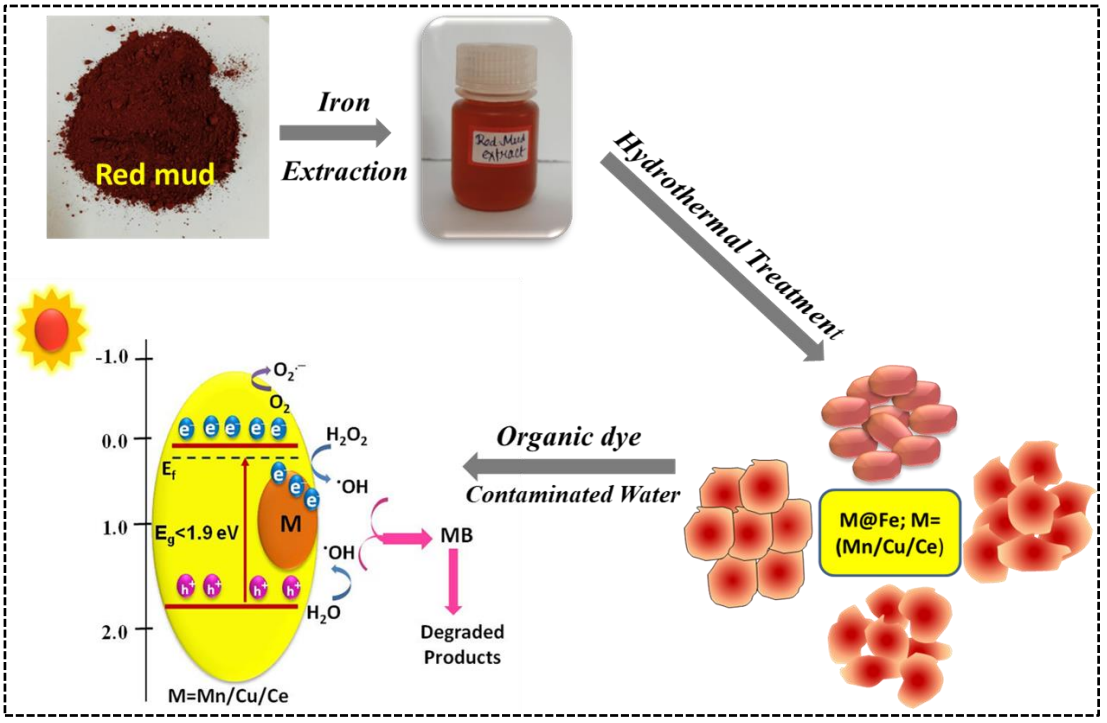

Publication from this Chapter:

Adwitiya Chakraborty, Soumita Samajdar, Srabanti Ghosh and Milan Kanti Naskar, "Visible light induced photocatalytic removal of organic dye using metal doped iron oxide based catalysts derived from red mud", ***New Journal of Chemistry,*** **2024, 48, 10401-10414.**

4.1 Introduction

In recent days, iron oxide-based photocatalysts have gained significant attention due to their remarkable resistance to corrosion, low toxicity, great chemical stability, and narrow band gap energy.[1,2] Fe_2O_3 with suitable valence band-edge, is an outstanding catalyst for the photo-squalor of unrefined pollutants and is not only abundant in nature but also mass-producible.[3]Alpha Fe_2O_3 (hematite) possesses specific advantages over other phases of iron oxide, such as magnetite (Fe_3O_4) and gamma Fe_2O_3 (maghemite), which contribute to its unique utility in various research fields like energy storage and conversion, sensors and detectors, catalysis, biomedical applications etc.[4–7] Despite of having all those advantages, photocatalytic activity in Fe_2O_3 is often overwhelmed by its hole diffusion length (approximately, 10 nm) and an extremely short electron–hole recombination time.[8,9] In order to facilitate the photocatalytic activity of Fe_2O_3, doping with different metals or non-metal ions is essential by tuning its band gap as well as providing better anchoring sites. Recently, photocatalytic degradation of MB in the presence of Ni doped hematite has been reported by Asma *etal.*[10] Shahid *et al.* studied photocatalytic properties of α-Fe_2O_3/NiOnanowires.[11] Hyun *et al.* reported that photocatalytic efficiency of hematite nanocrystals increases with doping with Manganese.[12]

However, achieving high photo-catalytic activity using low-cost resources is still a significant challenge. Many synthesis methods require high energy inputs, which can offset the cost advantages of using low-cost materials. For the development of low-cost catalysis, utilization of waste based precursors could be very significant in terms of energy and environment. Utilizing red mud as a precursor as photocatalysts offers environmental advantages by repurposing of an industrial waste product. In the present study, a sustainable route is developed to synthesize iron oxide based photocatalysts extracted from red mud, followed by doping with Mn, Cu and Ce for the degradation of MB, an organic water pollutant. The structural, optical, morphological, and photocatalytic activity of the synthesized catalysts were investigated.

4.2 Experimental section

4.2.1 Materials and Methods

The industrial waste red mud (RM) was obtained from Utkal Aluminium International Ltd., Odisha, India. Tetrapropyl ammonium hydroxide (TPAH) (1M in water), hydrochloric acid (37 wt%), cerium (III) chloride heptahydrate ($CeCl_3.7H_2O$) were purchased from Sigma Aldrich.

Methylene blue (MB), copper (II)chloride dihydrate ($CuCl_2.2H_2O$), manganese (II) chloride tetrahydrate ($MnCl_2.4H_2O$) were purchased from Merck, India.The experiment was carried out using Millipore water.

Preparation of bare and doped iron oxide based materials from red mud

Synthesis of bare iron oxide photocatalyst

The iron in RM was extracted as reported earlier in our previous work.[13] In brief, the extraction of Fe (III) from RM involved leaching of 40 gm of crushed RM powder with 400 mL of 6 (M) HCl under reflux conditions at 90 °C for 3h.In order to synthesize iron oxide-based adsorbent, the requisite amount of tetra propyl ammonium hydroxide solution was added dropwise into 10 mL of RM extract under stirring for 30 min, maintaining a pH of 8–9. The as-generated brown solid mass was placed into a hydrothermal autoclave lined with Teflon followed by heating at 150 °C/24 h. The reddish brown product was collected by repeated centrifugation and washing followed by drying at 60 °C/6h. The prepared sample was designated as FETP. Fig.4.1 shows schematically the synthesis of iron oxide extracted from RM.

Synthesis of metal doped photocatalysts

For the synthesis of Mn, Cu, and Ce doped iron oxide, 10 mL aqueous solutions of $MnCl_2.4H_2O$ (0.106 gm), $CuCl_2$, $2H_2O$ (0.096 gm) and $CeCl_3.7H_2O$ (0.096 gm) were added separately into 10 mL RM extract under stirring for 10 min keeping Fe:M (Mn/Cu/Ce)=10:1 (mol ratio). TPAH was added dropwise into the above solutions to maintain the pH of 8–9, and stirring was continued for another 20 min. A brown-colored precipitate as-obtained from each experiment was placed into a Teflon-coated hydrothermal autoclave followed by heating at 150 °C/24 h. The as-synthesized products were collected by repeated centrifugation and washing, followed by drying at 60 °C/6 h. The prepared products were designated as FMNTP, FCUTP and FCETP for Mn, Cu and Ce doped α-Fe_2O_3, respectively. Fig. 4.1 illustrates the preparative steps of the above products.

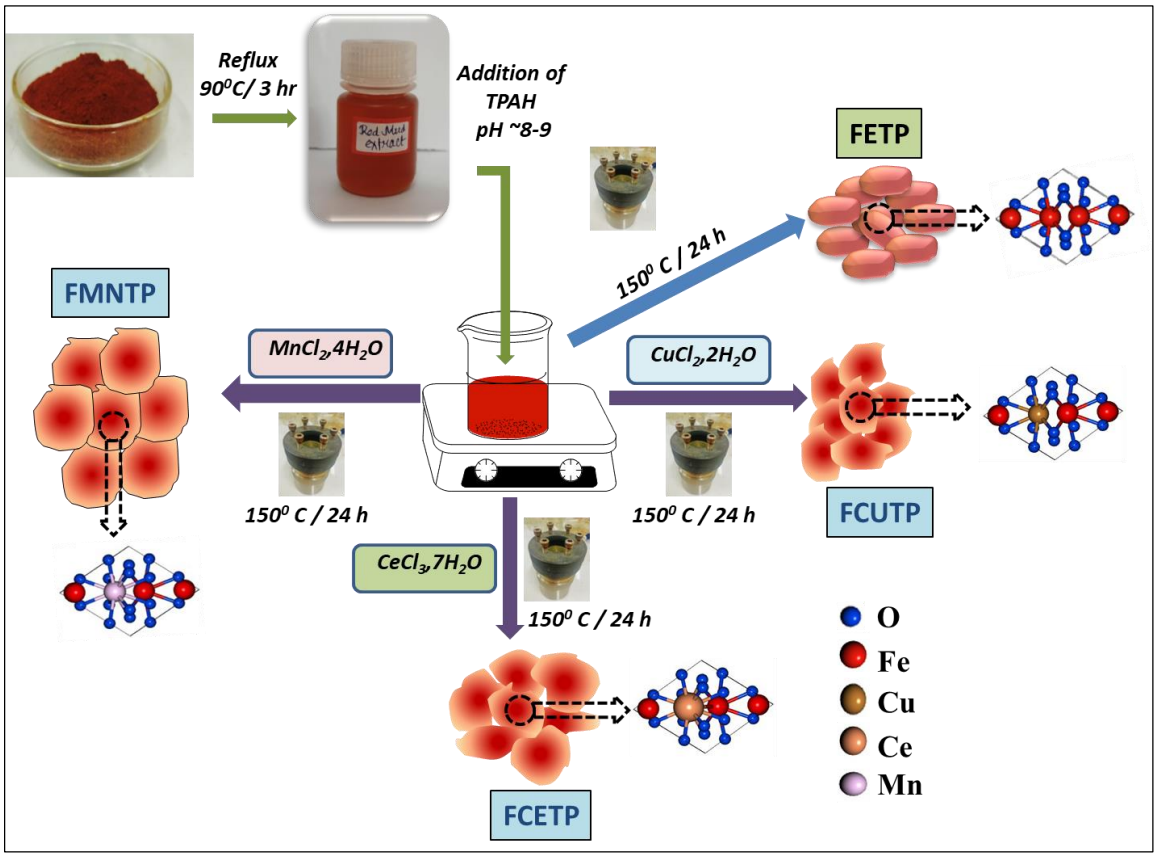

Figure 4.1: Schematic diagram for the preparation of bare and doped iron oxide extracted from red mud.

4.2.2 *Characterization*

The materials were subjected to X-ray diffraction (XRD) analyses utilizing a Ni-filtered Cu-K_α radiation (λ = 0.15418 nm) and a Philips X'Pert Pro PW 3050/60 powder diffractometer operating at 40 kV and 30 mA.The Raman spectrum was recorded using a RENISHAW spectrometer with 785 nm radiation from a diode laser source with 20X objective lense at room temperature.The characteristic vibration bands of the synthesized samples were verified using Fourier transform infrared (FTIR; Spectrum two, Perkin Elmer) with a resolution of 4 cm^{-1}. Transmission electron microscopy (TEM) with a Tecnai G2 30ST (FEI) apparatus working at 300 kV and FESEM (Model: Zeiss, Supra^{TM} 35VP, Oberkochen, Germany) operating at a 10 kV accelerating voltage were used to analyze the microstructure of the particles. Measurements of BET surface area, and nitrogen adsorption-desorption were carried out using a Quantachrome (ASIQ MP) apparatus at the temperature of liquid nitrogen (77 K). Before measurement, the sample was kept for degassing for 3 h at 200 °C under vacuum. The total pore volume was calculated using the amount of nitrogen adsorbed at a relative pressure (p/p_o)

of around 0.99 and the Barrett-Joyner-Halenda (BJH) method was used to calculate pore size distribution. Using a PHI 5000 Versa probe III Scanning XPS microprobe (ULVAC-PHI, USA), X-ray photoelectron spectroscopy (XPS) experiments were performed. A Jasco V-730 UV-vis spectrophotometer was used to record UV-visible spectra in the 200–800 nm wavelength range. The photoluminescence properties were conducted by QM-5,NIR Fluorescence spectrophotometer with an excitation wavelength of 350 nm in the range of 370-700 nm.

4.2.3 Photocatalytic Study

The synthesized products were used for photocatalytic degradation of MB solution under visible (λ= 465 nm) light irradiation at room temperature in the photo reactor using 300W Xenon lamp. In a typical photocatalytic test, 0.02 gm of the sample was mixed with 50mL of 1.56×10^{-5} M MB dye solution followed by stirring for about 60 min in dark to achieve adsorption equilibrium. Photocatalytic experiments were carried out in a batch type reaction system. Aliquots were taken out by filtering and the filtrates were analysed using a UV-visible spectrophotometer. Rest of the dye solution was irradiated by visible light under constant stirring in the presence of 30% H_2O_2. After regular intervals, an aliquot of the sample was collected from the reactor and analysed using the proper analytical techniques in order to monitor the progress of the reaction. The diminishing absorption intensity at λ_{max}= 664 nm reveals photo-catalytic degradation of the MB. The photo-catalytic activity was calculated by following equation:

$$\text{Percentage (\%) degradation} = \left(1 - \frac{C_t}{C_0}\right) \times 100 \qquad (4.1)$$

where C_0 and C_t are concentration of MB before and after irradiation, respectively.

The Total Organic Carbon analyser (Shimadzu Corporation) was used to examine the removal of total organic carbon (TOC), taking into account the variation in the concentrations of total carbon (TC) and inorganic carbon (IC). The percentage reduction in TOC value is shown in the following equation.

$$\text{TOC (\%)} = \left(1 - \frac{TOC_f}{TOC_o}\right) \times 100 \qquad (4.2)$$

4.2.4 Photochemical measurements

Photo-electrochemical activity of the materials was determined by preparing thin films on glass substrates coated with fluorine-doped tin oxide using a spin coater. The solution was drop cast on the glass slides up to 3 layers and put to calcination at 350 °C for a time duration of 2 h. A galvanostat-potentiostat (ZIVE SP1) was employed to conduct the photo-electrochemical experiments under 150 W Xenon lamp as the illumination source. The measurements were accomplished with the help of three-electrode configuration with KCl saturated Ag/AgCl and platinum wire as reference electrodes and counter electrodes respectively. Linear sweep voltammetry measurements were performed by varying the potential from –0.2 V to 1.0 V vs Ag/AgCl using 0.1 M Na_2SO_4 as electrolyte. Transient photocurrent measurements were performed at a fixed bias of 0.6 V vs Ag/AgCl, under consecutive dark and light conditions with an interval of 20 sec. Electrochemical impedance spectroscopy measurements were obtained in a frequency range from 0.1 Hz to 100 kHz. Mott-Schottky experiments were conducted at three different frequencies of 200, 500 and 1000 Hz which helps to determine the semiconducting behaviour and flat-band potential.

4.3 Results and discussion

4.3.1 Characterization of bare and doped iron oxide

The X-ray powder diffraction patterns shown in Fig. 4.2(a) revealed the presence of a hematite-like phase as almost a single phase in all four samples where all of the diffraction peaks could be indexed to rhombohedral structure of α-Fe_2O_3 with R3c space group (JCPDS file no. 33-0664). For the as-prepared Mn/Cu/Ce-doped α-Fe_2O_3, no other crystalline phase corresponding to their oxides and its related secondary or impurity phase was detected in the diffraction pattern. However, to observe the effect of doping in host lattice structure, the high intensity peak corresponding to (110) plane was monitored. The inset in Fig. 4.2(a) displays that a lower angle shifting occurred for Cu and Ce doped samples where the former showed higher degree of shifting in comparison to that of pure hematite. This observation can be explained based on the ionic radius differences between the Cu^{2+}(0.073nm) and Ce^{3+}(0.101nm) /Ce^{4+} (0.097 nm) dopants and Fe^{3+}(0.065nm).[14,15] The crystal lattice expands when a dopant with a larger ionic radius is introduced. This causes tensile stress, which may increase the distances between nearby atoms, causing peak shifting in a lower angle.[16,17] However, the higher extent of peak shifting in case of Cu doped sample could be due to the higher polarizing power of Cu^{2+}

compared to Ce^{3+}/Ce^{4+} having larger ionic radius. On the other hand, a very nominal shifting of 0.01° at higher angle was observed in case of Mn doped sample. The observation suggests that Mn could exist in +II or +III state which has similar ionic radius[18,19] with Fe^{3+} that causes subtle differences in the electronic structure or charge distribution between the dopant and host ions leading to a slight shift in the lattice positions.

The samples were subsequently examined by Raman spectroscopy (Fig.4.2(b)) to support the XRD results. Hematite with its corundum structure falls into D3d point group. They include two $A1_g$ modes involving symmetric stretching of oxygen atoms and five E_g modes involving symmetric stretching and bending of iron-oxygen bond. The intense peak at ~225 cm^{-1} and the weak peak around 495 cm^{-1} correspond to $A1_g$ modes, and the peaks around 251, 298, 411, and 613 cm^{-1} represent the E_g modes of α-Fe_2O_3 assigned as FETP.[20,21] The additional peak around 667 cm^{-1} corresponds to IR active E_u mode as reported in literature.[22] However, no such significant peak shifting was observed after doping of α-Fe_2O_3 samples. This observation suggests that dopant has insignificant effect on the vibrational modes associated with the lattice vibrations or molecular bonds. Therefore, it is suggested that the corresponding dopant has integrated into the crystal lattice without causing major structural distortions.

FTIR study of the synthesized bare and doped iron oxide based samples are shown in Fig. 4.2(c). Similar types of band were found in the case of the un-doped and doped α-Fe_2O_3. The relative intensities and position of these bands have not changed significantly except with the minor distortion in the band area spanning from 470 to 581 cm^{-1} which represents the distinctive stretching vibration of the Fe-O bond.[23]Mn-O/Cu-O/Ce-O vibrational peaks are predicted to resemble those in the Fe-O range (460-600 cm^{-1}), which makes them quite difficult for precise identification.[24,25]However, with doping, the intensity of the Fe-O peak was also found to decrease, which could be attributed to the distortion of Fe-O crystal lattice caused by the presence of corresponding dopants.[26,27]The O-H stretching and bending vibrations of the absorbed water molecules in the samples were identified with the absorption bands at 3432 and 1629 cm^{-1}, respectively. A small band at 1115 cm^{-1} corresponding to the bending vibration of hydroxyl group (M–OH) was observed in all the samples.[28–30] FTIR study implies that the dopant cations have no significant effect on the vibrational characteristics of undoped α-Fe_2O_3.

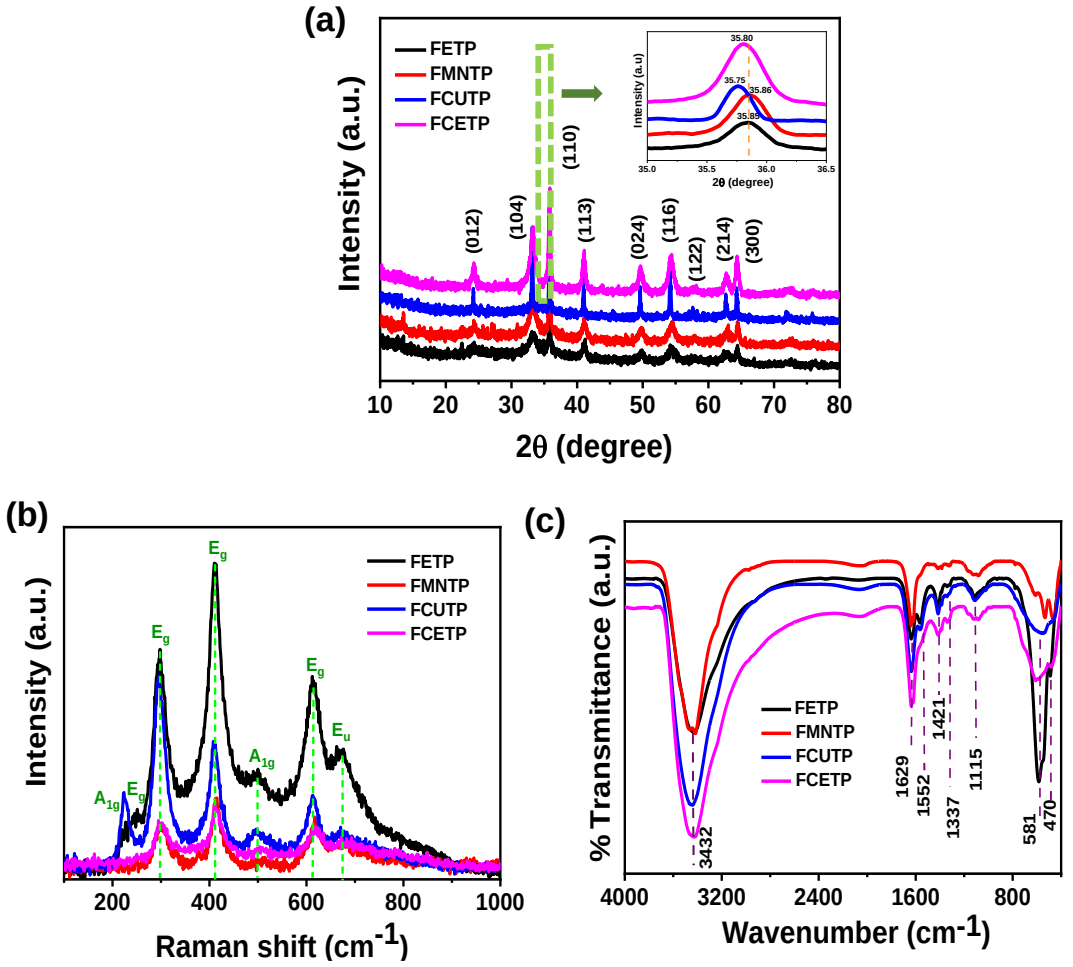

Figure 4.2: (a) XRD pattern, (b) Raman spectra and (c) FTIR spectra of bare and doped α-Fe_2O_3.

Fig. 4.3(a) shows the N_2 adsorption-desorption isotherms of the samples (i) FETP, (ii) FMNTP (iii) FCUTP and (iv) FCETP. According to the IUPAC classification, the curves show type IV isotherms, indicating the mesoporous characteristics of the samples. The BET surface area follows the order as: FCETP>FCUTP>FETP>FMNTP. It is worth noting that during precipitation and subsequent hydrothermal reaction process, Ce^{3+}/Ce^{4+} and Cu^{2+}ions provide additional nucleation sites, leading to the formation of solid products with larger surface areas,[31] while Mn^{2+}/Mn^{3+} shows no significant effect on BET surface area of α-Fe_2O_3. FCUTP and FCETP samples exhibited H2 type hysteresis loops above the relative pressure (p/p_o) of 0.45 signifying ink-bottle-like mesopores, whereas H3 type hysteresis loop was exhibited by FMNTP and FETP signifying narrow slit like pores. Here, pore geometry also plays an important role in changing the surface area of the samples. Fig. 4.3(b) displays the corresponding BJH pore size distributions where the pore diameter of all the samples is in the

range of 3.3-3.7 nm. Table 4.1 shows BET surface area, pore volume and pore size values of all samples. Among all the samples Cu doped α-Fe_2O_3 (FCUTP) shows maximum pore volume compared to other samples. In particular, Ce doped α-Fe_2O_3 (FCETP) having higher BET surface area indicates lower pore volume than Cu and Mn doped α-Fe_2O_3.

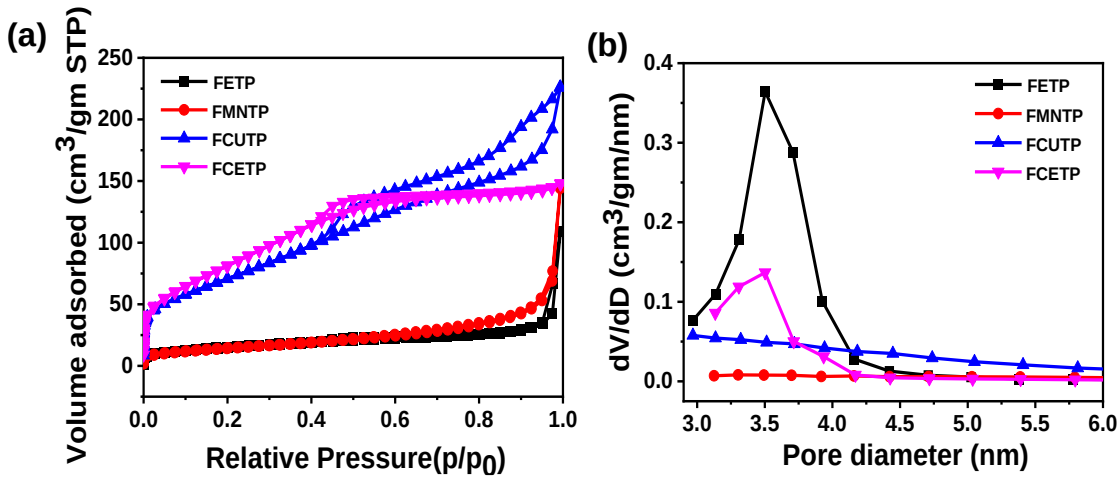

Figure 4.3: (a) BET isotherms, (b) BJH pore size distributions of bare and doped α-Fe_2O_3.

Table 4.1: The textural properties of bare and doped α-Fe_2O_3.

Sample ID	S_{BET} (m^2/gm)[a]	$V_{p\text{-}Total}$ (cm^3/gm)[b]	D_{BJH} (nm)[c]
FETP	53.90	0.168	3.49
FMNTP	51.9	0.224	3.33
FCUTP	263.9	0.35	3.70
FCETP	312.5	0.111	3.50

[a] Specific surface area, [b] Total pore volume, [c] Pore diameter

The X-ray photoelectron spectroscopy (XPS) determines the valence states of Fe and O ions and the surface chemical compositions of the representative bare and doped samples. Fig.4.4 shows (a) survey peaks of FETP, FMNTP, FCUTP and FCETP, and (b) Mn2p, (c) Cu2p and (d) Ce3d peaks for samples FMNTP, FCUTP and FCETP, respectively. Fig. 4.4(e) Fe2p and (f) O1s shows the deconvoluted XPS spectra of bare and doped α-Fe_2O_3, respectively. The binding energies around 710.7-711.4eV and 723-724eV are indicative of Fe $2p_{3/2}$ and Fe $2p_{1/2}$ in the high resolution Fe 2p spectra, which correspond to Fe^{3+} in α-Fe_2O_3 with two satellite peaks, clearly distinguishable at ~717.7eV and ~731eV.[32]However, a peak around 709.2-709.8

eV was found in the case of all the samples except FCUTP, which could be the indication of formation of intermediate γ-Fe_2O_3 phase at the surface prior to the formation of stable α-Fe_2O_3.[33] The peaks at binding energies of 712.9, 711.3 and 710.3 eV indicate the presence of Fe-O bond.[34,35] However, the peak position at ~714.8 eV of FCUTP is due to the presence of Fe^{3+}ions.All of these observations therefore, rule out the presence of Fe^{2+} species in the samples. The oxygen atoms bonded to iron (lattice oxygen) and oxygen atoms of hydroxyl groups (-OH) render peak positions of ~528.6-529.4 eV and ~530-530.2 eV respectively. The defect sites arising due to low oxygen coordination exhibited peaks at ~531.1 eV, whereas binding energies at 531.8-532.7 eV confirm the presence of chemisorbed and/or physisorbed water (Fe-OH) molecules on metal surfaces.[36,37]In the XPS spectrum of Mn2p (Fig.4.4(b)) for sample FMNTP, two distinct peaks were discernible with binding energies of 640.35 and ~651.5 eV for $Mn2p_{3/2}$ and $Mn2p_{1/2}$, respectively. Herein, Mn remains as (+II) and (+III) states in the hematite lattice.[38] Nevertheless, satellite shake-up peaks at around 645.58 eV and 653.2 eV are the signatures of $Mn2p_{3/2}$ and $Mn2p_{1/2}$, respectively.[39,40] Fig. 4.4(c) shows Cu $2p_{3/2}$ and Cu $2p_{1/2}$ binding energies of FCUTP at around 931.8 and 951.8 eV, respectively with their separation of 20 eV, indicating the presence of Cu^{2+}in the lattice.[41,42] The Ce3d spectrum of FCETP was deconvoluted into five primary peaks at 891.3 (Ce $3d_{3/2}$), 897.6 (Ce $3d_{5/2}$), 907.9 (Ce $3d_{3/2}$), 903.10 (Ce $3d_{5/2}$), and 895.2 (Ce $3d_{5/2}$) eV, the former 3 peaks are due to Ce^{3+} while the latter 2 peaks are assigned to Ce^{4+}(Fig. 4.4(d)). It confirms the coexistence of Ce^{3+} and Ce^{4+}in the lattice.[43,44] All of the above findings confirm the successful doping of metal ions in the hematite lattice.

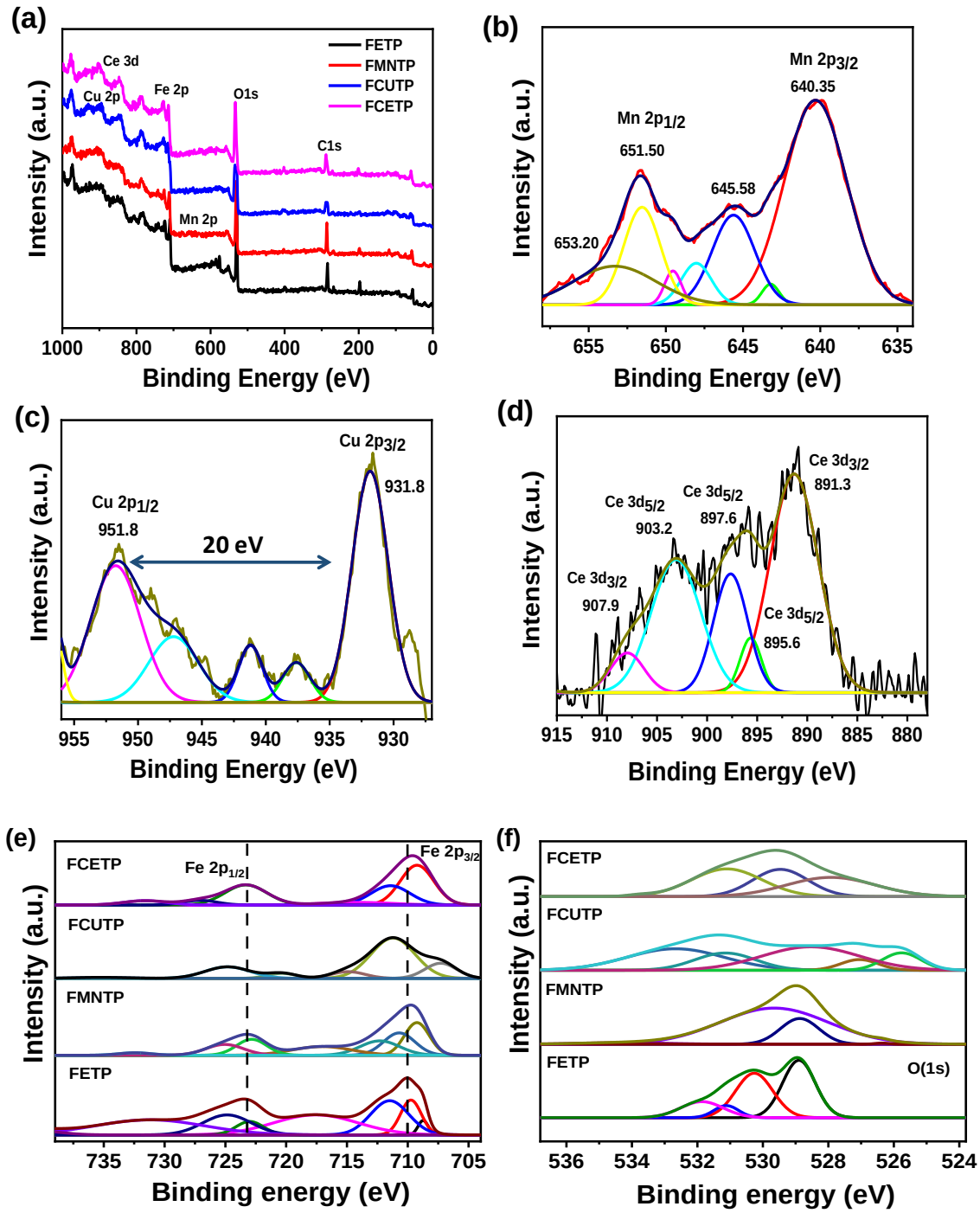

Figure 4.4: XPS spectra of (a) Survey, (b) Mn (2p), (c) Cu(2p), (d) Ce (3d), (e) Fe2p and (f) O1s for bare and doped α-Fe_2O_3.

The morphology of a catalyst is crucial for catalytic degradation as it influences the surface area, accessibility of active sites, mass transport, thereby controlling surface/volume ratio.[45] The FESEM and TEM images of the doped and bare α-Fe_2O_3 samples are shown in

Figs. 4.5 and 4.6, respectively. Fig. 4.5(a) shows the FESEM image of well dispersed quasi-ellipsoid shaped α-Fe_2O_3 particles with an average width of 300-320 nm and of length of 600-670nm.The Mn-doped α-Fe_2O_3 (FMNTP) resembled plate like morphology (Fig.4.5(b)) whereas, agglomerated particles were noticed for Cu (FCUTP) and Ce doped α-Fe_2O_3 (FCETP) (Fig. 4.5(c) and Fig. 4.5(d)).

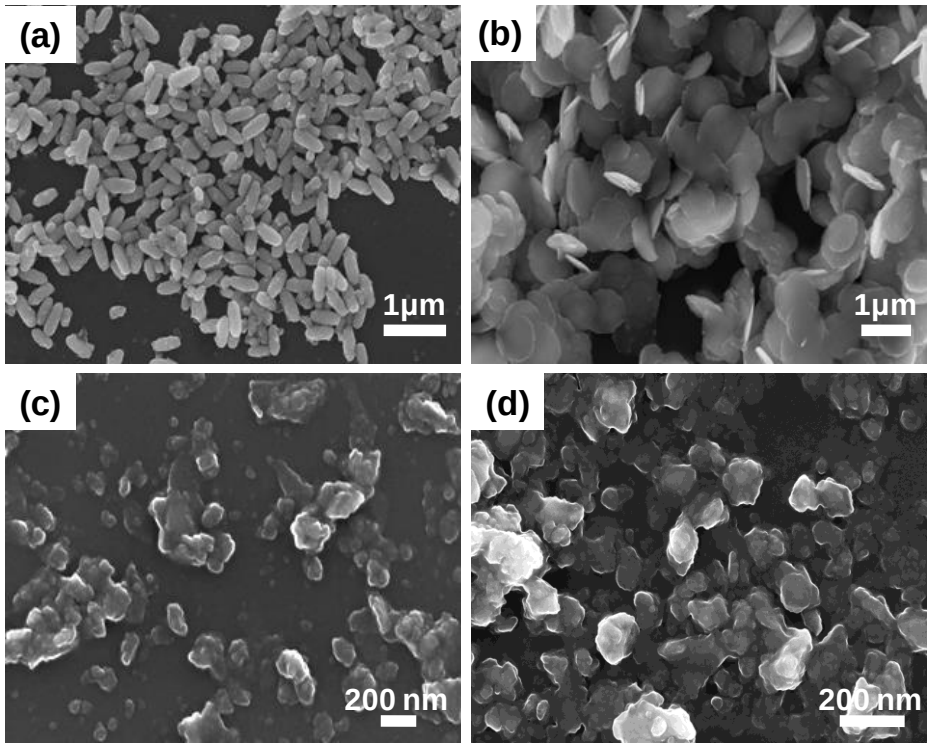

Figure 4.5: FESEM images of bare and doped α-Fe_2O_3 particles :(a) FETP, (b)FMNTP, (c) FCUTP and (d)FCETP.

A similar kind of microstructural feature is also clearly observed in TEM images for all the samples (Fig. 4.6). In the absence of any dopant cations, quasi-ellipsoid shaped α-Fe_2O_3 particles was noticed (Fig. 4.6(a)). TEM images of FMNTP, FCUTP and FCETP (Fig. 4.6(b)-(d)) exhibit highly porous microstructure of the samples. Fig.4.6(e)-(h) show the lattice fringe spacing in the range of ~0.26-0.28 nm for all the samples which was in good agreement with the spacing of the (110) lattice plane of α-Fe_2O_3. A slight increase in lattice spacing of FCUTP and FCETP is due to ionic size mismatch of Cu^{2+} and Ce^{3+}/Ce^{4+} with Fe^{3+}in the lattice, which goes in accord with the XRD peak shifting in lower angle.

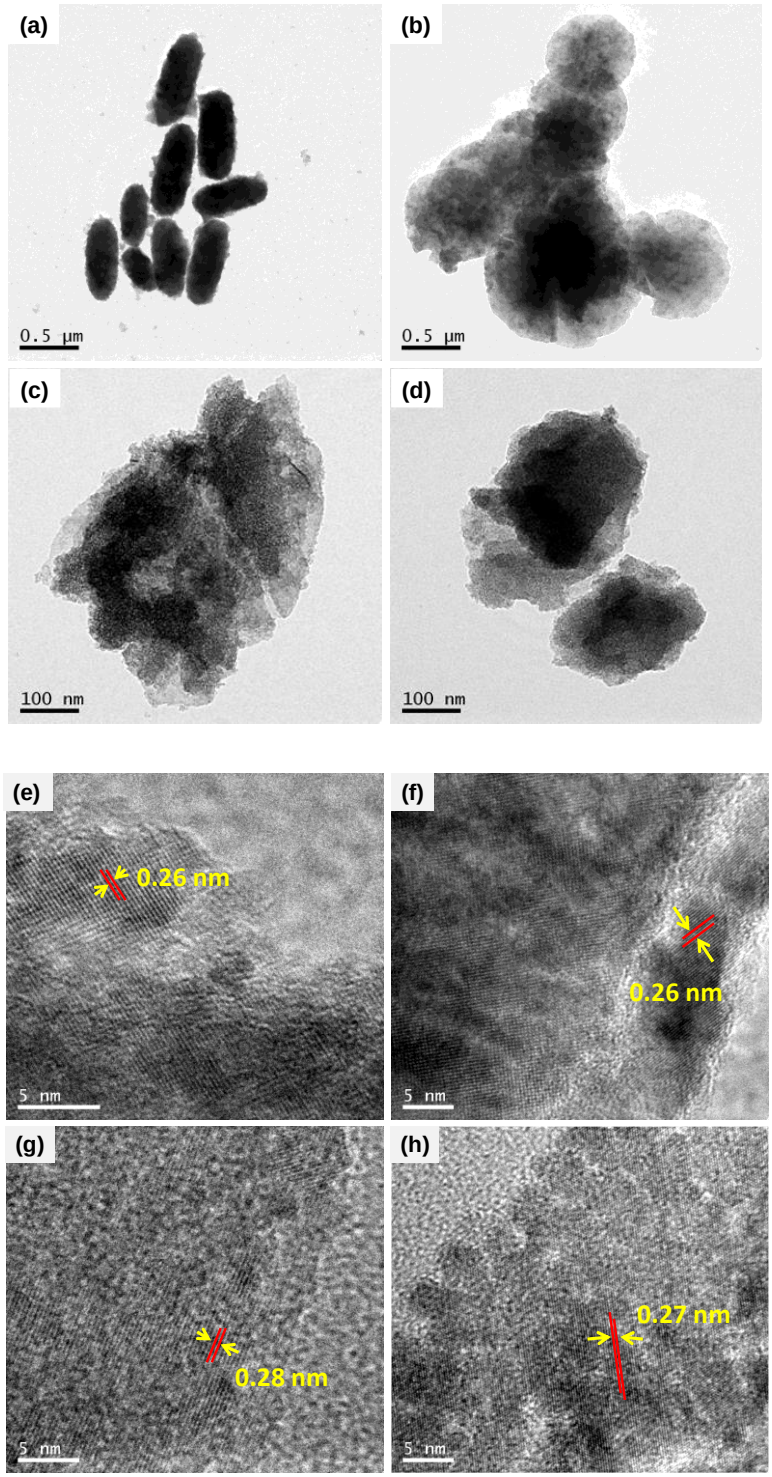

Figure 4.6: TEM images of bare and doped α-Fe_2O_3 particles: (a) FETP, (b) FMNTP, (c) FCUTP and (d) FCETP; HRTEM image of (e) FETP (f) FMNTP (g) FCUTP and (h) FCETP.

EDX analysis confirms the doping concentrations (wt%) of Mn, Cu and Ce in α-Fe_2O_3 particles as 3.48, 3.69 and 3.25% for the samples (a) FMNTP, (b) FCUTP and (c) FCETP, respectively (Fig.4.7).

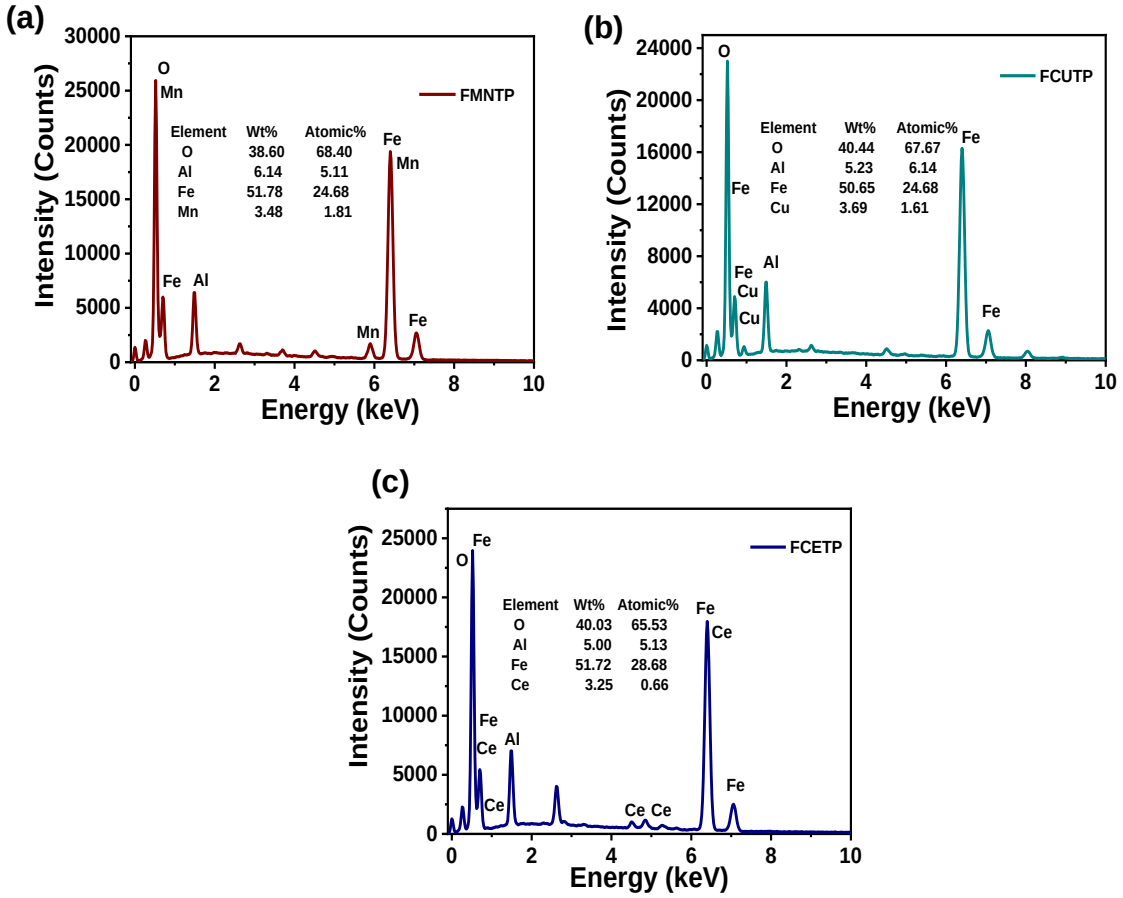

Figure 4.7: EDX spectra of doped α-Fe_2O_3 particles (a) FMNTP, (b) FCUTP and (c) FCETP.

4.3.2 Optical properties

The diffuse reflectance spectra reveal that FETP after metal doping exhibits stronger absorption in the visible region. It has been observed from the Kulbelka-Munk (K-M) plots that bandgap narrowing occurs with doping of Mn, Cu and Ce atoms into α-Fe_2O_3 lattice from 1.9 eV (for bare α-Fe_2O_3) to 1.2, 1.7 and 1.6 eV, respectively (Fig. 4.8(a)-(d)). This lowering of bandgap after metal doping further enhances visible light harvesting, which leads to an improvement in the photocatalytic performance.

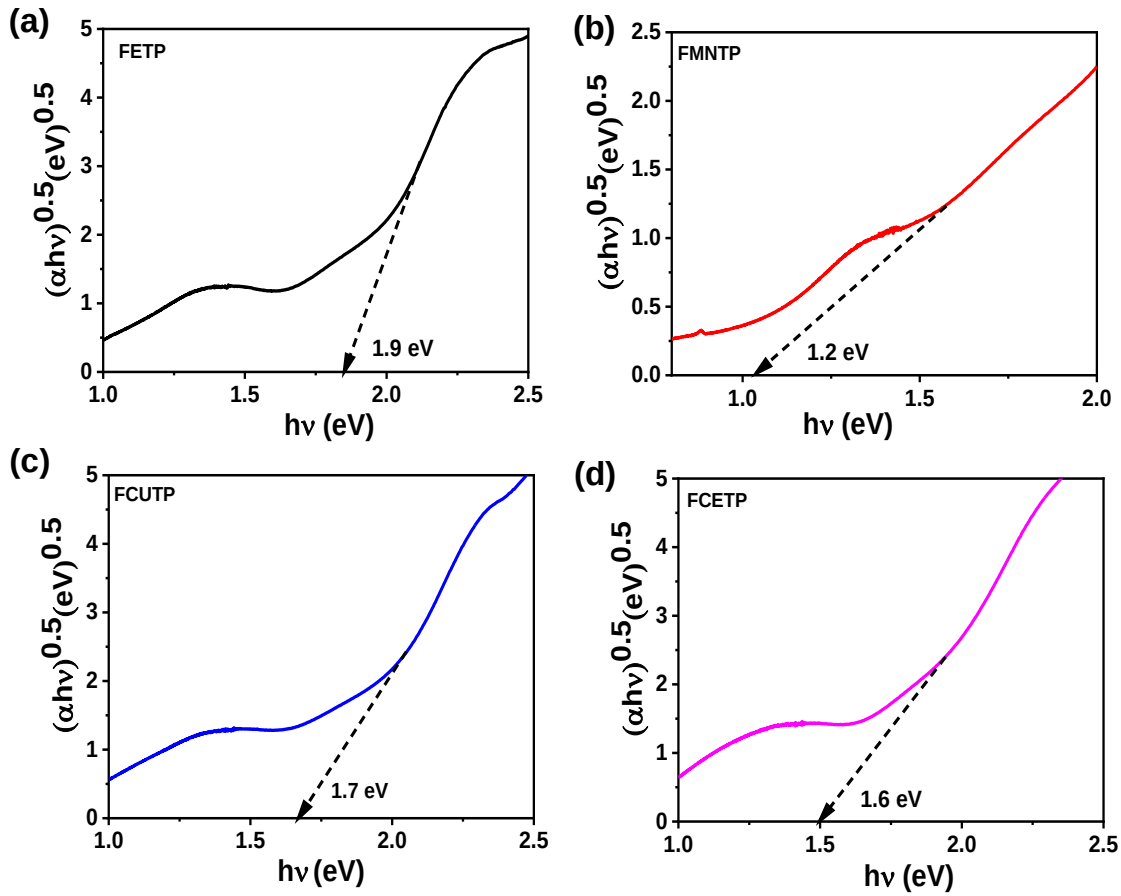

Figure 4.8: K-M Plots of (a) FETP, (b) FMNTP, (c) FCUTP and (d) FCETP.

4.3.3 Methylene blue degradation studies

Photocatalytic activity of iron oxides was examined by degradation of MB in the presence of visible light ($\lambda > 420$ nm). Within 60 min, all samples achieved adsorption equilibrium. The adsorption effectiveness of doped samples was observed to be higher in the case of FCUTP and FCETP with larger surface area compared to Mn doped (FMNTP) and un-doped α-Fe_2O_3 (FETP). Fig. 4.9 shows UV-Visible absorption spectra of MB degradation for the bare and doped α-Fe_2O_3 samples: (a) FETP, (b) FMNTP (c) FCUTP and (d) FCETP. The results of the blank test indicate that there was a little MB self-degradation under light. It was found that the distinctive absorbance peak at 664 nm gradually diminished over time. Fig. 4.9(e) shows the amount of photodegradation of MB over time for the samples FETP, FMNTP, FCUTP and FCETP respectively. The maximum % dye removal efficiency was shown by FCUTP (~91%) followed by FCETP (85.3%) and FMNTP (75.7%) within 60min of exposure time. Table 4.2 shows comparative data for MB dye removal efficiency.

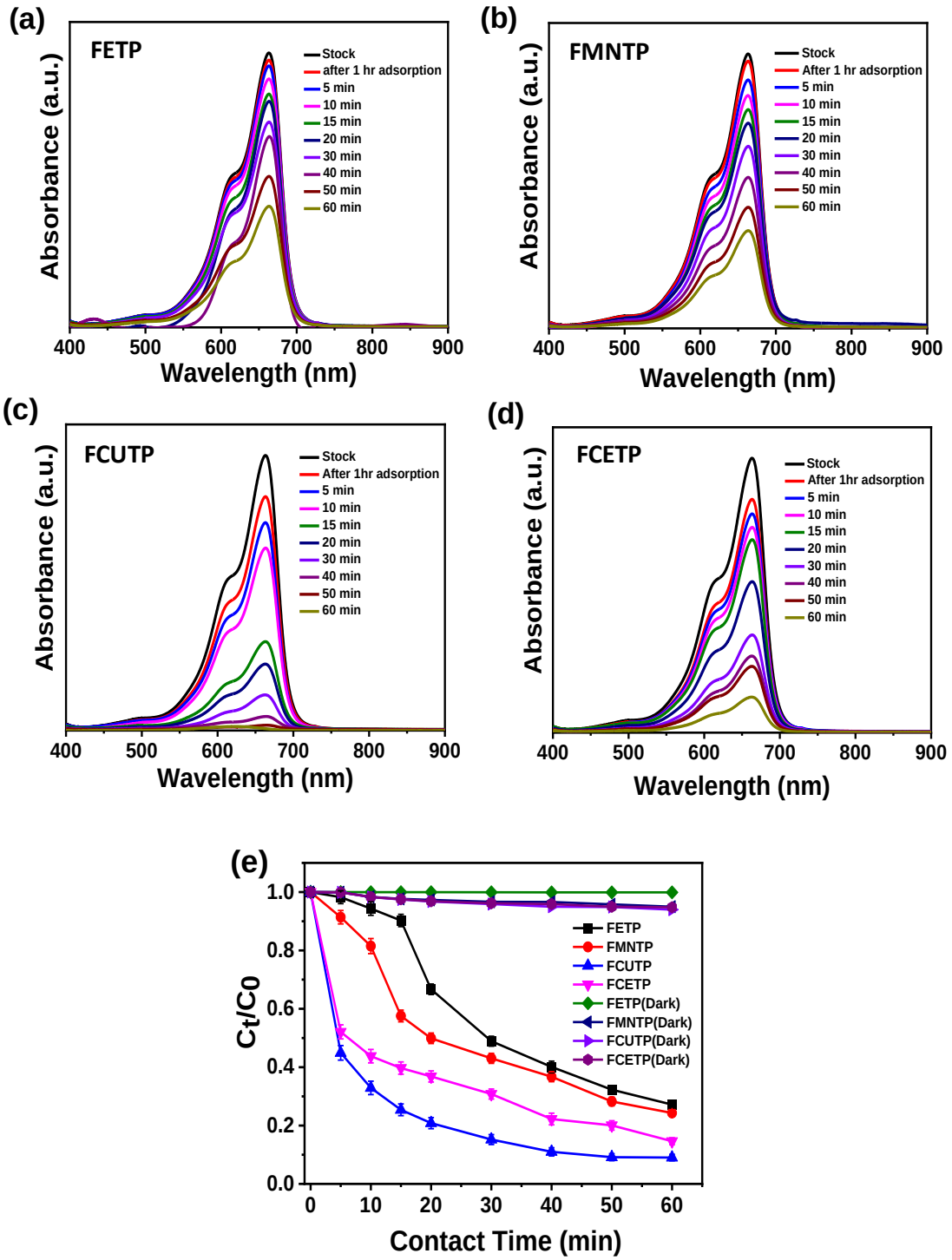

Figure 4.9: (a)-(d) UV-Visible absorption spectra and (e) degradation of MB for bare and doped α-Fe_2O_3 samples.

Table 4.2: The removal % of MB in the presence of different photocatalyst.

Sample ID	Removal %	Rate constant (min^{-1})	Ref
$MnTiO_3/TiO_2$ catalyst	76.0	0.005	46
GF/TiO_2 NTA	65.9	0.008	47
CuO nano particle	78.0	0.012	48
RM derived Cu dopedα-Fe_2O_3 catalysts	90.9	0.040	Present work

The stability of the photocatalyst was explored by testing reusability of the best performing Cu doped photocatalyst (FCUTP) under optimal conditions. Removing the photocatalyst from the reaction solution after each cycle, it was washed with distilled water followed by drying at 60 °C to remove organic contaminants. As shown in Fig. 4.10(a), there was no significant change in the photocatalytic activity of up to three cycles followed by gradual decrease in removal efficiency of MB. Furthermore, XRD analysis of the FCUTP sample were carried out to confirm the change in the crystalline structure before and after the 4^{th} cycle, as shown in Fig. 4.10(b). The crystal structure of FCUTP sample was nearly identical to the pristine sample, as revealed from XRD analysis conducted after four sequential photodegradation reactions. This outcome unequivocally confirmed the good stability of the photocatalyst.

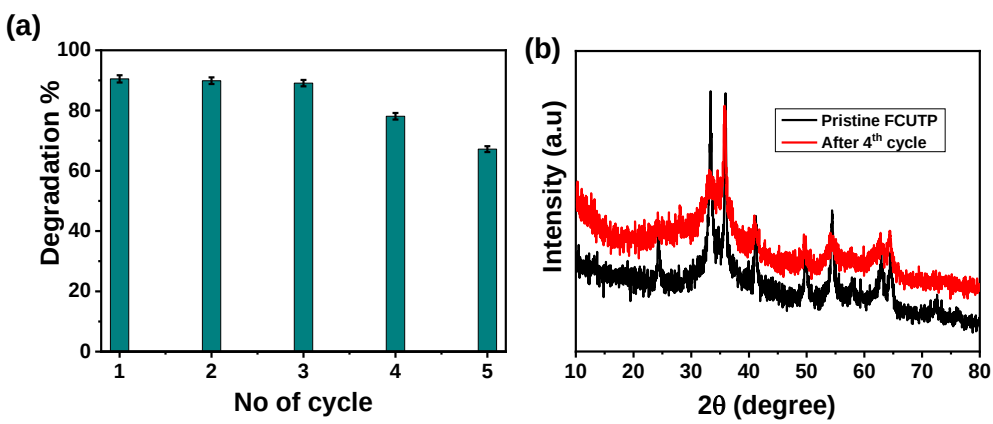

Figure 4.10: (a) Recyclability test (b) XRD pattern of FCUTP for photostability test.

Fig.4.11 shows the logarithm plots of absorbance $-\ln(C_t/C_0)$ versus reaction time (t) for all the samples where the pseudo-first order kinetics was found to be followed.

$$\ln(C_t/C_0) = -Kt \qquad (4.3)$$

Where, C_0 represents the initial concentration of dye and C_t represents the concentration of dye at reaction time t(min) and K represents the rate constant of reaction.

Table 4.3 represents the, percentage of adsorption, percentage of pollutant degradation and rate constants of the samples. It shows that % adsorption and degradation of MB as well as rate constant significantly increased with Cu doping (FCUTP) followed by Ce doping (FCETP). Instead of lower surface area of Cu doped α-Fe_2O_3 than Ce doped α-Fe_2O_3, the former shows higher % adsorption because of increased pore volume. However, with Mn doping (FMNTP) an insignificant % of adsorption and degradation of MB was noticed because of lower surface area. The effect of dopant cations in α-Fe_2O_3 lattice on the adsorption and degradation mechanism of MB has been explained shortly in Section 3.5.

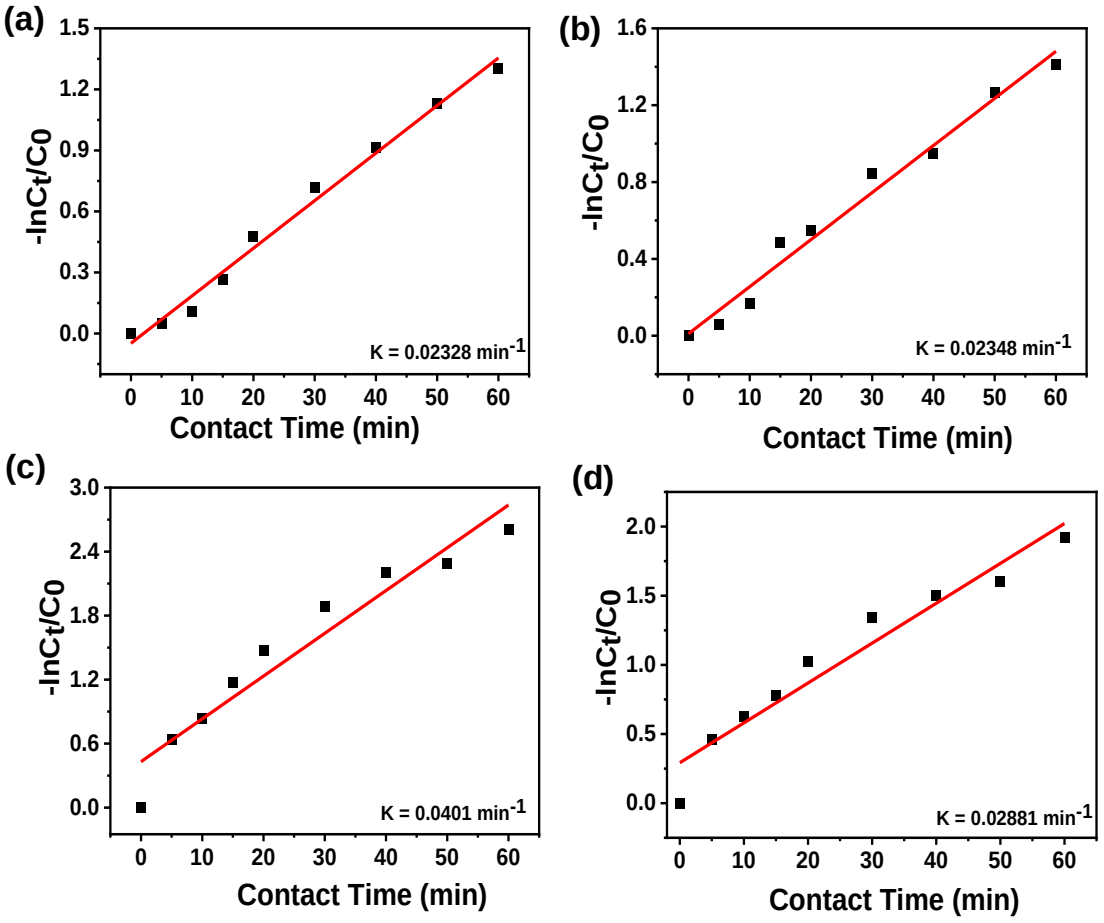

Figure 4.11: The logarithm plots of the absorbance ($-\ln(C_t/C_0)$) with reaction time for bare and doped α-Fe_2O_3 sample: (a) FETP, (b) FMNTP, (c) FCUTP and (d) FCETP.

The experiment under simulated solar light (CX-05E, AC input 200-240 , 300 W Xe lamp) was also performed using the best performing Cu doped α-Fe_2O_3 photocatalyst (FCUTP). Accordingly photocatalytic rate constant (K) (Fig. 4.12 (b)) was calculated by re-plotting photodegradation ratio (Fig. 4.12 (a)) following first order reaction equation as discussed earlier. Interestingly, in presence of solar light, a comparable photocatalytic efficiency was achieved with rate constant of 0.0369 min^{-1}.

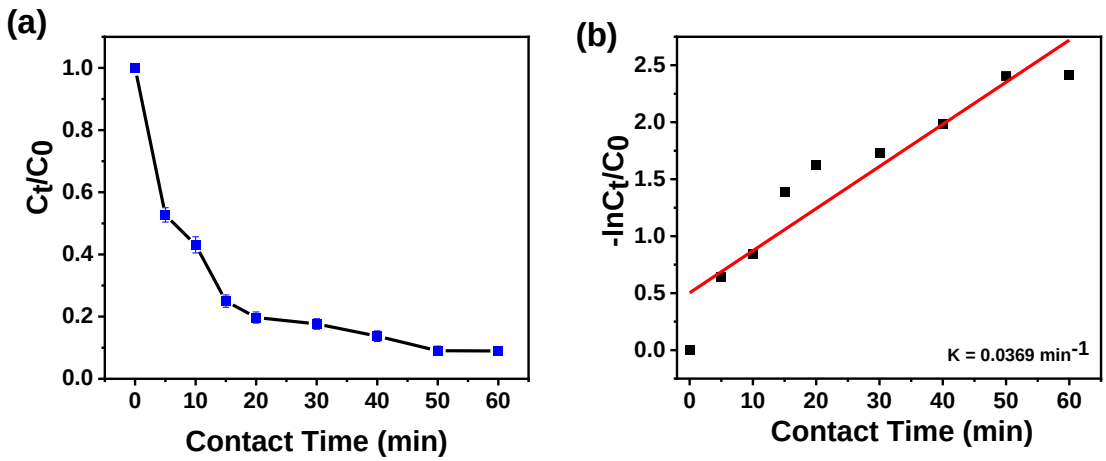

Figure 4.12: (a) Degradation of MB with time, (b) The logarithm plots of the absorbance ($-\ln(C_t/C_0)$) with reaction time for Cu doped α-Fe_2O_3 sample (FCUTP).

Table 4.3: The %adsorption and %degradation of MB, rate constant of the bare and doped α-Fe_2O_3 sample.

Sample ID	% of MB adsorption	% of MB degradation	Rate constant (K) in min^{-1}
FETP	4.78	72.9	0.02326
FMNTP	7.82	75.7	0.02348
FCUTP	17.8	90.9	0.04010
FCETP	15.6	85.3	0.02881

4.3.4 Quenching Studies

The photocatalytic process is commonly occurred with some important photo-induced reactive species, such as hydroxyl radicals (•OH), holes in HOMO (h^+), and electrons in LUMO (e^-).[49] Typically, isopropyl alcohol (IPA), a specified scavenger of •OH radicals, was employed under optimum conditions to identify the responsible free radicals against the best performing Cu doped system. The dye removal efficiency was significantly reduced on addition of IPA indicating the strong influence of •OH radical during oxidation process. Notably, in the presence of IPA, the removal percentage decreased from 90.9 % to 81.6 % in 60 min of reaction time. The results demonstrated that •OH radicals were the predominant reactive species causing effective breakdown of the conjugated system. However, addition of $AgNO_3$ (an electron scavenger) also showed a negative impact on the rate of reaction, indicating the role of electrons as a reactive species for the photocatalytic degradation process.

Fig. 4.13 illustrates TOC reduction for the concerned dye utilising the best-performing material FCUTP in different reaction times with 0.4 gm/L of catalyst concentration. In 60min, ~91% colour and ~84.7% TOC removal yielded the highest levels of decolorization and mineralization, respectively. However, after being exposed to visible light for 90 minutes, 86.5% of the TOC content was attained without any effect on decolouration.

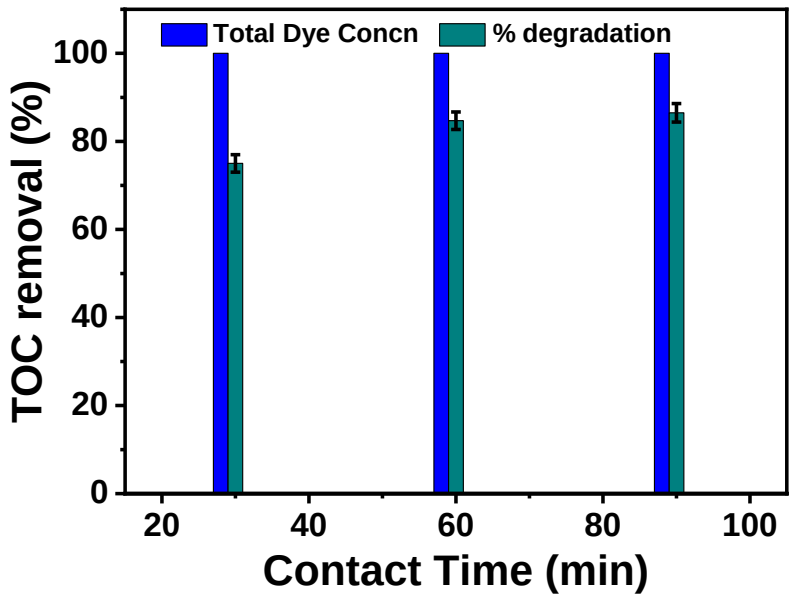

Figure 4.13: TOC removal% at different reaction time.

4.3.5 Photoelectrochemical Performance and Mechanistic Study

In order to explore how doping of a single semiconductor with various metal atoms can influence the rate of charge carrier recombination and facilitate interfacial charge transfer, the photoelectrochemical investigation was carried out. Linear Sweep Voltammetry measurements were performed under light irradiation condition in order to determine the photo response of the as-synthesized materials of bare α-Fe_2O_3, and 3 wt% doping content of Mn, Cu and Ce each. Fig. 4.14(a) shows that among all samples, the highest photocurrent density of ~1.1μA /cm^2 was obtained for FCUTP at 0.9 V vs Ag/AgCl, which is equivalent to 2-fold augmentation as compared to bare FETP (0.5 μA /cm^2). FMNTP and FCETP exhibit a photocurrent density of 0.91μA /cm^2 and 0.8 1μA /cm^2 at 0.9 V vs Ag/AgCl, respectively. Moreover, there has been a slight cathodic shift in the onset potential for Cu, Mn and Ce doped FETP with respect to pure FETP, which also indicates an enhancement in the photoelectrochemical performance after doping with the metal atoms. Fig. 4.14(b) represents the linear sweep voltammogram of FCUTP with 0.5 and 2% doping concentrations of Cu. It was observed that FETP with 3% Cu doping exhibits the highest photocurrent density (Fig. 4.14(a)) as compared to other compositions (Fig. 4.14(b)). The transient photocurrent measurements have been carried out in order to determine the stability of the materials against photo corrosion (Fig. 4.14(c)). It was observed that FETP samples after doping with Mn, Cu and Ce are fairly stable under light irradiation.

Electrochemical impedance measurements were carried out to understand the charge transport and migration at the electrode and electrolyte interface. Fig. 4.13(d) shows the Nyquist plots of the photoanodes, which have been further fitted with the Randles-equivalent circuit model as represented in the inset of the corresponding figure and Table 4.4. The lowest charge transfer resistance was observed for FCUTP (576 kΩ) as compared to bare FETP (1950 kΩ) which reveals that the charge transfer and conductivity improves considerably at the electrode-electrolyte interface after doping with Cu.

Table 4.4: Fitting parameters of Nyquist plots.

Material	R_S/Ω	$R_{CT}/k\Omega$	$C_{CT}/\mu Mho$	W/Ω
FETP	72.5	1950	4.5	60100
FMNTP	130	1511	5.6	0.009
FCUTP	60.8	576	9.0	0.001
FCETP	58.3	1790	4.1	0.006

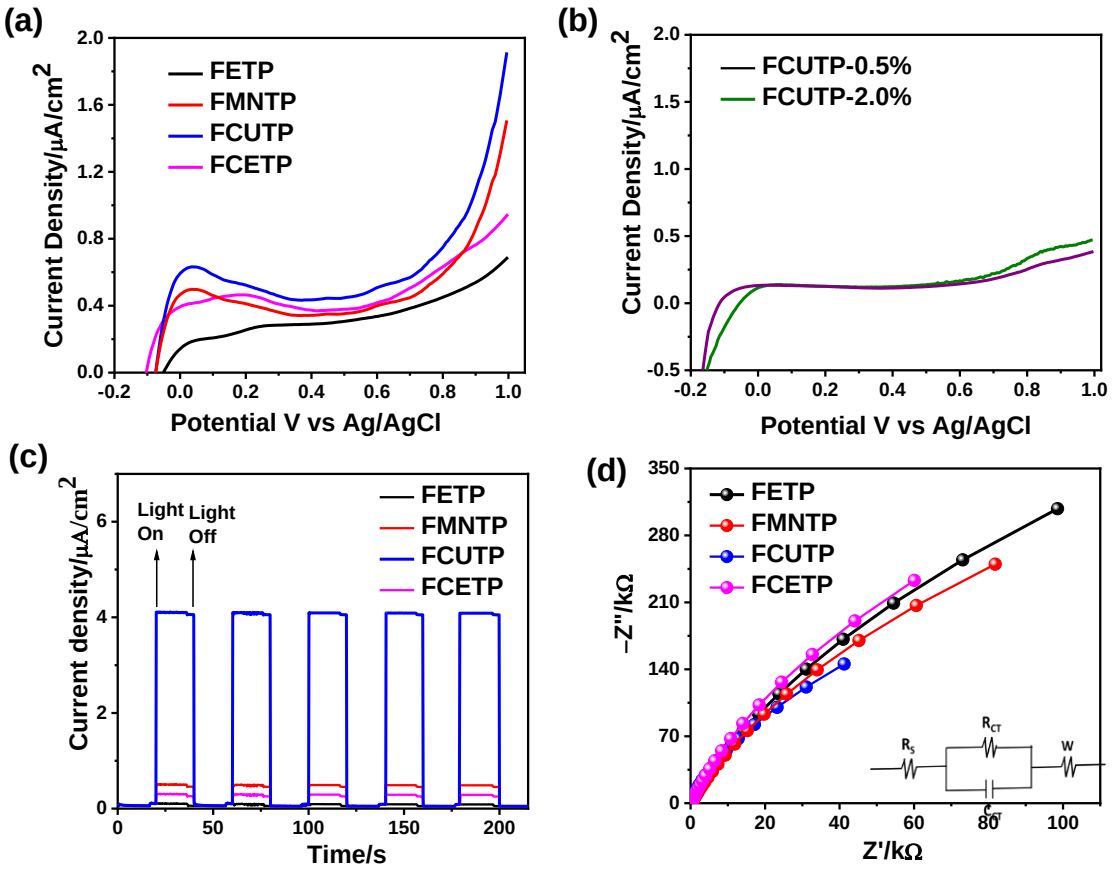

Figure 4.14: Linear Sweep Voltammogram of (a) FETP, FMNTP, FCUTP, FCETP, (b) FCUTP-0.5%, FCUTP-2%, (c) Transient photocurrent spectra, (d) Nyquist plots of FETP, FMNTP, FCUTP, FCETP.

In order to gain insight into the relative band structure, the flat band potential (E_{fb}), nature of semi conductivity and charge carrier concentration (N_d) have been determined using Mott-Schottky analysis. The Mott-Schottky equation is as follows:

$$\frac{1}{C^2} = \frac{2}{q\varepsilon_0\varepsilon N_d}\left(E_{app} - E_{fb} - \frac{kT}{q}\right) \qquad (4.4)$$

Here, the junction capacitance is denoted by C, the donor density is represented by N_d, ε and ε_0 represent the dielectric constant of the semiconductor and the absolute permittivity of vacuum, respectively. E_{app} and E_{fb} specify the applied potential and the flat band potential, respectively. The Boltzmann constant is indicated as k, and q denotes the elementary charge of an electron.[50,51] It was observed that pure FETP shows n-type semiconductivity which does not change upon doping with different metals. The flat band potentials (E_{fb}) for FETP, FMNTP, FCUTP and FCETP were noted as –0.32, –0.37, –0.38 and –0.40 V vs Ag/AgCl, respectively (Fig. 4.15). On the basis of difference in conduction band (CB) and E_{fb}, the conduction band minima (CBM) has been calculated as shown in Table 4.5. Furthermore, the valence band (VB) position has been estimated from the bandgap values and position of CBM of the as-synthesized materials.

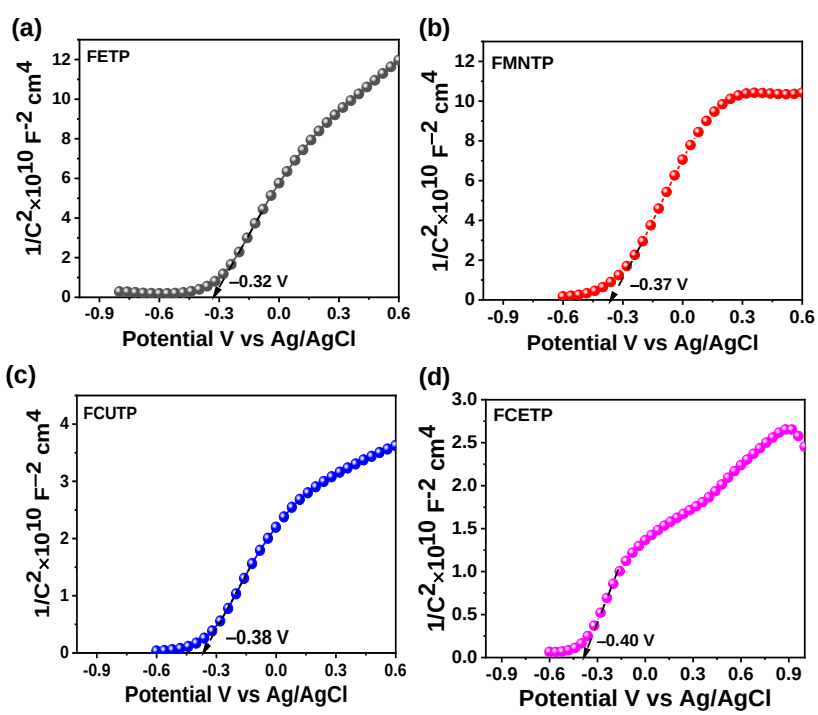

Figure 4.15: Mott-Schottky plots of (a) FETP (b) FMNTP (c) FCUTP (d) FCETP.

Interestingly, the charge carrier concentration of FETP increases after doping of different metals (Table 4.5). Moreover, FCUTP exhibits the highest charge carrier concentration (17.5×10^{18} cm^{-3}) among the as-synthesized materials which is 4.1 times higher than that of bare FETP (4.3×10^{18} cm^{-3}). The relative energy band diagram of bare FETP and FETP after doping with various metals has been presented in Fig 4.17.

Table 4.5: Position of conduction band, valence band and donor density of as-synthesized materials.

Material	**E_{fb} vs Ag/AgCl(V)**	**E_{fb} vs RHE (V)**	**CBM (eV)**	**Bandgap (eV)**	**VB (eV)**	**$N_d(cm^{-3})$**
FETP	–0.32	0.29	0.09	1.9	1.99	4.3×10^{18}
FMNTP	–0.37	0.24	0.04	1.2	1.24	10.4×10^{18}
FCUTP	–0.38	0.23	0.03	1.7	1.73	17.5×10^{18}
FCETP	–0.40	0.21	0.01	1.6	1.61	4.8×10^{18}

The Photoluminescence (PL) spectra of α-Fe_2O_3 and the doped hematite, excited at 350 nm is depicted in Fig. 4.16. Each material shows strong luminescence band at 404nm and 429 nm which might correspond to blue emission caused by electron and hole recombination. The emission arises from radiative recombination process where excited electrons in the CB recombine with holes in the VB releasing photons with equivalent energy. The presence of ionized oxygen vacancies and structural flaws creates additional energy levels leading to emission in longer wavelength ~452nm.[52–54] Notably, the decrease in PL intensity in case of doped samples suggest lowering in electron-hole pairs recombination rate; thereby, indicating enhanced charge carrier separation efficiency which is consistent with other experimental findings.[55] The intensity was found to be lowest in case of Cu doped α-Fe_2O_3 (FCUTP) which can be correlated with the highest photocurrent generation as observed from the photoelectrochemical measurements.

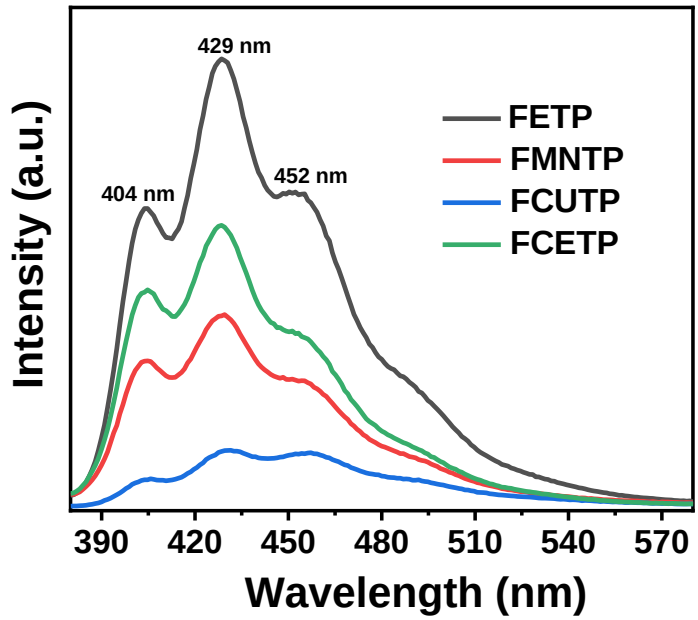

Figure 4.16: PL spectra of bare and doped α-Fe_2O_3.

For mechanistic approach of photocatalytic degradation of MB, it is understood that during catalytic breakdown of H_2O_2 in the presence of catalysts, H_2O_2 acts as a significant source of •OH production in the Fenton reaction. In this case, hydroxyl (•OH) and peroxide (HO_2•) radicals are produced when H_2O_2 is adsorbed on the catalytic surface.[56] The active sites of the catalytic surface get reacted by means of these radicals. Adsorbed H_2O_2 triggers a reaction in addition to the free radicals where a chain process drives the reactions forward. Ultimately, the released hydroxyl (•OH) radicals degrade the MB dye.

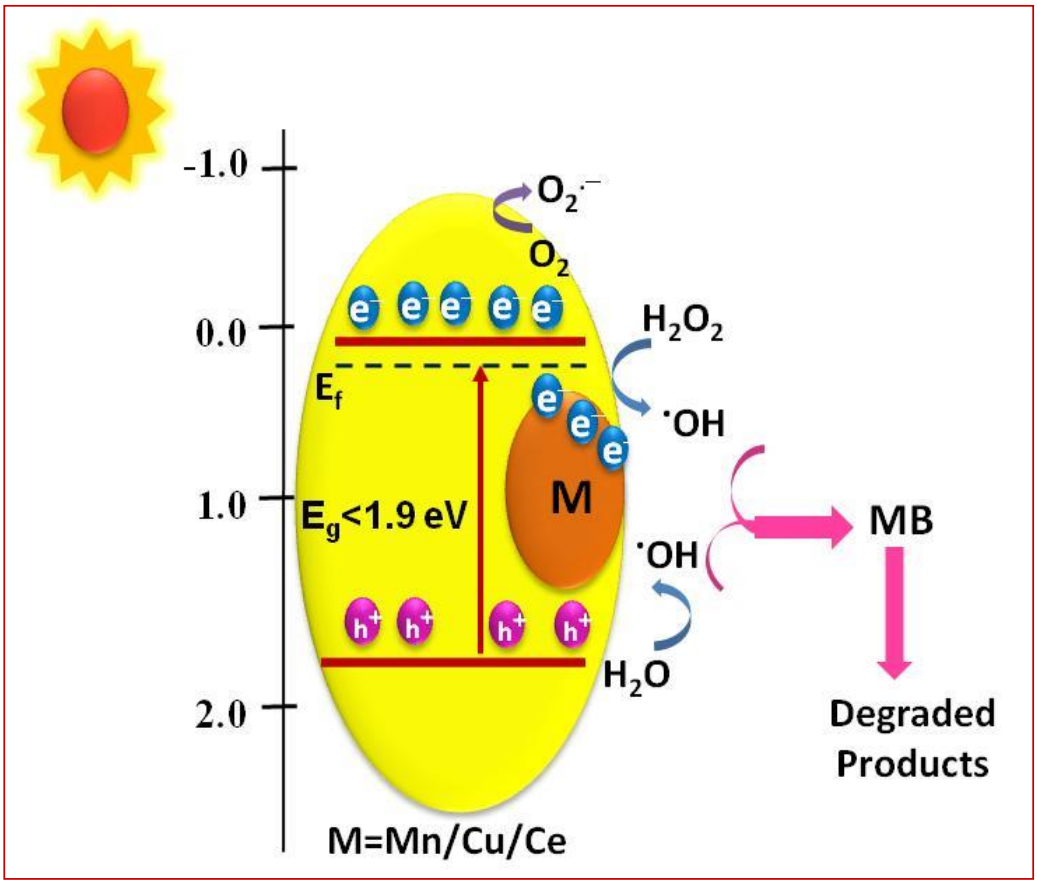

Figure 4.17: Schematic representation of relative energy band diagram of doped α-Fe_2O_3.

The enhanced photocatalytic activity of α-Fe_2O_3 doped with Cu, Ce, and Mn was ascribed to several factors like increased surface area, reduced band gap energy, decreased electron-hole recombination rate and enhanced electron-hole production efficiency in comparison to undoped α-Fe_2O_3. Cu doped α-Fe_2O_3 exhibited superior photocatalytic performance despite higher band gap energy and a smaller surface area compared to Ce doped Iron oxide. This can be explained by the higher photo response as observed from photoelectrochemical measurements. With exposure of light, it generates more free electrons in the redox reaction during the photocatalytic process. Instead of having lower band gap energy and slightly higher photo response of Mn doped sample as compared to Ce doped sample, the former showed lower photocatalytic performance. The low surface area of Mn doped sample with decrease in catalytic active sites could be the reason for its poorer catalytic performance. It is inferred that a synergistic effect of adsorption and photocatalysis takes part for photocatalytic degradation of MB with a number of governing factors like surface area, pore volume, band gap energy and photo response of the metal doped α-Fe_2O_3.

4.4 Conclusion

In this study, metal doped iron oxide-based catalysts derived from red mud were effectively synthesized by a simple hydrothermal process followed by their degradation study of methylene blue. The Ce doped α-Fe_2O_3 shows a maximum surface area of 312.5 m^2/gm while Cu doped sample renders maximum pore volume of 0.36 cm^3/gm. Microstructural studies reveal well-dispersed quasi-ellipsoid shaped α-Fe_2O_3 particles for undoped samples that get agglomerated with metal doping. XPS study confirms the presence of Mn^{2+}/Mn^{3+}, Cu^{2+}, Ce^{3+}/Ce^{4+} in α-Fe_2O_3 lattice wherein Fe exists as Fe^{3+}state.Cu doped α-Fe_2O_3 shows maximum % adsorption and photocatalytic degradation of MB due to its higher pore volume and photo response ability with significant increase in charge carrier concentration (17.5×10^{18} cm^{-3}). Nyquist plots for the metal-doped samples demonstrates a considerable lowering in the charge transport resistance in comparison to the pristine iron oxide. Experiments on radical capture reveals that electrons in addition to the hydroxyl radical produced from H_2O_2 are essential for the breakdown of MB solution. Iron oxide-based photocatalysts derived from red mud presents a viable, environmentally acceptable way to effectively remove organic dye from water. Additionally, the eco-friendly nature of iron oxide photocatalysts aligns with the growing emphasis on sustainable technologies including solar fuel production and CO_2 photoreduction.

References

1 Y. Cong, M. Chen, T. Xu, Y. Zhang and Q. Wang, *Appl. Catal B.*, 2014, **147**, 733–740.

2 G. K. Pradhan, N. Sahu and K. M. Parida, *RSC Adv.*, 2013, **3**, 7912–7920.

3 C. Singh, A. Goyal and S. Singhal, *Nanoscale*, 2014, **6**, 7959–7970.

4 A. A. Jahagirdar, N. Dhananjaya, D. L. Monika, C. R. Kesavulu, H. Nagabhushana, S. C. Sharma, B. M. Nagabhushana, C. Shivakumara, J. L. Rao and R. P. S. Chakradhar, *Spectrochim. Acta A. Mol. Biomol. Spectrosc.*, 2013, **104**, 512–518.

5 P. Xu, G. M. Zeng, D. L. Huang, C. L. Feng, S. Hu, M. H. Zhao, C. Lai, Z. Wei, C. Huang and G. X. Xie, *Sci.Total Environ.*, 2012, **424**, 1–10.

6 J. Gu, S. Li, E. Wang, Q. Li, G. Sun, R. Xu and H. Zhang, *J. Solid State Chem.*, 2009, **182**, 1265–1272.

7 C. N. C. Hitam and A. A. Jalil, *J. Environ Manage.*, 2020, **258**, 110050.

8 N. J. Cherepy, D. B. Liston, J. A. Lovejoy, H. Deng and J. Z. Zhang, *J. Phys. Chem B.*, 1998, **102**, 770–776.

9 T. K. Townsend, E. M. Sabio, N. D. Browning and F. E. Osterloh, *Energy Environ. Sci.*, 2013, **6**, 407–425.

10 A. M. Alenad, M. S. Waheed, S. Aman, N. Ahmad, A. R. Khan, R. Y. Khosa, M. Z. Ansari, S. A. Khan, H. M. T. Farid and T. A. M. Taha, *Mater. Res. Bull.*, 2023, **165**, 112306.

11 S. Khan, Z. Ajmal, S. Mahmood and M. ul Haq, *New J.Chem.*, 2023, **47**, 10333–10346.

12 H. G. Cha, H. S. Noh, M. J. Kang and Y. S. Kang, *New J.Chem.*, 2013, **37**, 4004–4009.

13 A. Chakraborty, P. K. Sinha and M. K. Naskar, *ACS Omega*, 2023, **8**, 29281–29291.

14 T. Takashima, H. Fukasawa, T. Mochida and H. Irie, *ACS Appl. Nano Mater.*, 2023, **6**, 23381–23389.

15 V. G, R. Subrayan, A. Pandiyan, S.-W. Cha and S. B. Krishna Moorthy, *J. Phys. Chem.C.,* 2019, 123, 541-553.

16 Q. Dou and Y. Zhang, *Langmuir*, 2011, **27**, 13236–13241.

17 N. Dhananjaya, H. Nagabhushana, B. M. Nagabhushana, B. Rudraswamy, C. Shivakumara, K. Narahari and R. P. S. Chakradhar, *Spectrochim. Acta A. Mol. Biomol. Spectrosc.*, 2012, **86**, 8–14.

18 R. Karmakar, S. K. Neogi, A. Banerjee and S. Bandyopadhyay, *Appl. Surf. Sci.*, 2012, **263**, 671–677.

19 W.-C. J. Wei, D.-R. Huang and D. Wang, *Materials*, 2016, **9**, 922.

20 C. W. Kim, A. U. Pawar, T. Hawari, N. H. Ahn, D. K. Lee, L. Yang, R. P. Sivasankaran, J. Tang, Z. Zhuo and Y. S. Kang, *Sci. Rep.*, 2022, **12**, 20972.

21 M. Testa-Anta, M. A. Ramos-Docampo, M. Comesaña-Hermo, B. Rivas-Murias and V. Salgueiriño, *Nanoscale Adv.*, 2019, **1**, 2086–2103.

22 A. Yogi and D. Varshney, *J.Adv. Cerams.*, 2013, **2**, 360–369.

23 K. Raja, M. M. Jaculine, M. Jose, S. Verma, A. A. M. Prince, K. Ilangovan, K. Sethusankar and S. J. Das, *Superlattices Microstruct.*, 2015, **86**, 306–312.

24 R. Satheesh, K. Vignesh, A. Suganthi and M. Rajarajan, *J. Environ. Chem. Eng.*, 2014, **2**, 1956–1968.

25 M. Bielicka, U. Klekotka, O. Nowakowska, D. Satuła and B. Kalska-Szostko, *Adv. Powder Technol.*, 2023, **34**, 103925.

26 V. Kumar, D. S. Ahlawat, S. A. Islam and A. Singh, *Mater. Sci. Eng. B.*, 2021, **272**, 115327.

27 Y. Yang, X. Huang, Y. Yang, C. Wu, B. Lei, Q. Peng and G. Wang, *Int. J. Electrochem Sci.*, 2019, **14**, 3673–3683.

28 Y. Zhang, M. Yang and X. Huang, *Chemosphere*, 2003, **51**, 945–952.

29 J. Bandara, J. A. Mielczarski and J. Kiwi, *Langmuir*, 1999, **15**, 7670–7679.

30 A. Chakraborty and M. K. Naskar, *Mater. Adv.*, 2022, **3**, 8544–8556.

31 Ö. Kerkez-Kuyumcu, E. Kibar, K. Dayıoğlu, F. Gedik, A. N. Akın and Ş. Özkara-Aydınoğlu, *J. Photochem. Photobiol A Chem.*, 2015, **311**, 176–185.

32 L. Feng, S. Gai, F. He, P. Yang and Y. Zhao, *ACS Nano.*, 2020, **14**, 7245–7258.

33 S. Arumugam, Y. Toku and Y. Ju, *Sci. Rep.*, 2020, **10**, 5407.

34 A. P. Grosvenor, B. A. Kobe, M. C. Biesinger and N. S. McIntyre, *Surface and Interface Analysis: An International Journal devoted to the development and application of techniques for the analysis of surfaces, interfaces and thin films*, 2004, **36**, 1564–1574.

35 L. Li, P. Ma, S. Hussain, L. Jia, D. Lin, X. Yin, Y. Lin, Z. Cheng and L. Wang, *Sustain. Energy Fuels*, 2019, **3**, 1749–1756.

36 A. Samanta and S. Jana, *ACS Appl. Nano Mater.*, 2021, **4**, 5131–5140.

37 L. U. Yi, C. Le, L. U. Chunhua, N. I. Yaru and X. U. Zhongzi, *J.Rare Earths*, 2013, **31**, 1183–1190.

38 H. G. Cha, H. S. Noh, M. J. Kang and Y. S. Kang, *New J. Chem.*, 2013, **37**, 4004–4009.

39 R. Grissa, H. Martinez, S. Cotte, J. Galipaud, B. Pecquenard and F. Le Cras, *Appl. Surf. Sci.*, 2017, **411**, 449–456.

40 D. Sun, L. Peng, K. Cheng and Y. Zheng, *J.CO2 Util.*, 2023, **68**, 102382.

41 M. A. Dar, S. H. Nam, Y. S. Kim and W. B. Kim, *J. Solid State Electrochem.*, 2010, **14**, 1719–1726.

42 D. Tahir and S. Tougaard, *J.Condensed Matter.Phys.*, 2012, **24**, 175002.

43 Z. You, K. Yue, J. Zhang, P. Ke, D. Gu, Q. Guo and W. Luo, *Optik.*, 2019, **176**, 241–245.

44 N. Suganthi and K. Pushpanathan, *Trans. Nonferrous Met. Soc. China*, 2019, **29**, 811–820.

45 R. Satheesh, K. Vignesh, A. Suganthi and M. Rajarajan, *J. Environ. Chem. Eng.*, 2014, **2**, 1956–1968.

46 S. Alkaykh, A. Mbarek and E. E. Ali-Shattle, *Heliyon*.,2020,6, e03663.

47 X. Cheng, H. Liu, Q. Chen, J. Li and P. Wang, *Carbon N Y.*, 2014, **66**, 450–458.

48 G. Sorekine, G. Anduwan, M. N. Waimbo, H. Osora, S. Velusamy, S. Kim, Y. S. Kim and J. Charles, *J. Mol. Struct.*, 2022, **1248**, 131487.

49 W. Zhou, M. Cao, S. Su, N. Li, X. Zhao, J. Wang, X. Li and C. Hu, *J. Mol. Catal A. Chem.*, 2013, **371**, 70–76.

50 S. Ghosh, S. Bera, S. Sardar, S. Pal, F. V. A. Camargo, C. D'Andrea and G. Cerullo, *ACS Appl. Mater. Interfaces.*, 2023, **15**, 18867–18877.

51 K. Sivula, *ACS Energy Lett.*, 2021, 6, 2549–2551.

52 A. R. Alzahrani, *Green Process. Synth.*, 2023, **12**, 20230126.

53 W. E. Pottker, R. Ono, M. A. Cobos, A. Hernando, J. F. D. F. Araujo, A. C. O. Bruno, S. A. Lourenço, E. Longo and F. A. La Porta, *Ceram. Int.*, 2018, **44**, 17290–17297.

54 L. H. Oliveira, A. P. De Moura, F. A. La Porta, I. C. Nogueira, E. C. Aguiar, T. Sequinel, I. L. V Rosa, E. Longo and J. A. Varela, *Mater. Res. Bull.*, 2016, **81**, 1–9.

55 N. Wang, B. Han, J. Wen, M. Liu and X. Li, *Colloids Surf A. Physicochem. Eng. Asp.*, 2019, **567**, 313–318.

56 M. Roy, S. Ghosh and M. K. Naskar, *Phys. Chem. Chem. Phys.*, 2015, **17**, 10160–10169.

Chapter 5

Summary and Future Directions

4.1 Summary

The present Ph.D. thesis work demonstrates the synthesis of agro waste and industrial waste based nano adsorbents. Agro waste rice husk ash was utilised for the synthesis of zeolite based adsorbents (MgO-zeolite and alumina gel@zeolite X composites) whereas industrial waste red mud was utilised for the synthesis of iron oxide based adsorbents and iron oxide based photocatalysts. The crystal structures, textural, microstructural and spectroscopic properties of the synthesized mesoporous materials and composites were analysed. The synthesized materials were employed as adsorbent/photocatalyst for the removal of different water pollutants. The thesis comprises of four Chapters

In **Chapter 1**, A general overview of water pollutants with various removal methods, their advantages and disadvantages was focused. Herein, different types of agricultural and industrial waste products, their uses and adverse effects was discussed. The significant emphasis has been given on the adsorption and photocatalysis processes due to their merits over other processes towards the removal of water contaminants.

In **Chapter 2,** the use of zeolite based adsorbent derived from rice husk ash was discussed in two subsections.

In chapter 2A, a facile template free synthesis of zeolite A-MgO composite was described in the presence of zeolite A, $MgCl_2$ and urea solution under hydrothermal reaction at 150 ºC for 5 h followed by calcination at 600 ºC/2 h. The simultaneous crystallization of MgO and NaA zeolite within the composite was confirmed by XRD and FTIR analysis. FESEM studies revealed formation of nano-sheet like MgO particles (50-70 nm) adhering to the the surface of NaA zeolite crystals (1µm). The sample exhibited a BET surface area of 69 m^2/gm and a pore size of 3.9 nm, suggesting the structural integrity of the zeolite with additional surface area and porosity through the incorporation of MgO nano-sheets. XPS study reflects the presence of Mg^{2+} indicating successful incorporation of Mg^{2+} in the composite material. Employing 1 gm/L of the Zeolite A-MgO composite dosage, 94% removal efficiency of fluoride was achieved within 90 min at pH 6.8. A probable mechanism for the adsorption of fluoride from aqueous solution was discussed.

In chapter 2B, a simple sol-gel synthesis of alumina gel@zeolite X nanocomposite was discussed prepared from rice husk ash derived zeolite X and alumina sol. The synthesized nano composite was characterized by XRD, FTIR, XPS, nitrogen adsorption-desorption study and FESEM and TEM. The aggregation pattern observed from microstructural studies infers a close

association between the nanoscale alumina particles (50 to 100 nm) and the micron-sized zeolite X particles (0.5 to 1 μm). This synthesized material with BET surface area 257 m^2/gm was employed for fluoride (F^-) ion adsorption with batch and column studies. In batch studies, the Langmuir model best described the adsorption isotherm, showing a maximum adsorption capacity of 103.6 mg/gm with an adsorbent dose of 0.5 gm/L. In column studies, the adsorption capacity q_0 (mg/gm) increased with higher initial fluoride concentrations and faster flow rates, but decreased with increasing bed heights. The breakthrough curves in column studies were analysed using different mathematical models. Among them, the Thomas model provided a best fit with the experimental data, while the bed depth service time (BDST) model determined the adsorption capacity of 2933.55 mg/L under the optimum conditions.

In **Chapter 3,** hydrothermally (150 °C/6-24 h) synthesized iron oxide (α-Fe_2O_3) derived from red mud in the presence of NH_4OH was discussed. The crystalline phase of α-Fe_2O_3 was confirmed by X-ray diffraction study which was further supported by Raman spectroscopic analysis. Microstructural investigation of the synthesized products obtained at 150 °C/24 h reveals the formation of flake-like structure. With increasing reaction time, the BET surface area decreased in the order of 347, 331 and 136 m^2/gm for 6 (FENH6), 12 (FENH12) and 24 h (FENH24), respectively. To study de-arsenification of water with the prepared iron oxide, influence of various factors like contact time, adsorbate and adsorbent concentrations, pH and temperature toward adsorption capacity was discussed. The highest adsorption capacity for As(V), ranging from 32 to 41 mg/gm, was achieved with an adsorbent dose of 0.25 gm/L. The adsorption process followed pseudo-second order kinetics and was best described by the Langmuir isotherm model. A tentative adsorption mechanism was also proposed.

In **Chapter 4,** hydrothermal synthesis of iron oxide based photocatalysts at 150 °C/24 h in the presence of tetra propyl ammonium hydroxide was illustrated. The incorporation of various metal (Mn, Cu, Ce) dopant ions into the α-Fe_2O_3 lattice significantly enhanced the photocatalytic performance of the catalysts in degrading methylene blue (MB) dye. The synthesized products were characterized by XRD, FTIR, UV–Visible spectroscopy, XPS, Raman spectroscopy, nitrogen adsorption-desorption study, FESEM, TEM, solid state UV and photoluminescence (PL) spectroscopy. The formation of rhombohedral α-Fe_2O_3 phase in the synthesized samples was confirmed by XRD and Raman spectroscopy. The incorporation of the metal dopants was assessed by XPS studies. The mesoporosity of all the samples was

evident from N_2 adsorption-desorption studies which showed highest surface area for Ce doped α-Fe_2O_3 (312.5 m^2/gm) followed by Cu doped (263.9 m^2/gm), bare α-Fe_2O_3 (53.9 m^2/gm) and Mn doped α-Fe_2O_3 (51.9 m^2/gm). This study revealed that doping of Mn, Cu, and Ce in α-Fe_2O_3 structure significantly impacts its photocatalytic performance. Kulbelka-Munk (K-M) plots showed that the bandgap of α-Fe_2O_3 decreased from 1.9 eV to 1.2, 1.7 and 1.6 eV with the incorporation of Mn, Cu, and Ce metal ions, respectively, enhancing light absorption. Electrochemical impedance spectroscopy demonstrates that the Cu-doped α-Fe_2O_3 showed lowest charge transfer resistance, indicating improved charge transfer and conductivity at the electrode-electrolyte interface compared to undoped Fe_2O_3 (FETP). Photocatalytic tests revealed highest removal efficiency (91%) of Cu doped α-Fe_2O_3 for degradation of MB dye followed by Ce-doped (85.3%) and Mn-doped α-Fe_2O_3 (75.7%) within 60 minutes. An interrelationship amongst the morphology, textural properties and the photocatalytic efficiency of α-Fe_2O_3 photocatalysts was established.

4.2 Future directions

The current thesis work provides a profound research direction on the synthesis and tuning properties of agro and industrial waste derived mesoporous adsorbents and photocatalysts for removal of water contaminants. Sustainable decontamination of major inorganic and organic water pollutants from water using waste based mesoporous materials is still demanding and challenging task. With the motivation of present dissertation work, future research direction could be proposed as follows:

i) Simultaneous removal of different inorganic and organic pollutants by using composite adsorbent material with tuned morphology and surface properties derived from different agro and industrial waste based products could address several critical challenges in environmental remediation and resource management.

ii) Mesoporous zeolite and iron oxide-based materials and composites extend many possibilities beyond environmental uses. Due to their unique structural and chemical properties, they are finding increasing demand in energy storage, renewable energy, and biomedical fields. The synthesis techniques described in this thesis can be adopted to prepare other mesoporous metal oxides and composites with tailored properties and broader applications.

iii) The future work plan also includes utilization of exhausted sludge to prepare glass-ceramic foam, aiming to prevent further secondary pollution. The main concept behind immobilizing toxic components in a glass-ceramic host is to synthesize a robust material that can be safely disposed or repurposed for beneficial uses. The glass-ceramic foams could be applied as building materials due to their thermal and acoustic insulating properties. Thus, it may explore new applications to maximize its potentiality in sustainable waste management.

The present dissertation work is significant for the benefit of living beings in terms of environment and health issues.

List of publications emanating from the thesis work

1. **A. Chakraborty** and M. K. Naskar*, “Study on the synthesis and structural properties of Zeolite A- MgO composite for defluoridation of water.” *Trans. Indian ceram. Soc*., 2021,80 (3),199-207.

2. **A. Chakraborty** and M. K. Naskar*, “Sol-gel synthesis of alumina gel@zeolite X nanocomposite for high performance water defluoridation: Batch and column adsorption study.” *Mater. Adv*., 2022,3,8544-8566.

3. **A. Chakraborty**, P.K. Sinha and M. K. Naskar*, “Low temperature processing of iron oxide nanoflakes from red mud extract toward favorable de-arsenification of water.” *ACS Omega,* 2023, 8, 32, 29281-29291.

4. **A. Chakraborty**, S. Samajdar, S. Ghosh and M. K. Naskar*, “Visible light induced photocatalytic removal of an organic dye using metal doped iron oxide based catalysts derived from red mud.” *New J. Chem*., 2024, 48, 10401-10414.

List of other publications / patent filed

1. S. Das, I. H. Chowdhury, **A. Chakraborty**, M. K. Naskar, M. Sarkar and S.K.M Islam*, "Porous organic polymer (POP) nanosheets: an efficient photo-catalyst for visible-light assisted CO_2 reduction." *Mater. Adv.*,2022, 3, 7, 3165-3173.

2. P. Bose, A. Hazra Chowdhury, **A. Chakraborty**, I. Hazra Chowdhury and M. K. Naskar*, "Solvothermal synthesis of spherical alumina: Delving into the formation mechanism and morphological change with phase transformation." *Chemistry Select*, 2023, 8, 1, e202203279.

3. P. Sarkar, I. H. Chowdhury, **A. Chakraborty**, M. Goswami, M. K. Naskar, A. Khan and S.K.M Islam*, "Visible light assisted photocatalytic CO_2 reduction and N_2-Fixation over TiO_2/ covalent organic framework heterojunction photocatalyst." *Ind. Eng. Chem. Res.,* 2024, 63, 13, 5591-5607.

4. T. Sarkar, M. K. Naskar, **A. Chakraborty**, P. K. Roy and S. Chakraborty*, "Preparation of high-strength waste-derived eco friendly ceramic foam as face brick and its estimation of building energy consumption for thermal insulation." *J. Build. Eng.,*2024, 88, 109043.

5. P. Bose, S. Basak,* I. Hazra Chowdhury, **A. Chakraborty** and M. K. Naskar, "Influence of Anions on the tunning properties of Nanostructured NiO for the Catalytic Oxidation of Carbon Monoxide." *Chemistry Select,*2024 (accepted)

❖ Patent filed in India: *"A process for the preparation of Fe-Ca composite using red mud extract and egg shell for removal of arsenic and iron from water"* (Name of inventors: Dr. Milan Kanti Naskar, **Ms. Adwitiya Chakraborty,** Dr. Shirshendu Chakraborty), Application number: **202311033471, dated 11.05.2023**.

Conference presentations

1. Poster presentation for the paper entitled "MgO modified rice husk ash derived zeolite for defluoridation of water" in the National conference on "**2nd Indian Materials Conclave and 31st Annual General Meeting of MRSI**" organized by CSIR-CGCRI, Kolkata during 11th-14th February, 2020.

2. Poster presented for the paper entitled "CTAB modified rice husk ash derived zeolite for defluoridation of water" at International conference on "**Engineering Sciences and Technologies for Environmental Care (ESTEC-2020)**" organized by CSIR-NEIST, Jorhat, Assam, India during 20th-22th February, 2020.

3. Poster presented for the paper entitled "Template-Free Synthesis of Rod Shaped γ-MnOOH toward organic dye adsorption" at International conference on "**Global trends in Traditional to Space Ceramics (GT-TSC'22)**" organized by the Indian Ceramic Society in association with the Department of Ceramic Engineering, IIT-BHU, Varanasi, during 8th-9th December 2022.

4. Poster presented for the paper entitled "Rice husk ah derived alumina gel@zeolite X for defluoridation of water; batch and column studies" at National conference on "**Emergent Materials for Energy and Environmet (EMEE-2023)**" organized by the Indian Institute of Technology Roorkee, (Department of Chemistry) IIT Roorkee, during 4th-5th March 2023.

5. Oral Presentation for the paper entitled "Low temperature processing of iron oxide nanoflakes from red mud extract toward favourable de-arsenification of water" in the National conference on "**The 34 Annual General Meeting of MRSI and 5 Indian Materials Conclave from December 12 - 15, 2023**)", organized by IIT BHU, Varanasi in collaboration with Materials Research Society of India (MRSI) during 12th-15th December 2023.